Properties of hot and dense strongly interacting matter

Eigenschaften heißer und dichter stark wechselwirkender Materie
Zur Erlangung des Grades eines Doktors der Naturwissenschaften (Dr. rer. nat.)
genehmigte Dissertation von M.Sc. Gábor András Almási aus Pécs
Tag der Einreichung: 16.05.2017, Tag der Prüfung: 19.06.2017
Darmstadt 2017 — D 17

1. Gutachten: Prof. Dr. Bengt Friman
2. Gutachten: Prof. Dr. Jens Braun

TECHNISCHE
UNIVERSITÄT
DARMSTADT

Fachbereich Physik
Institut für Kernphysik

Properties of hot and dense strongly interacting matter
Eigenschaften heißer und dichter stark wechselwirkender Materie

Genehmigte Dissertation von M.Sc. Gábor András Almási aus Pécs

1. Gutachten: Prof. Dr. Bengt Friman
2. Gutachten: Prof. Dr. Jens Braun

Tag der Einreichung: 16.05.2017
Tag der Prüfung: 19.06.2017

Darmstadt — D 17

Bitte zitieren Sie dieses Dokument als:
URN: urn:nbn:de:tuda-tuprints-67480
URL: http://tuprints.ulb.tu-darmstadt.de/6748

Erklärung zur Dissertation

Hiermit versichere ich, die vorliegende Dissertation ohne Hilfe Dritter nur mit den angegebenen Quellen und Hilfsmitteln angefertigt zu haben. Alle Stellen, die aus Quellen entnommen wurden, sind als solche kenntlich gemacht. Diese Arbeit hat in gleicher oder ähnlicher Form noch keiner Prüfungsbehörde vorgelegen.

Darmstadt, den 16. Mai 2017

(G. A. Almasi)

Abstract

In this thesis we consider effective models of quantum chromodynamics to learn about the chiral- and deconfinement phase transitions. In Chapter 1 we review basic properties of strongly interacting matter and the foundations of finite temperature field theory. We review furthermore the nonperturbative functional renormalization group (FRG) approach. In Chapter 2 we introduce the quark-meson (QM) model and its extensions including the Polyakov-loop variables and repulsive vector interactions between quarks. We then discuss features of the model both in the mean-field approximation and in the renormalization group treatment. A novel method to solve the renormalization group equations based on the Chebyshev polynomials is presented at the end of the chapter.

In Chapter 3 the scaling behavior of the order parameter at the chiral phase transition is studied within effective models. We explore universal and nonuniversal structures near the critical point. These include the scaling functions, the leading corrections to scaling and the corresponding size of the scaling window as well as their dependence on an external symmetry breaking field. We consider two models in the mean-field approximation, the QM and the Polyakov-loop-extended quark-meson (PQM) models, and compare their critical properties with a purely bosonic theory, the $O(N)$ linear sigma model in the $N \to \infty$ limit. In these models the order parameter scaling function is found analytically using the high temperature expansion of the thermodynamic potential. The effects of a gluonic background on the nonuniversal scaling parameters are studied within the PQM model. Furthermore, numerical calculations of the scaling function and the scaling window are performed in the QM model using the FRG.

Chapter 4 contains a study of the critical properties of net-baryon-number fluctuations at the chiral restoration transition in a medium at finite temperature and net baryon density. The chiral dynamics of quantum chromodynamics is modeled by the PQM Lagrangian, that includes the coupling of quarks to vector meson and temporal gauge fields. The FRG is employed to properly account for the $O(4)$ criticality at the phase boundary. We focus on the properties and systematics of ratios of the net-baryon-number cumulants χ_B^n, for $1 \leq n \leq 6$, near the phase boundary. The results are presented in the context of the recent experimental data of the STAR Collaboration on fluctuations of the net proton number in heavy-ion collisions at RHIC. We show that the model results for the energy dependence of the cumulant ratios are in good overall agreement with the data, with one exception. At center-of-mass energies below 19.6 GeV, we find that the measured fourth-order cumulant deviates considerably from the model results, which incorporate the expected $O(4)$ and $Z(2)$ criticality. We assess the influence of model assumptions and in particular of repulsive vector-interactions, which are used to modify the location of the critical endpoint in the model, on the cumulants ratios.

Then finally in Chapter 5 we explore the influence of finite-volume effects on baryon-number fluctuations in the quark-meson model. We employ the FRG in a finite volume, using a smooth regulator function in momentum space. We compare the results for a smooth regulator with those for a sharp (or Litim) regulator, and show that in a finite volume, the latter may produce unwanted artifacts. In a finite volume there are only apparent critical points, about which we compute the ratio of the fourth- to the second-order cumulant of quark number fluctuations. When the volume is sufficiently small the system has two apparent critical points; as the system size decreases, the location of the apparent critical point can move to higher temperature and lower chemical potential.

At the end of the thesis, conventions are collected in Appendix A. Basic properties of the unitary groups are presented in Appendix B. In Appendix C, definition and relations of Chebyshev polynomials are provided. Finally, in Appendix D initial conditions and model parameters are given.

Zusammenfassung

In dieser Arbeit betrachten wir effektive Modelle der Quantenchromodynamik, um sowohl den chiralen als auch den Deconfinement-Phasenübergang zu untersuchen. In Kapitel 1 rekapitulieren wir grundlegende Eigenschaften stark wechselwirkender Materie und thermischer Feldtheorie bei endlicher Temperatur. Weiterhin wiederholen wir den nichtperturbativen Zugang der funktionalen Renormierungsgruppe (FRG). In Kapitel 2 führen wir das Quark-Meson (QM)-Modell sowie dessen Erweiterungen durch Polyakov-Loop-Variablen (PQM-Modell) und repulsive vektorielle Wechselwirkungen zwischen Quarks ein. Anschließend erörtern wir Eigenschaften des Modells sowohl in der Molekularfeldnäherung als auch im Renormierungsgruppenzugang. Abschließend wird eine neue Methode die Renormierungsgruppengleichungen zu lösen basierend auf Chebyshev-Polynomen vorgestellt.

In Kapitel 3 untersuchen wir das Skalierungsverhalten des Ordnungsparameters am chiralen Phasenübergang im Rahmen der effektiven Modelle. Wir erforschen universelle und nichtuniverselle Strukturen in der Nähe des kritischen Punktes. Diese umfassen die Skalierungsfunktionen, die führenden Korrekturen zum Skalierungsverhalten und die entsprechende Größe des Skalierungsbereichs sowie deren Abhängigkeiten von einem äußeren symmetriebrechenden Feld. Wir betrachten zwei Modelle in der Molekularfeldnäherung, nämlich das QM-Modell sowie das PQM-Modell, und vergleichen deren kritische Eigenschaften mit denen eines rein bosonischen Modells, nämlich des O(N) linearen Sigma-Modells im $N \to \infty$ Grenzfall. In diesen Modellen berechnen wir die Skalierungsfunktion des Ordnungsparameters analytisch durch Benutzung einer Hochtemperaturentwicklung des thermodynamischen Potentials. Die Effekte eines gluonischen Hintergrunds der nichtuniversellen Skalierungsparameter werden dann im PQM-Modell untersucht. Weiterhin führen wir numerische Berechnungen der Skalierungsfunktionen sowie des Skalierungsbereichs im QM-Modell im FRG-Formalismus durch.

Kapitel 4 enthält eine Untersuchung der kritischen Eigenschaften von Baryonenzahl-Fluktuationen am chiralen Phasenübergang in einem Medium bei endlicher Temperatur und nichtverschwindender Baryonendichte. Die chirale Dynamik der Quantenchromodynamik wird durch die Lagrangedichte des PQM-Modells modelliert, die die Kopplung der Quarks an Vektormesonen und zeitliche Eichfelder enthält. Die FRG berücksichtigt an der Phasengrenze die kritischen O(4)-Phänomene. Wir konzentrieren uns auf die Eigenschaften und Systematiken der Verhältnisse von den Baryonzahl-Kumulanten χ_B^n für $1 \leq n \leq 6$ in der Nähe der Phasengrenze. Die Ergebnisse werden im Kontext der jüngsten experimentellen Befunde der STAR-Kollaboration auf dem Gebiet der Fluktuationen der Netto-Protonenzahl in Schwerionenkollisionen am RHIC dargestellt. Es stellt sich heraus, dass, bis auf eine Ausnahme, die Ergebnisse basierend auf den Modellrechnungen für die Energieabhängigkeit der Verhältnisse der Kumulanten insgesamt gut mit den Daten übereinstimmen. Bei Schwerpunktsenergien unter 19.7 GeV finden wir allerdings eine erhebliche Abweichung der Kumulanten vierter Ordnung von den Modellergebnissen, die die erwarteten O(4) und Z(2) Kritikalitäten enthalten. Weiterhin beurteilen wir den Einfluss der Modellannahmen und insbesondere der repulsiven vektoriellen Wechselwirkungen, die benutzt werden, um die Lage des kritischen Endpunktes zu verändern, auf die Verhältnisse der Kumulanten.

In Kapitel 5 schließlich untersuchen wir den Einfluss von Volumeneffekten auf die Fluktuation der Baryonenzahl im QM-Modell. Wir benutzen die FRG in einem endlichen Volumen, wobei wir eine glatte Regulatorfunktion im Impulsraum verwenden. Dann vergleichen wir die Ergebnisse bei der Verwendung eines glatten Regulators mit denen eines harten (oder Litim-) Regulators und zeigen, dass letzterer in einem endlichen Volumen potentiell ungewollte Artefakte generieren kann. In einem endlichen Volumen gibt es nur dem Schein nach kritische Punkte, bei denen wir das Verhältnis der Quarkzahl-Fluktuation-Kumulanten vierter und zweiter Ordnung berechnen. Wenn das Volumen genügend klein ist, existieren zwei dem Schein nach kritische

Punkte; wenn die Systemgröße abnimmt, kann sich die Lage eines dem Schein nach kritischen Punktes zu höheren Temperaturen und kleineren chemischen Potentialen verschieben.

Am Ende dieser Dissertation werden die verwendeten Konventionen in Anhang A zusammengestellt. Grundlegende Eigenschaften von unitären Gruppen werden in Anhang B dargestellt. In Anhang C stellen wir die Definition und einige Relationen der Chebyshev-Polynome vor. Abschließend geben wir in Anhang D die benutzten Anfangsbedingungen und Modellparameter an.

Contents

Chapter 1

Introduction to strong interactions

1.1 Aspects of quantum chromodynamics

The term strong interactions originally referred to a fundamental force that is responsible for the binding of protons and neutrons into nuclei, and more generally for the interaction of nucleons (protons, neutrons) and other hadrons, in addition to the electromagnetic and weak interactions. Early in the 1960's, a large number of hadrons had been discovered, and it was conjectured by Gell-Mann [1] and Zweig [2] that these hadrons are not fundamental particles, but rather are composite objects, bound states, with a substructure. According to their model, there are baryons containing 3 quarks, and mesons consisting of a quark and an antiquark. The first experimental evidence [3–5] came from the *Stanford Linear Accelerator Center* (SLAC) showing in deeply intelastic electon-nucleon scatterings that protons contain smaller, point-like scattering centers, and hence, are not elementary [6].

Today it is widely believed that strong interactions are governed by an underlying gauge theory of quarks and gluons, namely by *Quantum Chromodynamics* (QCD). The fundamental degrees of freedom of the theory are the spin ½ quarks and the spin 1 gluons. The gluons are gauge bosons and mediate the interaction between quarks. There are six quark species distinguished by their *flavor*. The quark flavors different in mass and electric charge. Their basic properties are summarized in Table 1.1. Additionally both the quarks and the gluons carry *color charge*. Quarks carry one of 3 possible colors, antiquarks one of 3 possible anticolors, and gluons carry one of the 8 possible nonsinglet color-anticolor combination. Gluons, the force carriers of the theory, interact with all objects with nonvanishing color charge. In contrast to electromagnetism, the force carriers are charged, meaning that in QCD there are purely gluonic self-interactions.

Before going into details of the theory let us point out two experimental observations that has to be explained by QCD:

- Quarks and gluons are not observed in nature as free particles.
- The masses of mesons and baryons consisting of light quarks are more than one order of magnitude larger than the sum of the masses of the constituents (except for the pions).

These observations are crucial to understand in QCD, because they touch very fundamental properties of the theory, namely the structure of the spectrum. The absence of free quarks and gluons at low temperatures and densities is called *confinement*, and is very challenging to understand conceptually. The contribution of interactions to the masses of bound states, or the *dynamical generation of mass*, is related to the spontaneous breaking of *chiral symmetry* and will be discussed in detail later on.

One of the difficulties posed by QCD is coming from the behavior of the coupling constant. Just as in the quantum theory of electromagnetism, *Quantum Electrodynamics* (QED), the coupling constant of the theory *runs*, meaning at different energy scales the effective coupling constant is different. In QED, at energy scales accessibly in experiments it is small, and increases with increasing energy. By contrast, in QCD the coupling constant vanishes at high

quark	symbol	mass [MeV]	charge [e]
up	u	$2.3+0.7-0.5$	$+2/3$
down	d	$4.8+0.5-0.3$	$-1/3$
strange	s	95 ± 5	$-1/3$
charm	c	1275 ± 25	$+2/3$
bottom	b	4180 ± 30	$-1/3$
top	t	$173210\pm 510\pm 70$	$+2/3$

Table 1.1.: Data for the masses are taken from the Particle Data Book [7].

energy scales, a property referred to as asymptotic freedom [8–11], and is large at low energies, as illustrated in Fig. 1.1. This has the consequence that, at the energy scale relevant for the hadronic world, the coupling constant is large, and perturbative calculations do not converge. This makes QCD extremely difficult to solve and only involved nonperturbative calculations or effective models are expected to provide a useful description of the low energy regime of QCD.

As mentioned above, QCD is a gauge theory. The gauge symmetry corresponds to $SU(3)$ rotations in color space[1]. The force carriers, the gluons, couple to the color charge. The Lagrangian density of QCD is given by

$$\mathcal{L}=\bar{\psi}_{i,f}\left(i\gamma^{\mu}D^{ij}_{\mu}-m_f\delta^{ij}\right)\psi_{j,f}-\frac{1}{4}F^{a}_{\mu\nu}F^{\mu\nu}_{a}, \tag{1.1}$$

where ψ and $\bar{\psi}=\psi^{\dagger}\gamma^{0}$ are the quark field operators, A is the gluon field operator, and m^f is the quark mass matrix. The indexes $i,j\in[1,3]$ are labels of the fundamental representation of the SU(3) color group, while a, b and $c\in[1,8]$ are those of the adjoint representation. The covariant derivative D_μ is a matrix in color space and is given by

$$D^{ij}_{\mu}\equiv\partial_{\mu}\delta_{ij}-igA^{ij}_{\mu},\qquad A_{\mu}\equiv t^{a}A^{a}_{\mu} \tag{1.2}$$

where t^{a}_{ij} are the generators of the fundamental representation of the SU(3) group and are given in Appendix B. Furthermore, g stands for the gauge coupling. Lastly, the gluon field tensor F is defined by

$$F^{a}_{\mu\nu}=\partial_{\mu}A^{a}_{\nu}-\partial_{\nu}A^{a}_{\mu}+gf_{abc}A^{b}_{\mu}A^{c}_{\nu}, \tag{1.3}$$

where f_{abc} denotes the $SU(3)$ structure constants. The structure constants are provided in Appendix B.

The QCD Lagrangian is invariant under SU(3) gauge transformations. These transformations can be characterized by 8 fields χ^a and in general have the form

$$U(x)=\exp\left(-i\chi^{a}(x)t^{a}\right). \tag{1.4}$$

The quarks and gluon fields transform under these gauge transformations as

$$\begin{aligned}\psi_{i,f}(x)&\rightarrow U(x)^{ij}\psi_{j,f}(x),\\ A^{\mu}(x)&\rightarrow U(x)\left(A^{\mu}(x)-\frac{i}{g}U^{\dagger}(x)\partial^{\mu}U(x)\right)U^{\dagger}(x).\end{aligned} \tag{1.5}$$

Later on we will return to the discussion of the gauge invariance and relate it to one of the key features of strong interaction, namely confinement, the absence of free color charges at low temperatures and densities.

---

[1] $SU(N)$ denotes the group of the special unitary $N\times N$ matrices. More details can be found in Appendix B.

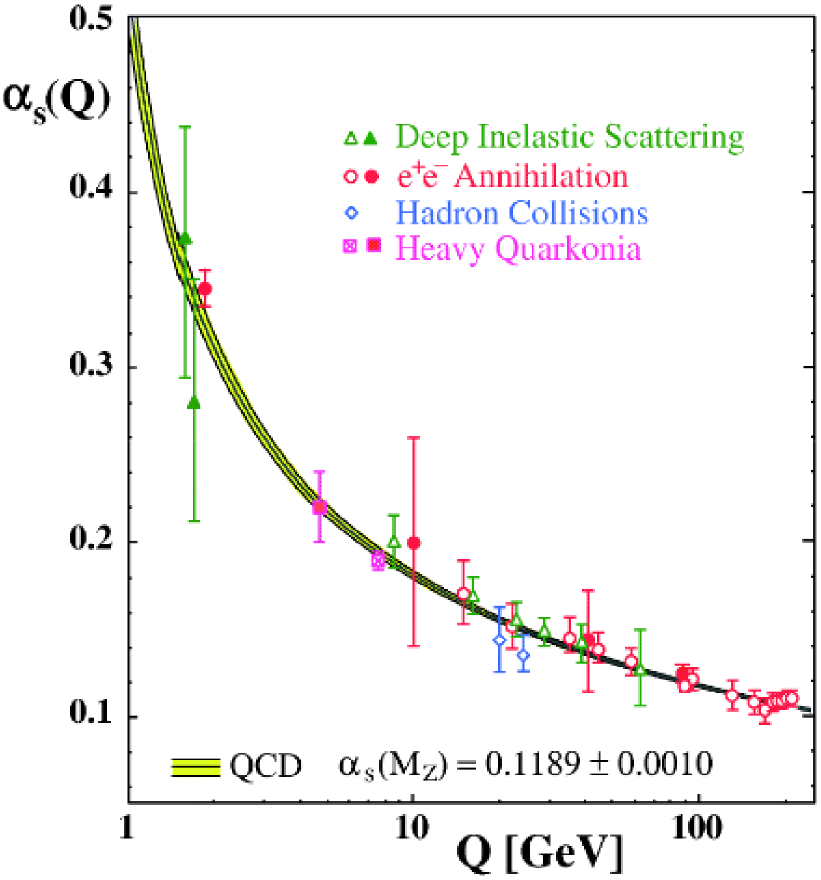

Figure 1.1.: The behavior of the strong coupling constant extracted from various sources and compared to theoretical calculations. Figure taken from [12].

1.2 Chiral symmetry

Apart from the local gauge invariance, QCD has several other symmetries. Since it is a relativistic quantum field theory, it features Poincaré symmetry, i.e. it is invariant under rotations and translations in spacetime. Moreover, it exhibits various global internal symmetries. The corresponding transformations are global, leave the color space unchanged and transform only the quark fields. For this reason it is sufficient to consider only the quark part of the QCD Lagrangian,

$$\mathcal{L}_q = \bar{\psi}_f \left(i\gamma^\mu D_\mu - m_f \right) \psi_f . \tag{1.6}$$

Note that we dropped the color indexes as they are irrelevant for this study. We are interested in transformations that leave the Lagrangian invariant and act in the flavor space and possibly in the Lorentz-space. These transformations can be generally written as

$$\psi_f(x) \rightarrow \exp\left(-i\epsilon^a T^a\right), \psi_f(x), \qquad \psi_f^\dagger(x) \rightarrow \psi_f^\dagger(x) \exp\left(i\epsilon^a T^a\right), \tag{1.7}$$

where a labels the Hermitian generators T of the transformation group and ϵ^a parametrize its elements. Note that since the transformations are independent of the spacetime location, they commute with the derivative. According to Noether's theorem, for each continuous global symmetry we can construct a conserved current. The conserved current corresponding to the transformation (1.7) is given by

$$J_\mu^a(x) = \bar{\psi}_f(x) \gamma_\mu T^a \psi_f(x), \tag{1.8}$$

while the related conserved charge is

$$Q^a = \int d^3x J_0^a(x) = \int d^3x \psi_f^\dagger(x) T^a \psi_f(x). \tag{1.9}$$

The conserved charge associated with a transformation is a very important operator and characterizes the behavior of the different states $|s\rangle$ and operators O of the system under the transformation,

$$|s'\rangle = \exp\left(-i\epsilon^a Q^a\right)|s\rangle, \tag{1.10}$$

$$\mathcal{O}' = \exp\left(-i\epsilon^a Q^a\right)\mathcal{O}\exp\left(+i\epsilon^a Q^a\right). \tag{1.11}$$

For any state of the system that is invariant under the transformation, the related conserved charged vanishes.

Now we take specific examples of symmetry transformations of the Lagrangian. The most obvious symmetry is obtained by setting the generator to $T^a = 1$. This choice yields the $U(1)$ symmetry group, and the conserved charge is the net quark number, i.e. the number of quarks *minus* the number of antiquarks. This symmetry is related to the conservation of baryon number. A second $U(1)$ symmetry, the so-called axial $U(1)$ symmetry, is obtained with the choice $T^a = \gamma_5$. This transformation is a symmetry of the classical theory, however it is broken by the axial anomaly in the quantum theory. Due to this, this symmetry is not realized.

Two further symmetries are present in the theory in the chiral limit, where all quark masses considered vanish. The related invariance is called *chiral symmetry*. This notion proves to be exceptionally useful when considered for the two light quark flavors, the up and down quarks. To understand the nature of these transformations first we disregard all quark masses. In that case, the Lagrangian of the noninteracting quark model with massless quarks reads

$$\mathcal{L}_0 = \bar{\psi}_f\left(i\gamma^\mu\partial_\mu\right)\psi_f. \tag{1.12}$$

The quark operators can be projected onto purely left-handed and purely right-handed states by the projectors

$$P_L = \frac{1-\gamma_5}{2}, \qquad P_R = \frac{1+\gamma_5}{2}. \tag{1.13}$$

Defining the left- and right-handed quark fields, which have definite chirality, as

$$q_f^L = P_L\psi_f, \qquad \psi_f^R = P_R\psi_f, \tag{1.14}$$

and using the basic properties of the projectors

$$P_R + P_L = 1, \qquad P_R P_L = P_L P_R = 0, \tag{1.15}$$

one can write the Lagrangian as

$$\mathcal{L}_0 = \bar{\psi}_f^L\left(i\gamma^\mu\partial_\mu\right)\psi_f^L + \bar{\psi}_f^R\left(i\gamma^\mu\partial_\mu\right)\psi_f^R. \tag{1.16}$$

In this form it is clear that the left- and right-handed fields separate and one may transform them independently. Chirality of massless particles is conserved. This yields an additional $SU(2)$ symmetry transformation for both the left-handed and right-handed fermions. The invariance under these transformations together is usually referred to as chiral symmetry and denoted by $SU(2)_L \otimes SU(2)_R$.

The chiral transformations can also be formulated in terms of the *vector transformation* and the *axialvector transformation*. They are given by the triplets of generators

$$T_V^j = \frac{\tau^j}{2}, \qquad T_A^j = \frac{\tau^j}{2}\gamma_5 \tag{1.17}$$

respectively, where τ represents the Pauli matrices defined in Appendix B. The conserved charges are then the vector- and axial charges and can be written as

$$Q_V^j = \int d^3x \psi^\dagger(x)\frac{\tau^j}{2}\psi(x), \qquad Q_A^j = \int d^3x \psi^\dagger(x)\frac{\tau^j}{2}\gamma_5\psi(x). \tag{1.18}$$

Their commutation relations can be calculated by applying canonical anticommutation relations of the quark fields and are given by

$$\left[Q_V^j, Q_V^k\right] = i\epsilon_{jkl}Q_V^l, \qquad \left[Q_A^j, Q_A^k\right] = i\epsilon_{jkl}Q_V^l, \qquad \left[Q_V^j, Q_A^k\right] = i\epsilon_{jkl}Q_A^l. \tag{1.19}$$

One can see that the vector transformations form a closed algebra by themselves, however the axial-vector transformations do not. This has the consequence that vector transformations form a closed group, however pure axial-vector transformations do not. To relate the vector and axialvector transformations to the left-handed and right-handed transformations,one can write the left-handed and right-handed charges as

$$Q_L^j = \frac{1}{2}\left(Q_V^j - Q_A^j\right), \qquad Q_R^j = \frac{1}{2}\left(Q_V^j + Q_A^j\right). \tag{1.20}$$

They form two separate closed algebras as

$$\left[Q_L^j, Q_L^k\right] = i\epsilon_{jkl}Q_L^l, \qquad \left[Q_R^j, Q_R^k\right] = i\epsilon_{jkl}Q_R^l, \qquad \left[Q_L^j, Q_R^k\right] = 0. \tag{1.21}$$

This was expected, since the left-handed and right-handed transformations commute with each other as they act on different part of the Lagrangian and there are no mixed terms. Due to the closure of the left and right algebras, the chiral symmetry group can be written as $SU(2)_L \otimes SU(2)_R$, however not as $SU(2)_V \otimes SU(2)_A$.

Finite quark masses break chiral symmetry, since the mass term expressed by the left- and right-handed operators is given by

$$\bar{\psi}m\psi = \bar{\psi}_L m\psi_R + \bar{\psi}_R m\psi_L. \tag{1.22}$$

In the general case neither the left-handed, nor the right-handed transformations are symmetry transformation anymore due to the mixed term. The quark masses gathered in Table 1.1 show however, that the masses of the two light quark flavors are much smaller than the relevant QCD scales, where the hadron masses lie. Because of this, one expects that the light quark masses can be treated as a perturbation, and chiral symmetry proves to be an important concept for these two flavors.

It is also worth to note that if one considers only the two light quark flavors with degenerate masses, the vector-transformation is still a symmetry transformation and forms an $SU(2)$ group, usually denoted as $SU(2)_V$. The conserved charge related to this symmetry, the vector charge, is called the isospin.

There are two ways a symmetry can be realized in a system. One possibility is called the Wigner-Weyl realization, in which case the ground state of the system shares the symmetries of the dynamics. That would mean that the ground state is invariant under the symmetry

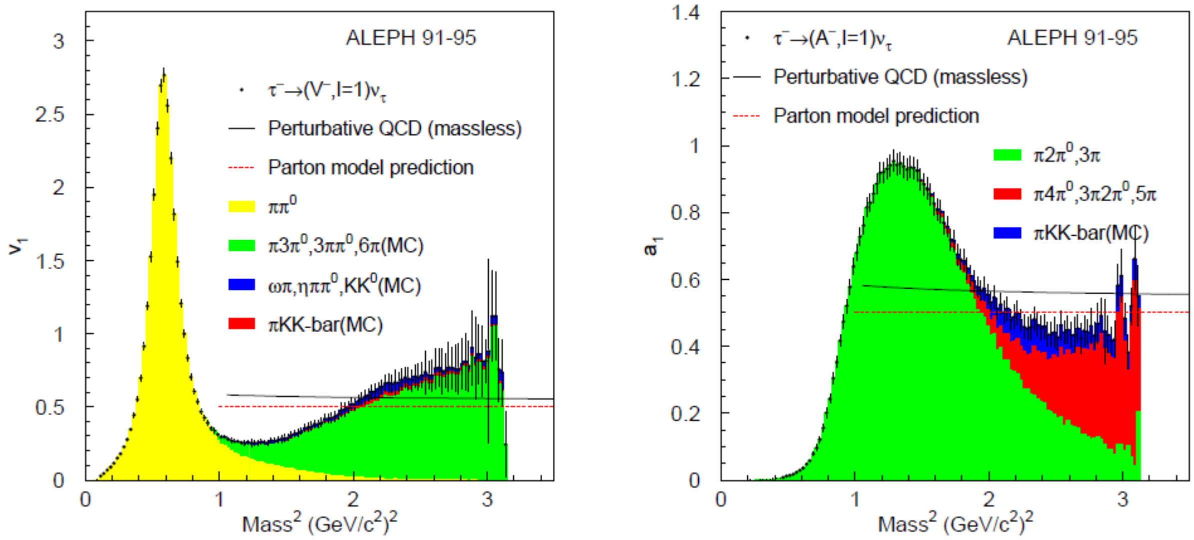

Figure 1.2.: Decay of the τ lepton into even and odd number of pions corresponding to decays through the isovector-vector and isovector-axialvector currents measured by the ALEPH collaboration. In a chirally symmetric scenario the two curves have to agree. Figure taken from [13].

transformations of the Hamiltonian. In the case of chiral symmetry it would mean, that the vacuum has vanishing vector and axial charge,

$$Q_A^j \left|0\right\rangle = 0, \qquad Q_V^j \left|0\right\rangle = 0. \tag{1.23}$$

In this case the spectrum of the theory has to be degenerate: for each state $|A\rangle$, that has nonvanishing axial or vector-charge, a continuum of new states $|B\rangle = \exp\left(-i\epsilon^a Q^a_{A/V}\right)|A\rangle$ can be found that are degenerate. This would have the consequence that each particle with a definite parity has to have a degenerate particle with opposite parity. For QCD this is clearly not the case, since for example the lowest pseudoscalar mesons, the pions, do not have a scalar counterpart with similar mass. Another clear experimental proof of the breakdown of chiral symmetry is given by the τ lepton decay measurements. Chiral symmetry constrains the spectral information in the vector and axialvector channels for any decay of a chirally invariant state have to be identical. This is clearly violated by the data of the ALEPH collaboration [13], showing that the ρ and a_1 mesons, which are the dominant resonances in the corresponding channels, have very different spectral functions.

Experiments suggest thus that in vacuum chiral symmetry is broken, much more than what would be expected from the explicit breaking by the small light quark masses. This leads us to the conclusion that the ground state of the theory, the QCD vacuum, is not invariant under chiral symmetry even in the chiral limit, the chiral symmetry is *spontaneously broken*. The ground state in the chiral limit is degenerate, and the different ground states are related to each other through the symmetry transformations of the dynamics. This is the so-called Nambu-Goldstone realization of the symmetry. In this case the excited states do not have to come in parity pairs. Furthermore, the Goldstone-theorem states that for all generators that describe transformations not leaving the ground state unchanged, there exists a massless excitation in the system, a so-called *Goldstone boson*, with identical quantum numbers. In the case of QCD, even with vanishing quark masses, the axial transformations are broken in the vacuum. This has the consequence that the vacuum does not have a definite axial charge, and there is a triplet of Goldstone bosons, namely the pions. The pions are however experimentally not massless, and that is the consequence of the finiteness of the current quark masses. As discussed before, the current quark masses break chiral symmetry *explicitly*. Due to the smallness of the current quark masses, the pions are still below all other excitations of the system, and they are often referred to as pseudo-Goldstone bosons.

The breaking of the chiral symmetry can be quantified. To this end let us consider the auxiliary operator $P_j(x) = \bar{\psi}(x) i\gamma_5 \frac{\tau_j}{2} \psi(x)$ and take its commutator with the axial charge Q_j^A,

$$[Q_j^A, P_k(x)] = -\frac{i}{2}\delta_{jk}\bar{\psi}(x)\psi(x), \tag{1.24}$$

where we have used the canonical anticommutation relations of the fermion fields. Taking the vacuum expectation values of both sides yields

$$\left\langle 0 \left| Q_j^A P_k - P_k Q_j^A \right| 0 \right\rangle = -\frac{i}{2}\delta_{jk}\left\langle \bar{\psi}(x)\psi(x) \right\rangle. \tag{1.25}$$

In the case of spontaneous symmetry breaking, the vacuum does not have a definite axial charge, and hence the left hand side does not necessarily vanish, in contrast to the Wigner-Weyl realization of the symmetry. Consequently the right hand side also does not vanish, and there is a nonvanishing scalar isoscalar quark condensate in the system. We will refer to it as the *chiral condensate*. This condensate serves as an order parameter for the chiral symmetry: it is nonzero when chiral symmetry is broken, and vanishes when chiral symmetry is exact. The dynamical mass generation in QCD, i.e that the quarks appear much heavier than their current quark mass, can be traced back to their interaction with the chiral condensate.

1.3 Confinement and the Polyakov-loop variables

Just as we were able to quantify the restoration of chiral symmetry by finding an appropriate order parameter, it is desirable to identify one for the confinement-deconfinement phase transition as well [14]. To this end, we continue the theory analytically to purely imaginary times. According to the basics of finite temperature field theory, an analytically continued $d+1$ dimensional theory to purely imaginary times $\tau = it$ corresponds to a d dimensional system in a thermal bath with constant temperature. The temperature of the heat bath is related to the size of the imaginary time direction: $T = 1/L_\tau$. For this correspondence to work we also have to specify the boundary conditions

$$\phi(x, L_\tau) = \phi(x, 0) \qquad \text{for bosons,} \tag{1.26}$$

$$\psi(x, L_\tau) = -\psi(x, 0) \qquad \text{for fermions.} \tag{1.27}$$

in the finite temporal direction. These boundary conditions express that thermal expectation values are given by traces. The sign difference in the boundary conditions for fermions and bosons stems from the fact, that in field theory, the fermion fields have anticommuting Grassmann numbers, while the bosons take commuting complex or real numbers. To be able to discuss QCD at finite temperature, we have to analytically continue the gluon-fields as well, since they are Lorentz vector fields themselves. Hence we replace the zero component of the gluon field, A_0, by $A_4 = iA_0$.

Having discussed the basics of finite temperature field theory, now we are ready to discuss the question of confinement. First we consider a simplified theory, namely the pure $SU(N_c)$ gauge theory, in which there are no dynamical quarks, and the gluons are the only dynamical degrees of freedom. To study confinement, the inseparability of color charges, we place an infinitely heavy, static test quark-antiquark pair in the system, and try to separate them. The free energy of a test quark-antiquark pair in a distance r to each other, as shown in Refs. [15, 16], is given by

$$e^{-\beta F_{q\bar{q}}} = \left\langle \ell(0)\bar{\ell}(r) \right\rangle, \tag{1.28}$$

where $l(r)$ and $l^\dagger(r)$ are the Polyakov-loop variables [17]. They are defined through the thermal Wilson line

$$L(x) = \mathcal{P}\exp\left(ig \int_0^\beta d\tau A_4^a(x,\tau) t^a \right), \tag{1.29}$$

as

$$\ell(r) = \frac{1}{N_c}\mathrm{Tr}L(x), \quad \bar{\ell}(r) = \frac{1}{N_c}\mathrm{Tr}L^\dagger(x), \tag{1.30}$$

where $N_c = 3$ denotes the number of colors. The thermal Wilson line is a path ordered product that loops around the imaginary time direction and depends only on the imaginary time component of the gauge field, $A_4 = iA_0$. The Wilson line, L, is not gauge invariant. If we take the color trace however, just as in the Polyakov-loop variables, ℓ and $\bar{\ell}$, the result is invariant under topologically trivial gauge transformations. To study the confining properties of the system, we move the static quarks to increasingly large distances and probe their free energy. If they are distant enough and cluster decomposition holds, we get

$$e^{-2\beta F_q} = \lim_{r\to\infty} \left\langle \ell(0)\ell^\dagger(r) \right\rangle = \left\langle \ell(0) \right\rangle \left\langle \ell^\dagger(0) \right\rangle = \left| \left\langle \ell(0) \right\rangle \right|^2, \tag{1.31}$$

where we defined the single quark free energy, $F(q)$, as $\lim_{r\to\infty} F_{q\bar{q}}/2$. If it is finite, it means that a quark-antiquark pair can be separated from each other with finite amount of energy, and hence there is no confinement. If there is confinement, this quantity has to diverge. Using these arguments, Eq. (1.31) tells us that in case of confinement, the expectation value of the Polyakov-loop variables, $l(x)$ and $\bar{l}(x)$, have to vanish. Also, in the deconfined phase the expectation value is finite. Thus, the Polyakov-loop is a candidate for the order parameter of confinement, at least in $SU(N_c)$ gauge theory.

To fully understand the role of the Polyakov-loop variable, we have to study gauge transformations in finite temperature field theory in more detail. As discussed before in Sec. 1.1, in QCD, the quark and gluon fields are subject to an $SU(3)$ local gauge invariance that transforms the fields as given in Eq. (1.5). Strictly speaking, in QCD, the gauge transformation field $U(x,\tau)$ has to fulfill the boundary conditions

$$U(x,0) = U(x,L_\tau) \tag{1.32}$$

to keep the boundary condition for quarks satisfied. In pure $SU(N_c)$ gauge theory however, in which there are no quarks and the only degrees of freedom are the gauge fields, the boundary conditions for the gauge transformations are not that strict [18]. It can be seen, that the boundary condition

$$A^\mu(x,L_\tau) = A^\mu(x,0) \tag{1.33}$$

is fulfilled by the transformed fields

$$A'^\mu(x,\tau) = U(x,\tau)\left(A^\mu(x,\tau) - \frac{i}{g}U^\dagger(x,\tau)\partial^\mu U(x,\tau) \right) U^\dagger(x,\tau). \tag{1.34}$$

if the gauge transformation fulfills

$$U(x,L_\tau) = zU(x,0), \tag{1.35}$$

where z is arbitrary element of the center of the $SU(N_c)$ group[2]. For a matrix group, all elements that are proportional to the unit matrix are automatically members of the center of the group. Keeping in mind, that the determinant of the matrices in $SU(N_c)$ has to be unity, these are

$$z_k = e^{i\vartheta_k} \times I_{N_c \times N_c}, \quad \vartheta_k = \frac{2k\pi}{N_c}, \quad k = 0, 1, \cdots, N_c - 1, \tag{1.36}$$

where I denotes the unit matrix. It turns out, that for $SU(N_c)$ these are all the elements of the center. The subgroup they form is the order-N_c cyclic group, $Z(N_c)$.

We found thus that the possible gauge transformations can be partitioned into N_c subclasses based on global topological properties. Equivalently, one can say that, apart from the connected local gauge transformations with trivial boundary conditions, there exists a global transformation of $Z(N_c)$ that changes the topological properties of the gauge transformation. Now let us consider the gauge transformation of the Polyakov loop defined in Eq. (1.29). By applying the transformation rule for the gauge field and taking into account the path-ordering, one finds that the thermal Wilson line transforms as

$$L(x) \to U(x, L_\tau)L(x)U^\dagger(x, 0). \tag{1.37}$$

If we consider a gauge transformation with nontrivial topology, i.e.

$$U(x, L_\tau) = z_k U(x, 0) \equiv e^{ik2\pi/N_c} U(x, 0), \tag{1.38}$$

we find that the Polyakov-loop transforms as

$$\ell'(x) = z_k \ell(x), \qquad \bar{\ell}'(x) = z_k^{-1} \bar{\ell}(x) \tag{1.39}$$

Thus, the Polyakov-loop is not invariant under the global $Z(N_c)$ transformations, and serves as an order parameter for the $Z(N_c)$ symmetry. At small temperatures the system is in the confined phase, the Polyakov-loop expectation value vanishes, $Z(N_c)$ symmetry is realized. At high temperatures in the deconfined phase however, the Polyakov loop takes a nonzero value, hence the center symmetry is spontaneously broken. Based on the breaking of the $Z(N_c)$ symmetry it is possible to predict the order of the deconfinement transition in pure Yang-Mills theory [19–21]. For two colors, $N_c = 2$, a second order transition is expected, for $N_c = 3$ a soft first order transition, and for $N_c = 4$ a strong first order transition is found.

Now let us turn to QCD. In the heavy-quark limit, in which all quark masses are very large, there are effectively no dynamical quarks in the system, and the confining properties of the theory should agree with the $N_c = 3$ Yang-Mills theory. Lattice QCD (LQCD) simulations show [22] that in this case there is indeed a first order phase transition at around $T_0 \approx 270$ MeV. If the quarks have finite mass however, there are dynamical quarks in the system, and the quark fields have to satisfy the boundary conditions in the Euclidean-time direction. That would only allow periodic gauge transformations, hence quarks break the $Z(3)$ center symmetry. It is expected that the larger the quark masses are, the smaller the explicit symmetry breaking is, and the better the $Z(3)$ symmetry is realized.

At finite net baryon density the quark-antiquark symmetry is broken, and the free energy of quarks and antiquarks are different. This means that the Polyakov-loop variables, ℓ and $\bar{\ell}$ have in general have different expectation values, however both of them remain real [23].

1.4 The phase diagram of QCD

In the previous section we discussed two important approximate symmetries of QCD, namely the chiral symmetry and the center symmetry of the $SU(3)_c$ color gauge group. They are valid in

---

[2] The center of a group G is defined to be the largest set of group elements that commute with each and every element of G. The center of the group is a group itself.

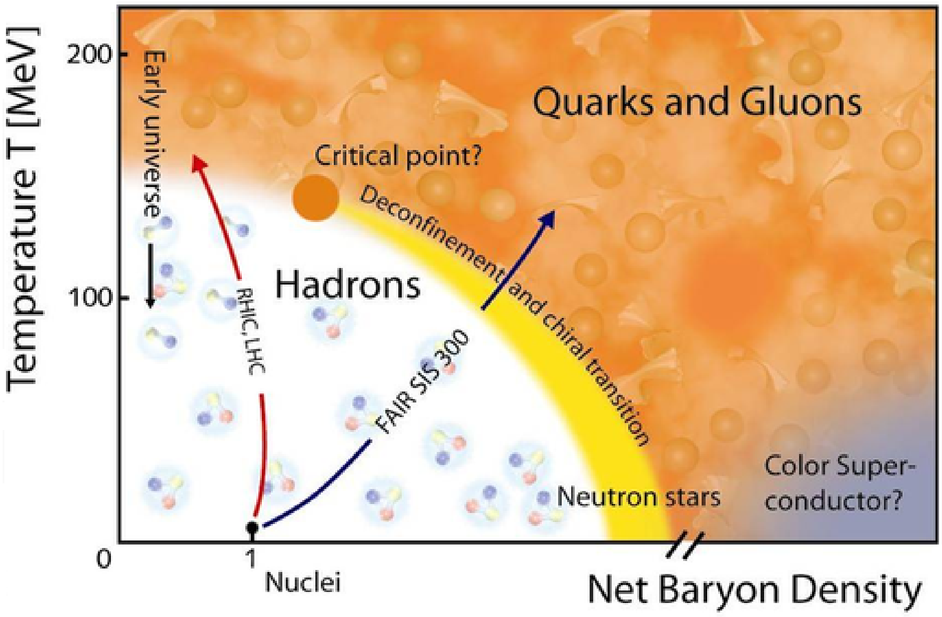

Figure 1.3.: Schematic phase diagram of strongly interacting matter. Picture taken from [24] .

opposite limits of QCD. Chiral symmetry is exact at vanishing quark masses and a second order chiral phase transition of the $O(4)$ universality class is expected at some finite temperature [25]. Conversely, the center symmetry is good at infinite quark masses, when dynamical quarks are absent, and yields a first order deconfinement phase transition. Since the physical quark masses in QCD are nonzero and finite, neither of these symmetries are exact. However, both approximate symmetries prove to be conceptually important.

Lattice QCD simulations provide first principle results on the thermodynamics of QCD at vanishing net-baryon density. Simulations including the two light quark flavors and the strange quarks with physical masses show that at zero baryon chemical potential, there is a smooth crossover phase transition from a chirally broken, confined phase, to a chirally restored and deconfined phase [26]. The transition temperatures, although not defined unambiguously[3], seem to coincide [27].

Owing to the *sign problem* of lattice QCD, the order of and the relation between these transitions at large net-baryon densities is still an open issue. It has been conjectured, that at a nonzero net baryon density the chiral transition could turn into a first order transition. The endpoint of this conjectured line of first order transitions is the *chiral critical endpoint of QCD* (CEP) [28–31], which is the subject of intense theoretical and experimental studies. Various methods have been invented to circumvent the sign problem allowing calculations at finite density [32–34], but so far even the existence of a critical point remains an open question. Due to the difficulties in ab initio calculations, certain effective models of QCD that lie in the same universality class as QCD, e.g. the Polyakov-loop-extended Nambu-Jona-Lasinio (PNJL) [35–41] and the Polyakov–quark-meson (PQM) models [42–50], were applied to study the chiral and deconfinement phase transitions. These models do not have the nonabelian gauge interaction, which would make the calculations difficult, but they do exhibit spontaneous and explicit chiral symmetry breaking and they simulate the deconfinement transition by coupling the quarks to the Polyakov-loop variables. These models yield a chiral CEP in the phase diagram for reasonable values of the model parameters. However, since the dynamics of these models is greatly

---

[3] Since a crossover transition is a smooth transition, a transition temperature is not uniquely defined. A common device for the definition of the transition temperature is the peak location of the order-parameter susceptibility. An alternative definition of the transition temperature is given by the inflection point of the order parameter.

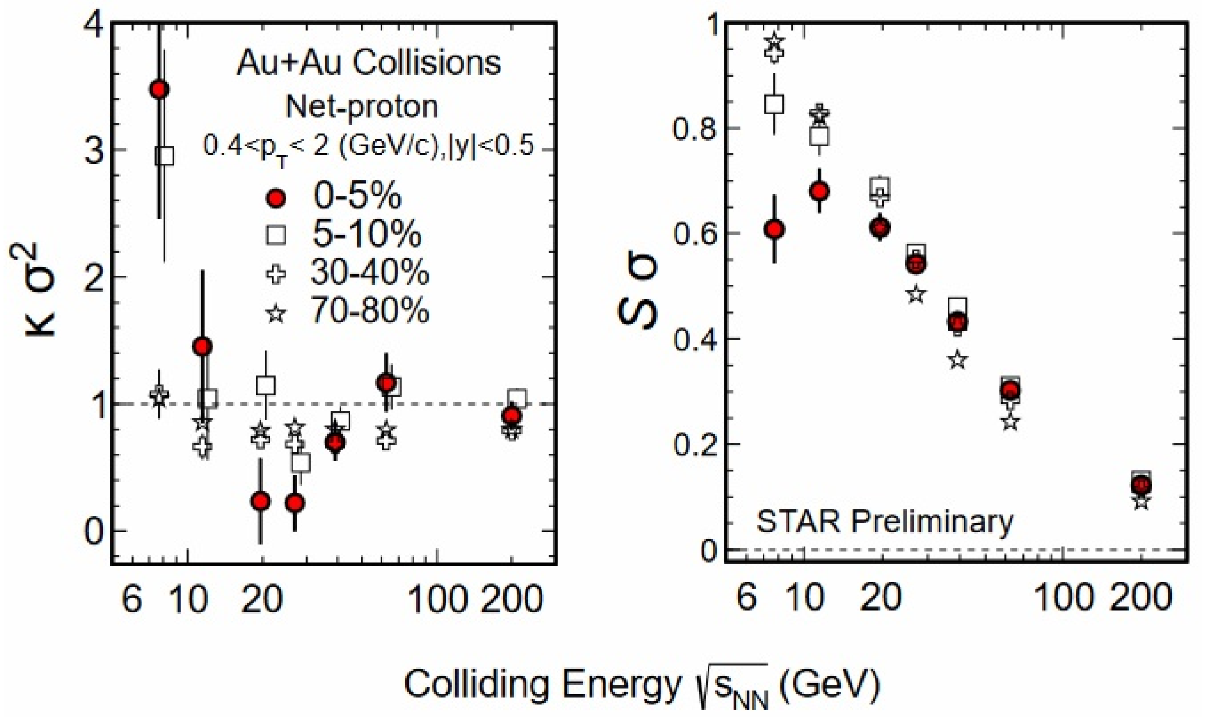

Figure 1.4.: Ratios of baryon number cumulants measured by the STAR collaboration. The increase in the kurtosis may signal the presence of a critical end-point in the phase diagram. Plot taken from Ref. [54].

simplified, they can at best provide qualitative results at nonzero net-baryon densities. There are ongoing studies that focus on the systematic tuning of these models to match QCD as well as possible using functional methods [51–53].

From the experimental side, the phase diagram of QCD is probed by heavy-ion collisions carried out in the *Large Hadron Collider* (LHC), *Relativistic Heavy Ion Collider* (RHIC), and at the future *Facility for Antiproton and Ion Research* (FAIR) facilities. By performing collisions at different energies, different densities can be reached. Particle yields measured at these experiments suggest that the strongly interacting matter formed in such collisions freezes out chemically at a very well defined temperature for each density, providing a chemical freeze-out line in the phase diagram [55]. The aim of the *Beam Energy Scan* (BES) program of RHIC [56] is to study various observables on this freeze-out line to pin down the location of the conjectured CEP.

The CEP is a point of second order phase transition in the phase diagram, a true critical point, which results in a divergent correlation length. At such a point fluctuations of conserved charges are enhanced significantly, providing a valuable tool for studying the phase structure of QCD [57–68]. In the BES program, systematic measurements of the net-baryon number, charge and strangeness are planned and carried out.

1.5 Introduction to quantum field theories

In order to be able to study the problems of confinement and chiral symmetry restoration introduced in the previous sections, we review here some basic quantum field theoretical methods. Quantum field theories (QFTs) are valuable tools to theoretically investigate both scattering amplitudes and systems in thermal equilibrium. QFTs provide a powerful framework for exploring the dynamics of relativistic quantum systems. Symmetries are very important in physics, and in this formalism they are accounted for in a systematic manner. Any relativistic QFT is constructed such that it is automatically compatible both with the special theory of relativity and with quantum mechanics.

In this work, we focus on thermal field theories, and we consider only static properties of systems. Hence, we do not study scattering or any real time phenomena in this work. We thus assume that the system under consideration had sufficient time to reach thermal equilibrium, and consequently, that the excitation probabilities are given by thermal distributions. In order to get a qualitative insight into the methods of thermal field theory, we first consider a one-component scalar field theory in $D = d + 1$ dimensions described by the action

$$S = \int d^D x \mathcal{L} = \frac{1}{2}\partial_\mu \Phi \partial^\mu \Phi + U(\Phi), \tag{1.40}$$

where D denotes the number of dimensions. The Hamiltonian of the system is obtained by a Legendre transformation,

$$H = \int d^{D-1}x \left(\frac{\partial \mathcal{L}}{\partial \partial^0 \Phi} \partial^0 \Phi - \mathcal{L} \right) = \int d^{D-1}x \left(\frac{1}{2}(\partial^0 \Phi)^2 + \frac{1}{2}(\nabla \Phi)^2 - U(\Phi) \right). \tag{1.41}$$

Using the Hamiltonian, all thermodynamic properties of the system can be deduced from the partition function. Starting from a statistical mechanical analogue, the partition function is given by the trace

$$Z = \sum_{\{\text{state } s\}} \langle s | \exp(-\beta H) | s \rangle \tag{1.42}$$

where $\beta = 1/T$ is the inverse temperature. Noticing that this formula is essentially a traced transition amplitude with imaginary time difference $\Delta t = -i\beta$, one can apply Feynmans path integral formalism replacing the real time variable by the imaginary one, yielding

$$Z = \int \mathcal{D}\Phi \exp\left(iS[t \to -i\tau]\right)\Big|_{\Phi(\tau=0)=\Phi(\tau=\beta)}, \tag{1.43}$$

where $\int \mathcal{D}\Phi$ denotes a functional integration over all possible field configurations. This formula shows that the trace in the partition function can be evaluated by a path integral over periodic field configurations in the time direction. The argument of the exponential written explicitely is

$$iS[t \to -i\tau] = -\int_0^\beta d\tau \int d^{D-1}x \left(\frac{1}{2}(\partial^0 \Phi)^2 + \frac{1}{2}(\nabla \Phi)^2 - U(\Phi) \right) \equiv -S_E, \tag{1.44}$$

where we defined the *Euclidean action* S_E, which is one of the basic building blocks of our method. Note, that unlike the ordinary real time path integrals, here the argument of the exponential is real rather than imaginary. This has the advantage that the oscillatory integrands appearing in real time field theories are replaced by exponentially converging ones. Hence, it is much easier to perform calculations.

Thus, the thermodynamic properties of a d-dimensional system can be obtained by considering a $D = d + 1$-dimensional theory with a Euclidean metric. The analytic continuation of the theory from the Minkowski metric to the Euclidean metric is called a *Wick rotation* and results in a change of variables $t \to -i\tau$. This prescription works for a wider class of field theories, not just for the one-component scalar theory we described here. In the general case, the partition function of the field theory at finite temperature can be obtained through the following steps:

- consider a $d+1$-dimensional field theory and perform a Wick rotation. This results in the replacement $t \to -i\tau$, and in similar transformations for any Lorentz vector or higher Lorentz tensor fields in the system.
- limit the imaginary-time direction to the interval $[0, \beta]$, where $\beta = 1/T$ is the inverse temperature.
- apply boundary conditions in the imaginary time direction that account for the trace in the partition function. These correspond to periodic boundary conditions for boson fields and antiperiodic boundary conditions for fermion fields.

This procedure then enables us to calculate the partition function at finite temperature using Feynman path integrals in a Euclidean metric. The partition function can in turn be used to extract static thermal information of the system such as entropy and energy density.

The formalism of QFTs offers a systematic way to calculate correlation functions, or as it is also called, n-point functions. Correlation functions determine scattering amplitudes and the expectation values of a wide variety of quantities, in particular in thermal field theory they provide a measure of the fluctuations in the system. They are defined as expectation values of products of quantum fields, Φ_i,

$$\left\langle \Phi_i(x)\Phi_j(y)\Phi_k(z)... \right\rangle . \tag{1.45}$$

In general they can be related to different particle species as well. A special example is the 2-point function

$$G^{(2)}_{ij}(x,y) = \left\langle \Phi_i(x)\Phi_j(y) \right\rangle , \tag{1.46}$$

which can be understood as the propagator of a particle. It also gives a measure of the correlation or anticorrelation between a degree of freedom at point x and at point y. For two correlated (anticorrelated) fields the correlation function is positive (negative). For two independent fields the correlation function vanishes.

In Minkowski and Euclidean field theories the calculation of correlation functions is completely analogous. Here, we employ the notation of Euclidean field theory. Using the Euclidean action, the expectation value of an arbitrary operator $\hat{O}$ is given by

$$\left\langle \hat{O} \right\rangle = \frac{\int \mathcal{D}\Phi \, \hat{O} \exp\left(-S_E[\Phi]\right)}{\int \mathcal{D}\Phi \exp\left(-S_E[\Phi]\right)} . \tag{1.47}$$

The term $\exp\left(-S_E[\Phi]\right)$ acts as a probability weight. Introducing an external classical field $J(x)$, one defines the generating functional

$$Z[J] = \int \mathcal{D}\Phi \exp\left(-S_E[\Phi] + \int d^D x J(x)\Phi(x) \right) , \tag{1.48}$$

which then generates all correlation functions:

$$\begin{aligned} G^{(n)}(x_1, x_2, \cdots, x_n) &= \frac{1}{Z[J]} \frac{\delta^n Z[J]}{\delta J(x_1)\delta J(x_2)\cdots\delta J(x_n)} \\ &= \frac{1}{Z[J]} \int \mathcal{D}\Phi\Phi(x_1)\Phi(x_2)\cdots\Phi(x_n) \exp\left(-S_E[\Phi] + \int d^D x J(x)\Phi(x) \right) . \end{aligned} \tag{1.49}$$

This formula clearly depends on the external field $J(x)$. If there is no such field present in the system, it can be simply put to zero. We will find however that in some models there can be a term in the Lagrangian that is linear in the fields, and hence that term can be understood as a coupling to an external source. The formula for the expectation value of an operator (1.47) can then be generalized to nonvanishing external sources as

$$\langle \hat{O} \rangle_J \equiv \frac{\int \mathcal{D}\Phi \hat{O} \exp\left(-S_E[\Phi] + \int d^D x J \Phi\right)}{\int \mathcal{D}\Phi \exp\left(-S_E[\Phi] + \int d^D x J \Phi\right)}. \tag{1.50}$$

The generating functional $Z[J]$ generates all contributions to the correlation functions. Some of them, however, can be resummed, and the same physical content can be provided in a more compact way. The generating functional of connected diagrams, for example, is given by

$$W[J] \equiv \ln Z[J] \tag{1.51}$$

and provides only those contributions that consist of only one diagrammatically connected part. The connected Green functions are then given by

$$G_c^{(n)}(x_1, x_2, \cdots, x_n) = \frac{\delta^n W[J]}{\delta J(x_1) \delta J(x_2) \cdots \delta J(x_n)}. \tag{1.52}$$

From the knowledge of all connected correlators, the disconnected ones can of course be calculated if needed. It is instructive to calculate the first two functional derivatives of $W[J]$ with respect to the external source J explicitly:

$$\frac{\delta W[J]}{\delta J(x)} = \frac{1}{Z[J]} \int \mathcal{D}\Phi \Phi(x) \exp\left(-S_E[\Phi] + \int d^D y J(y) \Phi(y)\right) = \langle \Phi \rangle_J \equiv \phi(x), \tag{1.53}$$

$$\frac{\delta^2 W[J]}{\delta J(x) \delta J(y)} = \frac{1}{Z[J]} \frac{\delta^2 Z[J]}{\delta J(x) \delta J(y)} - \frac{1}{Z[J]^2} \frac{\delta Z[J]}{\delta J(x)} = \langle \Phi(x) \Phi(y) \rangle_J - \phi(x) \phi(y). \tag{1.54}$$

The first one provides the expectation value of the field, denoted by $\phi(x)$, while the second one gives the propagator of the particle. Clearly, this formula yields the nontrivial correlation between the fields at x and y, and subtracts the trivial correlation due to the nonvanishing expectation value.

As one identifies the generating functional Z with the partition function of classical statistical physics, the generating functional of connected diagrams, $W[J]$, is the analogue of the Gibbs free energy whose natural parameters are the temperature and the external magnetic field[4]. Just as in a simple classical magnetic system, where the Gibbs free energy depends explicitly on the external magnetic field, the natural variable of W is the external field J. In classical magnetic systems however, to study the development of magnetization through a macroscopic alignment of spins, the Helmholtz free energy is a more appropriate thermodynamic potential to use. Its natural variable is the global magnetization, and is obtained from the Gibbs free energy through a Legendre transformation. Since we wish to study the formation of a chiral condensate in QCD, we follow this analogy and consider one more generating functional, namely the generating functional for the one particle irreducible diagrams, the *effective action*. This provides a further compactification of the calculations. The effective action is a function of the expectation value of the field, $\phi(x)$, and is obtained by the Legendre transformation

$$\Gamma[\phi] = \sup_J \left(\int d^D x \phi(x) J(x) - W[J] \right). \tag{1.55}$$

---

[4] Note, however, that there is a sign difference in the definition using the partition function.

The sup in the formula enforces stationarity with respect to $J(x)$ such that

$$\frac{\delta W[J]}{\delta J(x)} = \phi(x). \tag{1.56}$$

Using this relation, the first two functional derivatives are simple to calculate:

$$\frac{\delta \Gamma[\phi]}{\delta \phi(x)} = J(x), \tag{1.57}$$

$$\frac{\delta^2 \Gamma[\phi]}{\delta \phi(x)\delta \phi(y)} = \frac{\delta J(x)}{\delta \phi(y)} = \frac{1}{\frac{\delta^2 W[J]}{\delta J(x)\delta J(y)}} = \left(G_c^{(2)}(x,y)\right)^{-1}. \tag{1.58}$$

Hence, the first derivative equals the external field needed to produce $\phi(x)$ as an expectation value, while the second derivative yields the inverse propagator. To complete the analogy with statistical physics, for a given external field J, the pressure in the system at finite temperature T and in volume V is given by

$$P = \frac{T}{V} W[J] = \frac{T}{V} \sup_{\phi} \left(\int d^D x \phi(x) J(x) - \Gamma[\phi] \right). \tag{1.59}$$

With this, we conclude the general introduction to field theory and proceed with an introduction to a formalism that provides a symmetry preserving scheme for computing the effective action $\Gamma[\phi]$.

1.6 The functional renormalization group

The effective action contains all information on a quantum field theoretical system. However, the functional integrals cannot be performed analytically for interacting theories. Hence the challenge is to find a practicable strategy for the calculation of the effective action.

A solution to this problem is offered by the functional renormalization group. A central quantity in this approach is the effective average action, Γ_k, which depends on a parameter k and interpolates between the well-known classical action S_E and the unknown quantum effective action Γ. We derive a flow equation for Γ_k, and solve it starting from S_E towards Γ. The parameter k is a renormalization scale with the dimension of a momentum. The idea is to suppress the fluctuations in the system depending on the current value of k. Initially, for high values of k, all fluctuations are frozen out, so that the theory is classical. At the end, at $k = 0$, all fluctuations are included so that all quantum effects are captured. For values of k in between, we implement Wilson's idea of systematically integrating out the fluctuations momentum shell by momentum shell by changing k. This procedure is illustrated in Fig. 1.5.

In order to exploit these ideas, we add the scale dependent term

$$\Delta S_k[\Phi] = \frac{1}{2} \int_x \int_y \Phi(x) \hat{R}_k(x,y) \Phi(y) \tag{1.60}$$

to the Euclidean action, where $\hat{R}_k(x,y)$ is the so-called regulator. We choose $\hat{R}_k(x,y)$ such that for $k \to \infty$ it suppresses all fluctuations in the system, and that for $k \to 0$ it vanishes. This will ensure us that at $k \to \infty$ all functional integrations can be performed by simply substituting the expectation value of the field in the formulas, neglecting the fluctuations. It also guarantees that at $k \to 0$ the effect of the regulator is removed and all quantum fluctuations are recovered. We will later clarify what this means for the regulator and which choices we can make.

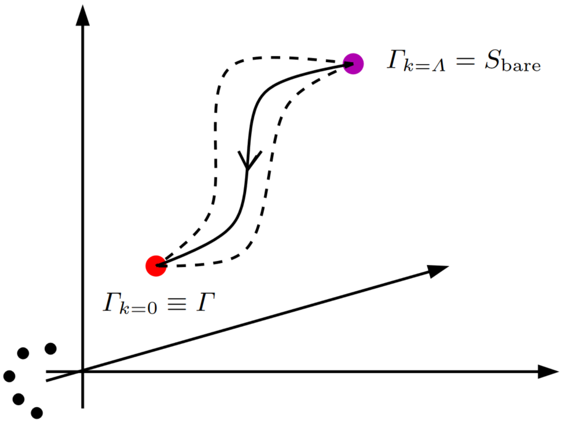

Figure 1.5.: Illustration of the idea behind the FRG. First all fluctuations are suppressed by a regulator function and then the regulator is gradually removed. Different regulators provide different flows for the effective average action Γ_k, however in the $k=0$ limit they all lead to the full quantum effective action $\Gamma_{k=0}=\Gamma$. It should be noted that truncations of Γ_k may spoil this property, and due to this, the choice of regulator may affect the final result. Different regulators induce disparate spurious effects. Figure taken from Ref. [69].

Using the scale dependent action, we define the effective average action

$$\begin{aligned}\Gamma_k[\phi] = \sup_J \Bigg(\int d^d x \phi(x) J(x) - \Delta S_k[\phi] \\ - \ln \int \mathcal{D}\Phi \exp\left(-S_E[\Phi] - \Delta S_k[\Phi] + \int d^D x J(x)\Phi(x) \right) \Bigg). \end{aligned} \tag{1.61}$$

Obviously we recover the effective action in the $k \to 0$ limit, where the regulator vanishes. In the $k \to \infty$ limit, where all fluctuations are regulated, we can drop the functional integral and substitute the expectation value of the field yielding

$$\Gamma_{k\to\infty}[\phi] = S_E[\phi]. \tag{1.62}$$

To derive a flow equation for the effective average action $\Gamma_k[\phi]$, we apply a k derivative on (1.61). Due to the stationarity with respect to variations of $J(x)$, we can ignore a possible scale dependence of the source giving

$$\partial_k \Gamma_k[\phi] = \frac{\int \mathcal{D}\Phi \left(\partial_k \Delta S_k[\Phi] - \partial_k \Delta S_k[\phi]\right) \exp\left(-S_E[\Phi] - \Delta S_k[\Phi] + \int d^D x J(x)\Phi(x)\right)}{\int \mathcal{D}\Phi \exp\left(-S_E[\Phi] - \Delta S_k[\Phi] + \int d^D x J(x)\Phi(x)\right)}. \tag{1.63}$$

Definition the regulated propagator

$$\begin{aligned} G_k(x,y) &= \langle \Phi(x)\Phi(y)\rangle_{J,k} - \phi(x)\phi(y) \\ &= \frac{\int \mathcal{D}\Phi \left(\Phi(x)\Phi(y) - \phi(x)\phi(y)\right) \exp\left(-S_E[\Phi] - \Delta S_k[\Phi] + \int d^D x J(x)\Phi(x)\right)}{\int \mathcal{D}\Phi \exp\left(-S_E[\Phi] - \Delta S_k[\Phi] + \int d^D x J(x)\Phi(x)\right)}. \end{aligned} \tag{1.64}$$

and using the explicit form of the scale dependent action (1.60), we obtain the flow equation

$$\begin{aligned} \partial_k \Gamma_k[\phi] &= \frac{1}{2} \int d^D x \int d^D y G_k(x,y) \partial_k \hat{R}_k(y,x) = \frac{1}{2} \int d^D x \int d^D y \left(\Gamma_k^{(2)} + \hat{R}_k\right)^{-1} \partial_k \hat{R}_k \\ &= \frac{1}{2} \mathrm{Tr} \left\{ \left(\Gamma_k^{(2)} + \hat{R}_k\right)^{-1} \partial_k \hat{R}_k \right\}. \end{aligned} \tag{1.65}$$

In the last expression the trace is a shorthand notation for contracting the indexes of the operators, here in position space, and carrying out the integrals. For the last equality we used the identity (1.58). With this we arrived at the Wetterich equation, which defines the so-called functional renormalization group (FRG) approach [70, 71]. For reviews see Refs. [69, 72–74].

The derivation presented here was for a one-component scalar field theory. The approach can be readily extended to multicomponent scalar field theories, gauge theories, massive vector theories and to fermionic theories as well.

First, let us consider a theory with an N component scalar field with an $O(N)$ symmetry. In this case, each mode has to be regulated through a term identical to (1.60). The regulator may be different for different modes, it may even be nondiagonal. As a consequence, both the regulator, R_k, and the second functional derivative of the effective action, Γ_k, have two internal indexes. The trace in Eq. (1.65) has to be extended to include the internal indexes as well.

Now let us add fermions to the system. A system of fermions, unlike a system of bosons, has a wave function that is antisymmetric under the exchange of two identical fermions. Due to this difference, fermions in quantum field theories are not represented by complex valued fields, but rather by fields that take anticommuting Grassmann variables as values. To account for this difference, a fermion regulator term of the form

$$\Delta S_{k,F}[\bar{\Psi},\Psi]=\int_x\int_y \bar{\Psi}(x)\hat{R}_{k,F}(x,y)\Psi(y) \tag{1.66}$$

is introduced. The fermionic regulator may be different from the introduced bosonic regulator. The resulting flow of the effective average action is then driven by both fermionic and bosonic contributions,

$$\partial_k\Gamma_k[\phi]=\frac{1}{2}\mathrm{Tr}\left\{\left(\Gamma_k^{(2,0,0)}+\hat{R}_{k,B}\right)^{-1}\partial_k\hat{R}_{k,B}\right\}-\mathrm{Tr}\left\{\left(\Gamma_k^{(0,1,1)}+\hat{R}_{k,F}\right)^{-1}\partial_k\hat{R}_{k,F}\right\}. \tag{1.67}$$

Here, the $\Gamma_k^{(2,0,0)}$ denotes the second functional derivative of the effective average action with respect to boson fields, While $\Gamma_k^{(0,1,1)}$ denotes the functional derivative with respect to a fermion field and its conjugate. The traces denote spatial integration, as well as a summation over the bosonic and fermionic internal indexes.

To illustrate how the FRG works, let us consider a toy model, the scalar field theory in $3+1$ dimensions. For the time being let us simply postulate the flow equation, and derive it later for the quark-meson model in Sec. 2.4[5]. We consider the theory in the so-called local potential approximation (LPA), in which the scale dependence of the effective average action is due only to the potential term

$$\partial_k\Gamma_k=\frac{V}{T}\partial_k U_k. \tag{1.68}$$

Furthermore we use a regulator of the form

$$\hat{R}_k(x,y)=R_k(i\vec{\nabla}_x)\delta(x-y), \tag{1.69}$$

which is diagonal in momentum space and regulates only spatial momenta. Under this assumptions the flow equation at low temperatures reads

$$\partial_k U_k=\frac{1}{4}\int\frac{d^3q}{(2\pi)^3}\frac{\partial_k R_k(q)}{\sqrt{m^2+q^2+R_k(q)}}, \tag{1.70}$$

---

[5] The contribution discussed here can be obtained from the flow equation (2.102) by dropping the quark and pion contributions.

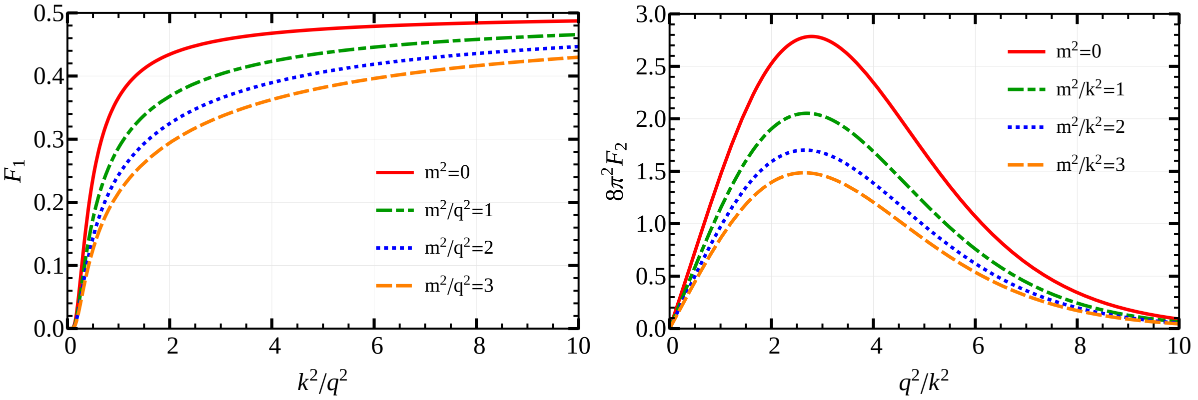

Figure 1.6.: Left: contribution of a single mode to the flow as a function of the scale parameter k. Right: contribution of momentum shells at a fixed RG scale as a function of the momentum.

where q is the 3-momentum and m is the mass of the particle. The contribution of a single mode is

$$F_1 = \frac{\partial_k R_k(q)}{4\sqrt{m^2 + q^2 + R_k(q)}}, \tag{1.71}$$

whereas the contribution of a momentum shell in units of k^2 reads

$$F_2 = \frac{4\pi q^2}{(2\pi)^3 k^2} F_1 = \frac{q^2}{8\pi^2 k^2} \frac{\partial_k R_k(q)}{\sqrt{m^2 + q^2 + R_k(q)}}. \tag{1.72}$$

Both F_1 and F_2 are dimensionless. Let us analyze these flow contributions. In order to implement the ideas discussed earlier, we require that the regulator is nonnegative for all k and q, that it vanishes in the $k \to 0$ limit and that it suppresses all fluctuations in the $k \to \infty$ limit. An appropriate choice for example is the exponential regulator,

$$R_k(q) = \frac{q^2}{e^{q^2/k^2} - 1}, \tag{1.73}$$

which we use for the finite-volume studies in Chapter 5. For this regulator the contribution of a single mode as a function of the RG scale, k, is plotted in the left panel of Fig. 1.6. The mode contribution is approximately constant in the region $k \gg q$, however it drops where $k \approx q$ and approaches zero smoothly. For $k \ll q$ the mode does not contribute anymore, the fluctuations of momentum q are frozen out. On the right panel of Fig. 1.6 it is shown that for this regulator, the momentum shell at a given RG scale contributing the most is around $q^2 \approx 3k^2$. Low momentum shells are suppressed by the phase space volume, high momentum shells by the exponential suppression of the regulator. This resembles Wilson's idea of integrating out fluctuations shell by shell, since by decreasing k, the momentum shell contributing most is gradually shifted to lower momenta. With this we finish the general discussion of the FRG. In Chapter 2, after some basic introduction to the model, we will discuss the quark-meson model within the FRG approach in detail.

Chapter 2

The quark-meson model

As discussed in the previous chapter, the thermodynamics of QCD can at present be computed systematically only at vanishing net baryon density using the formalism of lattice QCD. To gain insight into the phase structure of QCD at nonzero densities, the application of an effective model is needed. In the models usually considered, the nonabelian gauge interaction is treated approximately leading to simplified dynamics. These models are constructed such that the dynamics, apart from the realization of the current quark masses, is chirally invariant. This means that the Hamiltonian of these models exhibit the $SU(2)_L \otimes SU(2)_R$ symmetry introduced in the previous chapter. In the ground state of these theories, just as in QCD, the chiral symmetry is, however, spontaneously broken. One such model is the *quark-meson* (QM) model [75]. The fundamental degrees of freedom of the model are the quarks and some of the low-lying meson fields of the QCD spectrum. In the simplest realization of the model there are the two light quark flavors, u and d, and the interaction between the quarks is mediated by the pseudoscalar pion triplet π^i and the scalar sigma meson σ. The four meson fields together form a multiplet of the chiral symmetry group. To determine their transformation rules under chiral transformations, we identify the meson fields with the following quark field bilinears [76]:

$$\vec{\pi} \equiv i\bar{\psi}\gamma_5\vec{\tau}\psi, \qquad \sigma \equiv \bar{\psi}\psi, \tag{2.1}$$

where $\psi = \{u, d\}$ denotes the quark fields. These bilinears transform under an infinitesimal vector transformation Λ_V and an axialvector transformation Λ_A with infinitesimal parameters $\{\theta^1, \theta^2, \theta^3\}$ as follows[1]:

$$\bar{\psi}\psi \xrightarrow{\Lambda_V} \psi^\dagger\left(1+i\frac{\tau^j}{2}\theta^j\right)\gamma^0\left(1-i\frac{\tau^k}{2}\theta^k\right)\psi \approx \bar{\psi}\psi \tag{2.2}$$

$$\begin{aligned} i\bar{\psi}\gamma_5\tau^j\psi \xrightarrow{\Lambda_V} i\psi^\dagger\left(1+i\frac{\tau^k}{2}\theta^k\right)\gamma^0\gamma_5\tau^j\left(1-i\frac{\tau^l}{2}\theta^l\right)\psi &\approx i\bar{\psi}\gamma_5\tau^j\psi + \frac{1}{2}\bar{\psi}\gamma_5\left[\tau^j, \tau^k\right]\psi\theta^k \\ &= i\bar{\psi}\gamma_5\tau^j\psi + \epsilon_{jkl}\theta^k i\bar{\psi}\gamma_5\tau^l\psi \end{aligned} \tag{2.3}$$

$$\bar{\psi}\psi \xrightarrow{\Lambda_A} \psi^\dagger\left(1+i\gamma_5\frac{\tau^j}{2}\theta^j\right)\gamma^0\left(1-i\gamma_5\frac{\tau^k}{2}\theta^k\right)\psi \approx \bar{\psi}\psi - i\bar{\psi}\gamma_5\tau^j\psi\theta^j \tag{2.4}$$

$$\begin{aligned} i\bar{\psi}\gamma_5\tau^j\psi \xrightarrow{\Lambda_A} i\psi^\dagger\left(1+i\gamma_5\frac{\tau^k}{2}\theta^k\right)\gamma^0\gamma_5\tau^j\left(1-i\gamma_5\frac{\tau^l}{2}\theta^l\right)\psi &\approx i\bar{\psi}\gamma_5\tau^j\psi + \frac{1}{2}\bar{\psi}\left\{\tau^j, \tau^k\right\}\psi\theta^k \\ &= i\bar{\psi}\gamma_5\tau^j\psi + \bar{\psi}\psi\theta^j. \end{aligned} \tag{2.5}$$

---

[1] These transformation properties can be shown for arbitrary finite transformations as well using Eq. (B.7) and an analogous identity for the axial-vector interaction. The derivation is, however, slightly more involved technically for finite transformations, and hence to be as transparent as possible, we discuss the transformation rules for infinitesimal transformations. Nevertheless, for simply connected groups, the transformation rules of the Lie algebra defines the transformation of the group elements uniquely [77].

We retained only at most linear terms in the parameters $\{\theta^1, \theta^2, \theta^3\}$. Based on these calculations we obtain the transformation rules of the meson fields in the model under chiral transformations,

$$\sigma \xrightarrow{\Lambda_V} \sigma, \quad \vec{\pi} \xrightarrow{\Lambda_V} \vec{\pi} + \vec{\theta} \times \vec{\pi}, \qquad \sigma \xrightarrow{\Lambda_A} \sigma - \vec{\theta}\vec{\pi}, \quad \vec{\pi} \xrightarrow{\Lambda_A} \vec{\pi} + \sigma\vec{\theta}. \tag{2.6}$$

First let us note that the $O(4)$ invariant combination

$$\rho = \frac{1}{2}\left(\sigma^2 + \vec{\pi}^2\right), \tag{2.7}$$

is invariant under the chiral transformations (2.6) to leading order in θ^i. This reflects the fact that there exists a homomorphic mapping of the group $SU(2) \times SU(2)$ onto $SO(4)$ and helps us to construct an effective field theory that is chirally symmetric and to implement the quark interactions through meson exchange. In view of this, in the quark-meson model, we couple the pion field to the pseudoscalar quark combination, and the sigma field to the scalar quark combination with the same coupling constant, the Yukawa coupling g_s. The quark part of the Lagrangian then reads

$$\mathcal{L}_q = i\bar{\psi}\gamma^\mu\partial_\mu\psi - g_s\bar{\psi}\psi\sigma - g_s i\bar{\psi}\gamma_5\vec{\tau}\psi\vec{\pi} = \bar{\psi}(i\gamma^\mu\partial_\mu - g_s(\sigma + i\gamma_5\vec{\tau}\vec{\pi}))\psi. \tag{2.8}$$

Note that, in a chirally symmetric theory, the quarks are massless. In QCD, the current quark masses break the symmetry explicitly, so for a successful modeling of QCD explicit breaking of the chiral symmetry is needed. Adding a quark mass term is, however, not the only way to implement this, and for simplicity, in the quark-meson model, the chiral symmetry is broken by a purely mesonic term.

The dynamics of the meson fields are also constrained by chiral symmetry, hence the $O(4)$ invariant ρ proves to be helpful here again. The mesonic part of the Lagrangian reads

$$\mathcal{L}_{mes} = \frac{1}{2}\partial_\mu\sigma\partial^\mu\sigma + \frac{1}{2}\partial_\mu\vec{\pi}\partial^\mu\vec{\pi} - U_m(\sigma, \vec{\pi}), \tag{2.9}$$

and the interaction between the mesons is given by the potential

$$U_m(\sigma, \vec{\pi}) = U_{ch}(\rho) - H\sigma \equiv \lambda\rho^2 + m^2\rho - H\sigma. \tag{2.10}$$

Here $U_{ch}(\rho)$ is the chirally invariant part of the potential, which depends only on the chiral invariant ρ. For simplicity, we assume only a quadratic and a quartic term for the mesonic interactions in the Lagrangian. The term $-H\sigma$, which explicitly breaks chiral symmetry, simulates the nonvanishing current quark masses in QCD. The strength of the symmetry breaking field H can be related to the quark masses using the Gell-Mann-Oaks-Renner relation, as discussed below.

Putting the pieces together, the full Lagrangian of the QM model reads

$$\mathcal{L}_{QM} = \frac{1}{2}\partial_\mu\sigma\partial^\mu\sigma + \frac{1}{2}\partial_\mu\vec{\pi}\partial^\mu\vec{\pi} + \bar{\psi}(i\gamma^\mu\partial_\mu - g_s(\sigma + i\gamma_5\vec{\tau}\vec{\pi}))\psi - \frac{\lambda}{4}(\sigma^2 + \vec{\pi}^2)^2 - \frac{m^2}{2}(\sigma^2 + \vec{\pi}^2) + H\sigma, \tag{2.11}$$

which, after Wick rotation $t \to -i\tau$ and expressing the Gamma matrices with their Euclidean counterparts, translates to the Euclidean action

$$\begin{aligned} S_E &= -iS[t \to -i\tau] = -\int d\tau \int d^dx \mathcal{L}_{QM}[t \to -i\tau] \\ &= \int d\tau \int d^dx \left(\frac{1}{2}\partial_\mu\sigma\partial_\mu\sigma + \frac{1}{2}\partial_\mu\vec{\pi}\partial_\mu\vec{\pi} + \bar{\psi}(\gamma_\mu^E\partial_\mu + g_s(\sigma + i\gamma_5\vec{\tau}\vec{\pi}))\psi + U_m(\sigma, \vec{\pi})\right). \end{aligned} \tag{2.12}$$

By implementing the explicit symmetry breaking field this way, we just added a linear term in the σ field to the action. Based on Eq. (1.48), a linear term in the action can be identified with a constant external source term $J[x]$ conjugate to the field, which in turn simplifies the formalism.

The model has several free parameters that must be determined, namely g_s, m^2, λ and H. These parameters are, irrespective of the method one uses to solve the model, constrained by vacuum properties of the system: the masses of the pion and the sigma mesons, the constituent quark masses and the pion decay constant. After fixing these parameters, no further parameters enter at finite temperature or density. We will discuss this issue more specifically in the next section using the mean-field approximation.

To learn about the phase diagram of matter in this model, we study the system at finite temperature and density. Due to baryon number conservation in a closed system, the operator of net baryon number,

$$B = \frac{1}{3}\int d^d x \psi^\dagger \psi = \frac{1}{3}\int d^d x \bar{\psi}\gamma^0\psi, \tag{2.13}$$

yields a conserved charge. For simplicity, we do not consider a closed system, but rather we describe the theory in the grand canonical ensemble, where the system can exchange energy and particles with a thermal and particle reservoir. In general, the total baryon number in subsystems is not conserved, since particle exchange is possible with the surroundings. For large systems there is no essential difference between canonical and grand canonical ensembles, but the latter has the simplicity that the global conservation of charge does not have to be taken into account. Instead, we introduce the conjugate variable of the baryon number, namely the baryon chemical potential μ_B, which in turn determines the *expectation value* of the total net baryon number. In the grand canonical ensemble, the partition function, apart from the external field, is a function of the temperature and the chemical potential and is given by

$$\mathcal{Z} = \int \mathcal{D}\Psi\mathcal{D}\bar{\Psi}\mathcal{D}\sigma\mathcal{D}\vec{\pi}\exp\left(-S_E + \beta\mu_B B\right) = \int \mathcal{D}\Psi\mathcal{D}\bar{\Psi}\mathcal{D}\sigma\mathcal{D}\vec{\pi}\exp\left(-S_E + \int d\tau \int d^d x \bar{\psi}\mu\gamma^0\psi\right), \tag{2.14}$$

introducing $\mu \equiv \mu_q \equiv \mu_B/3$ for the quark chemical potential. The pressure, just as in Eq. (1.59), is given by

$$P(T,\mu) = \frac{T}{V}\ln\mathcal{Z}, \tag{2.15}$$

where the explicit dependence on the external field (current quark mass) has been dropped. In the grand canonical ensemble, the pressure can be used to extract the expectation value of the baryon number as follows,

$$\langle B\rangle = \frac{1}{\mathcal{Z}}\int \mathcal{D}\Psi\mathcal{D}\bar{\Psi}\mathcal{D}\sigma\mathcal{D}\vec{\pi}\, B\exp\left(-S_E + \beta\mu_B B\right) = T\frac{\partial}{\partial\mu_B}\ln\mathcal{Z} = V\frac{\partial P}{\partial\mu_B}. \tag{2.16}$$

Similarly, expectation values of higher powers of the baryon number can also be expressed by derivatives of the grand canonical potential as

$$\langle B^n\rangle = \frac{1}{\mathcal{Z}}\int \mathcal{D}\Psi\mathcal{D}\bar{\Psi}\mathcal{D}\sigma\mathcal{D}\vec{\pi}\, B^n\exp\left(-S_E + \beta\mu_B B\right) = \frac{T^n}{\mathcal{Z}}\frac{\partial^n}{\partial\mu_B^n}\mathcal{Z}. \tag{2.17}$$

These higher moments of the baryon number do not equal a single derivative of the pressure, but rather a combination of multiple derivatives. To see this, let us consider the second derivative of the pressure,

$$VT\frac{\partial^2 P}{\partial\mu_B^2} = \frac{T^2}{\mathcal{Z}}\frac{\partial^2\mathcal{Z}}{\partial\mu_B^2} - \left(\frac{T}{\mathcal{Z}}\frac{\partial\mathcal{Z}}{\partial\mu_B}\right)^2 = \langle B^2\rangle - \langle B\rangle^2, \tag{2.18}$$

which measures the fluctuations around $\langle B \rangle$. Equivalently,

$$\left\langle B^2 \right\rangle = VT \frac{\partial^2 P}{\partial \mu_B^2} + \left(V \frac{\partial P}{\partial \mu_B} \right)^2 . \tag{2.19}$$

As indicated by the first two moments of the baryon number, fluctuations of the baryon number are intrinsically related to derivatives of pressure with respect to the chemical potential. This motivates us to define the dimensionless susceptibilities of baryon number as

$$\chi_B^n = \frac{1}{T^{4-n}} \frac{\partial^n P}{\partial \mu_B^n}, \tag{2.20}$$

and the cumulants of the baryon number distribution in a volume V as

$$c_B^n = VT^3 \chi_B^n . \tag{2.21}$$

These are very important experimental observables. In Chapter 4, we are going to discuss their calculation in detail, and provide the relation between cumulants and moments of the distribution explicitly for the first four of them.

2.1 Mean-field approximation of the quark-meson model

To gain a qualitative insight into the phase diagram and chiral criticality of the quark-meson model, one may apply the mean-field (MF) approximation, in which the meson fluctuations are ignored and the meson fields are replaced by their spatially homogeneous classical expectation values

$$\langle \sigma \rangle \neq 0, \qquad \langle \vec{\pi} \rangle = 0. \tag{2.22}$$

In the following, in order not to overcomplicate our notation, the classical expectation values $\langle \sigma \rangle$ and $\langle \vec{\pi} \rangle$ will be denoted by σ and $\vec{\pi}$, respectively. Note that we do not allow the pions to take nonzero expectation value. This would correspond to a state with pion condensation [78]. In such a state parity is spontaneously broken, since the pion is a pseudoscalar.

In the mean-field approximation, the path integration over the boson fields is now dropped, and the logarithm of the partition function has the form

$$\begin{aligned} \frac{T}{V} \ln \mathcal{Z} = \frac{T}{V} \ln \int \mathcal{D}\Psi \mathcal{D}\bar{\Psi} \exp\left(-S_E + \beta \mu_B B\right)\right) = -(U_m(\sigma, 0) + \Omega_{q\bar{q}}) \equiv -\Omega_{ch}(T, \mu; \sigma) + H\sigma \\ \equiv -\Omega(T, \mu, H; \sigma), \end{aligned} \tag{2.23}$$

where

$$\Omega_{q\bar{q}}(T, \mu; \sigma) = -\frac{T}{V} \ln \int \mathcal{D}\Psi \mathcal{D}\bar{\Psi} \exp\left(- \int d\tau \int d^d x \bar{\psi}(\gamma_\mu^E \partial_\mu - \mu \gamma_0^E + g_s \sigma) \psi \right) \tag{2.24}$$

contains the contribution from the fermions. This path integral has the form of a free fermion gas, and can be evaluated by standard thermal field theory techniques. After eliminating the divergent vacuum fermion contribution and retaining only the finite part using dimensional regularization [47], one arrives at

$$\Omega_{q\bar{q}}(T, \mu; \sigma) = \Omega_{q\bar{q}}^{vac}(\sigma) + \Omega_{q\bar{q}}^{th}(T, \mu; \sigma), \tag{2.25}$$

$$\Omega_{q\bar{q}}^{th}(T, \mu; \sigma) = -\frac{N_c N_f T}{\pi^2} \int_0^\infty dp p^2 \left(\ln\left(1 + e^{(\mu - E_q)/T}\right) + \ln\left(1 + e^{(-\mu - E_q)/T}\right) \right), \tag{2.26}$$

$$\Omega_{q\bar{q}}^{vac}(\sigma) = -\frac{N_c N_f}{8\pi^2} g_s^4 \sigma^4 \ln\left(\frac{g_s \sigma}{M} \right). \tag{2.27}$$

Here, $\Omega_{q\bar{q}}^{vac}(\sigma)$ yields the renormalized quark and antiquark contribution in the vacuum and $\Omega_{q\bar{q}}^{th}(T,\mu;\sigma)$ contains the modifications due to finite temperature and density. The latter vanishes in the vacuum. In Eq. (2.27), M is an arbitrary renormalization scale. Any modification in M can completely be compensated by appropriate redefinition of the parameters λ and m^2. In the following, any specified λ and m^2 value is to be understood with the choice $M = g_s f_\pi$. Further more,

$$E_q = \sqrt{p^2 + g_s^2\sigma^2} \tag{2.28}$$

denotes the quark energy, $N_c = 3$ is the number of colors and $N_f = 2$ is the number of quark flavors.

To finish the introduction of the model, we address the question how to determine the external field, H, and the temperature and density dependent physical value of σ, which we denote by σ_M. In the previous chapter we showed that the functional derivative of $\ln Z[J]$ with respect to the external field yields the field expectation value (see Eq. (1.53)). Applying this finding to the spatially homogeneous external field in the theory, H, and for a homogeneous condensate, we find that

$$\frac{d}{dH}\left(\frac{T}{V}\ln\mathcal{Z}\right) = \frac{d}{dH}\left(-\Omega_{ch}(T,\mu;\sigma) + H\sigma\right) \overset{!}{=} \sigma \qquad \rightarrow \qquad \left.\frac{\partial\Omega_{ch}(T,\mu;\sigma)}{\partial\sigma}\right|_{\sigma=\sigma_M} = H. \tag{2.29}$$

The equation on the right is called the gap equation and expresses the fact that, since the physical value of σ, σ_M, in principle depends on H, the relation on the left can be fulfilled only if the expression $H\sigma - \Omega_{ch}$ is stationary with respect to σ. With this relation at hand, the pressure of the system is simply given by

$$P(T,\mu) = \frac{T}{V}\ln\mathcal{Z} = -\Omega_{ch}(T,\mu;\sigma_M) + H\sigma_M = -\Omega(T,\mu,H;\sigma_M), \tag{2.30}$$

which can be used to derive all thermal properties of the system in the grand canonical ensemble. If there are multiple values of σ fulfilling the gap equation, then the one with the highest pressure is chosen.

The only question that remained unanswered so far is the determination of the model parameters λ, m^2, g_s and H. In order to set the constitient quark mass, m_c, and to fulfill the Goldberger-Treiman relation, we require

$$g_s\sigma_M = m_c \approx 300\,\text{MeV}, \qquad \sigma_M(T=0,\mu=0) = f_\pi \approx 93\,\text{MeV}. \tag{2.31}$$

Furthermore, in order to have the same symmetry breaking strength as in QCD, we have to set

$$-\frac{m_u + m_d}{2}\left\langle 0\left|\bar{u}u + \bar{d}d\right|0\right\rangle = H\sigma_M(T=0,\mu=0) = Hf_\pi. \tag{2.32}$$

Using the Gellmann-Oaks-Renner (GOR) relation, this yields $H = m_\pi^2 f_\pi$. Finally we set the value of the sigma curvature mass in the vacuum

$$m_\sigma^2 = \left.\frac{\partial^2\Omega_{ch}(T=0,\mu=0;\sigma)}{\partial^2\sigma}\right|_{\sigma=\sigma_M}. \tag{2.33}$$

These conditions yield the parameters with the renormalization scale $M = g_s f_\pi$,

$$\lambda = \frac{m_\sigma^2 - m_\pi^2}{2f_\pi^2} + \frac{9g_s^4}{4\pi^2}, \quad m^2 = \frac{3m_\pi^2 - m_\sigma^2}{2} - \frac{3g_s^4 f_\pi^2}{2\pi^2}, \quad g_s = \frac{m_c}{f_\pi}, \quad H = m_\pi^2 f_\pi. \tag{2.34}$$

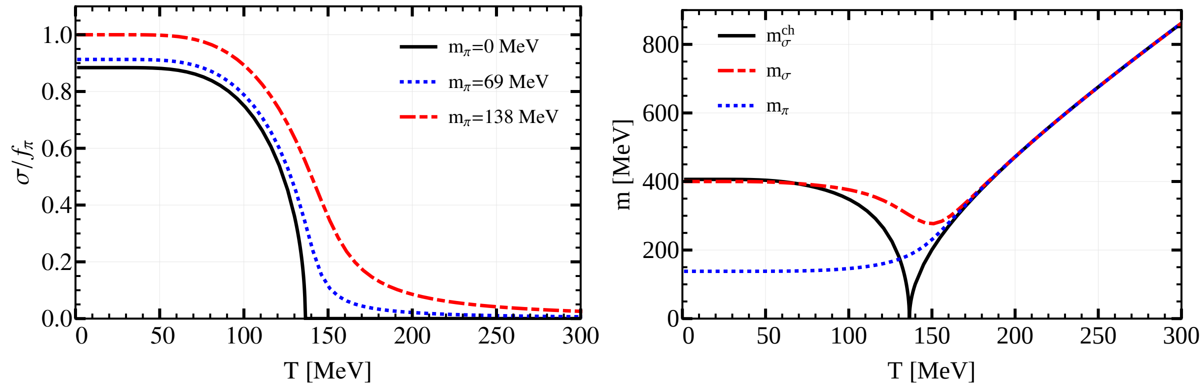

Figure 2.1.: Restoration of chiral symmetry in the quark-meson model at vanishing density. On the left the melting of the order parameter is depicted for different values of the symmetry breaking field, resulting in different vacuum pion masses. On the right, the screening masses of the mesons are shown for physical pion mass (blue and red curves), and in the chiral limit (black curve). The pions in the chiral limit below the chiral transition are massless, above they are degenerate with the sigma meson.

If not specified otherwise, we use $m_\sigma = 400$ MeV and $m_\pi = 138$ MeV. In the following we also consider setups with nonphysical pion masses. The chiral limit for example corresponds to $m_\pi = 0$. In these cases we do not change the parameters of the theory, λ, m^2 and g_s, and we only modify the external field H according to $H = m_\pi^2 f_\pi$. In other words, we do not refit the parameters when considering nonphysical pion masses. Thus, when the pion mass is set to unphysical values, only H is changed. We act in the more involved models discussed later analogously.

Now we are in a position to calculate thermodynamic properties of the QM model in the mean-field approximation. In Fig. 2.1 one sees that at vanishing density and with physical pion mass, the order parameter melts continuously with increasing temperature, approaching but never reaching zero. This is in qualitative agreement with lattice QCD findings. In the chiral limit, $m_\pi = 0$, the order parameter goes to zero continuously, but it is not analytic at the transition temperature T_c. This is a second order phase transition. This transition will be discussed in Chapter 3 in detail.

One shortcoming of the model can be seen by observing the behavior of the pressure at low temperatures and densities. Assuming a constant chiral condensate $\sigma_M = f_\pi$ and low occupation numbers, the pressure reads

$$
\begin{aligned}
P &= P_{vac} - \Omega_{q\bar{q}}^{th} \\
&= P_{vac} + \frac{N_c N_f T}{\pi^2} \int_0^\infty dp p^2 \left(\ln\left(1 + e^{\left(\mu - \sqrt{p^2 + g_s^2 f_\pi^2}\right)/T}\right) + \ln\left(1 + e^{\left(-\mu - \sqrt{p^2 + g_s^2 f_\pi^2}\right)/T}\right)\right), \\
&\approx P_{vac} + \frac{2 N_c N_f T \cosh(\mu/T)}{\pi^2} \int_0^\infty dp p^2 e^{-\sqrt{p^2 + g_s^2 f_\pi^2}/T} \\
&= P_{vac} + \cosh(\mu/T) f(T). \qquad (2.35)
\end{aligned}
$$

This, however, is in contradiction with experimental findings. Due to confinement, at low temperatures and densities, strongly interacting matter is well described by a weekly interacting gas of hadrons. The degrees of freedom carrying baryon number are then the baryons and the baryon resonances, rather then the quarks. In the hadron resonance gas (HRG) approximation [55, 79–81], the pressure has the form

$$
P_{HRG} = P_{vac} + \cosh(\mu_B/T) g(T) = P_{vac} + \cosh(3\mu/T) g(T), \qquad (2.36)
$$

as this will be discussed in Chapter 4. This difference shows up explicitly in fluctuation observables. Looking at the baryon number cumulants defined in the previous section, one finds that for example the ratio χ_B^4/χ_B^2 is unity in the HRG model, but approximately 1/9 in the QM model. In order to cure this problem, single quark fluctuations at low temperature have to be suppressed. In other words, confinement has to be accounted for. This can be done by coupling the quark fields to background temporal gluon fields in the form of the Polyakov loop variables. The resulting model, the Polyakov-loop-extended quark-meson model is presented in the subsequent section.

2.2 The Polyakov-loop-extended quark-meson model

The chiral QM model is an effective realization of the chiral sector of QCD. However, because the local $SU(N_c)$ invariance of QCD is replaced by a global symmetry in the model, color confinement is lost. Nevertheless, the confining properties of QCD can be approximately accounted for by including the expectation value of the Polyakov loop

$$\Phi = \frac{1}{N_c}\langle \mathrm{Tr}_c\, L(\vec{x})\rangle\,, \quad \bar{\Phi} = \frac{1}{N_c}\left\langle \mathrm{Tr}_c\, L^\dagger(\vec{x})\right\rangle, \tag{2.37}$$

with

$$L(\vec{x}) = \mathcal{P}\exp\left(i\int_0^\beta d\tau A_4(\vec{x},\tau)\right), \tag{2.38}$$

as a degree of freedom in a low-energy chiral effective model, like the QM model [37, 42, 46, 48, 82, 83]. Here $A_4 = iA_0$ is the temporal component of the Euclidean gluon field, $\beta = 1/T$ and $\mathcal{P}$ denotes path ordering. Thus, the Polyakov-loop-extended quark-meson (PQM) model effectively combines both the chiral symmetry and confinement of QCD.

The Lagrangian of the PQM model reads

$$\mathcal{L} = \bar{q}\left(i\gamma^\mu D_\mu - g_s(\sigma + i\gamma_5\vec{\tau}\vec{\pi})\right)q + \frac{1}{2}\left(\partial_\mu\sigma\right)^2 + \frac{1}{2}\left(\partial_\mu\vec{\pi}\right)^2 - U_m(\sigma,\vec{\pi}) - \mathcal{U}(T;\Phi,\bar{\Phi}). \tag{2.39}$$

The coupling between the effective gluon field and quarks is implemented through the covariant derivative, $D_\mu = \partial_\mu + iA_\mu$, where the spatial components of the gluon field are neglected, i.e. $A_\mu = \delta_{\mu 0}A_0$. Here $\mathcal{U}(T;\Phi,\bar{\Phi})$ is the effective potential for the thermal expectation value of the Polyakov loop. It is constructed such that it respects the $Z(N_c)$ global symmetry, with parameters chosen to reproduce the thermodynamics of pure lattice gauge theory [38, 40, 84]. The various choices for the applied Polyakov-loop potential are discussed in Appendix D.

The thermodynamic potential of the PQM model in the mean-field approximation is given by [47]

$$\Omega(T,\mu;\sigma,\Phi,\bar{\Phi}) = U_m(\sigma,0) - \frac{N_c N_f}{8\pi^2}g_s^4\sigma^4\ln\left(\frac{\sigma}{f_\pi}\right) + \Omega_f^{th}(T,\mu;\sigma,\Phi,\bar{\Phi}) + \mathcal{U}(T;\Phi,\bar{\Phi}), \tag{2.40}$$

where the meson and vacuum fermion contributions are identical to that in the QM model, shown in Eqs. (2.23) and (2.27), whereas the thermal fermionic contribution is modified due to the coupling of quarks to the Polyakov loop background

$$\Omega_f^{th}(T,\mu;\sigma,\Phi,\bar{\Phi}) = -\frac{N_f T}{\pi^2}\int_0^\infty dp p^2\left(\ln g^{(+)}(T,\mu;\sigma,\Phi,\bar{\Phi}) + \ln g^{(-)}(T,\mu;\sigma,\Phi,\bar{\Phi})\right) \tag{2.41}$$

with

$$g^{(+)}(T,\mu;\sigma,\Phi,\bar{\Phi}) = 1 + 3\Phi e^{-(E_q-\mu)/T} + 3\bar{\Phi} e^{-2(E_q-\mu)/T} + e^{-3(E_q-\mu)/T},$$
$$g^{(-)}(T,\mu;\sigma,\Phi,\bar{\Phi}) = g^{(+)}(T,-\mu;\sigma,\bar{\Phi},\Phi). \tag{2.42}$$

Clearly, in the limit Φ → 1 in Eq. (2.41), one recovers the fermion part of the effective potential of the QM model, see Eq. (2.26).

In the mean-field approximation, the expectation value of σ and of the Polyakov loop, Φ and $\bar{\Phi}$, are determined by requiring that the thermodynamic potential is stationary [2],

$$\frac{\partial\Omega}{\partial\sigma} = \frac{\partial\Omega}{\partial\Phi} = \frac{\partial\Omega}{\partial\bar{\Phi}} = 0. \tag{2.43}$$

The model parameters are fixed by requiring that the vacuum physics is reproduced, as indicated in Sec. 2.1 for the QM model. Since the coupling to the Polyakov loop variables only effects the thermal contribution, the same initial conditions can be used as in the QM model.

2.3 Quark-meson model with repulsive interaction

Another extension of the quark-meson model is to include a repulsive vector interaction between the quarks. This is realized by coupling the quarks to a massive vector-meson field, ω. The Lagrangian of the model reads

$$\begin{aligned}\mathcal{L} =& \bar{q}\left(i\gamma^\mu D_\mu - g_s(\sigma + i\gamma_5\vec{\tau}\vec{\pi}) - g_\omega\gamma^\mu\omega_\mu\right)q + \frac{1}{2}\left(\partial_\mu\sigma\right)^2 + \frac{1}{2}\left(\partial_\mu\vec{\pi}\right)^2 - U_m(\sigma,\vec{\pi})\\ &+ \frac{1}{2}m_\omega^2\omega^2 - \frac{1}{4}F_{\mu\nu}F^{\mu\nu},\end{aligned} \tag{2.44}$$

where $F^{\mu\nu} = \partial^\mu\omega^\nu - \partial^\nu\omega^\mu$. For nonvanishing vector coupling g_ω, the ω field is coupled to the chiral sector through the fermionic part of the flow. In the mean-field approximation, assuming a homogeneous condensate, the temporal component of the ω field gains a nonvanishing expectation value at nonzero density, while the spatial components vanish in a system with zero net quark current. In the following, the nonvanishing expectation value will be denoted simply by ω.

An inspection of the Lagrangian (2.44) reveals that a nonvanishing ω field effectively acts as a shift of the quark chemical potential. Thus, it is convenient to introduce an effective quark chemical potential, $\nu = \mu - g_\omega\omega$. Then the grand canonical potential reads

$$\Omega(T,\mu;\sigma,\omega) = U_m(\sigma,0) + \Omega_{q\bar{q}}(T,\nu;\sigma) - \frac{1}{2}m_\omega^2\omega^2, \tag{2.45}$$

where $\Omega_{q\bar{q}}(T,\nu,\sigma)$ is the quark contribution without vector interaction, albeit with the effective chemical potential ν.

The physical value of ω, ω_M is obtained by extremizing $\Omega(T,\mu;\sigma,\omega)$, just as one obtains the physical value of the σ field. Since the calculation for vanishing and nonvanishing vector coupling can be related to each other, one can express all results in terms of quantities computed at vanishing vector coupling. We denote the thermodynamic potential density and net baryon density at vanishing vector coupling by $\tilde{\Omega}(T,\nu;\sigma)$ and $\tilde{n}(T,\nu;\sigma)$, respectively. The expectation value of the ω field is then determined by

$$\left.\frac{\partial\Omega}{\partial\omega}\right|_{\omega=\omega_M} = 0, \quad\Longrightarrow\quad g_\omega\omega_M = -G_\omega\frac{\partial\tilde{\Omega}}{\partial\nu} = G_\omega\tilde{n}(T,\nu;\sigma), \tag{2.46}$$

---

[2] The stationary point is a saddle point in the variables Φ and $\bar{\Phi}$. Nevertheless, for the effective Polyakov loop potentials employed in this work, the system is thermodynamically stable, as shown in ref. [39].

where $G_\omega = g_\omega^2/m_\omega^2$. This yields the relation between the real and the effective chemical potentials

$$\mu = \nu + G_\omega \tilde{n}(T,\nu;\sigma). \tag{2.47}$$

One can exchange the variable ω for the effective chemical potential ν, and require stationarity with respect to ν instead of ω. Moreover, the corresponding thermodynamic potential for nonzero vector coupling expressed in terms of ν is given by

$$\Omega(T,\mu;\sigma,\omega) = \tilde{\Omega}(T,\nu;\sigma) - \frac{(\mu-\nu)^2}{2G_\omega} \tag{2.48}$$

Thus if we find an extremum of the potential $\tilde{\Omega}$ with respect to σ at vanishing vector coupling and at chemical potential ν, it will correspond to an extremum of the potential at any finite vector coupling, at the chemical potential $\mu(\nu)$ given by Eq. (2.47) with the vector-field expectation value

$$g_\omega \omega_M = -G_\omega \frac{\partial \tilde{\Omega}}{\partial \nu} = G_\omega \tilde{n}(T,\nu;\sigma). \tag{2.49}$$

Knowing all extrema of the grand canonical potential at vanishing vector coupling for all chemical potential and temperature values, this procedure yields all the solutions of the gap equations at any finite vector coupling. It should be noted however that the knowledge of both the location of minima and maxima are required at vanishing vector coupling, because maxima, which are thermodynamically unstable without vector interaction, may become stable with the inclusion of vector repulsion. To illustrate this, let us consider the chiral susceptibility,

$$\chi^{ch} = -\frac{d^2\Omega}{dH^2} = \frac{d\sigma_M}{dH}. \tag{2.50}$$

Now using that the gap equations have to be fulfilled at a stationary point SP, regardless of the external field,

$$\frac{d}{dH}\left(\left.\frac{\partial \Omega[T,\mu;\sigma,\omega]}{\partial \sigma}\right|_{SP} \right) = 0, \qquad \frac{d}{dH}\left(\left.\frac{\partial \Omega[T,\mu;\sigma,\omega]}{\partial \nu}\right|_{SP} \right) = 0, \tag{2.51}$$

we obtain the following equations:

$$\left.\frac{\partial^2 \tilde{\Omega}}{\partial^2 \sigma}\right|_{SP} \frac{d\sigma_M}{dH} - \left.\frac{\partial \tilde{n}}{\partial \sigma}\right|_{SP} \frac{d\nu_M}{dH} = 1, \tag{2.52}$$

$$\left.\frac{\partial \tilde{n}}{\partial \sigma}\right|_{SP} \frac{d\sigma_M}{dH} + \left(\frac{1}{G_\omega} + \left.\frac{\partial \tilde{n}}{\partial \nu}\right|_{SP} \right) \frac{d\nu_M}{dH} = 0. \tag{2.53}$$

Using these relations we get for the chiral susceptibility

$$\chi^{ch} = \left.\left(\frac{\partial^2 \tilde{\Omega}}{\partial \sigma^2} + G_\omega \frac{\left(\frac{\partial \tilde{n}}{\partial \sigma}\right)^2}{1 + G_\omega \frac{\partial \tilde{n}}{\partial \nu}} \right)^{-1} \right|_{SP}. \tag{2.54}$$

Note that by dropping the second term we obtain the chiral susceptibility with vanishing vector coupling. At finite vector coupling, even if the first term is negative, hence thermodynamically unstable, the second term can yield a positive contribution that makes the chiral susceptibility positive, hence the system thermodynamically stable.

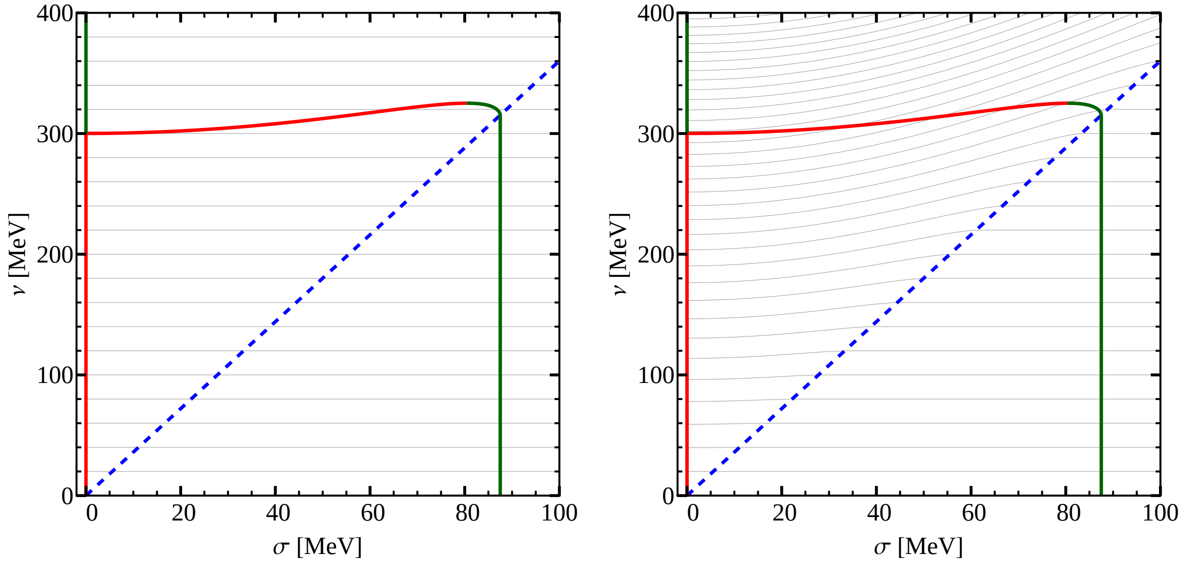

Figure 2.2.: Solutions of the gap equation at vanishing temperature and vector coupling. The red line corresponds to maxima of the grand canonical potential, whereas the green line corresponds to minima. The blue dashed line shows $\nu = g_s\sigma$, below which the potential is independent of the chemical potential and the density vanishes exactly. The gray lines correspond to lines of constant $\mu = \nu + G_\omega \tilde{n}(T,\nu;\sigma)$ in steps of 20 MeV. On the left $g_\omega = 0$, whereas on the right $g_\omega = g_s$. Alternatively, one may consider these plots showing the extrema of the grand canonical potential plotted on a ν grid (left) and on a μ grid (right) for $g_\omega = g_s$.

To see how the states that are unstable without vector repulsion influence the phase diagram, let us consider the quark-meson model at zero temperature in the chiral limit. We choose $m_\sigma = 570$ MeV, $m_\omega = 782$ MeV and $m_c = 335$ MeV. The grand canonical potential with vanishing vector coupling is given by

$$\begin{aligned}\tilde{\Omega} &= U_m(\sigma,0) - \frac{N_cN_f}{8\pi^2} g_s^4\sigma^4 \ln\left(\frac{\sigma}{f_\pi}\right) - \frac{N_cN_f}{\pi^2}\int_0^{p_F} dp p^2 \left(\nu - \sqrt{p^2+g_s^2\sigma^2}\right), \\ &= \begin{cases} U_m(\sigma,0) - \frac{N_cN_f}{8\pi^2}\left(\frac{2\nu^2-5g_s^2\sigma^2}{3}\nu p_F + g_s^4\sigma^4\ln\left(\frac{p_F+\nu}{g_sf_\pi}\right)\right) & \nu > g_s\sigma \\ U_m(\sigma,0) - \frac{N_cN_f}{8\pi^2} g_s^4\sigma^4 & \nu \le g_s\sigma \end{cases}\end{aligned} \tag{2.55}$$

where

$$p_F = \sqrt{\nu^2 - g_s^2\sigma^2}\,\theta(\nu^2 - g_s^2\sigma^2) \tag{2.56}$$

denotes the Fermi momentum and θ denotes the Heaviside step function,

$$\theta(x) = \begin{cases} 0 & \text{for} \quad x<0, \\ 1/2 & \text{for} \quad x=0, \\ 1 & \text{for} \quad x>0. \end{cases} \tag{2.57}$$

Accordingly, the density is given by

$$\tilde{n} = -\frac{\partial\tilde{\Omega}}{\partial\nu} = \frac{N_cN_f}{\pi^2}\int_0^{p_F} dp\, p^2 = \frac{N_cN_f}{3\pi^2}p_F^3 = \frac{N_cN_f}{3\pi^2}(\nu^2 - g_s^2\sigma^2)^{3/2}\theta(\nu^2 - g_s^2\sigma^2). \tag{2.58}$$

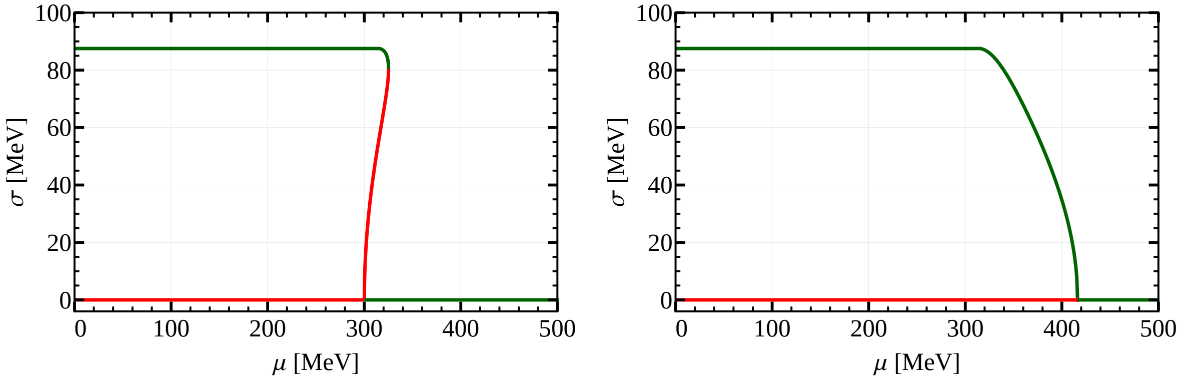

Figure 2.3.: Solutions of the gap equation at vanishing temperature. Left: $g_\omega = 0$, right: $g_\omega = g_s$. The green lines indicate thermodynamically stable states, where the chiral susceptibility, Eq. (2.54) is positive, whereas the red lines indicate thermodynamically unstable states with negative chiral susceptibility.

Since at zero temperature both the potential and the density can be obtained in a closed form, it is very easy to investigate the influence of vector interactions. In Fig. 2.2 all solutions of the gap equation are shown for vanishing vector coupling and lines of constant μ are plotted for vanishing and finite vector coupling. On the left it is found that for vanishing vector coupling, there is a range of chemical potentials, the spinodal region, where there are two minima and one maximum. On the right, for nonzero vector coupling, the lines of constant μ curve. There are lines that only cross lines of maxima, hence there are chemical potential values for which the originally unstable solutions will yield the stable solution with nonzero vector coupling. Note as well that on the right no line of constant μ has three solutions on it. This means that in that case, a first order transition can be ruled out. A first order transition needs namely at least two minima and a maximum in-between. This is in agreement with Fig. 2.3 as well, where the solutions of the gap equation are plotted as a function of μ for $g_\omega = 0$ and $g_\omega = g_s$. We find that at sufficiently large vector coupling the first order transition is replaced by a second order transition. This suggests that the critical endpoint shifts to lower temperatures and higher chemical potentials if vector repulsion is included. This is in agreement with earlier works in the NJL model [85].

To conclude this section let us calculate how the baryon number susceptibilities, which were introduced in Eq. (2.20), transform. For nonvanishing vector coupling, the baryon number susceptibilities can be expressed in terms of the corresponding susceptibilities $\tilde{\chi}_B^n$ for vanishing vector coupling. This is done using Eqs. (2.47) and (2.48). Using Eq. (2.47) one finds

$$\frac{d\nu}{d\mu} = \frac{1}{1 + 9T^2 G_\omega \tilde{\chi}_B^2(T,\nu)}, \tag{2.59}$$

which, using Eq. (2.48), leads to the following relations

$$\chi_B^1 = \tilde{\chi}_B^1, \tag{2.60}$$

$$\chi_B^2 = \frac{\tilde{\chi}_B^2}{1 + 9T^2 G_\omega \tilde{\chi}_B^2(T,\nu)}, \tag{2.61}$$

$$\chi_B^3 = \frac{\tilde{\chi}_B^3}{\left(1 + 9T^2 G_\omega \tilde{\chi}_B^2\right)^3}, \tag{2.62}$$

$$\chi_B^4 = \frac{\tilde{\chi}_B^4}{\left(1 + 9T^2 G_\omega \tilde{\chi}_B^2\right)^4} - \frac{27T^2 G_\omega \left(\tilde{\chi}_B^3\right)^2}{\left(1 + 9T^2 G_\omega \tilde{\chi}_B^2\right)^5}. \tag{2.63}$$

Here the cumulants $\tilde{\chi}_B^k$ are functions of temperature and the reduced chemical potential ν. Using these relations, we can compute the influence of the vector interaction on the baryon number cumulants, using the results obtained for vanishing vector coupling, $G_\omega = 0$.

2.4 FRG treatment of the quark-meson model

We now turn to the functional renormalization group treatment of the quark-meson model in three spatial dimensions at finite temperature and chemical potential. Our starting point is the Wetterich equation, Eq. (1.67). This equation is an exact equation, and in principle all fluctuations are properly accounted for. The equation is, however, a functional differential equation, which, in general, cannot be solved. This is the first point, where an approximation has to be made. The equation is solved by providing an ansatz for the effective average action. We work in the so-called local potential approximation (LPA), which corresponds to the ansatz

$$\Gamma_k = \int dV \left\{ \frac{1}{2}(\partial_\mu \sigma)^2 + \frac{1}{2}(\partial_\mu \vec{\pi})^2 + U_k(\rho) + \bar{\psi}(x)\left[\gamma_0^E(\partial_\tau - \mu) + \vec{\gamma}^E \vec{\nabla} + g_s(\sigma + i\vec{\tau}\vec{\pi}\gamma_5)\right]\psi(x) \right\}, \tag{2.64}$$

where

$$\int dV = \int d\tau \int d^3x \tag{2.65}$$

in $3+1$ dimensions, and

$$\rho = \frac{\sigma^2 + \vec{\pi}^2}{2}, \tag{2.66}$$

as introduced earlier. Here, σ and $\vec{\pi}$ denote the expectation value of the corresponding quantum fields, analogously to ϕ in Sec. 1.5. $U_k(\rho)$ stands for the chirally invariant part of the scale dependent mesonic potential. The ansatz (2.64) is clearly motivated by the form of the Euclidean action, Eq. (2.12), together with the finite density contribution to the grand canonical partition function, Eq. (2.14). It is clear that this form is chirally invariant, since no symmetry breaking term is introduced. The explicit symmetry breaking term in the action, since it is linear in the fields, can be and will be treated as an external field. As we will see during the derivation, a linear term in the fields does not influence the flow of Γ_k.

Note that the mesonic potential, U_k, carries all the scale dependence in this approximation, while the Yukawa coupling, g_s, is taken to be field and scale independent. We note that wave function renormalization factors are also not running. This can be justified by the smallness of the $O(4)$ critical exponent η that quantifies their flow [86].

As shown in Eq. (1.67), the contributions of the quarks and mesons to the flow derivative separate. To proceed, first we discuss the bosonic contribution and then the fermionic one. To explicitly evaluate the flow contributions, we rewrite the Wetterich equation in momentum space. The exact formulation in momentum space depends on the finiteness of the Euclidean dimensions. In all infinite (unbounded) directions the momenta can take any arbitrary values, however in finite (bounded) dimensions, momentum is quantized through boundary conditions and only certain discrete values are allowed. This is the case for example when a system in a finite volume or at finite temperature is considered. According to the standard finite temperature field theory formalism, boson fields obey periodic boundary conditions in the Euclidean time direction. Fermion fields are antiperiodic. This results in the quantization of energy. The frequencies allowed by the boundary conditions are called *Matsubara frequencies* and are given by

$$q_0^b(n) = 2n\pi T, \qquad q_0^f(n) = (2n+1)\pi T, \qquad n \in \mathbb{Z}, \tag{2.67}$$

for bosons and fermions, respectively. At this point however, the finiteness of dimensions does not make a difference in the derivation, and we simply use the symbol $\int_q$ to mean a summation over the momentum modes, be it an integral, a sum, or a combination thereof. To be explicit, in 3 infinite spatial dimensions and at finite temperature we have

$$\int_q = T \sum_n \int \frac{d^3q}{(2\pi)^3}, \tag{2.68}$$

where n labels the Matsubara frequencies (c.f. Eq. (2.67)). Let us further define a generalized Dirac delta function,

$$I(q,q') = \int dV\, e^{i(q+q')x}, \tag{2.69}$$

which is the identity operator under the multiplication

$$(A \cdot B)_{q,q'} = \int_{q''} A_{q,-q''} B_{q'',q'}. \tag{2.70}$$

Moreover, the definition Eq. (2.69) implies

$$I(q,-q) = I(0,0) = V/T, \tag{2.71}$$

which corresponds to the Euclidean system size[3]. In the case of three infinite spatial dimensions and finite temperature, the identity operator in momentum space reads

$$I(q,q') = \frac{(2\pi)^3}{T} \delta^{(3)}\left(\vec{q} + \vec{q}'\right) \delta_{n,-n'}, \tag{2.72}$$

where $\delta^{(3)}(\vec{q} - \vec{q}')$ is the three dimensional Dirac delta function, and $\delta_{n,n'}$ the Kronecker delta.

Regulators of the form

$$\hat{R}_k(x,y) = R_k(i\partial_x)\delta(x-y), \tag{2.73}$$

correspond to

$$\hat{R}_k(q,q') = R_k(q) I(q,q') \tag{2.74}$$

in momentum space. Using a regulator of this form, one obtains the bosonic part of the Wetterich equation in momentum space,

$$\partial_k \Gamma_k^B[\phi] = \frac{1}{2} \mathrm{Tr} \left\{ \left(\Gamma_k^{(2,0,0)} + \hat{R}_k \right)^{-1} \partial_k \hat{R}_k \right\} = \frac{1}{2} \mathrm{Tr}_\mathrm{i} \int_q \left\{ \left(\Gamma_k^{(2,0,0)} + \hat{R}_k \right)^{-1}_{q,-q} \partial_k R_k(q) \right\}, \tag{2.75}$$

where Tr_i denotes a trace over the internal indexes, i.e., here a summation over the sigma and pion fields. The functional derivatives are now to be taken with respect to the Fourier components of the fields,

$$\tilde{\sigma}(q) = \int dV\, \sigma(x) e^{-iqx}, \tag{2.76}$$

$$\tilde{\pi}_i(q) = \int dV\, \pi_i(x) e^{-iqx}. \tag{2.77}$$

---

[3] Here V denotes the three-volume, in contrast do dV, which refers to a four-volume element.

Using the ansatz Eq. (2.64) there are only two terms contributing, namely the kinetic term and the potential term. Using the notation

$$\phi = \{\sigma, \pi_1, \pi_2, \pi_3\}, \qquad \tilde{\phi} = \{\tilde{\sigma}, \tilde{\pi}_1, \tilde{\pi}_2, \tilde{\pi}_3\}, \tag{2.78}$$

the kinetic terms can be generally evaluated for the pion and sigma fields at the same time,

$$\frac{\delta^2}{\delta\tilde{\phi}_i(q)\delta\tilde{\phi}_j(q')}\int dV\,\frac{(\partial_\mu\phi_l)^2}{2} = \frac{\delta^2}{\delta\tilde{\phi}_i(q)\delta\tilde{\phi}_j(q')}\int_{q''}\frac{q''^2}{2}\tilde{\phi}_l(q'')\tilde{\phi}_l(-q'') = -qq'\delta_{ij}I(q,q'). \tag{2.79}$$

The second functional derivative of the potential term depends on the form of the condensate we are interested in. In this work, only homogeneous condensation is considered, such that the condensate takes the same value across the system. There are speculations that in the vicinity of the first order transition line inhomogeneous condensation may be the preferred state of the system [87–90]. This possibility will not be considered in this work. Hence, we evaluate the second functional derivative of the potential for a constant background field. In this case the potential term yields

$$\begin{aligned}\frac{\delta^2}{\delta\tilde{\phi}_i(q)\delta\tilde{\phi}_j(q')}\int dV\,U_k(\rho(x)) &= \int dV'\int dV''\,\frac{\delta\phi(x')}{\delta\tilde{\phi}(q)}\frac{\delta\phi(x'')}{\delta\tilde{\phi}(q')}\frac{\delta^2}{\delta\phi_i(x')\delta\phi_j(x'')}\int dV\,U_k(\rho(x))\\ &= \int dV'\int dV''\,e^{iqx'+iq'x''}\delta(x'-x'')\frac{\partial^2 U_k(\rho)}{\partial\phi_i\partial\phi_j} = \frac{\partial^2 U_k}{\partial\phi_i\partial\phi_j}I(q,q').\end{aligned} \tag{2.80}$$

In the second line we used the fact that the second derivative of the potential is constant over the whole domain for homogeneous condensation. Now let us put the pieces together. The inverse term in Eq. (2.75) can now be obtained analytically due to the simple structure,

$$\begin{aligned}\left(\Gamma_k^{(2,0,0)} + \hat{R}_k\right)^{-1}_{q,-q} &= \left\{\left(-qq'\delta_{ij} + \frac{\partial^2 U_k}{\partial\phi_i\partial\phi_j} + R_k(q)\right)I(q,q')\right\}^{-1}\Bigg|_{q'=-q}\\ &= \left(q^2\delta_{ij} + \frac{\partial^2 U_k}{\partial\phi_i\partial\phi_j} + R_k(q)\right)^{-1} I(q,-q) = \frac{V}{T}\left(q^2\delta_{ij} + \frac{\partial^2 U_k}{\partial\phi_i\partial\phi_j} + R_k(q)\right)^{-1}.\end{aligned} \tag{2.81}$$

Here we used the fact that $I(q,q')$ is the identity operator and hence its own inverse.

In the local potential approximation and for homogeneous condensation,

$$\partial_k\Gamma_k = \frac{V}{T}\partial_k U_k, \tag{2.82}$$

since the only scale dependent term is the mesonic potential. The flow of the mesonic potential due to bosonic fluctuations then reads

$$\partial_k U_k^B = \frac{1}{2}\mathrm{Tr}_i\int_q\left(q^2\delta_{ij} + \frac{\partial^2 U_k(\rho)}{\partial\phi_i\partial\phi_j} + R_k(q)\right)^{-1}\partial_k R_k(q). \tag{2.83}$$

We consider condensation only in the sigma direction. Hence, we assume that the expectation value of the pion fields vanishes. Condensation of pion fields is only expected at nonvanishing isospin chemical potential, in the presence of strong magnetic fields or possibly at high baryon densities and low temperatures. These possibilities are not considered here. In this case the nonvanishing elements of the second derivative of the potential are

$$\frac{\partial^2 U_k(\rho)}{\partial \sigma^2} = U_k'(\rho) + 2\rho U_k''(\rho) \equiv m_\sigma^2, \tag{2.84}$$

$$\frac{\partial^2 U_k(\rho)}{\partial \pi_i^2} = U_k'(\rho) \equiv m_\pi^2. \tag{2.85}$$

Since the Hessian of the potential is diagonal, the trace in Eq. (2.83) is trivial assuming a flavor independent regulator function. We also assume that the regulator only regulates the spatial momenta $\vec{q}$, and that it is independent of the Matsubara frequency. In this case the Matsubara summation in $\int_q$ can be performed analytically using the identity

$$\sum_{n=-\infty}^{\infty} \frac{1}{n^2\pi^2a^2 + b^2} = \frac{\coth \frac{b}{a}}{ab}. \tag{2.86}$$

This leads us to

$$\partial_k U_k^B = \frac{1}{4} \int \frac{d^3q}{(2\pi)^3} \left(\frac{\coth \frac{E_\sigma}{2T}}{E_\sigma} + \frac{3\coth \frac{E_\pi}{2T}}{E_\pi} \right) \partial_k R_k(\vec{q}), \tag{2.87}$$

with the meson energies

$$E_\sigma = \sqrt{\vec{q}^2 + m_\sigma^2 + R_k(\vec{q})}, \qquad E_\pi = \sqrt{\vec{q}^2 + m_\pi^2 + R_k(\vec{q})}. \tag{2.88}$$

Before specifying the form of the regulator, we consider the fermionic contribution to the flow. Based on Eq. (1.67) this reads

$$\partial_k \Gamma_k^F[\phi] = -\mathrm{Tr}\left\{ \left(\Gamma_k^{(0,1,1)} + \hat{R}_{k,F} \right)^{-1} \partial_k \hat{R}_{k,F} \right\} = -\mathrm{Tr}_i \int_q \left\{ \left(\Gamma_k^{(0,1,1)} + \hat{R}_{k,F} \right)^{-1}_{q,-q} \partial_k R_{k,F}(q) \right\}, \tag{2.89}$$

where Tr_i denotes a summation over all internal indexes. We assume a fermionic regulator of the form

$$\hat{R}_{k,F}(q,q') = i\vec{q}\vec{\gamma}^E R_{k,F}(\vec{q}) I(q,q'), \tag{2.90}$$

where R_k^F is a k and $\vec{q}$ dependent scalar to be specified later. Our starting point for evaluating the fermion contribution is the second functional derivative of the effective average action, Eq. (2.64), with respect to the quark fields. As in the bosonic case, the calculation is performed in momentum space, and the functional derivatives are taken with respect to the fields

$$\tilde{\psi}(q) = \int dV\, \psi(x) e^{-iqx}, \qquad \tilde{\bar{\psi}}(q) = \int dV\, \bar{\psi}(x) e^{-iqx}. \tag{2.91}$$

This yields

$$\begin{aligned} \Gamma_k^{(0,1,1)} &= \frac{\delta^2}{\delta\tilde{\psi}(q)\delta\tilde{\bar{\psi}}(q')} \int dV \left\{ \bar{\psi}(x) \left[\gamma_0^E(\partial_0 - \mu) + \vec{\gamma}^E \vec{\nabla} + g_s(\sigma + i\vec{\tau}\vec{\pi}\gamma_5) \right] \psi(x) \right\} \\ &= \left((iq_0 - \mu)\gamma_0^E + i\vec{q}\vec{\gamma}^E + g_s(\sigma + i\vec{\tau}\vec{\pi}\gamma_5) \right) I(q,q'), \end{aligned} \tag{2.92}$$

which is obtained by assuming homogeneous condensation and using similar manipulations to those performed in Eq. (2.80). Again, just as in the bosonic case, the inverse in momentum space can be trivially performed, yielding

$$\left(\Gamma_k^{(0,1,1)} + \hat{R}_{k,F}\right)^{-1}_{q,-q} = \frac{V}{T}\left((iq_0-\mu)\gamma_0^E + i\vec{q}\vec{\gamma}^E(1+R_{k,F}(\vec{q})) + g_s(\sigma + i\vec{\tau}\vec{\pi}\gamma_5)\right)^{-1}. \tag{2.93}$$

Hence, the fermion contribution can be written as

$$\begin{aligned}\partial_k U_k^F &= -\int_q \mathrm{Tr}_i \left\{\left((iq_0-\mu)\gamma_0^E + i\vec{q}\vec{\gamma}^E(1+R_{k,F}(\vec{q})) + g_s(\sigma + i\vec{\tau}\vec{\pi}\gamma_5)\right)^{-1} i\vec{q}\vec{\gamma}^E \partial_k R_{k,F}(\vec{q})\right\} \\ &= -\partial_k \int_q \mathrm{Tr}_i \ln\left\{(iq_0-\mu)\gamma_0^E + i\vec{q}\vec{\gamma}^E(1+R_{k,F}(\vec{q})) + g_s(\sigma + i\vec{\tau}\vec{\pi}\gamma_5)\right\}.\end{aligned} \tag{2.94}$$

Here we used the fact that in this approximation, the only k dependence in the fermionic part of the effective action is in the regulator term. The evaluation of the trace in Eq. (2.94) is performed as follows.

$$\begin{aligned}\partial_k U_k^F &= -\partial_k \int_q \mathrm{Tr}_\mathrm{i}\left\{\ln(g_s\sigma) + \ln\left(1 + \frac{1+R_{k,F}(\vec{q})}{g_s\sigma} i\vec{q}\vec{\gamma}^E + \frac{iq_0-\mu}{g_s\sigma}\gamma_0^E + \frac{i\vec{\tau}\vec{\pi}}{\sigma}\gamma_5\right)\right\} \\ &= -\partial_k \int_q \mathrm{Tr}_\mathrm{i}\left\{\ln(g_s\sigma) - \sum_{n=1}^{\infty}\frac{(-1)^n}{n}\left(\frac{1+R_{k,F}(\vec{q})}{g_s\sigma} i\vec{q}\vec{\gamma}^E + \frac{iq_0-\mu}{g_s\sigma}\gamma_0^E + \frac{i\vec{\tau}\vec{\pi}}{\sigma}\gamma_5\right)^n\right\} \\ &= -\partial_k \int_q \mathrm{Tr}_\mathrm{i}\left\{\ln(g_s\sigma) - \sum_{n=1}^{\infty}\frac{(-1)^n}{2n}\left(\frac{(1+R_{k,F}(\vec{q}))^2}{g_s^2\sigma^2}\vec{q}^2 + \frac{(q_0+i\mu)^2}{g_s^2\sigma^2} + \frac{\vec{\pi}^2}{\sigma^2}\right)^n\right\} \\ &= -\partial_k \int_q \frac{1}{2}\mathrm{Tr}_\mathrm{i} \ln\left((1+R_{k,F}(\vec{q}))^2\vec{q}^2 + (q_0+i\mu)^2 + g_s^2(\sigma^2+\vec{\pi}^2)\right) \\ &= -12\partial_k \int_q \ln\left((1+R_{k,F}(\vec{q}))^2\vec{q}^2 + (q_0+i\mu)^2 + g_s^2(\sigma^2+\vec{\pi}^2)\right).\end{aligned} \tag{2.95}$$

First we separate the coefficient of the unit matrix in Dirac space and expand the second logarithm around 1. We then discard all odd powers from the expansion, since the trace of any odd number of gamma matrices vanishes. In the next step, the gamma matrices are eliminated, using the anticommutation relations. After resumming the expression we notice that the remaining expression is proportional to the unit matrix both in flavor and Dirac spaces. Now performing the traces is trivial. The trace over color introduces an additional factor of 3. Using the quark energy and the constituent quark mass,

$$E_q = \sqrt{(1+R_{k,F}(\vec{q}))^2\vec{q}^2 + m_q^2}, \qquad m_q = g_s\sqrt{\sigma^2+\vec{\pi}^2}, \tag{2.96}$$

the expression can be further simplified. Finally, we choose the fermionic regulator function $R_{k,F}(\vec{q})$ such that

$$(1+R_{k,F}(\vec{q}))^2\vec{q}^2 = (\vec{q}^2 + R_k(\vec{q})) \tag{2.97}$$

holds, where $R_k(\vec{q})$ denotes the bosonic regulator introduced earlier. Now the bosonic and fermionic modes are regulated in an equivalent fashion. The formula then reads

$$\partial_k U_k^F = -12\int_q \frac{\partial_k R_k(\vec{q})}{E_q^2 + (q_0+i\mu)^2} \tag{2.98}$$

Further simplification can be achieved by analytically performing the Matsubara sum

$$\begin{aligned}
&T\sum_{n=-\infty}^{\infty}\frac{1}{E_q^2+((2n+1)\pi T+i\mu)^2}\\
&\quad=\frac{T}{2E_q}\sum_{n=-\infty}^{\infty}\left\{\frac{E_q-\mu}{(2n+1)^2\pi^2T^2+(E_q-\mu)^2}+\frac{E_q+\mu}{(2n+1)^2\pi^2T^2+(E_q+\mu)^2}\right\}\\
&\quad=\frac{1}{2E_q}\left\{\tanh\left(\frac{E_q-\mu}{2T}\right)+\tanh\left(\frac{E_q+\mu}{2T}\right)\right\}, \qquad (2.99)
\end{aligned}$$

where first we combine the negative and positive Matsubara modes to cancel the imaginary part, and then we use the identity

$$\sum_{n=-\infty}^{\infty}\frac{1}{(2n+1)^2\pi^2a^2+b^2}=\frac{\tanh\left(\frac{b}{2a}\right)}{2ab}, \qquad (2.100)$$

yielding

$$\partial_k U_k^F=-12\int\frac{d^3q}{(2\pi)^3}\frac{\partial_k R_k(\vec{q})}{4E_q}\left(\tanh\left(\frac{E_q-\mu}{2T}\right)+\tanh\left(\frac{E_q+\mu}{2T}\right)\right). \qquad (2.101)$$

By combining the bosonic and fermionic contributions, we obtain the FRG flow equation for a general $R_k(\vec{q})$ regulator function in the local potential approximation,

$$\begin{aligned}
\partial_k U_k&=\partial_k U_k^B+\partial_k U_k^F\\
&=\frac{1}{4}\int\frac{d^3q}{(2\pi)^3}\left(\frac{\coth\frac{E_\sigma}{2T}}{E_\sigma}+3\frac{\coth\frac{E_\pi}{2T}}{E_\pi}-12\frac{\tanh\left(\frac{E_q-\mu}{2T}\right)}{E_q}-12\frac{\tanh\left(\frac{E_q+\mu}{2T}\right)}{E_q}\right)\partial_k R_k(\vec{q}), \qquad (2.102)
\end{aligned}$$

where

$$\begin{aligned}
E_\sigma&=\sqrt{\vec{q}^2+m_\sigma^2+R_k(\vec{q})}, & E_\pi&=\sqrt{\vec{q}^2+m_\pi^2+R_k(\vec{q})}, & E_q&=\sqrt{\vec{q}^2+m_q^2+R_k(\vec{q})}\\
m_\sigma^2&=U_k'(\rho)+2\rho U_k''(\rho), & m_\pi^2&=U_k'(\rho), & m_q^2&=2g_s^2\rho. \qquad (2.103)
\end{aligned}$$

The energies in general depend both on the RG scale, k, and on the momentum, $\vec{q}$. These dependencies are understood implicitly. Introducing the Bose-Einstein and Fermi-Dirac occupation numbers,

$$n_B(E)=\frac{1}{e^{\beta E}-1}, \qquad n_F(E)=\frac{1}{e^{\beta(E-\mu)}+1}, \qquad \bar{n}_F(E)=\frac{1}{e^{\beta(E+\mu)}+1}, \qquad (2.104)$$

the flow equation can be brought into the form

$$\partial_k U_k=\frac{1}{4}\int\frac{d^3q}{(2\pi)^3}\left(\frac{1+2n_B(E_\sigma)}{E_\sigma}+3\frac{1+2n_B(E_\pi)}{E_\pi}-\frac{24}{E_q}\left(1-n_F(E_q)-\bar{n}_F(E_q)\right)\right)\partial_k R_k(\vec{q}). \qquad (2.105)$$

For a general regulator no further simplifications can be made. In general the solution of the flow equation involves an integral over momenta which is evaluated numerically. This is computationally demanding. A significant reduction in run time can be achieved by using the so-called optimized (or Litim) regulator [91, 92],

$$R_k(\vec{q})=\left(k^2-\vec{q}^2\right)\theta\left(k^2-\vec{q}^2\right), \qquad (2.106)$$

where θ denotes the Heaviside step function,

$$\theta(x) = \begin{cases} 0 & \text{for} \quad x < 0, \\ 1/2 & \text{for} \quad x = 0, \\ 1 & \text{for} \quad x > 0. \end{cases} \tag{2.107}$$

We note that with this regulator, momenta above the RG scale k do not contribute to the subsequent flow. They have already have completely integrated out. This is due to the vanishing of the term $\partial_k R_k(\vec{q})$. For all modes that do contribute, the energies are independent of the momentum, as

$$E_\sigma = \sqrt{k^2 + m_\sigma^2}, \qquad E_\pi = \sqrt{k^2 + m_\pi^2}, \qquad E_q = \sqrt{k^2 + m_q^2}. \tag{2.108}$$

For these modes, the derivative of the regulator is also independent of the momentum, since $\partial_k R_k(\vec{q}) = 2k$. Due to this, the momentum integrand is a constant and the integral is trivial to perform. The phase space contributing to the integral at the RG scale k is given by a sphere of radius k. Hence the flow using the Litim regulator is given in a closed form,

$$\partial_k U_k(\sigma, \vec{\pi}) = \frac{k^4}{12\pi^2} \left(\frac{\coth \frac{E_\sigma}{2T}}{E_\sigma} + \frac{3 \coth \frac{E_\pi}{2T}}{E_\pi} - 12 \frac{\tanh\left(\frac{E_q - \mu}{2T}\right)}{E_q} - 12 \frac{\tanh\left(\frac{E_q + \mu}{2T}\right)}{E_q} \right) \equiv F(\rho). \tag{2.109}$$

2.5 Thermodynamics in the FRG approach

For the time being we postpone the technical discussion of the solution of the flow equations and assume we have solved them and obtained the effective action in the chiral limit,

$$\Gamma = \frac{T}{V} U_{k=0}(\sigma, 0) \equiv \frac{T}{V} \Omega_{ch}(T, \mu; \sigma). \tag{2.110}$$

Based on Eq. (1.59), it is straightforward to calculate the pressure for any external field $J(x)$. For a homogeneous source term $J(x) = H$, we find

$$P(T, \mu) = \frac{T}{V} \sup_\sigma \left(\int d^D x \phi(x) J(x) - \Gamma[\phi] \right) = \sup_\sigma \left(H\sigma - \Omega_{ch}(T, \mu; \sigma) \right). \tag{2.111}$$

The physical value of the chiral condensate, σ_M, is determined by the gap equation

$$H = \left. \frac{\partial \Omega_{ch}(T, \mu; \sigma)}{\partial \sigma} \right|_{\sigma = \sigma_M}. \tag{2.112}$$

Note also that, based on Eq. (2.85), the value of the external field, H, is directly related to the pion mass

$$H = \sigma \left. \frac{\partial \Omega_{ch}(T, \mu; \sigma)}{\partial \rho} \right|_{\sigma = \sigma_M} = m_\pi^2 \sigma_M. \tag{2.113}$$

Just as in the mean-field treatment, the initial conditions are chosen such that in vacuum $\sigma_M = f_\pi$ holds and the desired values for the pion and sigma meson masses, and the constituent quark mass $m_c = g_s f_\pi$ are reproduced. At nonvanishing temperature and density, the same initial conditions are used as in the vacuum. The actual parameters of the initial potential depend on the ultraviolet cutoff Λ and on the solution method of the flow equations. Various choices for the parameters are specified in Appendix D.

Now we have delineated the basic setup. However, in order to obtain a more realistic description of strongly interacting matter, we augment the model in two respects, one that is relevant at high temperatures and one that is relevant at low temperatures.

At high temperatures the finite UV cutoff may cause problems. In order to recover the proper high temperature and high density behavior of thermodynamic quantities, i.e., the Stefan-Boltzmann limit, quark fluctuations above the UV cutoff scale Λ, where the flow is started, must be taken into account [45, 46, 93]. In this work, this is performed perturbatively. This means that for a given regulator, we compute the flow of the effective average action from $k = \infty$ to $k = \Lambda$, disregarding the meson fluctuations and the quark vacuum term for vanishing quark mass. This contribution is then added to the pressure. The perturbative treatment is justified by the fact that during the RG evolution, spontaneous symmetry breaking occurs at an intermediate scale, so at $k = \Lambda$ and above the chiral symmetry is unbroken and the quarks are effectively massless. Mesons on the other hand are massive and their fluctuations can be disregarded. By disregarding the vacuum quark fluctuations, we only take into account the finite temperature modifications. The divergent vacuum contribution in principle can be compensated by appropriate redefinition of the UV initial conditions. By considering the quarks massless, the procedure does not interfere with the RG flow (i.e., it does not introduce additional sigma dependence in the UV potential) and the result can be added to the pressure as a temperature dependent function independent of σ. The perturbative contribution reads

$$\begin{aligned} P_{pert} &= -\int_{\infty}^{\Lambda} dk\,(\partial_k U_k(T,\mu;\sigma=0) - \partial_k U_k(0,0;\sigma=0)) \\ &= 6\int_{\Lambda}^{\infty} dk \int \frac{d^3q}{(2\pi)^3}\left(\frac{n_F(E_q)+\bar{n}_F(E_q)}{E_q}\right)\partial_k R_k(\vec{q}) \\ &= -12T\int \frac{d^3q}{(2\pi)^3}\int_{\Lambda}^{\infty} dk\frac{d}{dk}\left(\ln\left(1+e^{\frac{\mu-E_q}{T}}\right)+\ln\left(1+e^{-\frac{\mu+E_q}{T}}\right)\right) \\ &= 12T\int \frac{d^3q}{(2\pi)^3}\left(\ln\left(1+e^{\frac{\mu-E_q^\Lambda}{T}}\right)+\ln\left(1+e^{-\frac{\mu+E_q^\Lambda}{T}}\right)\right), \end{aligned} \tag{2.114}$$

with

$$E_q^\Lambda = \sqrt{\vec{q}^2 + R_\Lambda(\vec{q})}. \tag{2.115}$$

In the third line of Eq. (2.114), the derivative acts on the quark energy, which gives

$$\frac{dE_q}{dk} = \frac{d}{dk}\sqrt{\vec{q}^2 + R_k(\vec{q})} = \frac{1}{2E_q}\partial_k R_k(\vec{q}). \tag{2.116}$$

Specifically, for the Litim regulator, a simpler formula can be obtained starting from Eq. (2.109),

$$P_{pert} = -\int_{\infty}^{\Lambda}\partial_k\Omega = \frac{2}{\pi^2}\int_{\Lambda}^{\infty} dk\, k^3(n_F(k)+\bar{n}_F(k)). \tag{2.117}$$

At low temperatures, in order to be able to describe strongly interacting matter at least on a qualitative level, confinement has to be effectively implemented. This is done by including the quark coupling to the Polyakov-loop in the FRG framework, following Refs. [45, 46, 50, 94, 95]. This is done on the mean-field level, i.e., the fluctuations of the Polyakov loop are disregarded. Hence, in the effective action, coupling of the quarks to the Polyakov loop has to be included and the chosen Polyakov-loop potential has to be added to the effective potential. During the RG flow the Polyakov loop is treated as a constant background field, which is not changed during the flow. On the other hand, the Polyakov loop affects the flows through their coupling to the quarks that results in the modified occupation numbers,

$$N(T,\mu;\sigma,\Phi,\bar{\Phi}) = \frac{1+2\bar{\Phi}e^{(E_q-\mu)/T}+\Phi e^{2(E_q-\mu)/T}}{1+3\bar{\Phi}e^{(E_q-\mu)/T}+3\Phi e^{2(E_q-\mu)/T}+e^{3(E_q-\mu)/T}}. \tag{2.118}$$

The flow equation of the PQM model using the Litim regulator then reads

$$\begin{aligned}\partial_k U_k(T,\mu;\sigma,\Phi,\bar{\Phi}) =& \frac{k^4}{12\pi^2}\left\{\frac{3}{E_\pi}\coth\left(\frac{E_\pi}{2T}\right)+\frac{1}{E_\sigma}\coth\left(\frac{E_\sigma}{2T}\right)\right.\\ &\left.-\frac{24}{E_q}\left(1-N(T,\mu;\sigma,\Phi,\bar{\Phi})-N(T,-\mu;\sigma,\bar{\Phi},\Phi)\right)\right\},\end{aligned} \tag{2.119}$$

and the effective potential is given by

$$\Omega(T,\mu;\sigma,\Phi,\bar{\Phi}) = U_{k=0}(T,\mu;\sigma,\Phi,\bar{\Phi})+\mathcal{U}(\Phi,\bar{\Phi})-H\sigma-P_{pert}(T,\mu;\Phi,\bar{\Phi}), \tag{2.120}$$

where $\mathcal{U}(\Phi,\bar{\Phi})$ is the Polyakov-loop potential introduced in Sec. 2.2. Note that the modified occupation numbers must be introduced also in the perturbative quark contribution. The expectation value of the chiral condensate and the Polyakov-loop variables are, similarly to the mean-field treatment, given by the gap equations

$$\frac{\partial\Omega}{\partial\sigma}=\frac{\partial\Omega}{\partial\Phi}=\frac{\partial\Omega}{\partial\bar{\Phi}}=0. \tag{2.121}$$

To end this section, we briefly discuss the inclusion of vector interactions in the FRG formalism. The Lagrangian of the model reads

$$\begin{aligned}\mathcal{L} =& \bar{q}\left(i\gamma^\mu D_\mu - g_s(\sigma+i\gamma_5\vec{\tau}\vec{\pi})-g_\omega\gamma^\mu\omega_\mu\right)q+\frac{1}{2}\left(\partial_\mu\sigma\right)^2+\frac{1}{2}\left(\partial_\mu\vec{\pi}\right)^2-U_m(\sigma,\vec{\pi})\\ &-\mathcal{U}(T;\Phi,\bar{\Phi})+\frac{1}{2}m_\omega^2\omega^2-\frac{1}{4}F_{\mu\nu}F^{\mu\nu},\end{aligned} \tag{2.122}$$

where $F^{\mu\nu}=\partial^\mu\omega^\nu-\partial^\nu\omega^\mu$ is the field strength tensor of the vector field. Similarly to the mean-field case, the ω field is coupled to the chiral sector through the fermionic part of the flow. The zero-component of the ω field gains a nonvanishing expectation value at nonzero density, while the spatial components vanish for a system at rest. In the following, ω will refer to the expectation value of the zero-component.

We apply the FRG formalism to include fluctuations of the σ and pion fields, while the ω meson is treated on the mean-field level. The MF treatment of the vector field is justified by recent FRG results obtained at vanishing chemical potential indicating that the vector meson mass remains above the cutoff during the FRG flow and that the temperature dependence of the screening mass is very weak [96, 97]. Therefore, it is expected that fluctuations of the vector fields decouple from the flow.

Just as in the MF case, a nonvanishing ω field effectively acts as a shift of the quark chemical potential. Thus, it is convenient to introduce an effective quark chemical potential again, $\nu=\mu-g_\omega\omega$, and continue using the formalism for vanishing vector coupling, albeit with modified initial conditions for the flow equation

$$\Omega_{k=\Lambda} = U_m(\sigma,0)|_{H=0}+\mathcal{U}(T;\Phi,\bar{\Phi})-\frac{1}{2}m_\omega^2\omega^2. \tag{2.123}$$

Since, for a given value of ω, this amounts to constant shift of the thermodynamic potential, it will not modify the RG flow. Thus, the only effect of a nonzero ω field on the flow is the replacement of the chemical potential μ by the previously defined effective chemical potential ν. Since the flow for vanishing and nonvanishing vector couplings can be related to each other, one can express all results in terms of quantities computed at vanishing vector coupling. We denote the thermodynamic potential density and net baryon density at vanishing vector coupling by $\tilde{\Omega}(T,\nu)$ and $\tilde{n}(T,\nu)$, respectively. The physical value of the ω field, ω_M, and hence the relation between the real and effective chemical potentials, are determined by requiring stationarity of the grand canonical potential with respect to variations of the ω field,

$$\left.\frac{\partial \Omega_{k=0}}{\partial \omega}\right|_{\omega=\omega_M} = 0, \quad \Longrightarrow \quad g_\omega \omega_M = -G_\omega \frac{\partial \tilde{\Omega}}{\partial \nu} = G_\omega \tilde{n}(T,\nu), \tag{2.124}$$

where $G_\omega = g_\omega^2/m_\omega^2$. This yields the relation between the real and the effective chemical potentials

$$\mu = \nu + G_\omega \tilde{n}(T,\nu). \tag{2.125}$$

Moreover, the corresponding thermodynamic potential for nonzero vector coupling is given by

$$\Omega(T,\mu;\sigma) = \tilde{\Omega}(T,\nu;\sigma) - \frac{(\mu-\nu)^2}{2G_\omega}. \tag{2.126}$$

Since we treat the ω field in the mean-field approximation, it is no surprise that Eqs. (2.124), (2.125) and (2.126) are identical to the ones obtained in Sect. 2.3. We note however, that for a first order phase transition, this procedure cannot be used to identify the critical value of thermal parameters in an RG scheme. As noted in Sec. 2.3, the unstable solutions at vanishing vector coupling, i.e., the local maxima, became important if one is interested in finite vector coupling results. These are inaccessible in our RG formalism owing to a flattening of the potential as a function of the order parameter. Nevertheless, outside the spinodal region, all thermodynamic quantities with nonvanishing vector coupling can be computed using RG results obtained with vanishing vector coupling. In particular, the baryon number cumulants are obtained according to Eqs. (2.60), (2.61), (2.62) and (2.63) analogously to the MF calculation.

2.6 Solution of the flow equation

2.6.1 Numerical techniques

Now let us discuss different approaches to solve the flow equations in the quark-meson model. In this subsection, for simplicity, the quark coupling to the Polyakov loop will be dropped. In the next subsection we then discuss how to deal with additional background fields such as the Polaykov loop.

We have to solve flow equations of the form shown in Eqs. (2.102) and (2.109). Mathematically speaking the flow equation is a nonlinear partial differential equation with variables k and σ. The boundary conditions are defined on the line $k = \Lambda$ and are given in the form of the mesonic potential in the classical action, as a function of σ. After exploiting the symmetries of the dynamics, this is a $1+1$ dimensional problem: we are granted a function of σ and we are interested in its evolution as the function of k.

Previously there have been two standard methods to solve the flow equation. One approach to the solution of this partial differential equation is given by the grid method [98]. Its essence is to discretize the order parameter space σ by sampling it at N_{grid} equidistant gridpoints. All partial derivatives with respect to σ are replaced with appropriate finite difference numerical derivatives evaluated on the grid. This way there are N_{grid} variables, namely the values of the potential at the gridpoints, which all depend on the renormalization scale k. Their flow is given by N_{grid} ordinary differential equations of the form (2.102) and are coupled to each other through the finite difference numerical derivatives. The coupled differential equations can be solved using standard ordinary differential equation (ODE) solver algorithms. In the present work a variable-coefficient linear multistep Adams method is used provided by the GNU Scientific Library (GSL) [99]. For the first and second order discrete numerical derivatives, 6-point and 7-point formulas were used, respectively. This choice ensures sufficient stability for the flows. It should be noted that when the potential is taken to be a function of $\sigma = \sqrt{2\rho}$, which is true in the σ direction, the meson masses are given by,

$$m_\sigma^2 = \frac{\partial U_k}{\partial \rho} + 2\rho \frac{\partial^2 U_k}{\partial \rho^2} = \frac{\partial^2 U_k}{\partial \sigma^2}, \qquad m_\pi^2 = \frac{\partial U_k}{\partial \rho} = \frac{1}{\sigma}\frac{\partial U_k}{\partial \sigma}. \tag{2.127}$$

An alternative method is the so-called Taylor method [100, 101]. This method focuses on the scale evolution of the minimum of the potential, since in the $k \to 0$ limit that corresponds to the physical point. This treatment depends on the external field (or equivalently, on the current quark masses) already during the flow, since the minimum of the potential is determined through the solution of the gap equation at each flow step.

Using the $\sigma \to -\sigma$ symmetry of the potential in the chiral limit, a suitable ansatz for the potential is

$$\begin{aligned} U_k(\sigma,\vec{\pi}) &= a_0(k) + a_1(k)(\rho-\rho_0(k)) + \frac{a_2(k)}{2}(\rho-\rho_0(k))^2 + \dots + \frac{a_K(k)}{K!}(\rho-\rho_0(k))^K - H\sigma \\ &= U_k^{ch}(\rho) - H\sigma. \end{aligned} \tag{2.128}$$

In the K-th order approximation the scale dependence of the potential is parametrized by the coefficients $a_0, a_1, a_2, \dots, a_K$ and by $\rho_0(k)$. The scale evolution of these coefficients obey coupled first order ordinary differential equations which we derive in the following. The parameter $\rho_0(k)$ is chosen such that it follows the minimum of the potential, so that the gap equation is always fulfilled at $(\sigma = \sqrt{2\rho_0(k)}, \vec{\pi} = 0)$:

$$\left.\frac{\partial U_k(\sigma,\pi)}{\partial \sigma}\right|_{\sigma=\sqrt{2\rho_0(k)},\vec{\pi}=0} = 0 \quad \Longrightarrow \quad a_1(k) = \frac{H}{\sqrt{2\rho_0(k)}}. \tag{2.129}$$

This condition can be used to fix $a_1(k)$ at any scales. Flow equations for the other coefficients can be obtained by considering the total scale derivative of different order ρ derivatives of the potential following the line $\rho = \rho_0(k)$:

$$\frac{d}{dk}\left.\frac{\partial^j U_k^{ch}(\rho)}{\partial \rho^j}\right|_{\rho=\rho_0(k)} = \frac{\partial}{\partial k}\left.\frac{\partial^j U_k^{ch}(\rho)}{\partial \rho^j}\right|_{\rho=\rho_0(k)} + \left.\frac{\partial^{j+1} U_k^{ch}(\rho)}{\partial \rho^{j+1}}\right|_{\rho=\rho_0(k)} \frac{d\rho_0}{dk}. \tag{2.130}$$

The left-hand side of the equation simply gives the scale derivative of the Taylor coefficients $a_0, a_1, a_2 \cdots$ for different j values, respectively. The first term on the right-hand side describes the evolution of the field derivatives of the potential with fixed order parameter value and can be obtained by taking field derivatives of Eq. (2.109). The second term on the right-hand side describes the change of the Taylor coefficients due to the shift of the origin of the Taylor expansion. Using the explicit form of the potential ansatz (2.128), we obtain the flow equations

$$\begin{aligned} d_k a_0 &= F(\rho_0) + a_1 d_k \rho_0, \\ d_k a_1 &= F'(\rho_0) + a_2 d_k \rho_0, \\ &\vdots \\ d_k a_K &= F^{(K)}(\rho_0), \end{aligned} \tag{2.131}$$

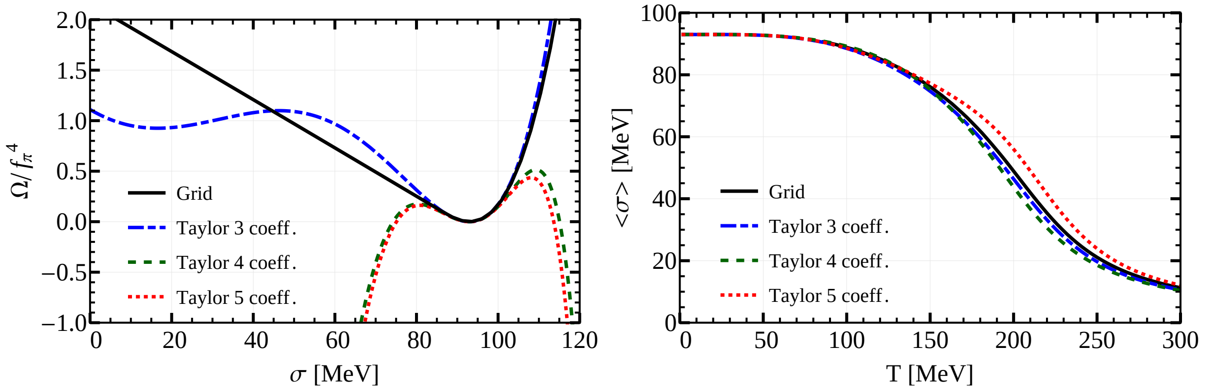

Figure 2.4.: Comparison of the grid and Taylor methods. On the left, the shape of the potential is depicted for $T = 0$. On the right, the temperature dependence of the chiral condensate is shown. The initial conditions were chosen in each case such that we reproduce the vacuum condensate $\sigma_M = f_\pi$, the sigma mass $m_\sigma = 650$ MeV, the quark mass $m_q = 335$ MeV using the cutoff scale $\Lambda = 950$ MeV.

where $F(\rho)$ is defined in Eq. (2.109). The last equation has only one term due to truncation. Since $a_1(k)$ can be determined from the gap equation (2.129), we would like to drop the flow equation for $a_1(k)$ and derive a flow equation for $\rho_0(k)$ instead. Differentiating the gap equation with respect to k yields

$$d_k a_1 = -\frac{H}{(2\rho_0)^{3/2}} d_k \rho_0. \tag{2.132}$$

Using this identity and the other flow equations, a flow equation for $\rho_0(k)$ can be derived and a_1 can be completely eliminated from the formulas. The final form of the system of differential equation reads

$$\begin{aligned}
d_k\rho_0 &= -\frac{F'(\rho_0)}{a_2 + \frac{H}{\sqrt{2\rho_0}}}, \\
d_k a_0 &= F(\rho_0) + \frac{H}{\sqrt{2\rho_0}} d_k\rho_0, \\
d_k a_2 &= F''(\rho_0) + a_3 d_k\rho_0, \\
&\vdots \\
d_k a_K &= F^{(K)}(\rho_0).
\end{aligned} \tag{2.133}$$

Both methods have their pros and cons. The grid method provides reliable information on the scale evolution of the grand canonical potential function for all values of the order parameter. This is crucial for example in the vicinity of a first order phase transition. In that case, at nonzero RG scale, multiple competing minima of the potential function can be present. This situation cannot be handled reliably using the Taylor method, because the validity of the expansion breaks down at a certain (in principle unknown) distance from the center of the expansion. The Taylor method, on the other hand, has the advantage that the order parameter can be calculated with many more significant digits, since it is given by a flow equation directly. The grid method has to extrapolate numerically from the grid points to extract the location of the minimum, which yields a poorer precision. Due to this, for studying the scaling behavior of quantities the Taylor method is better suited. There is also a big difference in numerical effort: using the grid method we need to solve 50-100 coupled differential equations that are sometimes very stiff and hard to handle. The Taylor method only requires the solution of approximately 5 coupled differential equations that usually do not behave too badly. In this thesis we will see examples for the application of both methods.

In Fig. 2.4 a comparison of the two methods is shown. We see that the potential calculated using the grid method is only well approximated by the Taylor method calculations in the vicinity of the minimum. Higher order truncations do not seem to get closer to the result provided by the grid method. On the other hand it can also be seen in the right panel that the temperature dependence of the condensate is captured reasonably well by all methods, at least at vanishing net density.

For the study of the baryon number cumulants, a different approach was employed, namely a pseudospectral method [102], where the potential is expanded in a Chebyshev series. Basic properties of the Chebyshev polynomials are reviewed in Appendix C. Similar methods have been previously applied to solve different problems within the FRG framework [103–105]. In this work the order parameter space from the interval $[-\sigma_{max}, \sigma_{max}]$ was projected onto $[-1, 1]$ by introducing

$$x = \frac{\sigma}{\sigma_{max}}. \tag{2.134}$$

The effective potential and its derivatives are expanded in terms of Chebyshev polynomials,

$$U_k(\sigma) = \sigma_{max}^4 \sum_{n=0}^{N-1} \alpha_n(k) T_{2n}(x), \tag{2.135}$$

$$U_k'(\sigma) = \sigma_{max}^3 \sum_{n=0}^{N-2} \beta_n(k) T_{2n+1}(x), \tag{2.136}$$

$$U_k''(\sigma) = \sigma_{max}^2 \sum_{n=0}^{N-2} \gamma_n(k) T_{2n}(x), \tag{2.137}$$

where the prefactor makes the Chebyshev coefficients dimensionless. A safe choice for the parameters is $\sigma_{max} = 400\,\mathrm{MeV}$, $N = 100$, however in many cases a simple truncation as $\sigma_{max} = 200\,\mathrm{MeV}$, $N = 20$ also suffices. A large value for N is especially important close to the chiral limit or when studying first order phase transitions to provide the neccessary precision. A low value for N induces fluctuations in the potential, since the high frequency modes are missing in the representation.

Note that in Eqs. (2.135), (2.136) and (2.137) we exploited the $\sigma \to -\sigma$ symmetry by allowing only even polynomials in the expansion of the effective potential. Based on the basic properties of the Chebyshev polynomials, the coefficients of the derivatives can be algebraically given in terms of the coefficients of the potential,

$$\beta_n(k) = \sum_{n'=1}^{N-n-1} 4(N-n')\alpha_{N-n'}(k), \tag{2.138}$$

$$\gamma_n(k) = \sum_{n'=1}^{N-n-1} 2(2N-2n'-1)\beta_{N-n'-1}(k). \tag{2.139}$$

Using these coefficients, the meson masses and hence the flow derivative can be evaluated at an arbitrary point x. In this work we evaluated the flow derivatives at the positive zeros of T_{2N},

$$x_i = \cos\left(\frac{\pi(i+1/2)}{2N}\right), \qquad i \in [0, 1, 2, \ldots, N-1]. \tag{2.140}$$

At the outermost point, x_0, we did not follow the evolution of the meson masses and use the meson masses calculated in the UV, at the beginning of the flow. This is done to provide stability for the flow on the boundary. Note that on the other side, x_{N-1} is not close to a boundary (it is close to $\sigma = 0$), hence there the flow derivative was evaluated ordinarily. This modification should not have physical relevance, since the end of the domain is always chosen such that it is appropriately far away from the physically relevant region $0 < \sigma < 100$ MeV.

After the calculation of the flow derivatives, the evolution of the coefficients, as shown in Appendix C, is simply given by

$$\partial_k \alpha_0(k) = \frac{1}{N} \sum_{i=0}^{N-1} g(x_i) T_0(x_i), \tag{2.141}$$

$$\partial_k \alpha_j(k) = \frac{2}{N} \sum_{i=0}^{N-1} g(x_i) T_{2j}(x_i), \qquad j \in [1, 2, \dots, N-1], \tag{2.142}$$

where g stands for the flow derivative calculated according to Eq. (2.102) or Eq. (2.109).

This pseudospectral method combines the advantages of the grid and Taylor methods in a sense. Just like in the Taylor method, the potential is known as an analytic function of σ, hence the expectation value of the order parameter can be evaluated with high precision. This property lets us to calculate higher order fluctuations (in this work up to sixth order) with ease. Furthermore, this method, just as the grid method, follows the evolution of the potential in the whole range of order parameter values, not only close to the minimum. This allows us to study first order transitions with this method as well. It turns out that exactly the same UV initial conditions can be used for the grid and pseudospectral methods, and the deviations between physical quantities calculated by the two methods are negligible. This property ensures that the expansion of the potential in Chebyshev polynomials converges and the flow equations are reliable and well-behaved. It turns out that the pseudospectral method is not only more precise than the grid method, but is also computationally much cheaper. For this reason this method was used to extract higher order fluctuations in Chapter 4, as well as for the finite volume studies in Chapter 5.

2.6.2 Solving the flow equations in the PQM model

Let us finally discuss how the thermodynamic properties are extracted in the PQM model. In general, regardless of the solution technique of the RG flow, the calculations are performed as follows. First, an initial guess is made for the Polyakov-loop variables Φ and $\bar{\Phi}$. Then RG flow equations are solved, using the initial conditions of the quark-meson model [4], with the Polyakov loop kept constant. The derivatives $\partial_\Phi \Omega$ and $\partial_{\bar{\Phi}} \Omega$ are evaluated based on the flow at the minimum of the potential, where $\partial_\sigma \Omega = 0$. Then, based on the derivatives, the guess for the Polyakov-loop variables is updated. This procedure is continued until all the gap equations are fulfilled up to the desired precision.

Once the value of the Polyakov loop has been found, all thermodynamic quantities can be computed from the effective action. Alternatively, flow equations can be derived for other thermodynamic quantities as well. In the calculations of Chapters 4 and 5, such a flow equation is solved for the density to obtain higher precision for the baryon number fluctuations. Hence, altogether four flow equations are solved; one for the pressure, two for the Polyakov-loop derivatives of the potential, and one for the density. In the pseudospectral method, these four quantities are expanded into an RG scale dependent Chebyshev-series and the evolution of the

---

[4] Just as in the mean-field case, the Polyakov loop does not couple to the vacuum quark fluctuations, hence the flow in the vacuum is unaltered by the Polyakov loop.

coefficients is trac——ked using the method presented in the previous section. The flow derivative for the pressure in the PQM model using the Litim regulator was presented in Eq. (2.119), and has the form

$$\frac{d}{dk}U_k = 3F_{bos}\left(m_\pi^2\right) + F_{bos}\left(m_\sigma^2\right) + F_{ferm}\left(\mu,\Phi,\bar{\Phi}\right), \tag{2.143}$$

where

$$F_{bos}(m^2) = \frac{k^4}{12\pi^2}\frac{\coth\left(\frac{\sqrt{k^2+m^2}}{2T}\right)}{\sqrt{k^2+m^2}}, \tag{2.144}$$

$$F_{ferm}(\mu,\Phi,\bar{\Phi}) = -\frac{2k^4}{\pi^2 E_q}\left(1 - N(T,\mu;\sigma,\Phi,\bar{\Phi}) - N(T,-\mu;\sigma,\bar{\Phi},\Phi)\right), \tag{2.145}$$

indicating the functional dependence only if it is relevant for the derivatives. The boson masses are still given by

$$m_\pi^2 = \frac{1}{\sigma}\frac{\partial U_k}{\partial\sigma}, \quad m_\sigma^2 = \frac{\partial^2 U_k}{\partial\sigma^2}. \tag{2.146}$$

The other flow equations, namely the flow equations for the derivatives of the potential can be obtained by taking a derivative of the flow derivative of the potential,

$$\frac{d}{dk}\frac{\partial U_k}{\partial\lambda_i} = \frac{\partial}{\partial\lambda_i}\frac{dU_k}{dk} = 3F'_{bos}\left(m_\pi^2\right)\frac{1}{\sigma}\frac{\partial^2 U_k}{\partial\lambda_i\partial\sigma} + F'_{bos}\left(m_\sigma^2\right)\frac{\partial^3 U_k}{\partial\lambda_i\partial^2\sigma} + \frac{\partial}{\partial\lambda_i}F_{ferm}(\mu,\Phi,\bar{\Phi}) \tag{2.147}$$

where λ_i and λ_j stand for any of the parameters $\{\mu,\Phi,\bar{\Phi}\}$, and the prime denotes derivative with respect to m^2. Initially, at the UV scale, the derivative of the potential with respect to the chemical potential or the Polyakov-loop variables all vanish and build up during the flow. After the flow, these derivatives are evaluated at the point where the σ gap equation, $\partial_\sigma U_{k=0} = H$, is fulfilled.

Having solved the additional flow equations, for any Φ and $\bar{\Phi}$ values, we obtain

$$\frac{\partial\Omega}{\partial\Phi} = \frac{\partial U_{k=0}}{\partial\Phi} + \frac{\partial\mathcal{U}(\Phi,\bar{\Phi})}{\partial\Phi} - \frac{\partial p_{pert}(\mu;\Phi,\bar{\Phi})}{\partial\Phi}, \tag{2.148}$$

$$\frac{\partial\Omega}{\partial\bar{\Phi}} = \frac{\partial U_{k=0}}{\partial\bar{\Phi}} + \frac{\partial\mathcal{U}(\Phi,\bar{\Phi})}{\partial\bar{\Phi}} - \frac{\partial p_{pert}(\mu;\Phi,\bar{\Phi})}{\partial\bar{\Phi}}, \tag{2.149}$$

where the second and third terms are independent of the flow and are elementary to evaluate. Then the physical values of Φ and $\bar{\Phi}$ are determined by the gap equations

$$\frac{\partial\Omega}{\partial\Phi} = \frac{\partial\Omega}{\partial\bar{\Phi}} = 0. \tag{2.150}$$

The search for the solution of the gap equation in the $\{\Phi,\bar{\Phi}\}$ space is performed using the Hybrid algorithm of the multidimensional rootfinding package of GSL [99]. Once the expectation value of the Polyakov-loop variables is known, the quark density is given by

$$n_q = -\frac{\partial\Omega}{\partial\mu} = -\frac{\partial U_{k=0}}{\partial\mu} + \frac{\partial p_{pert}(\mu;\Phi,\bar{\Phi})}{\partial\mu}. \tag{2.151}$$

Higher order susceptibilities of baryon number are obtained by taking numerical finite difference derivatives of the density. Their properties and behavior will be discussed in Chapter 4 in detail.

Chapter 3

Scaling properties of the *O(4)* chiral transition line

As discussed in Sec. 2.1, in the chiral limit of the quark-meson model at vanishing density, there is a second order chiral phase transition. This is in agreement with lattice QCD calculations [106–109]. The critical point corresponding to this transition belongs to the $O(4)$ universality class. At small but finite densities, the chiral transition is still expected to be of second order, and at each value of the chemical potential one finds a critical point in the $O(4)$ universality class. These critical points constitute an $O(4)$ critical line and this line is conjectured to end in a *tricritical point* (TCP).

In general, close to a critical point, models lying in the same universality class share certain properties, for example critical exponents. These are called *universal* properties. Other quantities, *nonuniversal* quantities, however differ from model to model. In order to successfully model QCD, both the universal and nonuniversal quantities should agree. Effective models such as the quark-meson or the Polyakov–quark-meson models belong to the same universality class regarding the chiral phase transition, as QCD. The question still remains, how well nonuniversal quantities are reproduced in these models. In this chapter, some of these nonuniversal quantities related to the chiral phase transition will be computed in effective models and confronted with each other and with lattice QCD simulations.

In the vicinity of a critical point, many thermodynamic quantities obey scaling laws. This can be described by the scaling theory of phase transitions. In the following, we focus on the QCD chiral phase transition and discuss the scaling properties of the chiral order parameter near the critical point. We consider effective models belonging to the universality class of the QCD chiral transition, and study the scaling of the order parameter and the leading order corrections to the scaling. We analyze scaling violations induced by finite quark masses in the context of recent LQCD findings, which indicate that for a physical value of the pion mass, QCD lies in the scaling regime of the underlying second order phase transition [106–109].

In the first part of this chapter we review the scaling theory of phase transitions around critical points. We show that the order parameter as a function of temperature and external symmetry breaking field can be rescaled to depend only on a single variable, the scaling variable. Hence, a reduced order parameter, x, will only depend on a simple combination of the two variables, not separately on both of them. Curves of the reduced order parameter with different external field values will fall on a universal curve. This scaling behavior however breaks down as one moves away from the critical point. We will apply two simple models, the quark-meson model in the mean-field approximation and a purely bosonic theory, the $O(N)$ linear sigma (LS) model [110–117] in the large-N approximation to gain a qualitative analytic understanding of the scaling and the emergence of the terms that break the scaling using the high temperature expansion. These findings will be verified by numeric calculations. Further numeric studies of scaling will be presented in the QM model within the FRG approach and in the PQM model within the mean-field approximation.

Furthermore, scaling in the QM model using the FRG and in the PQM model using mean-field approximation will also be numerically studied.

3.1 Universality and scaling

In the scaling theory of phase transitions the free energy density $f(T,H)$, which depends on the temperature T and on an external field H, in the vicinity of a critical point is split into a singular scaling part $f_s(T,H)$ and a regular part. When derivatives of the free energy are considered close to the critical point, the singular part dominates the regular part. In a given *universality class*, which is defined by the dimensions of the system and symmetries of the theory, the dominating singular part has a universal structure [118],

$$f_s(T,H) = F_0\,\bar{h}^{1+1/\delta} f_f\,(z)\,, \tag{3.1}$$

where

$$z = \frac{\bar{t}}{\bar{h}^{1/(\beta\delta)}}, \qquad \bar{t} \equiv \frac{t}{t_0} \equiv \frac{T-T_c}{T_c t_0}, \qquad \bar{h} \equiv \frac{h}{h_0} \equiv \frac{H}{H_0 h_0}. \tag{3.2}$$

Here, f_f is a universal scaling function, T_c is the critical temperature and F_0, t_0, H_0, h_0 are appropriately chosen nonuniversal constants. Moreover, δ, as well as β introduced in the following, are universal critical exponents. The reduced temperature and reduced external field, $\bar{t}$ and $\bar{h}$ are dimensionless. The scaling of the order parameter σ_M is obtained from Eq. (3.1) and yields

$$\sigma_M = \frac{\partial}{\partial H} f(T,H) \simeq \frac{\partial}{\partial H} f_s(T,H) = \sigma_0 \bar{h}^{1/\delta} f_G(z) \equiv \sigma_{\text{scaling}}. \tag{3.3}$$

Here, σ_0 is again an appropriately chosen constant and f_G is a further universal scaling function, obtained from f_f. Obviously, the reduced order parameter,

$$x = \frac{\sigma_M}{\sigma_0 \bar{h}^{1/\delta}} \simeq \frac{\sigma_{\text{scaling}}}{\sigma_0 \bar{h}^{1/\delta}} = f_G(z), \tag{3.4}$$

is a function of one variable only, the scaling variable z.

The functions f_f, f_G and the critical exponents are universal, as they do not depend on the details of the model, but only on its universality class. To fix the nonuniversal parameters t_0 and h_0, and thereby thenormalization of the reduced external field and reduced temperature, one has to specify the asymptotic behavior of the scaling functions. The normalization is done such that the scaling function f_G obeys

$$f_G(0) = 1, \qquad \text{and} \qquad \lim_{z\to-\infty} \frac{f_G(z)}{(-z)^\beta} = 1. \tag{3.5}$$

From these properties of the scaling function, one arrives at the following well know scaling behavior of the order parameter on the coexistence line $(T < T_c, H = 0)$ and at the pseudocritical point $(T = T_c, H > 0)$,

$$\sigma_{\text{scaling}} = \sigma_0 \tilde{\sigma} = \begin{cases} \sigma_0 \bar{h}^{1/\delta} & = \sigma_0 \left(\frac{H}{H_0 h_0}\right)^{1/\delta}, \quad T = T_c,\ H > 0, \\ \sigma_0 (-\bar{t})^\beta & = \sigma_0 \left(\frac{(-t)}{t_0}\right)^\beta, \quad H = 0,\ T < T_c. \end{cases} \tag{3.6}$$

This yields t_0 and h_0 once σ_0 and H_0 are specified. We choose $\sigma_0 = f_\pi \approx 93$ MeV and $H_0 = m_\pi^2 f_\pi \approx 1.77 \cdot 10^6\ \text{MeV}^3$.

Similarly to the order parameter, the related susceptibility also exhibits scaling. The scaling of the order parameter susceptibility in the vicinity of the critical point is obtained from Eq. (3.3) and reads

$$\chi_\sigma = \frac{\partial^2 f_s(T,H)}{\partial H^2} = \frac{\partial \sigma_{\text{scaling}}}{\partial H} = \chi_0 \bar{h}^{1/\delta-1}\left(f_G(z) - \frac{z f_G'(z)}{\beta}\right) \equiv \chi_0 \bar{h}^{1/\delta-1} f_\chi(z). \tag{3.7}$$

It is interesting to note that the maximum of the rescaled susceptibility as a function of scaling parameter is located at a fixed value of $z = z_p$, irrespective of the value of the external field H. From this, it follows that the pseudocritical temperature[1] $T_p(H)$ at a nonzero external field is given by [106]

$$\frac{T_p(H) - T_c}{T_c} = \frac{z_p}{z_0}\left(\frac{H}{H_0}\right)^{1/(\beta\delta)}, \tag{3.8}$$

where $z_0 = h_0^{1/(\beta\delta)}/t_0$ is a nonuniversal parameter. This parameter, as well as t_0 and h_0 are nonuniversal parameters describing scaling behavior about the critical point. We will evaluate them in different models and approximations later in this chapter and confront the results with lattice data.

The width of the crossover region, which is an important nonuniversal property of the phase transition, can be obtained from the susceptibility of the order parameter χ_σ. The universal part of χ_σ is a peaked function with a width of Δz, which depends only on the universality class. Thus, the width of the crossover region in temperature for a given external field is given by

$$\frac{\Delta T}{T_c} = \frac{\Delta z}{z_0}\left(\frac{H}{H_0}\right)^{1/(\beta\delta)}, \tag{3.9}$$

and is directly related to the nonuniversal parameter z_0.

The scaling theory of phase transitions provides definite predictions for the critical properties of various thermodynamic observables. These are characterized by the critical exponents of the corresponding universality class, which are ingrained in the scaling free energy. In particular, the scaling formula of the order parameter was given in Eq. (3.3). Sufficiently far away from the critical point, corrections to the universal scaling become significant and scaling breaks down. The regular part of the free energy contributes to the order parameter, σ_M. The reduced order parameter given in Eq. (3.4), x, will in this case depend on T and H separately, or equivalently both on z and $\bar{h}$. For small values of z and $\bar{h}$, the different $x(z,\bar{h})$ curves will collapse on the universal scaling curve $f_G(z)$. Away from the critical point they in general will not, and plotting the $x(z,\bar{h})$ curves for different external field values yields the so-called *magnetic equation of state*[2] [106, 118–120].

The deviations from the scaling forms determine the size of the scaling window, which is another model dependent nonuniversal quantity. In principle the scaling of different quantities breaks down at different points, yielding different scaling windows. In this work we consider the scaling window based on the breakdown of order parameter scaling, given in Eq. (3.3). To be precise, we define the scaling window of the second order transition as the region of the phase diagram, in which the deviation of the order parameter from the scaling formula, Eq. (3.3), is less then some percentage P, i.e.

$$\left|\frac{\sigma_M}{\sigma_{\text{scaling}}} - 1\right| < \frac{P}{100} \equiv p. \tag{3.10}$$

---

[1] We define the pseudocritical temperature as the location of the maximum of the chiral susceptibility.

[2] The magnetic equation of state was first investigated in spin systems, where the induced magnetization plays the role of an order parameter and the external symmetry breaking field is the magnetic field. In our model, however, it has nothing to do with magnetism.

Here, σ_{scaling} can be expressed in terms of T and H using Eq. (3.3),

$$\sigma_{\text{scaling}} = \sigma_0 \left(\frac{H}{H_0 h_0}\right)^{1/\delta} f_{\text{G}}\left(\frac{(T-T_{\text{c}})z_0}{T_{\text{c}}(H/H_0)^{1/\beta\delta}}\right). \tag{3.11}$$

In the next section we consider a model, where deviations from scaling are present, namely the Landau theory of second order phase transitions. We will construct the corresponding magnetic equation of state as a baseline for a quantitative description of more involved models.

3.2 The Landau theory

In mean-field theory, second order phase transitions are generically described by Landau theory [121]. There, the effective potential is a polynomial in the order parameter σ, with coefficients that are analytic functions of the temperature T. Assuming a symmetry under reflections, $\sigma \to -\sigma$, apart from a symmetry breaking term proportional to the external field H, the effective potential is an even polynomial in σ, and reads

$$\mathcal{L}(T,H;\sigma) = a(t)\frac{\sigma^2}{2} + b(t)\frac{\sigma^4}{4} + c(t)\frac{\sigma^6}{6} + d(t)\frac{\sigma^8}{8} + \cdots - H\sigma. \tag{3.12}$$

Here the T-dependent coefficients are parameterized as polynomials of the reduced temperature $t = T/T_c - 1$ and have the form

$$\begin{aligned} a(t) &= a_1 t + a_2 t^2 + a_3 t^3 + \ldots, \\ b(t) &= b_0 + b_1 t + b_2 t^2 + \ldots, \\ c(t) &= c_0 + c_1 t + \ldots, \\ d(t) &= d_0 + \ldots. \end{aligned} \tag{3.13}$$

For a given value of T and H, the order parameter, σ_M, is given by the location of the minimum of $\mathcal{L}(T,H;\sigma)$. This is determined by solving the gap equation

$$\left.\frac{\partial \mathcal{L}}{\partial \sigma}\right|_{\sigma=\sigma_M} = a(t)\sigma_M + b(t)\sigma_M^3 + c(t)\sigma_M^5 + d(t)\sigma_M^7 + \cdots = H. \tag{3.14}$$

For vanishing external field, and $b(t) > 0$ as well as $c(t), d(t) \geq 0$, there is a second order phase transition at $T = T_c$, where $a(t)$ vanishes. Around the corresponding critical point, the order parameter exhibits the following scaling properties

$$\sigma_M = \begin{cases} \left(\frac{H}{b_0}\right)^{1/\delta}, & T = T_c,\ H > 0, \\ \left(\frac{a_1(-t)}{b_0}\right)^{\beta}, & H = 0,\ T < T_c, \end{cases} \tag{3.15}$$

with $\delta = 3$ and $\beta = 1/2$, respectively. Comparing Eq. (3.15) to the general scaling behavior of the order parameter in Eq. (3.6), one can extract t_0 and h_0 in Landau theory,

$$h_0 = \frac{b_0 \sigma_0^3}{H_0}, \qquad t_0 = \frac{b_0 \sigma_0^2}{a_1}. \tag{3.16}$$

We note that both h_0 and t_0 depend on the normalization of the order parameter, while h_0 depends also on the normalization of the external field. Thus, a comparison of these parameters between different models has to be done with care. The model dependence can be reduced by considering the combination

$$z_0 = \frac{h_0^{2/3}}{t_0} = \frac{a_1 b_0^{2/3}}{b_0 H_0^{2/3}}, \tag{3.17}$$

which is independent of σ_0. Hence, one can compare the value of z_0 with other approaches, provided the normalization of the external field H_0 is known.

The mean-field magnetic equation of state is obtained from Landau's thermodynamic potential, by introducing the scaling variables

$$x = \frac{\sigma_M/\sigma_0}{\bar{h}^{1/3}} = \sigma_M \left(\frac{b_0}{H}\right)^{1/3}, \tag{3.18}$$

$$z = \frac{\bar{t}}{\bar{h}^{2/3}} = \frac{a_1 t}{b_0}\left(\frac{b_0}{H}\right)^{2/3}, \tag{3.19}$$

where $x > 0$ and z can take any real value. The variable z can be used to map out the phase diagram of the system. Thus, $|z| \ll 1$ corresponds to a system near the critical point $T = T_c$, while $z \ll -1$ refers to the phase with broken symmetry and $z \gg 1$ to the one where the symmetry is restored.

Using Eqs. (3.18) and (3.19), we express the reduced temperature and the order parameter in terms of x, z and H,

$$t = \frac{b_0 z}{a_1}\left(\frac{H}{b_0}\right)^{2/3} = \frac{z}{z_0}\left(\frac{H}{H_0}\right)^{2/3}, \qquad \sigma_M = x\left(\frac{H}{b_0}\right)^{1/3}. \tag{3.20}$$

The gap equation , Eq. (3.14), can be expressed in terms of the scaling variables x, z,

$$\big(x(x^2+z)-1\big) + \left(\frac{H}{b_0}\right)^{2/3}\left(\frac{c_0}{b_0}x^5 + \frac{b_1}{a_1}x^3 z + \frac{a_2 b_0}{a_1^2} x z^2\right) + \mathcal{O}\left(\left(\frac{H}{b_0}\right)^{4/3}\right) = 0. \tag{3.21}$$

The solution of the gap equation yields the magnetic equation of state $x = x(z, \bar{h})$ in Landau theory.

The universal scaling curve of mean-field theory, $x = f_G(z)$ is obtained by taking the limit $H \to 0$ in the gap equation. In this limit only the terms grouped in the first parenthesis in Eq. (3.21) survive. Once the universal curve $f_G(z)$ has been numerically determined, the scaling form of the order parameter is given by Eq. (3.11).

The terms proportional to $(H/b_0)^{2/3}$ in Eq. (3.21) provide the leading scaling violation. Since the latter depend on the parameters of the model, introduced in Eq. (3.13), they are nonuniversal and consequently model dependent. Thus, to quantify the deviations from universal scaling, we must specify the coefficients in the Landau effective potential. This will be done in the next section in the QM model. However, qualitative features of the scaling violation can be extracted from general considerations. We can distinguish three asymptotic regimes:

- $z \to -\infty$: In this limit the scaling curve behaves as $x(z) \simeq \sqrt{-z}$, and the sign of the scaling violation is determined by the sign of $(c_0/b_0 - b_1/a_1 + a_2 b_0/a_1^2)$.

- $z = 0$: At this point the scaling curve goes through $x = 1$, and the sign of c_0 determines the sign of the deviations.

- $z \to \infty$: In this limit the scaling curve behaves as $x \simeq 1/z$, and the sign of the correction is determined by the sign of a_2.

The discussion of the asymptotic behavior of the leading order scaling violation shows that, depending the model parameters, the sign of the deviation from the scaling curve can change as a function of z and can therefore cross the universal curve at several points. Indeed, Eq. (3.21) shows that in Landau-theory, the first order correction vanishes at points (x,z) where

$$\frac{c_0}{b_0} + \frac{b_1}{a_1}\left(\frac{z}{x^2}\right) + \frac{a_2 b_0}{a_1^2}\left(\frac{z}{x^2}\right)^2 = 0. \tag{3.22}$$

The roots of the second order equation are $z = \alpha^{\pm} x^2$, where

$$\alpha^{\pm} = -\frac{a_1}{2a_2 b_0}\left(b_1 \pm \sqrt{b_1^2 - 4a_2 c_0}\right). \tag{3.23}$$

Substitution of the roots into the universal curve yields the coordinates of the crossing points

$$z_c^{\pm} = \frac{\alpha^{\pm}}{(1+\alpha^{\pm})^{2/3}}, \qquad x_c^{\pm} = (1+\alpha^{\pm})^{-1/3}. \tag{3.24}$$

If α^+ and α^- are not real, or both of them are real and smaller than (-1), then the magnetic equation of state does not cross the universal scaling function, to leading order in H/b_0. On the other hand, if the coefficients $\alpha^{\pm}$ are real, and only one of them is larger than (-1), there is one crossing point. Finally, if both solutions are real and larger than (-1), then there are two crossing points.

Having discussed the structure of deviation from the scaling curve, now we turn to the calculation of the magnitude of the deviations. Based on Eq. (3.10), we are going to consider the size of the scaling window in two specific directions, namely on the pseudocritical line $T = T_c$, which we will refer to as h direction, and for vanishing external field, $H = 0$, which we will refer to as t direction. In the latter direction we distinguish between the broken phase, $T < T_c$, and the restored phase $T > T_c$. These cases correspond to three different parts of the magnetic equation of state plot.

The pseudocritical line, or the h direction corresponds to $z = 0$. On this line, the scaling form of the order parameter is given by

$$\sigma_{\text{scaling}} = \sigma_0 \bar{h}^{1/3}, \tag{3.25}$$

using the normalization condition for the order parameter scaling function, $f_G(0) = 1$. Hence, on this line,

$$\frac{\sigma_M}{\sigma_{\text{scaling}}} = x, \tag{3.26}$$

and the deviation of x from unity, δx, directly translates to the deviation of the order parameter from the scaling formula. In order to quantify this, we have to solve

$$\left(x^3 - 1\right) + \bar{h}^{2/3}\sigma_0^2\left(\frac{c_0}{b_0}x^5\right) + \mathcal{O}\left(\bar{h}^{4/3}\right) = 0 \tag{3.27}$$

up to leading order in $\bar{h}$, which yields

$$\delta x = -\frac{1}{3}\bar{h}^{2/3}\sigma_0^2\frac{c_0}{b_0}. \tag{3.28}$$

Thus, the scaling window in the h direction is, for a given tolerance level p and for small deviations, given by

$$H_{\rm sw} = H_0 h_0 \bar{h}_{\rm sw} = \left| \frac{3pb_0}{c_0} \right|^{3/2} b_0. \tag{3.29}$$

The leading-order expression for the scaling window on the coexistence line, which corresponds to the limit $z \to -\infty$, can be calculated analogously. There the scaling form of the order parameter is

$$\sigma_{\rm scaling} = \sigma_0 (-\bar{t})^{1/2} = \sigma_0 \bar{h}^{1/3} \sqrt{-z}, \tag{3.30}$$

and hence

$$\frac{\sigma_M}{\sigma_{\rm scaling}} = \frac{x}{\sqrt{-z}}. \tag{3.31}$$

The scaling window can be quantified by the deviations of the quantity $\frac{x}{\sqrt{-z}}$ from unity. Based on Eq. (3.21) and keeping the leading order term,

$$\frac{x}{\sqrt{-z}} - 1 \equiv \delta\left(\frac{x}{\sqrt{-z}}\right) = \frac{|\bar{t}|\sigma_0^2}{2} \left(\frac{c_0}{b_0} - \frac{b_1}{a_1} + \frac{a_2 b_0}{a_1^2} \right), \tag{3.32}$$

and the scaling window of tolerance p reads

$$t_{\rm sw} = t_0 \bar{t}_{\rm sw} = \left| \frac{2pb_0}{a_1 \left(\frac{c_0}{b_0} - \frac{b_1}{a_1} + \frac{a_2 b_0}{a_1^2} \right)} \right|. \tag{3.33}$$

The scaling window can also be defined in the t direction for the restored phase, $T > T_{\rm c}$. That corresponds to the limit $z \to \infty$ [3]. The derivation is completely analogous, yielding

$$\sigma_{\rm scaling} = \sigma_0 \bar{h}^{1/3} z^{-1}, \tag{3.34}$$

$$\frac{\sigma_M}{\sigma_{\rm scaling}} = xz, \tag{3.35}$$

$$(xz - 1) \equiv \delta(xz) = -|\bar{t}|\sigma_0^2 \frac{a_2 b_0}{a_1^2}, \tag{3.36}$$

and the scaling window of tolerance p reads

$$t_{\rm sw} = t_0 \bar{t}_{\rm sw} = \left| \frac{pa_1}{a_2} \right|. \tag{3.37}$$

Note that in the t direction, the size of the scaling window differs for $t > 0$ and $t < 0$.

In the knowledge of the Landau coefficients and after the selection of a tolerance level p, the scaling window can now be readily calculated. In the following section, we consider the quark-meson model in the mean-field approximation, in which the relevant quantities can be analytically obtained to leading order using the high temperature expansion [122, 123].

---

[3] Here we note that one has to be careful: the calculation cannot be performed in the chiral limit, since the order parameter vanishes identically. However, this can be circumvented by carrying out the calculation in small external fields, and then by taking the $H \to 0$ limit.

3.3 Quark-meson model in the mean-field approximation

In this section we consider the widely employed effective model of QCD, namely the quark-meson model, in the mean-field approximation, which was introduced in Sec. 2.1. In this approximation the fluctuations of the meson fields are ignored, and the transition belongs to the $O(4)$ universality class in four dimensions. The dynamics of the chiral symmetry breaking can be mapped onto a Landau effective potential $\Omega(T,\mu;\sigma)$, which is a polynomial in the order parameter σ. The effect of vacuum and thermal fluctuations of the fermion fields are accounted for in the effective potential, which was introduced in Sec. 2.1,

$$\begin{aligned}\Omega(T,\mu;\sigma) =& U_m(\sigma,0) - \frac{N_c N_f}{8\pi^2} g_s^4 \sigma^4 \ln\left(\frac{\sigma}{f_\pi}\right)\\ &- \frac{N_c N_f}{\pi^2}\int_0^\infty dp p^2 T\left(\ln\left(1+e^{(\mu-E_q)/T}\right)+\ln\left(1+e^{(-\mu-E_q)/T}\right)\right),\end{aligned} \tag{3.38}$$

where $E_q = \sqrt{p^2+g_s^2\sigma^2}$. This is supplemented by the gap equation Eq. (2.29), which determines the physical value of the sigma field. As pointed out in Ref. [47], both the vacuum and thermal contributions contain a nonanalytic term in σ, which cancel at nonzero temperature. This cancellation is crucial for obtaining a second order chiral transition in the chiral limit. Close to the critical point, where $H \approx 0$ and $T \approx T_c$, the order parameter σ is very small. Consequently, the contribution of the thermal fermion loop to the Landau effective potential can be computed in the high temperature expansion [122, 123]. We thus obtain the Landau free energy,

$$\Omega(T,H;\sigma) = a(t)\frac{\sigma^2}{2} + b(t)\frac{\sigma^4}{4} + c(t)\frac{\sigma^6}{6} + \cdots - H\sigma, \tag{3.39}$$

where, at vanishing net baryon density, the coefficients are functions of the reduced temperature t and the input parameters

$$\begin{aligned} a(t) &= \left(\frac{N_c N_f g_s^2 T_c^2(2t+t^2)}{6}\right),\\ b(t) &= \frac{m_\sigma^2 - m_\pi^2}{2f_\pi^2} + \frac{N_c N_f g_s^4}{2\pi^2}\left(\gamma_E - \ln\left(\frac{\pi T_c(1+t)}{g f_\pi}\right)\right),\\ c(t) &= -\frac{7\zeta(3) N_c N_f g_s^6}{32\pi^4 T_c^2(1+t)^2}.\end{aligned} \tag{3.40}$$

The second order chiral phase transition appears at

$$T_c^0 = \sqrt{\frac{3\left(m_\sigma^2 - 3m_\pi^2\right)}{N_c N_f g_s^2} + \frac{3 g_s^2 f_\pi^2}{2\pi^2}}. \tag{3.41}$$

In this approximation, the QM model is a particular realization of Landau theory. Consequently, the critical exponents are given by the mean-field critical exponents $\beta = 1/2$, $\delta = 3$. Using the coefficients of the effective potential, Eq. (3.40), we can compute h_0, t_0 and z_0 following the discussion in the previous section. Then we can explicitly determine the magnetic equation of state given in Eq. (3.21), including the leading order scaling violating term. Two special cases, namely $H = 0$ and $T = T_c$ are depicted in Fig. 3.1. As one approaches the critical point $T = T_c$, $H = 0$ on either line, the scaling form of the order parameter, Eq. (3.11), will

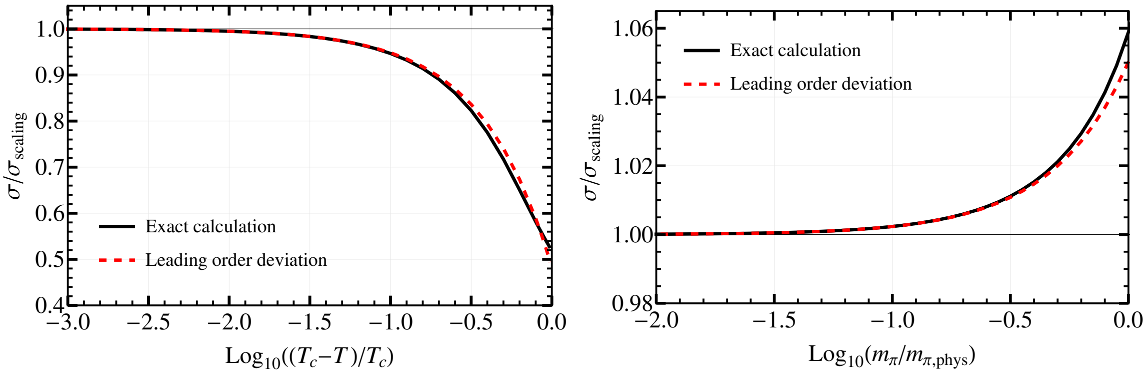

Figure 3.1.: The chiral condensate divided by the scaling formula Eq. (3.11) on the coexistence line (left) and at the pseudocritical point (right) in the quark-meson model. The solid black curves show a direct calculation of the order parameter, whereas the dashed red curves show the calculation of the leading order deviation based on the Landau coefficients and on Eqs. (3.28) and (3.32).

describe the order parameter more and more precisely, hence both curves approach unity for small temperature deviations and external fields. As we observe the system further away from the critical point, deviations from the scaling formula appear and become more relevant. In the QM model, these are however well captured by the leading order corrections, Eqs. (3.28) and (3.32) up to the physical pion mass and temperatures down to $T = 0$.

At finite, but small baryon chemical potentials, the chiral phase transition is still assumed to be of second order and to lie in the $O(4)$ universality class. The second order transition line ends at the tricritical point, which using the parameter set introduced in Sec. 2.1, lies at $\mu_{TCP} \approx 222$ MeV, $T_{TCP} \approx 60$ MeV. The location of the tricritical point was obtained by solving

$$\left.\frac{\partial^2\Omega}{\partial\sigma^2}\right|_{\sigma=0} = 0, \qquad \left.\frac{\partial^4\Omega}{\partial\sigma^4}\right|_{\sigma=0} = 0. \tag{3.42}$$

These expressions reflect the symmetry $\sigma \to -\sigma$ and determine the point on the phase boundary, where three extrema meet. Hence, the two lowest order nontrivial derivatives are required to vanish.

Since, in the chiral limit, the order parameter vanishes everywhere on the phase boundary , the high temperature expansion is applicable along this line all the way to the tricritical point. The Landau coefficients will of course in this case depend on the baryon chemical potential, and are given by

$$a(t,\mu) = \left(\frac{N_c N_f g_s^2 T_c(\mu)^2 (2t+t^2)}{6}\right), \tag{3.43}$$

$$\begin{aligned} b(t,\mu) = {} & \frac{m_\sigma^2 - m_\pi^2}{2 f_\pi^2} - \frac{N_c N_f g_s^4}{2\pi^2} \ln\left(\frac{\pi T_c(\mu)(1+t)}{g_s f_\pi}\right) \\ & - \frac{N_c N_f g_s^4}{2\pi^2} \frac{\psi^{(0)}\left(\frac{1}{2} + \frac{i\mu}{2\pi T_c(\mu)(1+t)}\right) + \psi^{(0)}\left(\frac{1}{2} - \frac{i\mu}{2\pi T_c(\mu)(1+t)}\right)}{2}, \end{aligned} \tag{3.44}$$

$$c(t,\mu) = \frac{N_c N_f g_s^6}{64\pi^4 T_c(\mu)^2 (1+t)^2} \left(\frac{\psi^{(2)}\left(\frac{1}{2} + \frac{i\mu}{2\pi T_c(\mu)(1+t)}\right) + \psi^{(2)}\left(\frac{1}{2} - \frac{i\mu}{2\pi T_c(\mu)(1+t)}\right)}{2}\right), \tag{3.45}$$

where

$$T_c(\mu) = \sqrt{(T_c^0)^2 - \frac{3\mu^2}{\pi^2}}, \qquad t = \frac{T - T_c(\mu)}{T_c(\mu)}, \tag{3.46}$$

furthermore $\psi^{(n)}$ denotes the Polygamma function, which is defined as the logarithmic derivative of the Gamma-function, $\psi^{(n)}(y) = \frac{d^{n+1}}{dz^{n+1}} \ln \Gamma(y)$. These coefficients can be expanded in powers of t,

$$a(t,\mu) = a_1(\mu)t + a_2(\mu)t^2 + \ldots, \tag{3.47}$$
$$b(t,\mu) = b_0(\mu) + b_1(\mu)t + \ldots, \tag{3.48}$$
$$c(t,\mu) = c_0(\mu) + c_1(\mu)t + \ldots. \tag{3.49}$$

Using these expansion coefficients, the parameters of the scaling form of the order parameter can be extracted at each value of the chemical potential,

$$h_0(\mu) = \frac{b_0(\mu)\sigma_0^3}{H_0}, \qquad t_0(\mu) = \frac{b_0(\mu)\sigma_0^2}{a_1(\mu)}. \quad z_0(\mu) = \frac{h_0(\mu)^{2/3}}{t_0(\mu)}. \tag{3.50}$$

The scaling form of the order parameter, just as introduced in Sec. 3.2, is given by the expression

$$\sigma_{scaling}(\mu, T, H) = \sigma_0 \left(\frac{H}{H_0 h_0(\mu)}\right)^{1/3} f_G\left(\frac{(T - T_c(\mu))z_0(\mu)}{T_c(\mu)(H/H_0)^{2/3}}\right). \tag{3.51}$$

The dependence on μ arises through the μ dependence of the nonuniversal parameters T_c, h_0 and z_0. How well this formula describes the order parameter close to the $O(4)$ transition line, is depicted in Fig. 3.2 for different values of baryon chemical potential. For each value of the chemical potential, $O(4)$ scaling applies as the critical point is approached. In the left panel one observes that in the chiral limit at a fixed value of reduced temperature, the deviations become stronger with increasing μ. This is expected, since the $O(4)$ scaling breaks down at the tricritical point. On the right one sees however that the picture is not this clear at the pseudocritical point $T = T_c(\mu)$, $H \neq 0$. With increasing chemical potential, while keeping the external field H constant, the leading order deviation seems to change sign: the correction to scaling is positive for small values of μ and negative for larger values. Close to the tricritical point, the deviations are again very high. To understand this behavior of the corrections to scaling, let us discuss some of the dimensionless Landau coefficients and combinations thereof on the left panel of Fig. 3.3. As expected from the Landau theory of phase transitions, the coefficient $b_0(\mu)$ goes to zero at the tricritical point, and the coefficient $c_0(\mu)$ takes a finite, positive value, as required for stability. The coefficient $b_0(\mu)$ approaching zero, explains why the deviations are enhanced based on Eqs. (3.28) and (3.32). The deviations from the scaling,

$$\frac{\sigma}{\sigma_{\text{scaling}}} - 1 = -\frac{1}{3}\bar{h}^{2/3}\sigma_0^2 \frac{c_0}{b_0}, \qquad \frac{\sigma}{\sigma_{\text{scaling}}} - 1 = \frac{|\bar{t}|\sigma_0^2}{2}\left(\frac{c_0}{b_0} - \frac{b_1}{a_1} + \frac{a_2 b_0}{a_1^2}\right), \tag{3.52}$$

for the pseudocritical point and the coexistence line respectively, both contain a term inversely proportional to b_0. That means the corrections diverge at the TCP. The coefficient $c_0(\mu)$ is negative at vanishing chemical potential, and positive at the tricritical point. Hence, it changes sign at some intermediate value of baryon chemical potential. This explains, why the deviations at the pseudocritical point change sign with increasing chemical potential. On the coexistence line, a different combination of coefficients, $c_0/b_0 - b_1/a_1 + a_2 b_0/a_1^2$ determines the strength of the deviations. As shown in the left panel of Fig. 3.3, this combination remains positive up

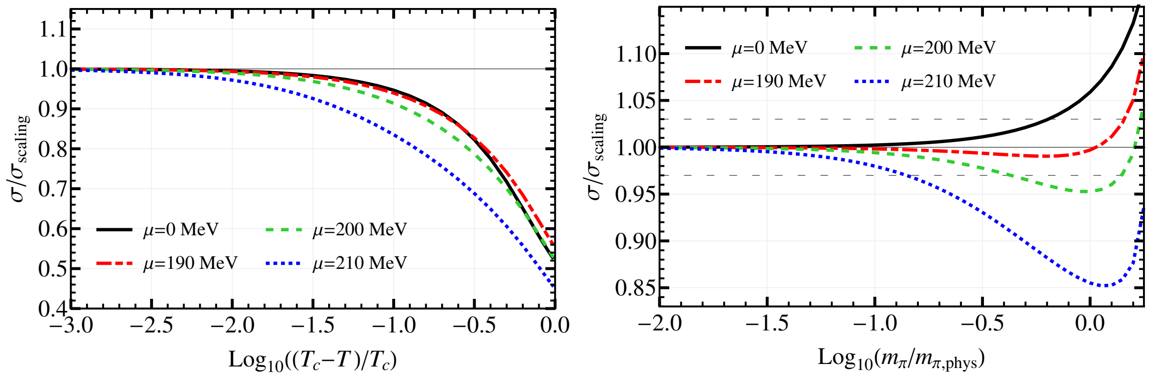

Figure 3.2.: Full calculation of the chiral condensate divided by the scaling formula Eq. (3.51) on the coexistence line (left) and at the pseudocritical point (right) in the quark-meson model at various bayron chemical potentials. On the right, the deviation level ±3% has been indicated by the horizontal black dashed lines.

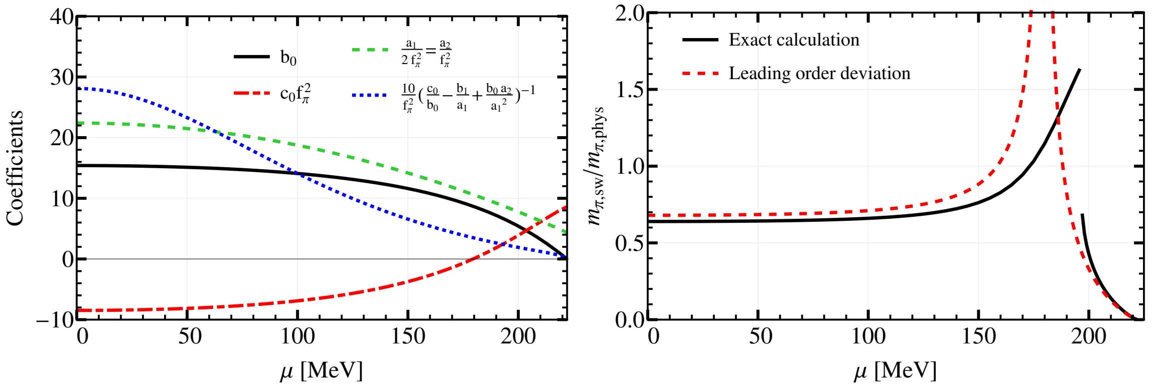

Figure 3.3.: Left: coefficients of the effective Landau-theory based on the high temperature expansion as a function of the baryon chemical potential. Right: size of the scaling window at $T = T_c(\mu)$ in the units of the physical pion mass $m_{\pi,phys} = 138$ MeV. The scaling window here was defined to be the point, where the deviation reaches 3%.

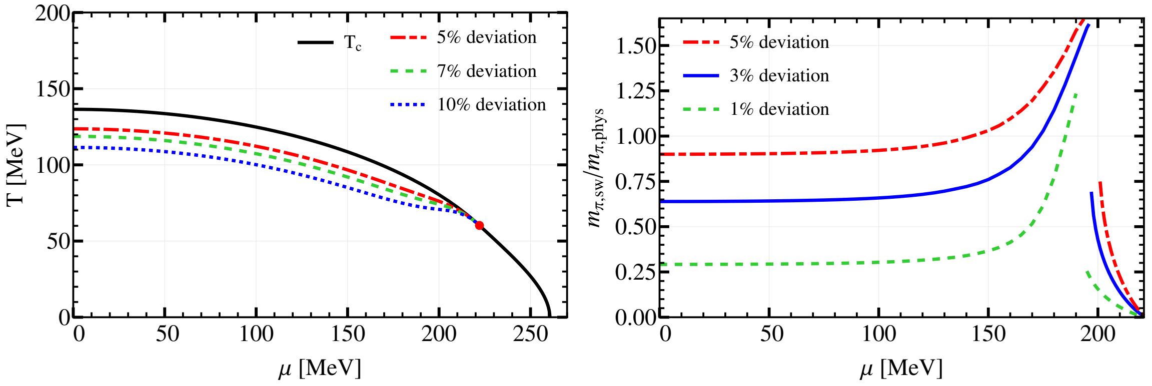

Figure 3.4.: Left: full calculation of the scaling window in the t direction (chiral limit) for different tolerance levels. The red dot indicates the TCP. Right: full calculation of the scaling window in the h direction ($T = T_c$) for different tolerance levels.

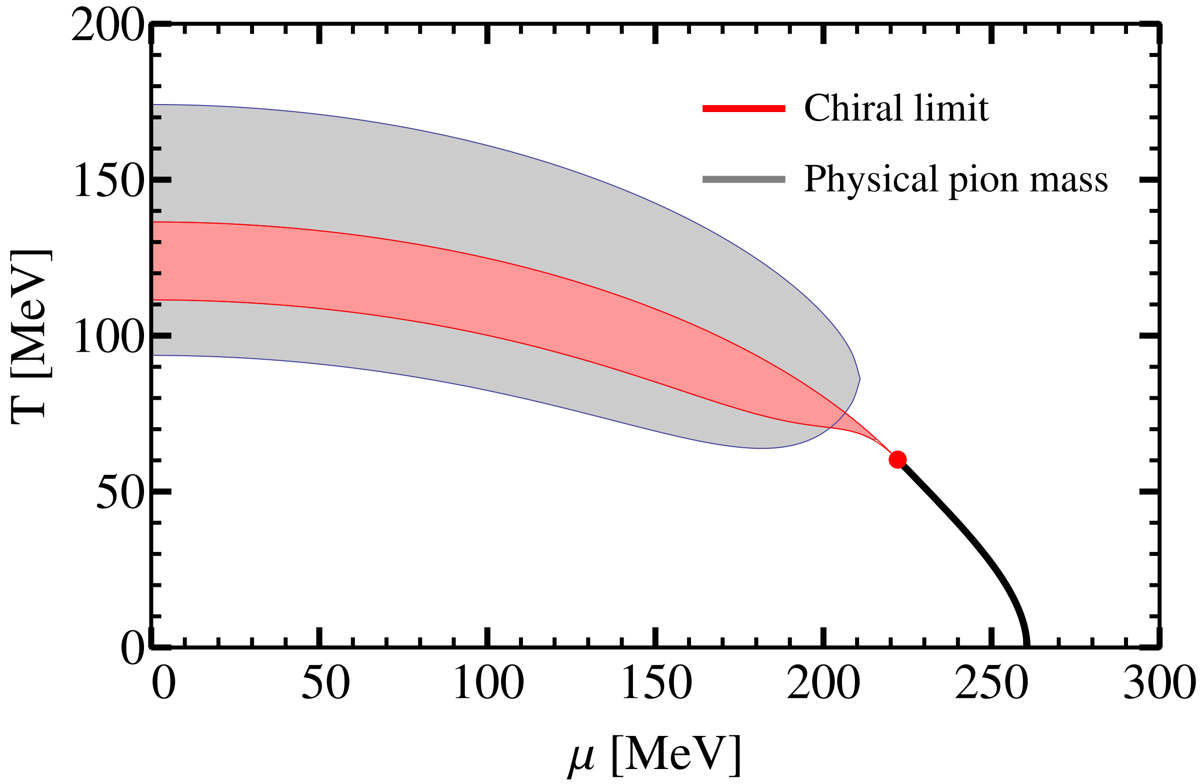

Figure 3.5.: The scaling region in the phase diagram, where the deviations from the scaling formula Eq. (3.51) are smaller, than 10%. The scaling for each curve was considered at fixed μ. The red region corresponds to the chiral limit, whereas the gray corresponds to physical pion mass. In the chiral limit, the upper boundary is the $O(4)$ transition line. Above that line, the condensate vanishes, hence the fulfillment of the scaling formula is ill-defined.

to the TCP and beyond. Note also that the fact that $c_0(\mu)$ changes sign does not depend on the initial conditions used. For stability, it must be positive at the tricritical point, and at vanishing density, it is negative (see Eq. (3.40)).

To end this section, we briefly discuss the behavior of the scaling window with increasing baryon chemical potential. The right panel of Fig. 3.3 shows that on the coexistence line the scaling window first increases with increasing chemical potential and then shrinks to zero at the tricritical point. This is expected based on our previous discussion on the strength of the deviations. One also sees that a leading order approximation to the deviation is fairly good at low chemical potentials and close to the tricritical point. This approximation obviously brakes down as the first order correction term changes sign, leading to a divergent scaling window based only on the leading order deviation. Interestingly, the scaling window obtained in the full calculation exhibits a discontinuity. This is associated with the sign change of the deviations. Up to a certain chemical potential, in the right panel of Fig. 3.3, the scaling window is set by the condition that the deviations reach +3%. However from a certain point onwards, −3% is reached first. This yields a sudden change in the scaling window. This is illustrated on the right panel of Fig. 3.2 as well by the horizontal dashed lines. Since in the t direction no such sign change of the deviations is present, the scaling window behaves smoothly. The scaling window in the h and t directions are compared to each other with different tolerance levels in Fig. 3.4.

By fixing the symmetry breaking term at a constant value, it is also possible to indicate the region of applicability of the scaling formula in the phase diagram. Here it is performed in the chiral limit and using physical pion mass. The result is depicted in Fig. 3.5. At first sight, it seems counter-intuitive that the scaling region is larger with physical pion mass than in the chiral limit. At physical pion mass, we are clearly further away from the critical point, then in the chiral limit. One however has to take into account that based on Fig. 3.1, the deviation from scaling has the opposite sign as one moves away from the critical point in the temperature direction, compared to the external field direction. This may, and in this case it does, lead to a partial cancellation of the deviations due to finite external field and those due to temperature differences.

Now having provided the framework for scaling studies in the quark-meson model, let us go beyond the mean-field approximation, and discuss scaling in the quark-meson model within the FRG framework.

3.4 Scaling in the quark-meson model using the FRG

In the FRG approach, the quark-meson model cannot be described by Landau theory anymore. The order parameter σ is obtained by solving the FRG flow equation at each point of the phase diagram. Here, to retain high numeric precision, we employ the Taylor method with 4 coefficients using the Litim regulator. This corresponds to the truncation

$$U_k(\sigma,\vec{\pi}) = a_0 + a_1(\rho-\rho_0(k)) + \frac{a_2}{2}(\rho-\rho_0(k))^2 + \frac{a_3}{3!}(\rho-\rho_0(k))^3 + \frac{a_4}{4!}(\rho-\rho_0(k))^4 - H\sigma, \quad (3.53)$$

and the flow equations for a_0, a_2, a_3, a_4 and ρ_0 are solved using the scheme introduced in Sec. 2.6. The calculation of the scaling behavior for a fixed value of the chemical potential μ goes as follows. First, we determine the critical temperature T_c by identifying the temperature where the condensate vanishes in the chiral limit $H = 0$. After that, we perform calculations of the order parameter at $T = T_c$ with very small external fields, and at very small reduced temperatures in the chiral limit. Then t_0, h_0, β and δ are obtained using linear fits based on

$$\log_{10}\frac{\sigma}{\sigma_0} = \begin{cases} -\beta\log_{10} t_0 + \beta\log_{10}|t|, & h = 0, t < 0, \\ -\frac{1}{\delta}\log_{10} h_0 + \frac{1}{\delta}\log_{10} h, & h > 0, t = 0, \end{cases} \quad (3.54)$$

which is based on Eq. (3.6) and where, as before,

$$t = \frac{T - T_c}{T_c}, \qquad h = \frac{H}{H_0}. \quad (3.55)$$

The exponents β and δ are thus determined by the slope of a linear double-logarithmic fit of σ against t and h, respectively, while the normalization constants t_0 and h_0 are determined by the intercepts of those fits.

The next step is to determine the universal scaling function $f_G(z)$. This is done by calculating the order parameter very close to the critical point, but now with $T \neq T_c$, $H \neq 0$. We choose the parameters such that the resulting z stays in the region of interest, for example $|z| < 5$, and that we stay close enough to the critical point to see the curves of different external fields fall on top of each other. After that, we identify the scaling window by changing the temperature and/or the external field and calculating the difference from the scaling formula,

$$\sigma_{scaling}(\mu, T, H) = \sigma_0\left(\frac{H}{H_0 h_0}\right)^{1/\delta} f_G\left(\frac{(T - T_c)z_0}{T_c(H/H_0)^{1/\beta\delta}}\right). \quad (3.56)$$

Here let us take a short detour to prove that the critical exponent δ, in the local potential approximation, can be obtained analytically, and we do not have to rely on numerical fits to obtain that. Furthermore, we also establish a relation between T_c and h_0. For simplicity, we consider the Litim regulator. However this behavior is independent of the employed regulator. In the vicinity of the critical point, the RG flow approaches a scaling solution. All quantities, including the order parameter, exhibit scaling with the RG scale k. Sufficiently close to the critical point, the order parameter and the masses of the particles are negligible compared to the temperature, and high temperature approximation can be applied. This yields the simplified flow equation

$$\partial_k U_k = \frac{k^4 T}{6\pi^2}\left(\frac{3}{k^2+U_k'} + \frac{1}{k^2+U_k'+2\rho U_k''}\right). \tag{3.57}$$

Note that the fermions decouple and their contribution was dropped. With a carefully performed dimensional analysis one can eliminate both the temperature T and the RG scale k from the flow that approaches a fixed point. We exchange the dimensionful variables U_k and ρ for the dimensionless variables $\hat{\rho}$ and u_k the following way:

$$\rho = Tk\hat{\rho}, \qquad U_k = U_0 + Tk^3 u_k(\hat{\rho}). \tag{3.58}$$

In case of a scaling solution, U_0 is an irrelevant constant. The derivatives appearing in the flow equation (3.57) can be simply expressed using the dimensionless variables,

$$U_k' = Tk^3 u_k' \frac{1}{Tk} = k^2 u_k', \qquad \rho U_k'' = (Tk\hat{\rho})Tk^3 u_k'' \frac{1}{(Tk)^2} = k^2 u_k''. \tag{3.59}$$

The same way we can express the flow derivative of U_k in terms of the dimensionless potential u_k as

$$\partial_k U_k = 3Tk^2 u_k + Tk^3\left(\partial_k u_k - u_k' \frac{\hat{\rho}}{k}\right). \tag{3.60}$$

Using these expressions the flow of u_k as a function of the dimensionless RG time $t = \log(k/\Lambda)$ yields

$$\partial_t u_k = \frac{\partial_k U_k}{Tk^2} - 3u_k + u_k'\hat{\rho} = \frac{1}{6\pi^2}\left(\frac{3}{1+u_k'} + \frac{1}{1+u_k'+2\hat{\rho}u_k''}\right) - 3u_k + u_k'\hat{\rho}. \tag{3.61}$$

We obtain a scaling solution by requiring that the solution converges to a fixed point, such that $\partial_t u_k = 0$. The scaling function that solves $\partial_t u_k = 0$ cannot be obtained analytically. The large field behavior of the potential, however, can be easily studied by looking for monotonously increasing power law solutions [100]. For such solutions and for large values of the field, $\hat{\rho}$, the first two terms on the right-hand side of Eq. (3.61) are negligible, and hence, the solution to the leading order in $\hat{\rho}^{-1}$ is determined by

$$0 = -3u_k + u_k'\hat{\rho}. \tag{3.62}$$

The solution to this equation is a cubic function, $u_k = A_0\hat{\rho}^3$. The potential can be systematically expanded in terms of $\hat{\rho}^{-1}$, which, beyond the leading order approximation, reads

$$u \sim A_0\hat{\rho}^3 + \frac{5N-4}{450\pi^2 A_0}\hat{\rho}^{-2} + \dots . \tag{3.63}$$

Here, $N = 4$ is the number of bosons. The formula contains an undetermined parameter, A_0. Its value is determined by requiring that the solution remains finite and analytic also for small and intermediate values of the field. This can only be performed numerically.

From this expansion one immediately can read off the critical exponent δ. One has to solve the gap equation,

$$\lim_{k\to 0}\left(k^2 u'\left(\frac{\rho}{kT}\right)-\frac{H}{\sqrt{2\rho}}\right)\Bigg|_{\rho=\rho_M}=0. \tag{3.64}$$

For any finite external field H the dimensionful order parameter ρ_M is finite, so the argument of the dimensionless potential diverges, hence it is justified to use the large field approximation. This yields

$$\frac{3A_0\rho_M^2}{T_c^2}=\frac{H}{\sqrt{2\rho_M}} \tag{3.65}$$

and one readily sees that

$$\sigma_M=\sqrt{2\rho_M}=\left(\frac{4HT_c^2}{3A_0}\right)^{1/5}. \tag{3.66}$$

This means that not only is $\delta=5$ determined, but also h_0. It depends on the model parameters only through T_c. Furthermore, based on these studies, the flow of the coefficients in the Taylor method in the vicinity of the critical point are expected to follow the scaling

$$a_2=\frac{kc_2}{T},\quad a_3=\frac{c_3}{T^2},\quad a_4=\frac{c_4}{kT^3},\quad \rho_0=\hat{\rho}_0 kT, \tag{3.67}$$

where c_2, c_3, c_4 and $\hat{\rho}_0$ are dimensionless constants.

These findings let us simplify our calculations and also provide us a way to crosscheck our numerical setup. A similar scheme for determining the critical exponent β is not known. Hence, we calculated it numerically using the Taylor method up to a_4 and obtained

$$\beta\approx 0.40292. \tag{3.68}$$

Using the techniques explained above we can obtain the scaling order parameter σ_{scaling} and calculate the deviations from scaling. This is performed for several chemical potential values on the pseudocritical line and on the coexistence line. It is found that, unlike in the mean-field studies, the deviations on the two lines have the same sign at low densities, and change sign at some intermediate value of the chemical potential. This is depicted in Fig. 3.6. Since the deviations change sign between $\mu=0$ and the TCP, the scaling window is expected to show a peak as a function of the chemical potential along the $O(4)$ line. This is depicted in Fig. 3.7. Note that the Taylor method, since it cannot handle competing minima, breaks down at chemical potential values slightly below the TCP. Hence, direct calculations cannot be performed all the way to the TCP. It is still indicated that the scaling window is small for small values of chemical potential, then shows a strong peak, and decreases. Based on tricritical scaling, it is expected that the scaling window vanishes at the TCP [124, 125].

It is notable that the size of the scaling window at low values of the chemical potential in the h direction using mean-field approximation and the FRG are very different, see the right panel of Figs. 3.4 and 3.7. Since the quark contribution in the two approximations is similar, this effect has to be due to the bosonic contribution. In order to qualitatively understand the bosonic contribution to the flow, let us consider a purely bosonic theory in where exact calculations are relatively simple to perform, namely the $O(N)$ symmetric linear sigma model in the large-N approximation.

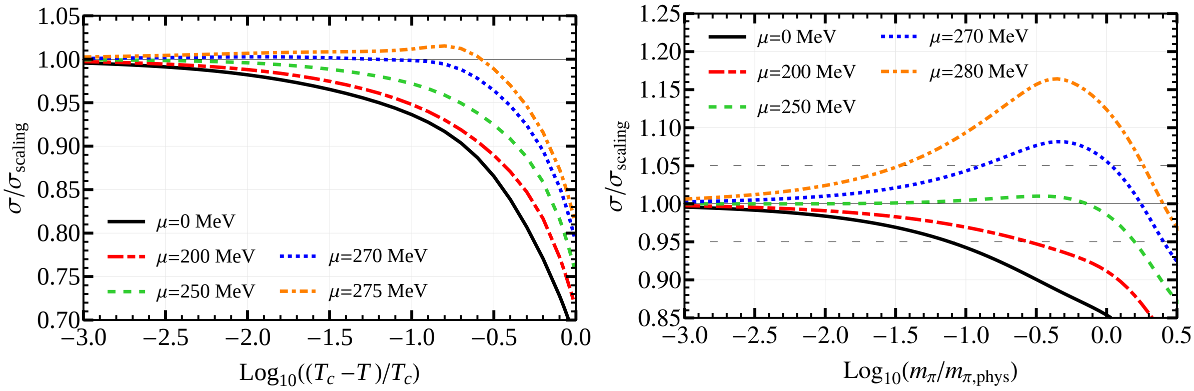

Figure 3.6.: Chiral condensate normalized by its scaling value defined by Eq. (3.56) for different chemical potential as a function of the reduced temperature and pion mass. As expected, we observe scaling near the critical point: the ratios approach unity. Deviations from scaling increase with increasing external field or negative reduced temperature.

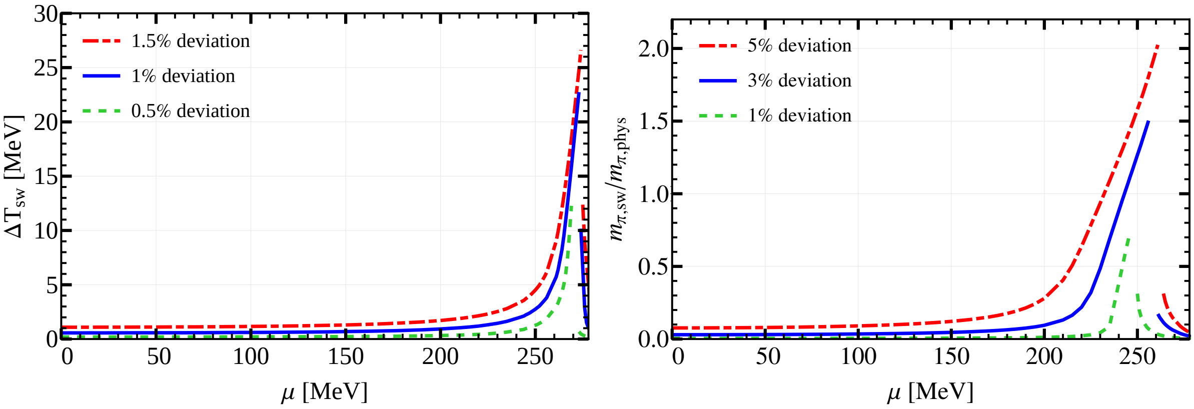

Figure 3.7.: FRG scaling window in the t direction (left) and in the h direction (right) at different thresholds. The scaling window shows an increase at intermediate values of the chemical potential similar to what was find in the MF treatment in the h direction.

3.5 *O(N)* linear sigma model in the large-*N* limit

In Sec. 3.2 we have introduced the Landau effective theory, which allowed us to explore various aspects of the magnetic equation of state in the mean-field approximation analytically. In this section we turn to the $O(N)$ symmetric linear sigma (LS) model, where the thermodynamic potential and the scaling properties near the critical point can be computed exactly in the large-N limit. The LS model in (3+1) dimensions is described by the Euclidean action

$$S_E = \int d^4x \left(\frac{1}{2}(\partial_\mu \sigma)^2 + \frac{1}{2}(\partial_\mu \pi_j)^2 + \frac{1}{2}m^2(\sigma^2 + \pi_j^2) + \frac{\lambda}{N}\left(\sigma^2 + \pi_j^2\right)^2 - \frac{\sqrt{N}}{2}H\sigma \right), \tag{3.69}$$

where the subscript j is an index in flavor space, spanned by the N-component vectors $\{\sigma, \pi_j\}$. The N dependent factors in Eq. (3.69) are introduced for later convenience.

For vanishing external field H, the action is invariant under rotations in the N dimensional flavor space. For negative values of m^2, this symmetry is spontaneously broken in the vacuum and the N-tuple $\{\sigma, \pi_j\}$ acquires a nonzero expectation value, a condensate. The coordinates

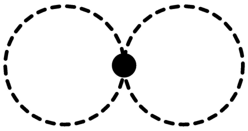

Figure 3.8.: The only contribution to Γ_2 in the $1/N$ expansion of the $O(N)$ sigma model for $N \to \infty$. The dashed lines are pion propagators, whereas the filled dot depicts the four-point vertex, with coupling strength λ/N.

in flavor space are chosen such that the condensate is in the σ direction. Consequently, the $N-1$ remaining fields, π_j, have vanishing expectation values. The condensate $\langle\sigma\rangle$ is an order parameter of the spontaneously broken $O(N)$ symmetry and the shifted field $\sigma' = \sigma - \langle\sigma\rangle$ represents the fluctuations of the σ field about its expectation value.

To determine the thermodynamic potential density $\Omega[T]$, we employ the $2PI$ formalism [126, 127]. The $2PI$ functional for this theory is given by

$$\Omega[T;\langle\sigma\rangle,G_\pi,G_\sigma] = \frac{T}{V}\Big(S_E[\langle\sigma\rangle] + \frac{N-1}{2}\mathrm{Tr}\ln G_\pi^{-1} + \frac{N-1}{2}\mathrm{Tr}\big(\big(D_\pi^{-1}-G_\pi^{-1}\big)G_\pi\big) + \frac{1}{2}\mathrm{Tr}\ln G_\sigma^{-1} + \frac{1}{2}\mathrm{Tr}\big(\big(D_\sigma^{-1}-G_\sigma^{-1}\big)G_\sigma\big) - \Gamma_2[\langle\sigma\rangle,G_\pi,G_\sigma]\Big), \tag{3.70}$$

where D_σ, D_π, G_σ and G_π are the bare and dressed propagators of the sigma and pion fields, respectively. Moreover, $\Gamma_2[\langle\sigma\rangle,G_\pi,G_\sigma]$ denotes the sum of all possible $2PI$ diagrams (with dressed propagators), while V and T are the volume and the temperature of the system. Finally, the trace in Eq. (3.70) is given by

$$\mathrm{Tr} = T\sum_n \int \frac{d^3q}{(2\pi)^3}, \tag{3.71}$$

where the sum is over the Matsubara frequencies.

The physical values of the dressed propagator and the expectation value of the field are determined by the stationarity conditions

$$\frac{\delta\Omega}{\delta\langle\sigma\rangle} = 0, \qquad \frac{\delta\Omega}{\delta G_\pi} = 0, \qquad \frac{\delta\Omega}{\delta G_\sigma} = 0. \tag{3.72}$$

The second and the third equations are just the Dyson equation for the pion and sigma fields respectively,

$$G^{-1} = D^{-1} - 2\frac{\delta\Gamma_2}{\delta G} = D^{-1} + \Sigma, \tag{3.73}$$

where $-2\,\delta\Gamma_2/\delta G$ is identified with the self-energy Σ. A tractable self-consistent scheme for calculating the thermodynamic potential starting from Eq. (3.70) is defined by a choice of the set of $2PI$ diagrams contributing to Γ_2 (for details see ref. [126]).

For convenience we simplify our notation by introducing $\phi \equiv 2\langle\sigma\rangle/\sqrt{N}$. With this choice the inverse bare Euclidean propagators are given by

$$D_\sigma^{-1}(q,n) = q^2 + \omega_n^2 + m^2 + 3\lambda\phi^2, \tag{3.74}$$

$$D_\pi^{-1}(q,n) = q^2 + \omega_n^2 + m^2 + \lambda\phi^2, \tag{3.75}$$

where $\omega_n = 2n\pi T$ is the Matsubara frequency and q denotes the momentum in the spatial direction. The bare mass-square of the σ and π fields are given by $m^2 + 3\lambda\phi^2$ and $m^2 + \lambda\phi^2$, respectively.

In the $O(N)$ linear sigma model, at $N \to \infty$, the contributions of sigma loops to $\Gamma_2[\langle\sigma\rangle, G_\pi, G_\sigma]$ are suppressed, due to $1/N$ factor introduced in the four-point coupling in the action. Consequently, to leading order in $1/N$, the only relevant contribution to the $2PI$ diagrams is the two-pion loop diagram shown in Fig. 3.8,

$$\Gamma_2[\phi, G_\pi] = -N\lambda(\mathrm{Tr}\,G_\pi)^2. \tag{3.76}$$

This in turn yields the pion self-energy

$$\Sigma_\pi(q,n) = 4\lambda \mathrm{Tr}\,G_\pi. \tag{3.77}$$

Since the fluctuations of the σ field are neglected in the large-N limit, the thermodynamic potential density depends only on the condensate $\langle\sigma\rangle$ and on the dressed pion propagator G_π. These are then determined by the first two equations of Eq. (3.72). Up to leading order in N the potential reads

$$\Omega[T;\phi,G_\pi] = U[\phi] + \frac{N}{2}\mathrm{Tr}\ln G_\pi^{-1} + \frac{N}{2}\mathrm{Tr}\left(\left(D_\pi^{-1} - G_\pi^{-1}\right)G_\pi\right) + N\lambda\left(\mathrm{Tr}G_\pi\right)^2, \tag{3.78}$$

with

$$U[\phi] = \frac{N}{4}\left(\frac{m^2}{2}\phi^2 + \frac{\lambda}{4}\phi^4 - H\phi\right). \tag{3.79}$$

The Dyson equation in this approximation yields

$$G_\pi^{-1}(q,n) = D_\pi^{-1}(q,n) + \Sigma_\pi(q,n) = q^2 + \omega_n^2 + m^2 + \lambda\phi^2 + 4\lambda\mathrm{Tr}G_\pi. \tag{3.80}$$

This is a self-consistent equation for the self-energy or equivalently for the renormalized pion mass. This is readily seen by rewriting the propagator in the compact form

$$G_\pi(q,n) = \left(q^2 + \omega_n^2 + M_\pi^2\right)^{-1}, \tag{3.81}$$

where the pion mass M_π is a solution of the equation

$$M_\pi^2 = m^2 + \lambda\phi^2 + 4\lambda\mathrm{Tr}G_\pi(M_\pi). \tag{3.82}$$

The boson loop integral $\mathrm{Tr}\,G_\pi$ can conveniently be expressed in terms of the logarithmic term in Eq. (3.78),

$$\begin{aligned}
\mathrm{Tr}(G_\pi) &= \frac{\partial}{\partial M_\pi^2}\mathrm{Tr}\ln(G_\pi^{-1}). \\
&= \frac{\partial}{\partial M_\pi^2} T\sum_n \int \frac{d^3q}{(2\pi)^3}\ln\left(q^2 + (2n\pi T)^2 + M_\pi^2\right) \\
&= \frac{\partial}{\partial M_\pi^2}\int \frac{d^3q}{(2\pi)^3}\left(\sqrt{q^2+M_\pi^2} + 2T\ln\left(1 - e^{-\sqrt{q^2+M_\pi^2}/T}\right)\right).
\end{aligned} \tag{3.83}$$

The first term is the UV divergent vacuum contribution, while the second term is the finite temperature contribution. Using dimensional regularization, we retain only the finite part of the vacuum integral, following [113, 128–130]. The renormalized vacuum contribution is then given by

$$\int \frac{d^3q}{(2\pi)^3}\frac{1}{2\sqrt{q^2+M_\pi^2}} \to \frac{1}{(4\pi)^2}\left(M_\pi^2\ln\frac{M_\pi^2}{M^2} - M_\pi^2 + M^2\right), \tag{3.84}$$

where M is an arbitrary renormalization scale. We choose $M = m_\pi = 138\,\mathrm{MeV}$, which simplifies the formulas somewhat.

Stationarity of the functional given in Eq. (3.78) yields hence the following system of equations for the renormalized pion mass M_π and the order parameter ϕ,

$$\begin{aligned} H &= M_\pi^2 \phi, \\ M_\pi^2 &= m^2 + \lambda\phi^2 + 4\lambda \mathrm{Tr} G_\pi. \end{aligned} \tag{3.85}$$

The model parameters λ, m^2 and H are chosen so as to reproduce the vacuum pion and sigma mass, as well as the pion decay constant. These conditions lead to the following constraints [113]:

$$\begin{aligned} &H = m_\pi^2 f_\pi, \qquad \lambda = \frac{m_\sigma^2 - m_\pi^2}{2 f_\pi^2}, \\ &m^2 = -\frac{m_\sigma^2 - 3m_\pi^2}{2} - \frac{\lambda}{4\pi^2}\left(m_\pi^2 \ln\frac{m_\pi^2}{M^2} - m_\pi^2 + M^2 \right) = -\frac{m_\sigma^2 - 3m_\pi^2}{2}, \end{aligned} \tag{3.86}$$

where in the last equality we used $M = m_\pi$. To derive the magnetic equation of state for this model, we again apply the high temperature expansion [122].

3.5.1 The magnetic equation of state of the LS model

Near the critical point, i.e. where $H \approx 0$, $\phi \approx 0$ and the pion mass $M_\pi \approx 0$, we can expand $\mathrm{Tr}(G_\pi)$ in powers of M_π / T by using the high temperature expansion,

$$\mathrm{Tr}(G_\pi) = \left(\frac{T^2}{12} + \frac{M^2}{16\pi^2} \right) - \frac{T}{4\pi} M_\pi + \frac{\ln\left(\frac{4\pi T}{M}\right) - \gamma_E}{8\pi^2} M_\pi^2 + \mathcal{O}\left(M_\pi^4\right). \tag{3.87}$$

Here γ_E is the Euler-Mascheroni constant.

By substituting the leading term in Eq. (3.87) into the gap equation, Eq. (3.85), one finds the critical temperature for the second order transition where $M_\pi = \phi = 0$,

$$m^2 + 4\lambda\left(\frac{T_c^2}{12} + \frac{M^2}{16\pi^2} \right) = 0 \rightarrow T_c = \sqrt{3} f_\pi^{ch}, \tag{3.88}$$

and

$$f_\pi^{ch} = f_\pi \left(\frac{m_\sigma^2 - 3m_\pi^2}{m_\sigma^2 - m_\pi^2} - \frac{1}{4\pi^2} \frac{m_\pi^2}{f_\pi^2} \right)^{1/2} \tag{3.89}$$

is the pion decay constant in the chiral limit [113]. In Eq. (3.89) we have set the renormalization scale to $M = m_\pi$. Using Eq. (3.85) we also find that for $H = 0$ and $M_\pi = 0$ the order parameter in the broken phase is given by

$$\phi = \sqrt{\frac{T_c^2 - T^2}{3}}. \tag{3.90}$$

Thus, near the critical point the order parameter scales as $\phi \sim (T_c - T)^{1/2} \sim (-t)^{1/2}$, with the critical exponent $\beta = 1/2$.

In order to obtain the exponent δ and the magnetic equation equation of state, we retain only the leading (linear) term in M_π in the second equation in Eq. (3.85). This leads to the system of equations

$$
\begin{aligned}
H &= M_\pi^2 \phi, \\
0 &= \lambda \left(\frac{T_c^2 - T^2}{3} - \phi^2 + \frac{T}{\pi} M_\pi \right).
\end{aligned}
\tag{3.91}
$$

Consequently, at $T = T_c$, we find

$$
\phi \sim H^{1/5}, \quad \text{and} \quad M_\pi \sim H^{2/5}. \tag{3.92}
$$

Thus, we find the critical exponent $\delta = 5$, as in the spherical model in three spatial dimension [118, 131]. We note that in four dimensions, the model yields $\beta = 1/2$ and $\delta = 3$, as in the mean-field case.

We are now ready to derive the magnetic equation of state, including the leading order scaling violating term. By eliminating the pion mass in Eq. (3.85) and using the high temperature expansion of the one-loop self-energy given in Eq. (3.87), one arrives at the gap equation

$$
\frac{T_c}{\pi}(1+t)\left(\frac{H}{\phi}\right)^{1/2} = \phi^2 + \frac{T_c^2}{3}(2t + t^2) + \frac{3\,\alpha}{4\,\pi^2}\frac{H}{\phi}, \tag{3.93}
$$

which is valid near the critical point, where t, H and ϕ are small. Here we introduced the short-hand notation

$$
\alpha = \frac{2}{3}\left[\ln\left(\frac{4\pi T_c}{M}\right) - \gamma_E \right] - \frac{4\,\pi^2}{3\,\lambda} \tag{3.94}
$$

and neglected the temperature dependence of the logarithm, which yields only terms of higher order in the scaling violating field. In analogy with Eqs. (3.2) and (3.4), we introduce the scaling fields z, x and $\bar{h}$ by means of

$$
H = \bar{h}\, h_0 H_0, \qquad t = z\, t_0 \bar{h}^{2/5}, \qquad \phi = x\, \phi_0 \bar{h}^{1/5}. \tag{3.95}
$$

The constants h_0 and t_0 are determined by the normalization conditions

$$
x(z=0) = 1, \qquad \lim_{z \to -\infty} x(z)/(-z)^\beta = 1, \tag{3.96}
$$

which are equivalent to Eq. (3.6). One finds

$$
h_0 = \frac{\phi_0^5\, \pi^2}{H_0\, T_c^2}, \qquad t_0 = \frac{3\,\phi_0^2}{2\,T_c^2}, \tag{3.97}
$$

which depend explicitly on the normalization scale ϕ_0[4], while the ratio

$$
z_0 = \frac{h_0^{2/5}}{t_0} = \frac{2}{3}\left(\frac{\pi^4 T_c^6}{H_0^2}\right)^{1/5} \tag{3.98}
$$

depends, as expected, only on H_0.

---

[4] In the quark-meson model this normalization scale was denoted by σ_0. The value for ϕ_0 will be set to f_π just as in the quark-meson model.

The gap equation, expressed in terms of the scaling variables, is now obtained by squaring Eq. (3.93) and consistently retaining terms up to order $\bar{h}^{2/5}$,

$$\left[x(x^2+z)^2-1\right]+\bar{h}^{2/5}\,t_0\left[(x^5-1+\alpha)(x^2+z)\right]=0. \tag{3.99}$$

In the limit $h \to 0$, only the first term in square brackets in Eq. (3.99) survives. This yields the universal scaling magnetic equation of state for the $O(N)$ linear sigma model in the $N \to \infty$ limit. More generally, for nonzero $\bar{h}$, the solution of Eq. (3.99) yields the magnetic equation of state, including the leading scaling violation.

The subleading term in Eq. (3.99) is not unique, since it may be modified by using the leading order (scaling) magnetic equation of state. The form given here was obtained by eliminating terms with noninteger powers of x as well as those involving higher powers than linear in z. Another form of this term leads to a modified magnetic equation of state for nonzero $\bar{h}$. However, the difference is of higher order, i.e. at least of order $\bar{h}^{4/5}$. Clearly, other forms of the leading scaling violating term in Eq. (3.21) can be obtained in an analogous manner. We note that the nonuniqueness of the leading symmetry breaking term does not affect the location of possible crossing points, discussed in Sec. 3.2.

3.6 Model dependence of scaling properties of the order parameter

In the preceding sections we have computed the magnetic equation of state in two models analytically: in the Landau theory of phase transitions and in the large-N limit of the $O(N)$ sigma model. Furthermore, we discussed in terms of the FRG treatment of the QM model how it can be numerically obtained in a theory. To assess the role of the gluon background in QCD, here we show results calculated in the PQM model as well, using mean-field approximation. This approximation was introduced in Sec. 2.2. Near the critical point, the thermodynamic potential is a polynomial in the order parameter σ, as in Eq. (3.12), with coefficients that can be extracted from Eq. (2.40) using the high temperature expansion [123]. In this case, however, the coefficients of the potential depend on the expectation value of the Polyakov loop and cannot be obtained in closed form. Thus, for the PQM model, the critical temperature, the coefficients of the Landau potential and the magnetic equation of state are computed numerically.

In the mean-field treatment of the QM and PQM models the scaling functions, $f_G(z)$, coincide and are given as a function of z by the solution of the gap equation

$$x(x^2+z)=1. \tag{3.100}$$

The corresponding equation in the $O(N)$ linear sigma model in the large-N limit differs from Eq. (3.100), and reads

$$x(x^2+z)^2=1. \tag{3.101}$$

In the FRG treatment of the QM model, the scaling function is not known analytically and is obtained numerically. In Fig. 3.9 we show the scaling functions, given by the solutions $x=f_G(z)$ of Eqs. (3.100) and (3.101). In the broken phase the universal curves are close to each other, while in the restored phase, they differ considerably. On a qualitative level, this behavior can be understood by considering the structure of the magnetic equation of state in the asymptotic regions $z \to \pm\infty$. For large negative z, the scaling function $f_G(z)$ is of the form $(-z)^{\beta}$, whereas for positive z it asymptotically approaches $z^{-\gamma}$. Since in both models the critical exponent $\beta = 1/2$, the two universal curves are very similar for $z<0$. On the other hand, $\gamma=1$ in the mean-field QM and PQM models and $\gamma=2$ in the large-N linear sigma model. This difference is clearly reflected in the universal scaling function in the restored phase, i.e. for $z>0$.

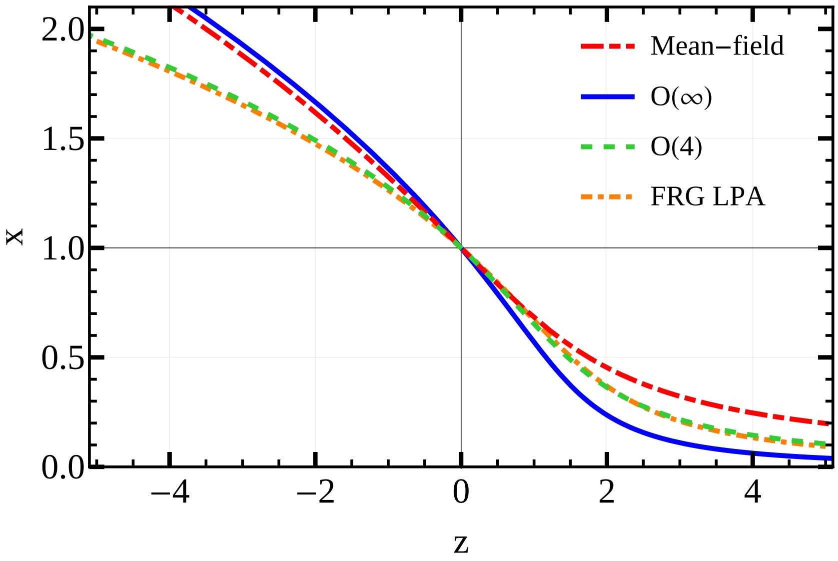

Figure 3.9.: The scaling function of the order parameter in mean-field models, the $O(N)$ linear sigma model in the $N \to \infty$ limit, and in the $O(4)$ universality class.

For comparison, the scaling function of the $O(4)$ universality class obtained in lattice simulations [132] is also shown. There are clear differences between the model results and the $O(4)$ universality class. Again, the characteristics can be understood in terms of the values of the γ and β exponents. Since the QM and PQM models belong to the $O(4)$ universality class [133], differences between the scaling properties of these models and the $O(4)$ universality class, seen in Fig. 3.9, disappear when the effect of fluctuations is properly included in the thermodynamic potential using the FRG. This is illustrated by showing the scaling function obtained in the quark-meson model using FRG. It is notable that the $O(4)$ scaling function is very well captured in the FRG calculation. This is a consequence of the small value of the critical exponent η in the $O(4)$ universality class and justifies the use of the local potential approximation in this system.

Recent LQCD studies [109] of the chiral phase transition with (2+1) flavors indicate that the scaling violation seen in the QCD magnetic equation of state remains moderate up to physical values of the light quarks masses. Moreover, the nonuniversal parameters h_0 and t_0 for QCD were determined. In this section we assess the scaling violation in the models presented above, and compare the nonuniversal parameters extracted in the models with the lattice QCD results. The numerical results presented in this section are based on the full thermodynamic potentials (Eqs. (3.38), (2.40) and (3.78)) without invoking the high-temperature expansion.

In Figs. 3.10 and 3.11 we show the scaling behavior of the order parameter for several values of the symmetry breaking term $H/H_0 = (m_\pi/m_{\pi\ phys})^2$. The leading-order corrections to the scaling functions of the QM, PQM models in the mean-field approximation and the corrections to the $O(N)$ sigma model in the large-N limit were discussed in the preceding section.

A comparison of the (mean-field) scaling properties of the order parameter in the QM and PQM models, shown in Fig. 3.10, shows that the coupling of quarks to the Polyakov loop enhances the scaling violation. This is particularly apparent in the broken phase, where the Polyakov-loop expectation value differs appreciably from unity. Nevertheless, up to the physical pion mass, both models are still in the scaling regime of the underlying second-order phase transition, as also found in LQCD.

In the scaling plot of the QM model, shown in Fig. 3.10, there are two distinct points, where the curves for different values of the pion mass cross. This behavior was anticipated in our discussion of Landau theory in Sec. 3.2. By substituting the coefficients of the Landau thermo-

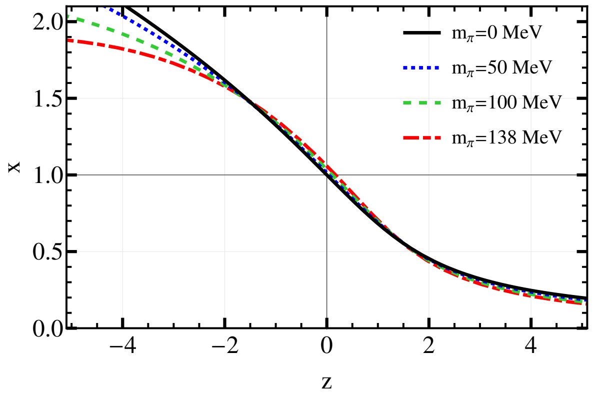

Figure 3.10.: The magnetic equation of state for the QM (left) and PQM (right) models. The black line corresponds to the universal scaling curve, which coincides in these two models.In both models the sigma mass was fixed to $m_\sigma = 400$ MeV, whereas the constituent quark mass in the vacuum was set to $m_q = 300$ MeV.

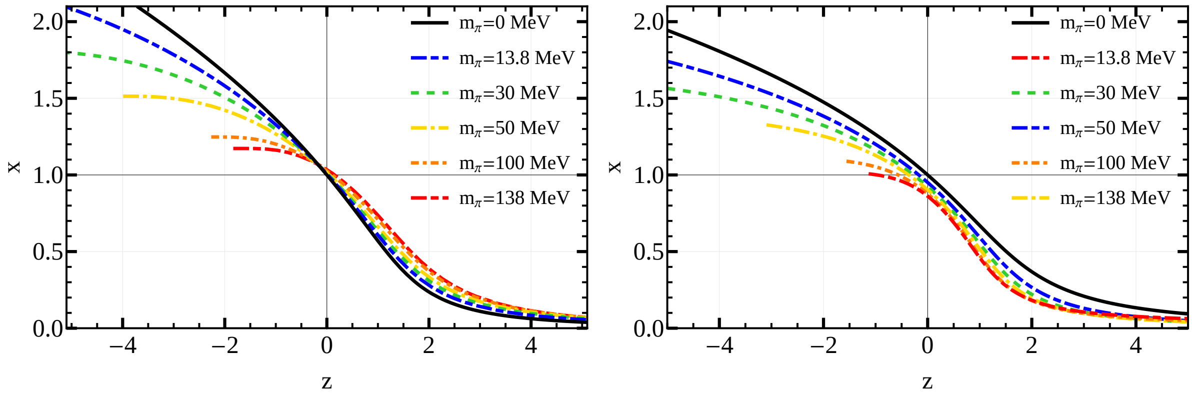

Figure 3.11.: The magnetic equation of state for the $O(N)$ linear sigma model in the $N \to \infty$ limit (left), and in the quark-meson model using FRG (right). The black lines correspond to the universal scaling curve of the $O(N = \infty)$ and $O(4)$ universality classes, respectively. The end points of the curves at negative z values correspond to $T = 0$. In the LS model calculation, $m_\sigma = 400$ MeV was chosen, whereas in the FRG we used the model parameters given in Eq. (D.6).

dynamic potential obtained in the QM model, given in Eq. (3.40), into Eqs. (3.23,3.24), we obtain the following (z, x) coordinates of the crossing points

$$C_1 = \{-1.31, 1.42\}, \qquad C_2 = \{1.50, 0.55\}, \tag{3.102}$$

in agreement with the numerical results shown in Fig. 3.10. Obviously, the crossing points are independent of the pion mass only as long as the subleading scaling violating terms are negligible.

In the PQM model, shown in the right panel of Fig. 3.10, the location of the crossing points depends on the strength of the symmetry breaking field for values of the pion mass below the physical one. This indicates that in the PQM model, the convergence of the expansion in powers of the symmetry breaking field in Eq. (3.21) is worse than in the QM model. The above behavior can be linked to the coupling of quarks with the Polyakov loop. In the low-temperature phase, the quark fluctuations are suppressed by the Polyakov loop, which results in a weaker dependence of the chiral condensate on the temperature. Consequently, close to the critical

Model	H_0	σ_0	t_0	h_0	z_0
QM $m_\sigma = 400\,\mathrm{MeV}$	$m_\pi^2 f_\pi$	f_π	0.34	6.99	10.64
QM $m_\sigma = 800\,\mathrm{MeV}$	$m_\pi^2 f_\pi$	f_π	0.30	13.57	19.10
PQM $m_\sigma = 400\,\mathrm{MeV}$	$m_\pi^2 f_\pi$	f_π	0.073	5.26	41.50
LS $m_\sigma = 400\,\mathrm{MeV}$	$m_\pi^2 f_\pi$	f_π	0.74	2.22	1.85
LS $m_\sigma = 800\,\mathrm{MeV}$	$m_\pi^2 f_\pi$	f_π	0.57	1.69	2.18
QM FRG $m_\sigma = 650\,\mathrm{MeV}$	$m_\pi^2 f_\pi$	f_π	0.50	1.19	2.19
Lattice (p4) $N_\tau = 4$ [107]	$\frac{m_\pi^2 f_\pi m_s}{m_l}$	$\frac{T_c^4 f_\pi}{m_s \left\langle \bar{\psi}\psi \right\rangle_l^{T=0}}$	0.00407	0.00295	53.92
Lattice (p4) $N_\tau = 8$ [107]	$\frac{m_\pi^2 f_\pi m_s}{m_l}$	$\frac{T_c^4 f_\pi}{m_s \left\langle \bar{\psi}\psi \right\rangle_l^{T=0}}$	0.00271	0.00048	27.27

Table 3.1.: Comparison of the nonuniversal constants t_0, h_0 and z_0 in different theories. The normalization of the order parameter σ_0 and the external field H_0 differs, thus the t_0 and h_0 values cannot be directly compared between different models. The z_0 column contains converted values to our normalization convention, thus the results of different models can be directly compared.

point, the chiral restoration as a function of temperature in the PQM model is sharper than in the QM model. This implies, that the size of the scaling window is reduced, and that deviations from scaling are larger in the PQM than in the QM model.

The difference in strength of the scaling violation found in the QM and PQM models is even more pronounced in the $O(N)$ sigma model and in the FRG calculation of the QM model. As shown in Fig. 3.11, the quark-meson model using the FRG and the $O(N)$ model exhibit stronger deviations from the universal scaling curve than the QM and PQM models in the mean-field approximation for the corresponding strength of the symmetry breaking field. The scaling of the order parameter in these calculations is preserved only for a very weak external field and the deviations from the universal line are substantial for the physical value of the pion mass. The qualitative differences in the universal scaling curves and in the strength of the scaling violation indicate that fluctuations of the meson fields, not accounted for in the mean-field models, play an important rôle in the determination of the magnetic equation of state.

In spite of the fact that deviations from the universal scaling curve are large in the $O(N)$ sigma model, the lines with different pion masses cross at a unique point. This suggests that close to the critical temperature, the subleading corrections in the magnetic equation of state are negligible up to the physical value of the pion mass. Applying the procedure discussed in the previous section, one finds that this crossing point appear at $z = -0.15$, $x = 1.06$, in agreement with the numerical results shown in Fig. 3.11. For the FRG calculation we do not find a crossing point.

The strong violation of scaling obtained with mesonic fluctuations is consistent with previous studies within the FRG approach [134]. However, in contrast to the FRG results of [134], we do not observe the approximate scaling of the order parameter for pion masses ~ 100 MeV to a nonuniversal line for $z > -1$.

3.6.1 Scaling violation and nonuniversal parameters

In previous sections we studied the leading-order corrections to the magnetic equation of state and scaling functions in the mean-field approximation to the QM and PQM models. Clearly such a calculation cannot reproduce the universal properties of the $O(4)$ criticality expected in QCD (in three dimensions). However, this can be achieved by systematically including fluctuations of the meson fields e.g. within the FRG approach. In this context we note that the mean-field

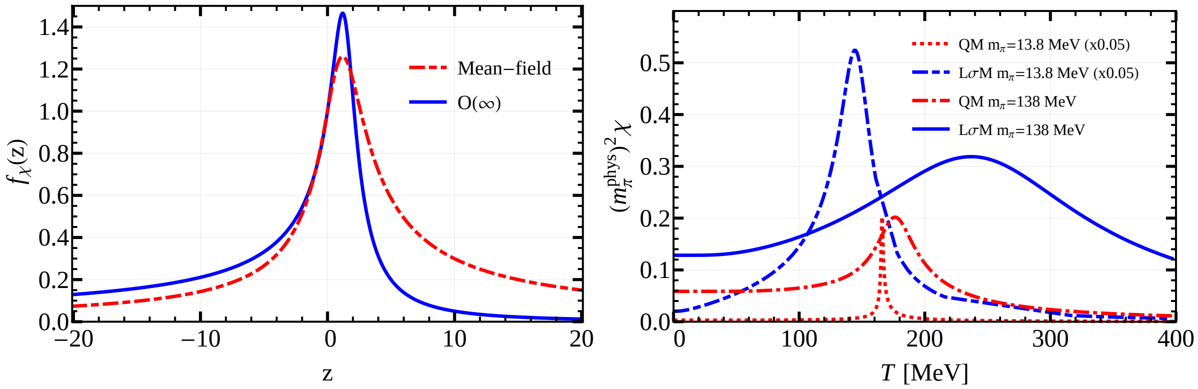

Figure 3.12.: Left figure: The universal scaling part of the chiral susceptibility in the QM model calculated within the mean-field dynamics and in the $O(N)$ LS model obtained in the $N \to \infty$ limit within high temperature expansion. Right figure: The chiral susceptibilities in the LS model in the $N \to \infty$ limit and in the QM model under mean-field approximation calculated at physical and at ten times lower pion mass.

approximation does reproduce the universal properties of the $O(4)$ model in four dimensions. The difference between the mean-field approach and $O(4)$, or equivalently between $O(4)$ in three and four dimensions, is illustrated in Fig. 3.9 on the level of the scaling functions. The scaling function for the $O(N \to \infty)$ sigma model, which belongs to another universality class in three dimensions, is also shown in Fig. 3.9. In spite of these differences, the mean-field models and the $(1/N)$ expansion of the $O(N)$ model allow us to explore the scaling violation in a transparent framework and to illustrate general features of the magnetic equation of state, which are expected to be independent of the universality class.

The differences in the strength of the scaling violation seen in Figs. 3.10 and 3.11 are connected with very different values of the nonuniversal parameters t_0, h_0 and z_0. This is seen in Table 3.1, where their values in the present model calculations, as well as in $(2+1)$-flavor LQCD are summarized. In the mean-field QM model and $O(N = \infty)$ linear sigma model, explicit expressions for h_0 and t_0 are given in Eqs. (3.16) and (3.97). In the mean-field PQM model these constants were obtained numerically, by fitting the order parameter to the asymptotic scaling laws Eq. (3.6). The calculations were done numerically in the FRG treatment of the QM model as well.

Clearly, the values of these nonuniversal parameters are not only model dependent, but are also influenced by the normalization convention of the external field and the order parameter. The constant z_0, however, does not depend on the choice of the normalization of the order parameter. Thus, the values of z_0 given in Table 3.1 can be directly compared between different models, since they were recomputed with the same normalization of the external field.

From Table 3.1 it is clear that the z_0 values obtained in the mean-field models are roughly compatible with the lattice results. On the other hand, models with bosonic fluctuations yield a much smaller z_0. One may worry that a comparison of a 2-flavor model calculation with $(2+1)$-flavor lattice QCD results could be misleading. However, we note that such a comparison makes sense, since the strange quark remains massive at the chiral transition and hence contributes only to the regular part of the free energy. This leads to small reduction of the chiral transition temperature, but has only a minor effect on the critical properties. Thus, for the purposes of this exploratory study, the neglect of the strange quark is reasonable.

As discussed in Sec. 3.1, the nonuniversal parameter z_0 influences the critical properties of relevant observables in the crossover regime. In particular, as shown in Eqs. (3.8) and (3.9),

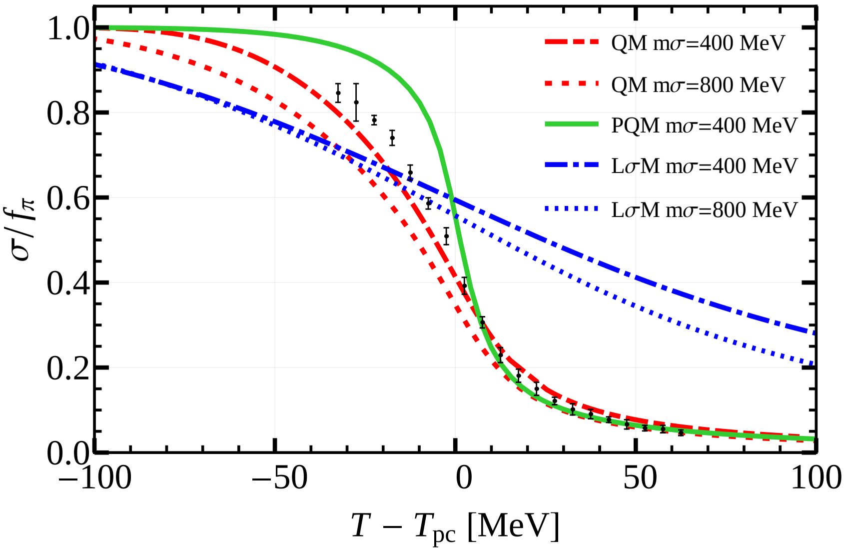

Figure 3.13.: The chiral order parameters in the QM and LS models calculated with different inputs for the vacuum sigma mass. The data points are lattice results from Ref. [27]. The pseudocritical temperature T_{pc} for these data is taken as the inflection point of the order parameter.

the constant z_0 determines the width of the transition region and the peak position of the order parameter susceptibility χ. In Fig. 3.12 we show the chiral susceptibility, computed in the QM and in $O(N \to \infty)$ linear sigma models. The left panel shows the universal part of the chiral susceptibility, whereas the right one depicts the temperature dependence of χ for $m_\pi/m_{\pi\,\rm phys} = 0.1$ and 1. Although the scaling functions of these models correspond to different universality classes, they are quantitatively rather similar. This, however is not the case for $\chi(T, m_\pi)$, since owing to the difference in the values of z_0, the crossover region in the LS model is considerably wider and the shift in the pseudocritical temperature with increasing pion mass is larger than in the QM model.

Moreover, due to comparable values of z_0 in the mean-field models and in LQCD, we expect that the melting of the chiral condensate in LQCD is better described by the mean-field QM and PQM models than by the LS model. This is indeed the case, as seen in Fig. 3.13, where the LQCD data is compared to model results. Models where bosonic fluctuations are included, such as the LS model in the $N \to \infty$ limit and the QM model in FRG, yield a much smaller value of z_0 than LQCD calculations. Hence, the reduction of the chiral condensate at the crossover transition is much smoother than in LQCD. Such a broadening of the transition region, when meson fluctuations are included, was observed also in the QM and PQM model mean-field and FRG calculations of Ref. [46].

By comparing different model results obtained in the present studies, together with previous FRG findings in the PQM model and LQCD results, we can confirm the rôle of the parameter z_0, which, using Eq. (3.9), determines the width of the transition in physical units. Again, this correlation is independent of the universality class, modulo minor variations in z_p. Thus, theories with a large z_0, roughly comparable with the lattice results, exhibit a relatively narrow transition region, as found in LQCD. This is the case for the QM and, in particular, for the PQM models in the mean-field approximation. On the other hand, theories with a small value of z_0, like the QM model with mesonic fluctuations included as well as the $O(N)$ sigma model at large N, exhibit a much smoother transition. Consequently, a viable effective model for the critical chiral dynamics of QCD should exhibit a value for z_0 comparable to that obtained in LQCD.

Moreover, we find that the scaling window depends on the parameter h_0 and on the nonsingular background, which in the Landau model, to leading order, is determined by the sixth-order coupling c_0. Thus, we conclude that in a given model the scaling window can be tuned to agree with lattice QCD by varying the nonuniversal parameter h_0 and the strength of the effective sixth-order coupling.

We note that adjusting model parameters to lattice QCD results for certain nonuniversal quantities does not guarantee that other nonuniversal quantities are reproduced by the model. However, for modeling the effect of critical fluctuations at the chiral transition, the width of the transition region and the size of the scaling window are, besides the universality class, the most important criteria for discriminating between models. Our study indicates how effective models can be tuned so that these key quantities are reproduced.

Chapter 4

Baryon-number cumulants at finite temperature and density

In the previous chapter we discussed scaling of the order parameter in different models of QCD. While it is very important to study the scaling properties to better understand the phase transitions of strongly interacting matter, the quantities discussed in the previous chapter, like the size of the scaling window or the strength of the deviations from scaling, are not directly experimentally measurable quantities. Heavy-ion collisions are almost exclusively the only experimental tools to learn about the phase diagram of strongly interacting matter, hence it is of utmost importance to consider quantities that can simultaneously be calculated theoretically and be related to experimental observables in heavy-ion collisions. One set of such observables is given by the fluctuations of conserved charges described by the cumulants of the conserved charge distributions [57–68].

Theoretically, as described in the introduction of Chapter 2, we work in the grand canonical ensemble, in which the system under study interacts with an infinitely large heat and particle bath. This way, the number of charges in the system, albeit globally conserved, will not be constant, but rather fluctuate about their expectation values. The latter are described in terms of the conjugate variables, the chemical potentials. There is a corresponding chemical potential for each conserved charge. If the system under consideration is large enough, calculations performed in the canonical and grand canonical ensembles converge to a common result. The grand canonical ensemble is much easier to treat, since the global charge conservation is lifted.

In the grand canonical ensemble, using different numerical techniques, the pressure is determined as a function of the temperature and the chemical potentials. In case of strongly interacting matter, the relevant conserved charges are the baryon number, B, the electric charge, Q, and the strangeness, S. The pressure is a function of the temperature and the related chemical potentials,

$$P = P(T, \mu_B, \mu_Q, \mu_S). \tag{4.1}$$

Given the pressure, one can compute the expectation values of the conserved charges as well as their fluctuations. Before going into the details of the calculation in the next section, we briefly discuss how to probe these charge distributions experimentally.

In heavy-ion collision experiments, among many other observables, the yields of outgoing particles are measured. In an ideal experimental scenario, all particles originating from the collision could be detected and precisely identified. Even in such an ideal experiment, precise measurement of conserved charge fluctuations would not be a trivial task. Due to conservation laws, the total number of charges coming from the collision are determined by that of the initial state. Hence, if one is interested in the fluctuations of these charges, one has to consider only a selection, a subset of the outgoing particles, and calculate the charge distributions of that subset. This in practice is performed by applying phase space cuts, namely only particles in a certain rapidity and transverse momentum window are considered. This has to be performed with special care. If the cuts are too loose, effects of the global conservation laws prevail and fluctuations are suppressed. However, if the cuts are too tight, only few effectively uncorrelated particles are detected. Hence, in this case a Poisson distribution is expected and the information about the genuine distribution is completely lost.

Since a real experiment is far from ideal, further complications arise. Not all particles are detected due to finite acceptance and reconstruction efficiency. In practice, since neutrons are chargeless, and hence difficult to detect, approximately 50% of the baryons are not seen in the experiment. Therefore, the distribution of net proton number is measured, and taken as a proxy for net baryon number distribution. Furthermore, not all protons are detected, since detectors rarely have 4π acceptance, and as mentioned, not all tracks are reconstructed successfully. This complicates the picture further.

We note here that in contrast to the conservation laws, which reduce fluctuations of the charges, there are effects that produce spurious fluctuations. Such an effect is caused for example by volume fluctuations [135–138]. Experimentally the volume cannot be controlled. Instead, it is usual to sort the events in bins based on the number of charged particles in the forward detector. Since a certain binning is involved, the total charged particle number will fluctuate from event to event. Furthermore, a fixed number of charged particles also corresponds to a range of impact parameters, and hence to a range of system volumes. These two effects will cause the volume to fluctuate and acquire a distribution at each centrality bin. The volume fluctuations modify the distribution of conserved charges.

4.1 Moments and cumulants

Mathematically speaking, the pressure in the grand canonical ensemble is essentially the *cumulant-generating function* of the conserved charge distributions. In this brief section we review how the cumulant-generating function of a distribution is defined and what one can learn about fluctuations using it.

Let us consider an n dimensional random variable, $\mathbf{X}$ and calculate the moments of its distribution. First, let us define the *moment-generating function* as a function of an n-vector, $\hat{\mu}$, which is the conjugate variable to X. The moment-generating function is defined as

$$M_X(\hat{\mu}) = \left\langle e^{\hat{\mu}\mathbf{X}} \right\rangle = \sum_{\mathbf{X}} p(\mathbf{X}) e^{\hat{\mu}\mathbf{X}}, \tag{4.2}$$

where the angle brackets stand for expectation value, and $p(\mathbf{X})$ is the probability of the variable taking the value $\mathbf{X}$. As the name suggests, the moment-generating function generates different moments of the distribution of the random variable $\mathbf{X}$,

$$\left.\frac{\partial^{i_1}}{\partial\hat{\mu}_1^{i_1}}\frac{\partial^{i_2}}{\partial\hat{\mu}_2^{i_2}}\cdots\frac{\partial^{i_n}}{\partial\hat{\mu}_n^{i_n}} M_X(\hat{\mu})\right|_{\hat{\mu}=0} = \sum_{\mathbf{X}} p(\mathbf{X}) X_1^{i_1} X_2^{i_2}\ldots X_n^{i_n} = \left\langle X_1^{i_1} X_2^{i_2}\ldots X_n^{i_n}\right\rangle. \tag{4.3}$$

The *cumulant-generating function* is then defined as the logarithm of the moment-generating function,

$$K_X(\hat{\mu}) = \ln M_X(\hat{\mu}) = \ln \sum_{\mathbf{X}} p(\mathbf{X}) e^{\hat{\mu}\mathbf{X}}. \tag{4.4}$$

The cumulant-generating function generates the cumulants of the distribution, analogously to how the moment-generating functional generates the moments,

$$\left.\frac{\partial^{i_1}}{\partial\hat{\mu}_1^{i_1}}\frac{\partial^{i_2}}{\partial\hat{\mu}_2^{i_2}}\cdots\frac{\partial^{i_n}}{\partial\hat{\mu}_n^{i_n}} K_X(\hat{\mu})\right|_{\hat{\mu}=0} \equiv c^{i_1,i_2,\ldots,i_n}. \tag{4.5}$$

The cumulants and the moments of the distribution both describe all fluctuations of the system. They contain exactly the same information, one can be expressed in terms of the other. One advantage of using the cumulants over using moments is that if the system is large enough, cumulants are proportional to the system size, while the moments have a complicated volume dependence. To prove this, let us consider the distribution of the sum of two independent random variables of the same distribution. This is a system consisting of two subsystems, which do not interact with each other, hence it is effectively the multiplication of the system size by two. The moment-generating function for the distribution for the sum of the variables is given by

$$M_{X+Y}(\hat{\mu}) = \sum_{\mathbf{X},\mathbf{Y}} p(\mathbf{X})p(\mathbf{Y})e^{\hat{\mu}(\mathbf{X}+\mathbf{Y})} = (M_X(\hat{\mu}))^2, \tag{4.6}$$

whereas the cumulant-generating function is simply

$$K_{X+Y}(\hat{\mu}) = \ln(M_X(\hat{\mu})^2) = 2K_X(\hat{\mu}). \tag{4.7}$$

This has the direct consequence that all cumulants of the distribution of the sum are exactly twice the cumulants of the original distribution. Cumulants of independent systems add linearly. However, this is not true for the moments, where a more complicated behavior is expected, since the square of the original moment-generating function is to be differentiated. Hence, it is clearly favorable to use cumulants in systems where the system size is much larger than the correlation length, and thus a linear dependence on the system size is assumed. This is naturally fulfilled when the infinite volume limit is considered.

To finish this general discussion of cumulants and moments, let us consider a simple one dimensional variable, denoted by B, having the net baryon number in mind. Based on the definition of cumulants, c_i, and the moments, m_i, their relation can be simply determined, yielding

$$c_1 = m_1, \tag{4.8}$$

$$c_2 = m_2 - m_1^2, \tag{4.9}$$

$$c_3 = m_3 - 3m_2m_1 + m_1^3, \tag{4.10}$$

$$c_4 = m_4 - 4m_3m_1 - 3m_2^2 + 12m_2m_1^2 - 6m_1^4, \tag{4.11}$$

or inverted

$$m_1 = c_1, \tag{4.12}$$

$$m_2 = c_2 + c_1^2, \tag{4.13}$$

$$m_3 = c_3 + 3c_2c_1 + c_1^3, \tag{4.14}$$

$$m_4 = c_4 + 4c_3c_1 + 3c_2^2 + 6c_2c_1^2 + 1c_1^4. \tag{4.15}$$

By looking at Eqs. (4.13), (4.14) and (4.15) it is clear that the moments of the distribution cannot increase with system size with a single power law due to the mixing of cumulants with different power.

4.2 Fluctuations of conserved charges in strongly interacting matter

Now let us turn back to our discussion of strongly interacting matter and apply our findings. In QCD, the pressure is defined by,

$$P = \frac{T}{V}\ln\mathcal{Z}_{GC} = \frac{T}{V}\ln\sum_{conf} e^{-S_E+\beta(\mu_B B+\mu_Q Q+\mu_S S)}, \tag{4.16}$$

where $\sum_{conf}$ is a shorthand for the appropriate functional integrals over all fields involved. The moments of the charges are given by

$$\left\langle B^i Q^j S^k \right\rangle = \frac{\sum_{conf} B^i Q^j S^k e^{-S_E+\beta(\mu_B B+\mu_Q Q+\mu_S S)}}{\sum_{conf} e^{-S_E+\beta(\mu_B B+\mu_Q Q+\mu_S S)}}, \tag{4.17}$$

where the denominator accounts for the proper normalization of the probability. Comparing this formula to Eqs. (4.2), (4.3) and (4.4), we can identify $\frac{PV}{T}$ with the cumulant generating function of the conserved charge distributions. The related cumulants can be obtained by taking the appropriate number of derivatives with respect to the reduced chemical potentials,

$$\hat{\mu}_B = \beta\mu_B, \qquad \hat{\mu}_Q = \beta\mu_Q, \qquad \hat{\mu}_S = \beta\mu_S. \tag{4.18}$$

The cumulants of the conserved charge distributions are hence given by

$$c^{ijk}_{BQS} = \frac{\partial^i}{\partial\hat{\mu}^i_B}\frac{\partial^j}{\partial\hat{\mu}^j_Q}\frac{\partial^k}{\partial\hat{\mu}^k_S}\frac{PV}{T}. \tag{4.19}$$

Furthermore, since the calculations are customarily performed in the infinite volume limit, it is useful to define the susceptibilities of the conserved charges as

$$\chi^{ijk}_{BQS} = \frac{\partial^i}{\partial\hat{\mu}^i_B}\frac{\partial^j}{\partial\hat{\mu}^j_Q}\frac{\partial^k}{\partial\hat{\mu}^k_S}\frac{P}{T^4} = \frac{c^{ijk}_{BQS}}{VT^3}. \tag{4.20}$$

These definitions are in agreement with the earlier definitions provided in Chapter 2 for the baryon number susceptibilities and cumulants in the quark-meson model.

Experimentally, in heavy-ion collisions, the strongly interacting matter is always probed in a finite volume; hence cumulants are measured rather than susceptibilities. In theoretical calculations the system is often considered in infinite volume; hence susceptibilities are calculated. To be able to confront the theoretical calculations with experimental results, ratios of these quantities are considered, since there the difference between cumulants and susceptibilities cancel,

$$\frac{c^{ijk}_{BQS}}{c^{lmn}_{BQS}} = \frac{\chi^{ijk}_{BQS}}{\chi^{lmn}_{BQS}}. \tag{4.21}$$

In particular, this has the advantage that the leading dependence on volume, which is experimentally hard to determine precisely, cancels. This does not mean however, that these ratios are independent of the system size as this only holds in the infinite volume limit.

In this chapter we will continue with the calculation of the baryon number cumulants of strongly interacting matter in an infinite volume, and compare our results with the available experimental data of the STAR collaboration. In the following chapter we will quantify the effects of finite volume in the quark-meson model without the Polyakov loop, with special attention to the quark number susceptibilities.

In order to gain a qualitative understanding of the behavior of the baryon number cumulants, let us first consider two asymptotic limits. At low temperatures and densities strongly interacting matter is well described by the hadron resonance gas (HRG) model [55, 79–81] that, as the name suggests, describes QCD matter as a noninteracting gas of hadrons. Here, for simplicity, we consider the case that there are no hadrons carrying a baryon number larger than 1 and we put the chemical potentials other than that of the baryon number (i.e. of electric charge, strangeness, etc.) to zero. Then the pressure can be written as

$$P(T,\mu_B) = P_M(T) + P_B(T,\mu_B) + P_B(T,-\mu_B), \tag{4.22}$$

where P_M is the partial pressure of mesons and P_B is the partial pressure of baryons. The third term accounts for the contribution of antibaryons. We are not particularly interested in the partial pressure of mesons, since the mesons do not contribute to the chemical potential dependence of the pressure. The pressure of the baryons can be further divided into a sum of partial pressures of different baryon species, since in this model they do not interact with each other. A baryon species of mass m in the Boltzmann approximation will contribute to the pressure with

$$P_i = \frac{T}{V}\ln \mathcal{Z}_i = \frac{Tg_i}{V}\ln\sum_n \frac{1}{n!}\left(e^{\beta\mu_B}Z_i\right)^n = \frac{Tg_iZ_i}{V}e^{\beta\mu_B}, \tag{4.23}$$

$$Z_i = V\int \frac{d^3p}{(2\pi)^3}e^{-\beta\sqrt{m_i^2+p^2}}, \tag{4.24}$$

where g_i is the degeneracy factor (corresponding to spin, isospin, etc.) and m_i is the mass of the resonance. Here we assumed that the occupation numbers are small which is a good approximation at low temperatures and densities. The factor $1/n!$ takes into account the indistinguishability of particles. This formula neither agrees with Fermi statistics, nor with Bose statistics. For fermions, no particles may occupy the same state, hence the formula overshoots the real pressure. For bosons however the cases when multiple particles occupy the same state are overly suppressed, hence the formula undershoots the real pressure. In the limit of small occupation numbers, i.e. at small temperatures and densities, both the pressure of the Fermi gas and the Bose gas asymptotically agrees with this formula.

The contribution of baryons to the pressure without antibaryons is proportional to $\exp(\beta\mu_B)$. Since this is the only dependence on the chemical potential, all cumulants of the baryon number equal, and the distribution of baryons is a Poisson distribution. Summing up the contribution of each baryon resonance with the antibaryon resonances, which come with opposite baryon charge, the pressure yields

$$P(T,\mu_B) = P_M(T) + 2P_B(T,0)\cosh\left(\frac{\mu_B}{T}\right). \tag{4.25}$$

Hence, in this approximation, the baryon number susceptibilities are given by

$$\chi_B^{2j} = 2P_B(T,0)\cosh\left(\frac{\mu_B}{T}\right), \qquad \chi_B^{2j+1} = 2P_B(T,0)\sinh\left(\frac{\mu_B}{T}\right). \tag{4.26}$$

The ratios of the cumulant ratios accordingly are

$$\frac{\chi_B^{2j}}{\chi_B^{2k}} = \frac{\chi_B^{2j+1}}{\chi_B^{2k+1}} = 1, \qquad \frac{\chi_B^{2j+1}}{\chi_B^{2k}} = \tanh\left(\frac{\mu_B}{T}\right). \tag{4.27}$$

Such a simple structure of cumulant ratios is the property of the Skellam distribution. Both the distribution of baryon number and the distribution of antibaryon number are given by the Poisson distribution. Hence, the distribution of their difference, the net baryon number, are given per definition by the Skellam distribution[1].

---

[1] The Skellam distribution is by definition the distribution of the difference of two Poisson distributed variables

Now let us consider strongly interacting matter at high temperatures. It is expected that QCD at sufficiently high temperatures behaves as a noninteracting gas of quarks and gluons. This is supported by lattice QCD calculations, which show that at sufficiently high temperatures the Stefan-Boltzmann (SB) limit is reached [139]. To determine the baryon-number cumulants in the SB limit, let us consider a gas of noninteracting massless quarks of N_c color and N_f flavor. Gluons do not contribute to these observables in this approximation, since they are not influenced by the chemical potential and are assumed to be noninteracting. The easiest way to obtain the partition function and hence the pressure is to exploit that each momentum mode is occupied independently. Due to the lack of interactions, different momentum modes are not coupled to each other. Each momentum mode can be occupied either by 0 or 1 quarks per color, flavor and spin state in the Fermi statistics. Since the logarithms of the partition functions add up for independent subsystems, the pressure of quarks and antiquarks reads

$$\begin{aligned} P = \frac{T}{V}\ln \mathcal{Z} &= 2N_cN_fT\int\frac{d^3p}{(2\pi)^3}\left\{\ln\left(1+e^{\beta(\mu_q-p)}\right)+\ln\left(1+e^{-\beta(\mu_q+p)}\right)\right\} \\ &= \frac{N_cN_fT^4}{\pi^2}\int_0^\infty dx\, x^2\ln\left(1+2\cosh(\beta\mu_q)e^{-x}+e^{-2x}\right) \\ &= 2N_cN_f\left(\frac{7\pi^2T^4}{360}+\frac{\mu_q^2T^2}{12}+\frac{\mu_q^4}{24\pi^2}\right) = 2N_cN_f\left(\frac{7\pi^2T^4}{360}+\frac{\mu_B^2T^2}{108}+\frac{\mu_B^4}{1944\pi^2}\right). \end{aligned} \tag{4.28}$$

where $\mu_q = \mu_B/3$ is the quark chemical potential. The factor 2 in the first and last lines is the spin degeneracy factor. In the first line, the first logarithm yields the pressure of quarks, whereas the second one contributes to the pressure of antiquarks. The last line of Eq. (4.28) implies that baryon number cumulants of order 5 or higher all vanish. A few ratios of the nonvanishing cumulants are

$$\frac{\chi_B^1}{\chi_B^2} = \frac{\mu_B}{T}\frac{1+\frac{1}{9\pi^2}\frac{\mu_B^2}{T^2}}{1+\frac{1}{3\pi^2}\frac{\mu_B^2}{T^2}}, \qquad \frac{\chi_B^3}{\chi_B^1} = \frac{1}{\frac{3\pi^2}{2}+\frac{\mu_B^2}{2T^2}}, \qquad \frac{\chi_B^4}{\chi_B^2} = \frac{1}{\frac{3\pi^2}{2}+\frac{\mu_B^2}{6T^2}}. \tag{4.29}$$

Thus, for small μ_B/T values

$$\frac{\chi_B^1}{\chi_B^2} \approx \frac{\mu_B}{T}, \qquad \frac{\chi_B^3}{\chi_B^1} \approx \frac{\chi_B^4}{\chi_B^2} \approx \frac{2}{3\pi^2}. \tag{4.30}$$

With increasing chemical potential all of the above ratios are reduced from their leading order value. The latter two ratios in Eq. (4.30) satisfy the inequality

$$\frac{\chi_B^3}{\chi_B^1} < \frac{\chi_B^4}{\chi_B^2}, \tag{4.31}$$

which in this approximation holds for all densities.

Thus we obtained the expected behavior of cumulant ratios both at low and high temperatures. In particular, as the temperature is increased, the ratio χ_B^4/χ_B^2 is expected to decrease from unity at low temperatures to $2/(3\pi^2)$ at high temperatures. To study how this change occurs, we need a model that includes interactions. Therefore, we now turn to the PQM model introduced earlier that shares the chiral critical properties with QCD and yields a better approximation of the baryon number cumulants when the whole phase diagram is considered than the toy models discussed above. In particular, at moderate values of the chemical potential, the PQM model exhibits a chiral transition belonging to the $O(4)$ universality class [25, 140]. For larger values of μ, it reveals a $Z(2)$ critical endpoint, followed by a first order phase transition [140]. Consequently, the PQM model embodies the generic phase structure expected for QCD, with the universal $O(4)$ and $Z(2)$ criticality encoded in the scaling functions. Furthermore, due to the coupling of the quarks to the background gluon fields, the PQM model incorporates "statistical confinement", i.e., the suppression of quark and diquark degrees of freedom in the low temperature, chirally broken phase [37, 47]. Consequently, by studying fluctuations of conserved charges in the PQM model, one can explore the influence of chiral symmetry restoration and of "statistical confinement" on the cumulants in different sections of the chiral phase boundary. This study is of particular interest in the context of heavy-ion collisions, where cumulants of conserved charges are expected to provide a characteristic signature for the QCD phase boundary and for the conjectured critical endpoint [57–61, 64, 66].

The PQM model in the following will be studied in the FRG formalism using the Litim regulator with the help of the Chebyshev expansion technique. Repulsion due to the exchange of vector mesons will also be considered.

4.3 Criticality of net-baryon-number cumulants in the (T,μ) plane

Generalized susceptibilities of conserved charges, which are given by higher-order derivatives of the thermodynamic pressure with respect to the corresponding chemical potentials, may exhibit a nonmonotonic dependence on the thermodynamic parameters. This is particularly the case in the vicinity of phase boundary and the CEP. In the critical region of the chiral transition, the strength of the fluctuations and the sign of the susceptibilities are by and large determined by the singular part of the free energy, which is encoded in the universal scaling functions, common to QCD and the PQM model. Thus, generic structures of the susceptibilities and relations between them near the phase boundary, can also be studied in the PQM model. Of particular interest is the behavior of susceptibilities along the $O(4)$ crossover line, and their modification as the CEP is approached. In the model calculations, the position of the CEP depends on the strength of the vector interaction. Thus, by changing the vector coupling g_ω, one can assess the dependence of critical fluctuations in different sectors of the phase boundary on the location of the CEP.

For nonvanishing light-quark masses, the chiral symmetry is explicitly broken, which implies that at finite temperatures and moderate values of the baryon chemical potential, the system exhibits a chiral crossover transition. Thus, at small μ_q, the fluctuations of conserved charges remain finite. However, because QCD matter at the physical values of the u and d quark masses is within the critical region of the second order phase transition, the fluctuations are still influenced by $O(4)$ criticality [106–109, 141]. At physical quark masses, a genuine phase transition in QCD with the associated singular behavior of fluctuations is expected only at the conjectured CEP and along the line of the first-order phase transition.

To explore the phase diagram with net-baryon-number fluctuations, we need to know the qualitative dependence of the net-baryon-number cumulants on temperature and baryon chemical potential. In Fig. 4.1 we show the T-dependence at $\mu_q = 0$, and in Figs. 4.2 and 4.3, the contour plots in the (T,μ_q)-plane of ratios of net-baryon-number susceptibilities. In the following, we focus on the ratios

$$\chi_B^{n,m} = \frac{\chi_B^n(T,\mu_B)}{\chi_B^m(T,\mu_B)}, \tag{4.32}$$

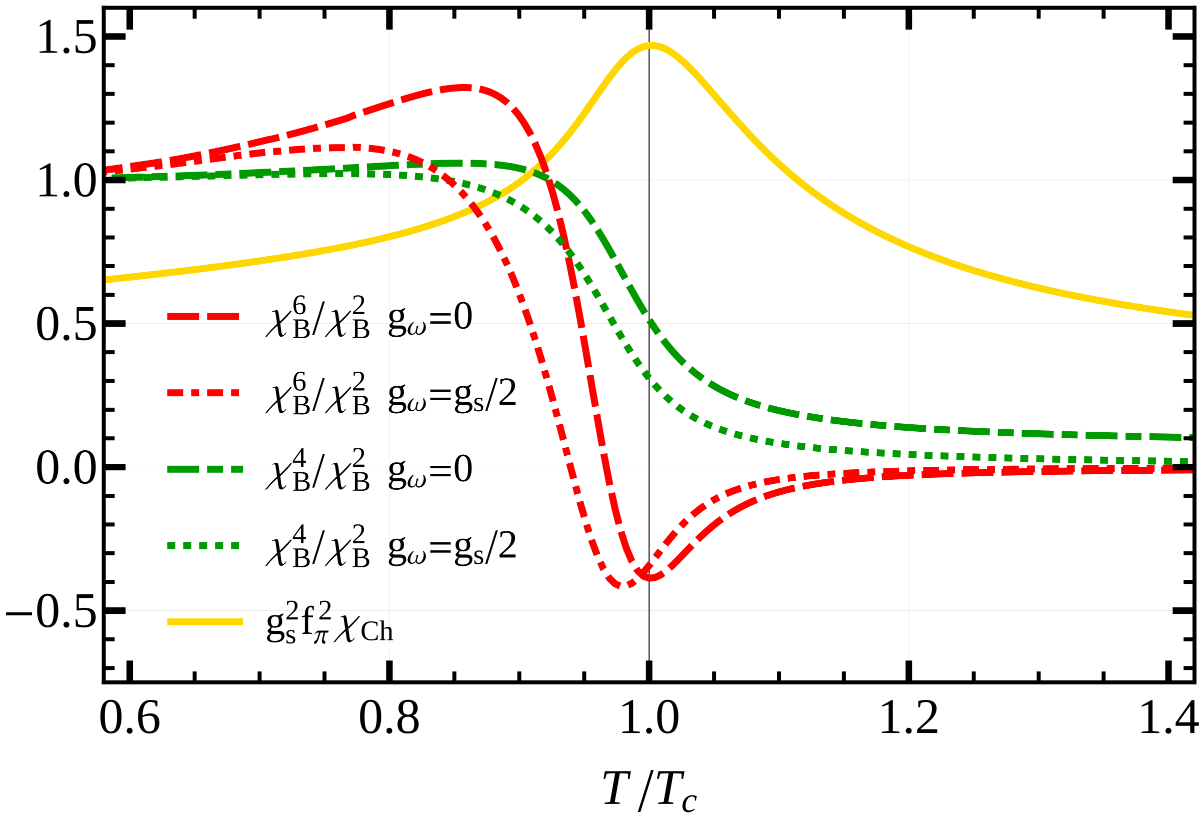

Figure 4.1.: The temperature dependence of ratios of net-baryon-number cumulants, χ_B^4/χ_B^2 and χ_B^6/χ_B^2 in the PQM model at vanishing net-baryon density for vanishing and nonzero vector coupling g_ω. Also shown is the chiral susceptibility, $\chi_{ch}(T)$. The vertical line indicates the location of the chiral crossover temperature.

paying special attention to

$$\chi_B^{1,2}(T,\mu_B) = \frac{M}{\sigma^2}, \qquad \chi_B^{3,1}(T,\mu_B) = \frac{S_B\sigma^3}{M}, \qquad \chi_B^{3,2}(T,\mu_B) = S_B\sigma, \qquad \chi_B^{4,2}(T,\mu_B) = \kappa\sigma^2, \tag{4.33}$$

where M is the mean, σ the variance, S_B the skewness and κ the kurtosis of the net-baryon-number distribution.

At vanishing chemical potential, all odd susceptibilities of net baryon number vanish, owing to the baryon-antibaryon symmetry. In addition, in the $O(4)$ universality class, the second and fourth order cumulants remain finite at the phase transition temperature at $\mu_q = 0$ even in the chiral limit, implying that only sixth and higher order susceptibilities diverge. Thus, for physical quark masses, only higher order cumulants, χ_B^n with $n > 4$, can exhibit $O(4)$ criticality at $\mu_q = 0$ [61]. A further consequence of the baryon-antibaryon symmetry is the equality of the ratios

$$\chi_B^{2m-1,2n-1} = \chi_B^{2m,2n} \tag{4.34}$$

for any integer m and $n \geq 1$ at $\mu_q = 0$. For $\chi_B^{3,1}$ $\chi_B^{4,2}$, the equality at small μ_q can be confirmed by a direct comparison of the right panel of Fig. 4.2 with the left panel of Fig. 4.3.

At finite net baryon density the singularity at the $O(4)$ line is stronger than at $\mu_q = 0$. Thus, in this case the third-order cumulant and all higher-order ones diverge at the critical line. The

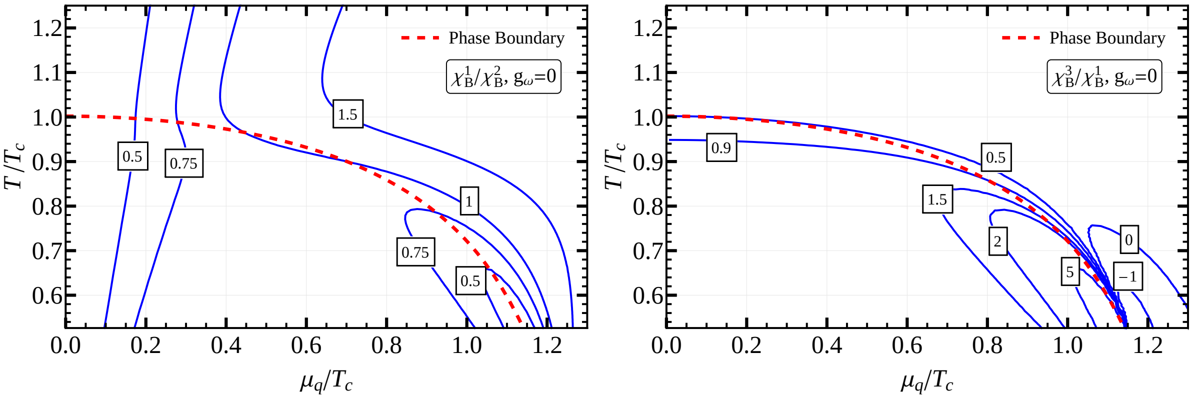

Figure 4.2.: Contour plots of the ratios χ_B^1/χ_B^2 and χ_B^3/χ_B^1 in the (T,μ)-plane, computed in the PQM model. The broken lines indicate the location of the chiral crossover phase boundary.

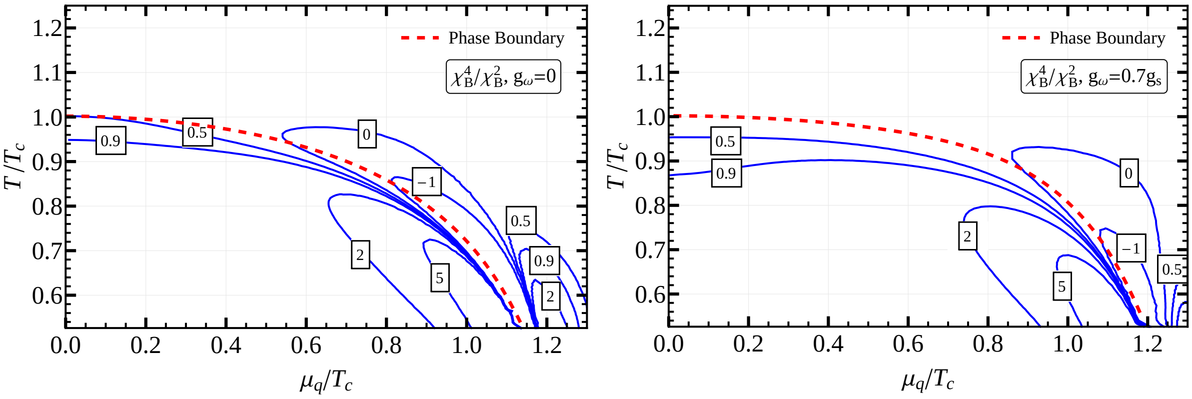

Figure 4.3.: Contour plots of the kurtosis ratio, χ_B^4/χ_B^2, in the (T,μ_q)-plane. The left-hand figure corresponds to PQM model results obtained with vanishing vector coupling $g_\omega = 0$, while the right-hand one shows results obtained with $g_\omega = 0.7 g_s$.

second order cumulant χ_B^2 remains finite, and diverges only at the tricritical point for vanishing quark masses, and at the CEP for nonzero quark masses.

In Fig. 4.1, results on the temperature dependence of several ratios $\chi_B^{n,m}$ of net-baryon-number susceptibilities are plotted at vanishing net-baryon density, together with the chiral susceptibility, χ_{ch}. The location of the maximum of the chiral susceptibility, χ_{ch}, defines the pseudocritical temperature, T_c. As shown in Fig. 4.1, the kurtosis $\kappa\sigma^2$ exhibits a rapid drop by approximately an order of magnitude at the phase boundary. This strong reduction of the kurtosis is attributed to the deconfinement transition, where the degrees of freedom carrying baryon number change from baryons to quarks [64, 65]. A qualitative understandning of this issue is obtained in the Boltzmann approximation, where the baryon contribution to the thermodynamic pressure is of the form $P_B(T,\mu_B) \simeq F(T)\cosh(B\mu_B/T)$. Here B is the baryon number of the relevant degrees of freedom and $F(T)$ a function of the corresponding excitation spectrum. At low temperatures, the degrees of freedom are baryons, with $B = \pm 1$, while at high temperatures they are quarks with $B = \pm 1/3$. Consequently, the kurtosis ratio, $\kappa\sigma^2 = \chi_B^4/\chi_B^2$, is approximately proportional to the square of the baryon number of the relevant degrees of freedom [64, 65]. This clarifies the cause for the rapid change of $\kappa\sigma^2$ at the crossover transition from $\simeq 1$ to $\simeq 1/9$, seen in Fig. 4.1. In the limit where the characteristic mass is small compared to the temperature, the kurtosis ratio is modified by quantum statistics, to $\kappa\sigma^2 = (1/9)(6/\pi^2)$.

We note that the kurtosis ratio is independent of the mass spectrum as well as of any kinematic cuts, as long as the Boltzmann limit remains valid.

The ratio $\chi_B^{6,2}$, also shown in Fig. 4.1, exhibits more structure at the chiral transition. The observed characteristic temperature dependence of this ratio, in particular with a region of negative values at $T \simeq T_c$, is a consequence of the residual chiral $O(4)$ criticality [61]. In the absence of chiral critical fluctuations, $\chi_B^{6,2}$ would show a similar behavior as $\kappa\sigma^2$, with a smooth reduction from unity at low temperatures towards zero above the deconfinement transition. The distinctive behavior of the $\chi_B^{6,2}$ and $\chi_B^{4,2}$ ratios was already obtained in the PQM model within the FRG approach [61], and agrees qualitatively with LQCD results [142]. Thus, the PQM model correctly captures the physics of QCD related to deconfinement and to the critical dynamics at the chiral transition. The negative values of $\chi_B^{6,2}$ at the chiral crossover were proposed as a signature for partial restoration of chiral symmetry in heavy ion collisions [61].

As shown in Fig. 4.1, in the presence of repulsive interactions, $\chi_B^{6,2}$ and the kurtosis ratios are modified. The vector interaction leads to a downward shift in temperature of the ratios relative to the phase boundary, as well as, a suppression of the sixth order susceptibility in the temperature range below T_c. Nevertheless, the qualitative form of the ratios is preserved. In particular, the characteristic structure, where the sixth order cumulant is negative in a range of temperatures near T_c owing to $O(4)$ criticality, is not eliminated by the repulsive interaction.

In Fig. 4.2 we show contour plots of the ratios $\chi_B^{1,2}$ and $\chi_B^{3,1}$ in the (T, μ_q)-plane. As noted above, all odd cumulants vanish at $\mu_q = 0$, owing to baryon-antibaryon symmetry. Consequently, $\chi_B^{1,2}|_{\mu_q=0} = 0$ for any T, while the ratio $\chi_B^{3,1}|_{\mu_q=0}$ is nonvanishing. At low and high T, relative to T_c, this ratio is consistent with unity and $2/(3\pi^2)$, respectively, as expected since $\chi_B^{3,1}|_{\mu_q=0} = \chi_B^{4,2}|_{\mu_q=0}$. As indicated in Figs. 4.1 and 4.2, the ratio $\chi_B^{3,1}$ decreases with temperature, and depends weakly on the chemical potential. Moreover, Fig. 4.2, shows that for $\mu_q < T$, $\chi_B^{1,2}$ increases with μ_q, and is only weakly dependent on the temperature. Thus, the ratio $\chi_B^{3,1}$ can be used as a measure of the temperature, while $\chi_B^{1,2}$ provides a gauge of the chemical potential.

At small μ_q/T, the properties of the first four susceptibilities, χ_B^n with $n = 1, .., 4$, and consequently their ratios near the chiral crossover are dominantly affected by the coupling of the quarks to the Polyakov loop, and the resulting statistical confinement. The critical chiral dynamics, i.e. the $O(4)$ and $Z(2)$ criticality at the chiral crossover transition and at the CEP, respectively, unfolds at larger μ_q/T. Near the CEP, there is a strong variation of the cumulants with T and μ_q, which increases with the order of cumulants. As shown in Figs. 4.2 and 4.3, the qualitative behavior of the cumulant ratios on lines going to the CEP depends strongly on the direction from which the CEP is approached. This behavior is governed by the critical properties encoded in the $O(4)$ and $Z(2)$ universal scaling functions.

The influence of the CEP on the characteristics of the various cumulant ratios can be studied by varying the value of the vector coupling, thus changing the position of the CEP in the (T, μ_q) plane. This is illustrated in Fig. 4.3 for the kurtosis ratio. A comparison of the results shown in the left and right contour plots shows that with increasing g_ω, the curvature of the phase boundary is reduced and the position of the CEP is shifted to lower T and larger μ_q [85]. As is clearly seen, when comparing the left and right plots of Fig. 4.3, there is a corresponding shift of the contours of $\chi_B^{4,2}$. These results illustrate the influence of the critical endpoint on the fluctuation observables. A shift of the CEP to larger net baryon density suppresses the magnitude of the net-baryon-number susceptibilities at a given T and μ_q.

4.4 Net-baryon-cumulant ratios and freeze-out in heavy-ion collisions

In heavy-ion collisions, the thermal fireball formed in the quark-gluon plasma phase undergoes expansion and passes through the QCD phase boundary at some point (T_c, μ_c) point, which depends on the collision energy, $\sqrt{s}$. Analysis of ratios of particle multiplicities indicate that at high beam energies (small values of μ_q/T), the freeze-out occurs at, or just below the phase boundary. Thus, the beam energy dependence of net-baryon-number susceptibilities can provide insight into the structure of the QCD phase diagram and information on the existence and location of the CEP. Consequently, it is of phenomenological interest to compute the properties of fluctuations of conserved charges along the chiral phase boundary. Since there, the critical structure and the relations between different susceptibilities are governed by the universal scaling functions, the generic behavior of ratios of net-baryon-number susceptibilities can be explored also in model calculations.

In Fig. 4.4 we show $\chi_B^{1,2}$, as well as skewness and kurtosis ratios of net baryon number, obtained in the PQM model along the chiral phase boundary, with and without vector repulsion. In the former case, the position of the CEP is shifted to smaller T and larger μ_q.

The ratio $\chi_B^{1,2}$ exhibits a maximum along the phase boundary. For small $(\mu_q/T)_c$ this ratio is well approximated by $\tanh(3\mu_q/T)$, while after reaching a maximum, it decreases as the CEP is approached. The cumulants χ_B^1 and χ_B^2 remain finite along the $O(4)$ line. However, at the CEP the variance of the net-baryon-number fluctuations diverges. This is the cause for the observed decrease of $\chi_B^{1,2}$ at larger $(\mu_q/T)_c$. For nonzero vector repulsion, this reduction is weakened, owing to the shift of the CEP to lower temperature. Let us note, that for $(\mu_q/T)_c < 0.5$, the $\chi_B^{1,2}$ ratio is hardly modified by the repulsive interactions. This can be traced back to a cancellation between the suppression of χ_B^2 at nonzero g_ω (2.61) and the shift of the chemical potential (2.125); both axes are scaled by the factor $(1 + 9T^2 G_\omega \tilde{\chi}_B^2(T,\nu))$, for small μ_q. On the other hand, the ratio χ_B^3/χ_B^2 is *reduced* by the factor $(1 + 9T^2 G_\omega \tilde{\chi}_B^2(T,\nu))$, for nonvanishing vector interaction. Hence, this ratio is reduced at all values of μ_q/T.

As seen in Fig. 4.4, the skewness ratio, $\chi_B^{3,1}$, is an increasing function of $(\mu_q/T)_c$ along the phase boundary and at the CEP it diverges [2]. There is also a clear suppression of this ratio along the phase boundary due to repulsive interactions, as seen also for $\chi_B^{3,2}$. At $(\mu_q/T)_c = 0$, the skewness and kurtosis ratios are equal to each other, and differ very little up to $(\mu_q/T)_c \simeq 0.5$. For larger $(\mu_q/T)_c$, the kurtosis is decreasing and skewness increasing along the phase boundary, in agreement with recent LGT results [143]. This behavior also reflects their properties near the critical point. As the CEP is approached along the phase boundary, the kurtosis diverges to minus infinity, while the skewness diverges to plus infinity, as noted above. Thus, both ratios become less singular as g_ω is increased, i.e., as the CEP is shifted to larger μ_q.

The characteristics of the various net-baryon-number susceptibilities on the phase boundary, shown in Fig. 4.4, are expected to be similar in QCD. This is because, they are, by and large, determined by $O(4)$ critical fluctuations and by "confinement", which are both common to QCD and the PQM model. This opens the possibility to verify directly, if these features of criticality are also reflected in the data on net-proton-number fluctuations obtained in heavy-ion collisions by the STAR Collaboration at several RHIC energies [54, 144, 145].

Clearly, a direct comparison of model results with data has to be taken with caution. Although, the model provides a viable description of the dynamics that drives the system towards chiral symmetry restoration, the spectrum of hadronic degrees of freedom in the low temper-

---

[2] Since the CEP is a singular point, the corresponding value of χ_B^3 depends on how the limit is taken. Owing to the curvature of the phase boundary, the CEP is approached slightly from below, which implies that χ_B^3 diverges to plus infinity.

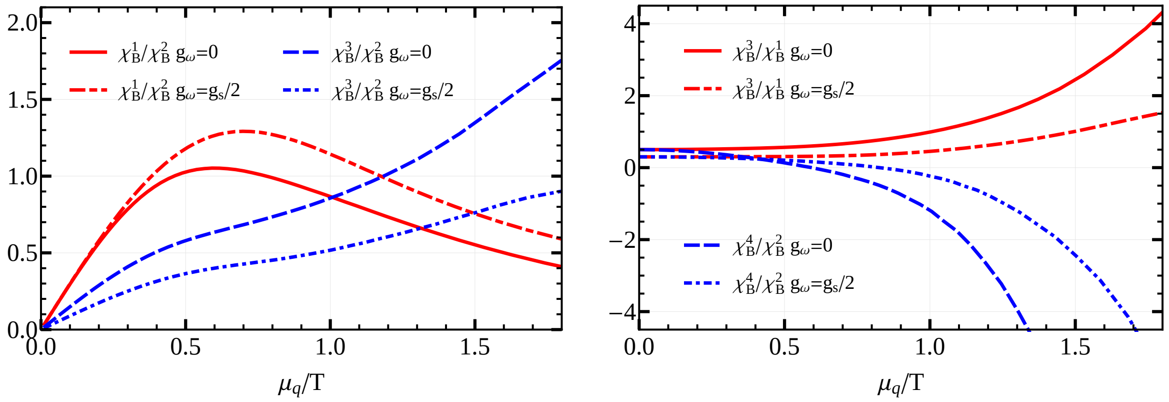

Figure 4.4.: Ratios of cumulants of net-baryon-number fluctuations in the PQM model computed on the chiral phase boundary with and without vector repuslion. The solid and long-dashed lines correspond to $g_\omega = 0$, and the dash-dotted lines to $g_\omega = g_s/2$.

ature phase is incomplete. Moreover, net-baryon-number fluctuations are in nucleus-nucleus collision experiments quantified by the net proton number. It has been extensively discussed, to what extent are net-proton-number fluctuations accurate proxies for those of the net baryon number [146–149]. Furthermore, there are kinematical cuts, imposed on the STAR data on the cumulants of net proton number, which are not accounted for in the model results. However, these differences are, to a large extent, eliminated by considering ratios of susceptibilities. This assumption is supported by the behavior of the ratio $\chi_B^{1,2}$, which, in spite of the differences discussed above, is well approximated by $\tanh(3\mu_q/T)$ (see Fig. 4.5) in LQCD, in the PQM model as well as in the STAR data. The fact that $\chi_B^{1,2}$ is well approximated by this functional form indicates that in the transition region, the effective degrees of freedom with nonvanishing baryon number have $B = \pm 1$.

A comparison of results obtained in the PQM model with data requires a correspondence between the collision energy $\sqrt{s}$ and the thermal parameters (μ_q, T). Here we employ the phenomenological relation, obtained by analysing the freeze-out conditions in terms of the hadron-resonance-gas model (HRG) [55, 79–81]. We then use the resulting dependence of μ_B and T on $\sqrt{s}$ to assign a value for the ratio (μ_q/T) to each of the STAR beam energies. We should note that, for $\mu_q/T < 1$, the phenomenological freeze-out line coincides within errors with the crossover phase boundary obtained in lattice QCD [27, 80]. This motivates a comparison of model results on net-baryon-number fluctuations near the phase boundary with data. Such an analysis was first done using LQCD results in Ref. [150].

In Fig. 4.5, we show the STAR data on net-proton-number susceptibility ratios and the corresponding PQM model results on net-baryon-number fluctuations computed along the phase boundary. The model results for the ratios $\chi_B^{1,2}$, $\chi_B^{3,1}$ and $\chi_B^{3,2}$ are in qualitative agreement with the data in the whole energy range. For the kurtosis ratio, $\chi_B^{4,2}$, this is the case also up to the SPS energy, i.e., for $\sqrt{s} \geq 20$ GeV. However, for $\mu_q/T > 0.5$, the data on the kurtosis ratio exhibits a qualitatively different dependence on μ_q/T than expected for the critical behavior of $\chi_B^{4,2}$, as the CEP is approached along the phase boundary.

As noted above, the ratio $\chi_B^{1,2}$ is, on the phase boundary, approximately given by $\chi_B^{1,2} \simeq \tanh(3\mu_q/T)$ up to $\mu_q/T \simeq 1$, as seen in Fig. 4.5. This form of the ratio of the lowest order cumulants is also obtained in the HRG model and is consistent with LQCD [63, 66]. Fig. 4.5 reveals that the data are consistent with this form as well. This fact clearly supports the use of the $\sqrt{s}$ dependence of μ_q/T obtained from the HRG model analysis of multiplicities in the comparison of the PQM model results with data.

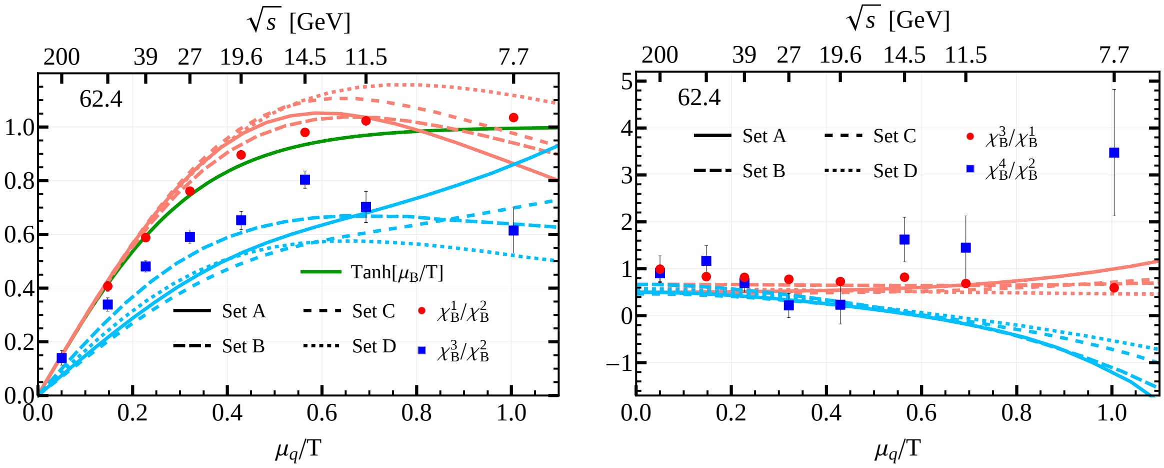

Figure 4.5.: Ratios of cumulants of net-baryon-number fluctuations in the PQM model, computed along the chiral phase boundary, for four sets of model parameters (for details see Appendix D). Also shown are the preliminary STAR data [54, 145], assuming the relation between the ratio (μ_q/T) and the collision energy obtained by analysing the chemical freeze-out conditions [79–81]. The green full line in the left-hand figure shows the baseline result, $\chi_B^{1,2} = \tanh(3\mu_q/T)$.

In order to assess the sensitivity of the fluctuation observables to model parameters, we show in Fig. 4.5 ratios of cumulants for four sets of model parameters. The different sets are obtained by varying the sigma meson mass and the form of the Polyakov-loop potential. The parameter sets are described in Appendix D. Fig. 4.5 shows that, although some quantitative differences can be identified at larger μ_q/T, the skewness, kurtosis and $\chi_B^{1,2}$ ratios along the phase boundary are qualitatively similar for the different sets of model parameters.

In the comparison of model predictions with data in Fig. 4.5, we assume that the freeze-out of the net-baryon-number fluctuations tracks the chiral phase boundary. Clearly, this simple assumption provides a qualitative understanding of the data. In order to obtain a more quantitative description, we follow Refs. [150–152], and determine the freeze-out conditions by fitting the data on the $\chi_B^{3,1}$ ratio, using the $(\sqrt{s})$-dependence of μ_q/T obtained from the fit of the HRG model to particle multiplicities [79–81].

In Fig. 4.6 the fluctuation ratios are shown along the freeze-out line, which is fixed through the skewness data. The model results are obtained for the four sets of initial conditions. Fig. 4.6 clearly shows that, along the freeze-out line, the spread of all fluctuations ratios considered for the various parameter sets is much weaker than that observed in Fig. 4.5 along the phase boundary. This indicates that moderate changes of the sigma mass and modifications of the form of the Polyakov loop potential may lead to a shift in the temperature scale but essentially with no change of the relative structure of the cumulant ratios.

The results presented in Fig. 4.6 clearly show that the model provides a very good description of the data on $\chi_B^{1,2}$ and $\chi_B^{3,2}$. Also the kurtosis data, obtained at higher collision energies, are consistent with model results. However, at $\sqrt{s} < 20$ GeV they exhibit a different trend, with the data increasing rapidly at lower energies, while the model result keeps decreasing. We conclude that an increase of $\chi_B^{4,2}$ ratio beyond unity, observed in the STAR data at $\sqrt{s} < 20$ GeV, is not expected in equilibrium on the chiral critical line nor on the freeze-out line.

As noted above, the ratio $\chi_B^{6,2}$ is particularly interesting for identifying criticality governed by the $O(4)$ universality class. This is seen in Fig. 4.1 at $\mu_q = 0$, where $\chi_B^{6,2}$ is negative at $T = T_c$. At $\mu_q > 0$, the influence of criticality is even more pronounced, as shown in Fig. 4.7. There, $\chi_B^{6,2}$ exhibits a highly nonmonotonic structure near the phase boundary.

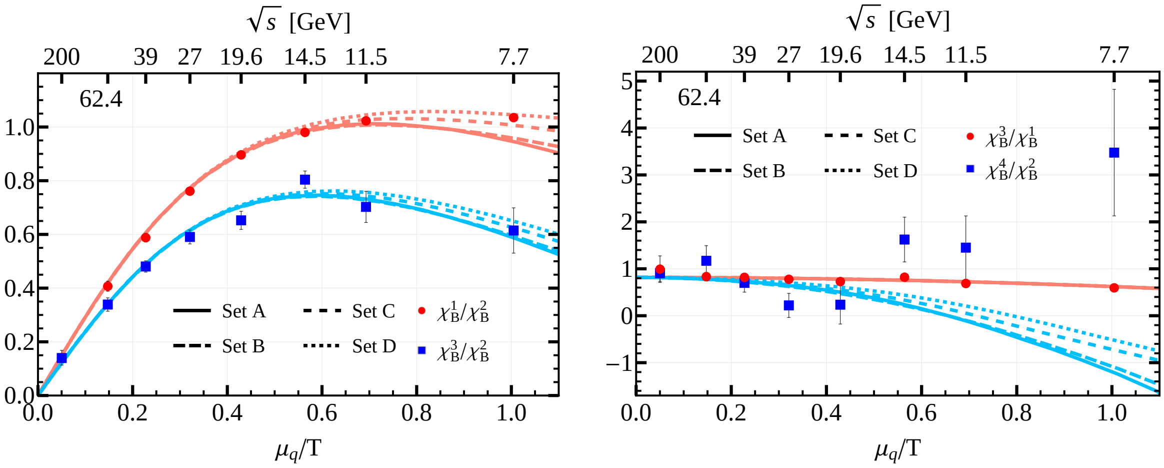

Figure 4.6.: Ratios of cumulants of net-baryon-number fluctuations in the PQM model along the freeze-out line, obtained by fitting χ_B^3/χ_B^1 to the STAR data. The four sets of model parameters used and the preliminary STAR data shown, are the same as in Fig. 4.5.

In the left panel of Fig. 4.7 we show the temperature dependence of the ratio $\chi_B^{6,2}$ near the phase boundary for $\mu_q = 0.1$ GeV. This ratio exhibits a very strong variation near the transition temperature. It is deeply negative below T_c and develops a maximum just above T_c. The value of $\chi_B^{6,2}$ is thus very sensitive to the freeze-out temperature.

On the right of Fig. 4.7 we show the ratios χ_B^4/χ_B^2, χ_B^5/χ_B^1 and χ_B^6/χ_B^2 computed, using the model parameters of set A, along the freeze-out line which is determined by fitting χ_B^3/χ_B^1 to data. At vanishing μ_q, $\chi_B^4/\chi_B^2 = \chi_B^3/\chi_B^1$ and $\chi_B^6/\chi_B^2 = \chi_B^5/\chi_B^1$, as a consequence of Eq. (4.34), while at larger μ_q/T, these ratios separate.

Let us note at this point that the equality of the ratios χ_B^4/χ_B^2 and χ_B^3/χ_B^1 in the STAR data at the highest energy is a strong indication that the fluctuations probed by these cumulants are in thermal equilibrium. It is very unlikely that a system not in equilibrium would yield ratios of cumulants that satisfy Eq. (4.34). Note that at $\mu_q = 0$, the critical $O(4)$ fluctuations yield divergent contributions only to χ_B^6 and higher cumulants [61]. Thus, the fluctuations probed by χ_B^4/χ_B^2 and χ_B^3/χ_B^1 are not critical. However, a measurement of the ratios involving the fifth and sixth order cumulants would probe whether the $O(4)$ critical fluctuations are in equilibrium or not. Obviously, this test of equilibration is meaningful only at small μ_q/T, i.e., only at the highest energies.

At moderate values of μ_q/T, the χ_B^6/χ_B^2 ratio is negative and deviates clearly from χ_B^5/χ_B^1. At still lower energies, it exhibits a strong increase towards the CEP, where it diverges. Similarly, χ_B^5/χ_B^1 decreases at moderate μ_q/T, and increases strongly as the CEP is approached. These results indicate that in heavy-ion collisions χ_B^6/χ_B^2 and χ_B^5/χ_B^1 will exhibit strong nonmonotonic dependencies on $\sqrt{s}$.

Recently, first results on χ_B^6/χ_B^2 in Au-Au collisions at $\sqrt{s} = 200$ GeV where reported by the STAR Collaboration for several centralities [153]. The data show a strong suppression of fluctuations compared to the kurtosis ratio. In mid-central and the most central collisions, the χ_B^6/χ_B^2 fluctuation ratio is negative, albeit with still very large statistical uncertainties. In fact, given the large errors for the most central collisions, the preliminary data is consistent with a vanishing χ_B^6. A value close to zero is consistent with the model results, shown in the right panel of Fig. 4.7.

The comparison of model results on ratios of net-baryon-number susceptibilities with the STAR data in Figs. 4.5 and 4.6 shows that the data, with the exception of kurtosis at low energies, follow general trends expected due to critical chiral dynamics. The ratios of net-baryon-

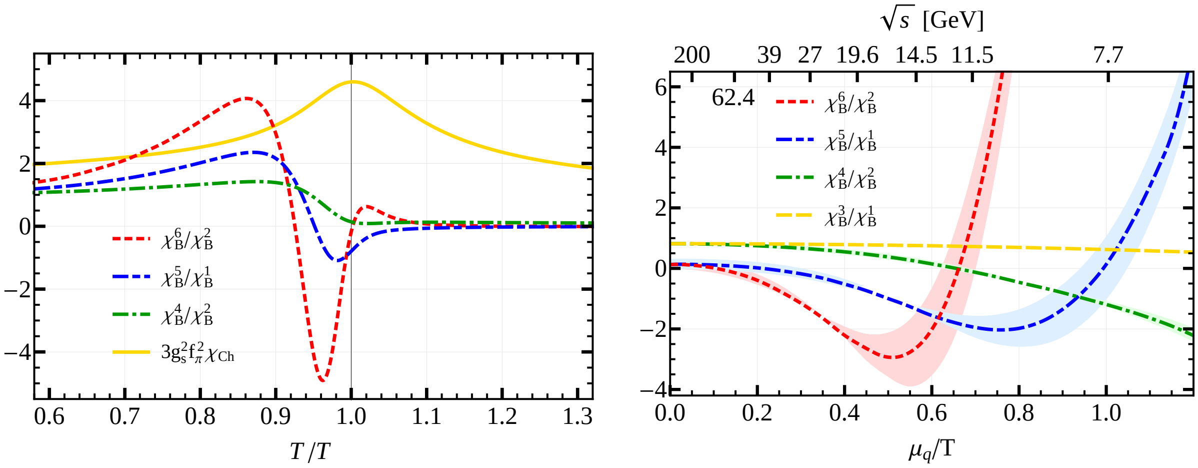

Figure 4.7.: Left-hand figure: The temperature dependence of ratios of net-baryon-number cumulants and the chiral susceptibility χ_{ch}, all computed in the PQM model at $\mu_q = 0.1$ GeV. The vertical line indicates the location of the chiral crossover temperature. Right-hand figure: The ratios χ_B^4/χ_B^2, χ_B^5/χ_B^1 and χ_B^6/χ_B^2 along the freeze-out line obtained by fitting χ_B^3/χ_B^1 (also shown) to data. These results were computed using the model parameters of set A (see Appendix D). The bands about χ_B^5/χ_B^1 and χ_B^6/χ_B^2 reflect the experimental error in χ_B^3/χ_B^1, which leads to an uncertainty in the freeze-out temperature.

number susceptibilities near the phase boundary involving net-baryon number cumulants χ_B^n with $n \geq 3$ are controlled mainly by the scaling functions in the $O(4)$ and $Z(2)$ universality classes, respectively. This observation indicates that, by measuring fluctuations of conserved charges in heavy-ion collisions, we are indeed probing the QCD phase boundary, and thus accumulating evidence for chiral symmetry restoration.

However, as discussed above, there are several uncertainties and assumptions which must be thoroughly understood before the QCD phase boundary can be pinned down with confidence. Possible contributions to fluctuation observables from effects not related with critical phenomena, like e.g. baryon-number conservation [147] and volume fluctuations [136, 138, 154–157] are being explored. We also mention the rather strong sensitivity of higher order net-proton-number cumulants on the transverse momentum range imposed in the analysis of the STAR data. Nevertheless, it is intriguing that the dynamics of the model provides a good description of the STAR data (except for χ_B^4 at the lowest energies), without all these effects of noncritical origin. It remains an important task to assess the effect of theses additional sources of fluctuations in the whole energy range probed by the experiments.

Chapter 5

Quark-meson model in finite volume

In the previous chapter we computed ratios of cumulants of the baryon number distribution, and compared them to experimental measurements. We noted that the volume factor formally cancels out from the *ratios* of the cumulants. This cancellation only occurs, if we perform the calculation in the infinite volume limit. In this chapter our aim is to quantify the volume dependence of these ratios in a system by performing calculations within the quark-meson model in a finite volume.

Theories can be studied in a finite volume by requiring certain boundary conditions. These usually fix either the dynamical fields, or their derivatives on the boundary. In the quark-meson model we consider strongly interacting matter within a rectangular cuboid, referred to in the following as the box, and fix the values of the meson and quark fields on the boundaries of the box by imposing either periodic or antiperiodic boundary conditions in the spatial direction. It should be noted that in the temporal direction the boundary conditions are fixed by the spin of the fields: the bosons always obey periodic boundary conditions, and fermions antiperiodic boundary conditions.

Apart from the standard cubical box that is most often considered, we also study finite volume effects in boxes that are elongated in one direction, i.e., in square cuboids. The motivation for such studies roots in the geometry of heavy ion collisions. The two colliding nuclei collide with almost the speed of light and passing through each other rapidly, hence the volume emitting particles can be elongated in the beam direction. This is especially true in peripheral collisions.

The boundary conditions quantize the momenta of fluctuations in the system. This has the consequence that when calculating any thermodynamic quantities, the integration over all modes in the system has to be replaced by a sum over the eigenmodes that are compatible with the boundary conditions. Denoting the length of the edges of the box by L_x, L_y and L_z, the momenta of the fluctuations obey

$$q_{PBC}(n_x, n_y, n_z)^2 = \left(\frac{2\pi n_x}{L_x}\right)^2 + \left(\frac{2\pi n_y}{L_y}\right)^2 + \left(\frac{2\pi n_z}{L_z}\right)^2 \tag{5.1}$$

for periodic boundary conditions, and

$$q_{APBC}(n_x, n_y, n_z)^2 = \left(\frac{\pi(2n_x+1)}{L_x}\right)^2 + \left(\frac{\pi(2n_y+1)}{L_y}\right)^2 + \left(\frac{\pi(2n_z+1)}{L_z}\right)^2 \tag{5.2}$$

for antiperiodic ones. In the FRG flow equations in a finite volume, summation over functions of these momenta will be needed. For this we use an algorithm presented in Ref. [158] and briefly outlined for cubic boxes, i.e. for $L_x = L_y = L_z \equiv L$, here.

Assume we would like to calculate a sum of a function $f(q^2)$ over all eigenmodes of the system. Since the evaluation of the function f in some cases can be time consuming, we utilize the symmetry of the function, namely that it only depends on q^2, not on the three components separately, as well as we can. For periodic boundary conditions, we can write

$$\sum_{modes} f(q^2) = \sum_{\vec{n}} f\left(\frac{4\pi^2}{L^2}\vec{n}^2\right) = \sum_{m=0}^{\infty}\left(\sum_{\vec{n}} \delta_{m,\vec{n}^2}\right) f\left(\frac{4\pi^2}{L^2}m\right) = \sum_{m=0}^{\infty} G^P(m) f\left(\frac{4\pi^2}{L^2}m\right). \tag{5.3}$$

where the function, the multiplicity of modes, $G^P(m) \equiv \sum_{\vec{n}} \delta_{m,\vec{n}^2}$ automatically takes the symmetries of the magnitude $\vec{n}^2 = n_x^2 + n_y^2 + n_z^2$ into account. The function $G^P(m)$ is to be computed once and tabulated for repeated use. This method gives a significant reduction in computational time, since the triple sum over n_x, n_y and n_z is replaced by a single sum over the magnitude.

For antiperiodic boundary conditions a similar compactification can be performed. In this case the square of the momentum in a cubic box as a function of the mode numbers is given by

$$\begin{aligned} q^2 &= \left(\frac{\pi(2n_x+1)}{L}\right)^2 + \left(\frac{\pi(2n_y+1)}{L}\right)^2 + \left(\frac{\pi(2n_z+1)}{L}\right)^2 \\ &= \frac{\pi^2}{L^2}\left(4(n_x^2+n_y^2+n_z^2+n_x+n_y+n_z)+3\right). \end{aligned} \tag{5.4}$$

The summation over these modes reads

$$\sum_{modes} f(q^2) = \sum_{m=0}^{\infty} G^{AP}(m) f\left(\frac{\pi^2}{L^2}(4m+3)\right), \tag{5.5}$$

with the multiplicity of modes

$$G^{AP}(m) = \sum_{\vec{n}} \delta_{m,n_x^2+n_x+n_y^2+n_y+n_z^2+n_z}. \tag{5.6}$$

This method proved very useful during the evaluation of the FRG flow equations in a finite volume.

5.1 FRG flow in finite volume

The derivation of the FRG flow equation in finite volume is completely analogous to the infinite volume derivation presented in Sec. 2.4. The only modifications that need to be implemented are the replacement of momentum integrals by mode summations, and the momentum space Dirac deltas by Kronecker deltas. The flow equation can be obtained from the infinite volume flow equation, Eq. (2.105), by replacing the momentum integral by a summation over the modes allowed by the boundary conditions,

$$\partial_k \Omega = \frac{1}{4L_xL_yL_z} \sum_{n_x,n_y,n_z} \left(\frac{1+2n_B(E_\sigma)}{E_\sigma} + 3\frac{1+2n_B(E_\pi)}{E_\pi} - 2\nu_q \frac{1-n_F(E_q)-\bar{n}_F(E_q)}{E_q} \right) \partial_k R_k(q). \tag{5.7}$$

where the energies are given by $E_x = \sqrt{m_x^2 + q^2 + R_k(q)}$ with

$$m_q = g_s\sigma, \qquad m_\sigma = \frac{\partial^2\Omega}{\partial\sigma^2}, \qquad m_\pi = \frac{1}{\sigma}\frac{\partial\Omega}{\partial\sigma}, \tag{5.8}$$

and $\nu_q = 12$. For finite volume studies presented in this chapter, we consider two different regulators. One of them is the Litim regulator introduced in Sect. 2.4, which has been previously employed in finite volume studies [134, 159–161],

$$R_k(q) = (k^2 - q^2)\theta(k^2 - q^2), \tag{5.9}$$

where θ denotes the Heaviside step function. The other is the exponential regulator

$$R_k(q) = \frac{q^2}{e^{q^2/k^2} - 1}, \tag{5.10}$$

which we used for illustrative purposes in the introduction. Just as in the infinite volume case, the Litim regulator provides particularly simple flow equations,

$$\partial_k\Omega = \frac{k}{2L_xL_yL_z}\left(\frac{1+2n_B(E_\sigma^{Lit})}{E_\sigma^{Lit}}+3\frac{1+2n_B(E_\pi^{Lit})}{E_\pi^{Lit}}-2\nu_q\frac{1-n_F(E_q^{Lit})-\bar{n}_F(E_q^{Lit})}{E_q^{Lit}}\right)\sum_{m=0}^{m_{max}}G(m), \tag{5.11}$$

with $E_x^{Lit} = \sqrt{m_x^2+k^2}$ and $G(m)$ denotes the multiplicity of the modes determined by the boundary conditions. Furthermore, m_{max} is chosen such that only those modes are counted, for which $q^2 < k^2$. For example, for cubic box $L_x = L_y = L_z \equiv L$ and periodic boundary conditions,

$$m_{max} = \frac{k^2L^2}{4\pi^2}. \tag{5.12}$$

The flow equation (5.11) is greatly simplified compared to (5.7) in the sense that the energies E_x^{Lit} and any functions thereof only have to be calculated once in a flow step, not for each mode separately, and the mode summation is reduced to a simple summation of the tabulated $G(m)$ multiplicity of modes. This yields a large saving of computing time, which makes the use of the Litim regulator very attractive. However, its implementation for finite volume calculations requires great care [162].

Similar simplification cannot be achieved in the case of the exponential regulator, and Eq. (5.7) has to be used. We can however replace the triple sum by a single sum using the multiplicity of modes,

$$\partial_k\Omega = \frac{1}{4L_xL_yL_z}\sum_{m=0}^{m_{cutoff}}\left(\frac{1+2n_B(E_\sigma)}{E_\sigma}+3\frac{1+2n_B(E_\pi)}{E_\pi}-2\nu_q\frac{1-n_F(E_q)-\bar{n}_F(E_q)}{E_q}\right)\partial_kR_k(q(m)), \tag{5.13}$$

where $q(m)$ is determined by the boundary conditions and is provided for cubic box for periodic and antiperiodic boundary conditions in Eqs. (5.1) and (5.2), respectively. To truncate the sum we only perform the summation up to an m_{cutoff} value, where

$$\partial_kR_k\left(q_{m_{cutoff}}\right) = 10^{-8}\ \text{MeV}. \tag{5.14}$$

The contribution of modes above that point can be safely neglected.

Fig. 5.1 shows a comparison of the behavior of the two regulators. On the left panel the evolution of the minimum is shown as a function of the RG scale k in an infinite volume and at a system size $L = 3$ fm. Even though the infinite volume flows based on the different regulators are qualitatively similar, one can see that at $L = 3$ fm the flows behave rather differently. The flow based on the exponential regulator at finite volume is smooth and it follows the infinite volume flow almost perfectly. It only deviates from its infinite volume counterpart at small values of k, where the small momentum fluctuations are probed. On the other hand, the flow based on the Litim regulator shows two clear nonanalicities, for example one at

$$k/\Lambda = \frac{2\pi}{L\Lambda} \approx 0.43. \tag{5.15}$$

The reason for this latter is that according to Eq. (5.12) for $k < \frac{2\pi}{L}$ only the zero mode contributes to the Litim flow, Eq. (5.11). The Litim regulator disregards contribution from all other terms and they are abruptly switched off. At higher RG scales six more modes contribute, namely the $\{n_x, n_y, n_z\} = \{\pm 1, 0, 0\}$ and its permutations. This sudden change in the number of modes taken into account causes this abrupt change in the evolution of the minimum. At the other nonanalicity, further modes start to contribute to the sum.

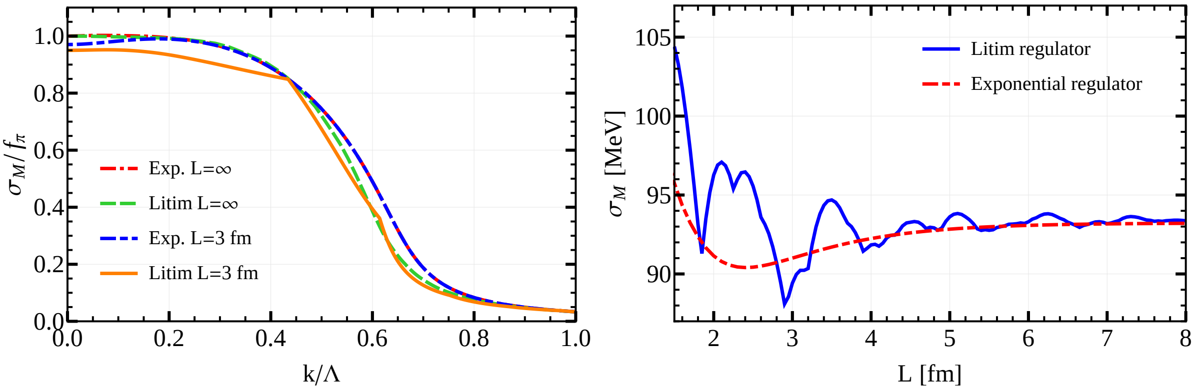

Figure 5.1.: Left: the flow of the minimum of the potential at vanishing temperature and chemical potential in a cubix box, normalized by f_π. The Litim and exponential regulators are compared in an infinite volume and at $L = 3$ MeV. Right: the chiral condensate at vanishing temperature and chemical potential as a function of system size with the two regulators.

This artifact is not present when using the exponential regulator, since the modes well above the RG scale contribute as well, and they are turned off smoothly in the RG evolution. Hence, the evolution of the minimum is smooth. The right panel of Fig. 5.1 shows that the nonanalicity produced by the Litim regulator shows up also in the volume dependence of the chiral condensate, and probably in other quantities as well. The reason for this is that in small volumes there are only few modes below the UV cutoff Λ, and whether a mode is located just below or just above the cutoff has a significant effect. This artifact does not show up when using the exponential regulator, because it takes modes above the UV cutoff also into account and switches the modes off smoothly. Thus, even though the Litim regulator yields fast flows, it produces unwanted artifacts as well. Hence, in the following we will only consider the exponential regulator.

5.2 Calculations at a finite volume in vacuum

In this section we focus on the vacuum results at a finite volume, i.e., $T \approx 0$, $\mu = 0$[1]. On the left hand side of Fig 5.2 the volume dependence of the condensate is shown for different anisotropic volumes described by the anisotropy parameter A. Regardless of the anisotropy parameter, curves with periodic boundary conditions show similar behavior: as the system size is decreased, first the value of the condensate decreases, then at $L \approx 2$ fm shows a minimum, and for very small volumes it shoots up. With antiperiodic boundary conditions one finds the opposite behavior: as the system size is decreased, the condensate is melting. The disparity at small volumes is connected with the different treatment of the zero mode. With the periodic boundary conditions, the zero mode is included, and its contribution is enhanced in small volumes, since it is proportional to $1/L^3$. With antiperiodic boundary conditions, the zero mode does not contribute, and in small volumes all fluctuations freeze out.

The absence of the zero mode when antiperiodic boundary conditions are employed has severe consequences. In a finite system, there cannot be spontaneous symmetry breaking. Spontaneous symmetry breaking can only occur, if two or more degenerate states are separated by an infinite energy barrier, such that it would take infinite time for the system to tunnel

---

[1] In the calculation, the temperature is not exactly put to zero, but rather to a small value, such that the finite temperature formalism can be applied.

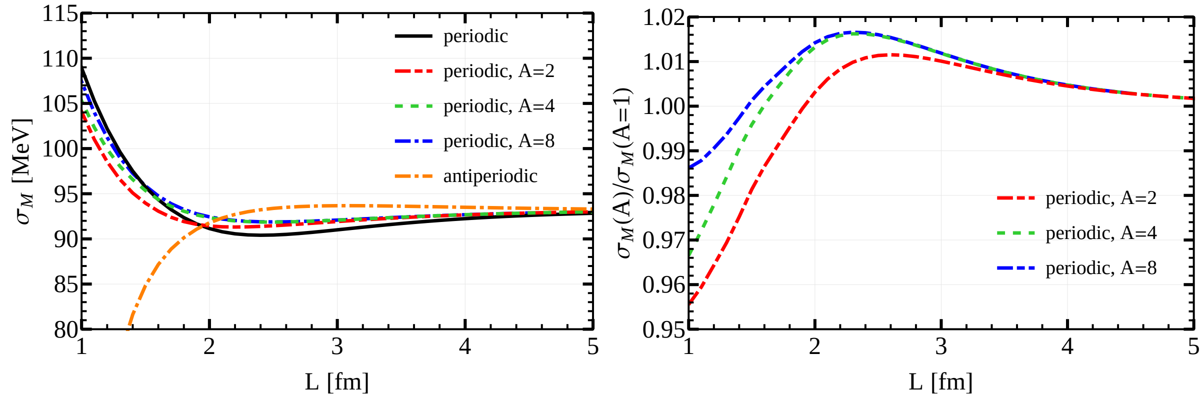

Figure 5.2.: The chiral condensate as a function of the system size, $L = L_x = L_y$ for the different anisotropy parameter $A \equiv L_z/L_{x,y}$. Left: direct comparison of the results using antiperiodic boundary conditions with that of the periodic boundary conditions with different anisotropy parameters. Right: The results are normalized by the corresponding values of the chiral condensate for the isotropic volume, $L_x = L_y = L_z = L$. Periodic boundary conditions are used.

from one state to the other. In a finite volume, due to the finiteness of the system, the energy barrier cannot be infinite, and tunneling always happens in a finite time. Hence, spontaneous symmetry breaking is not possible. The problem with antiperiodic boundary conditions applied in the FRG framework is that it cannot ensure this property and thus produces unphysical spontaneous symmetry breaking even in a finite volume. This can be understood as follows: during the RG flow in an infinite volume, a minimum in the effective potential evolves at an intermediate $k_{\chi SB}$ scale, at a nonvanishing field value, producing a nonconvex potential. As the regulator is removed, the potential flattens and regains its convexity in the $k = 0$ limit. In a finite volume, using antiperoidic boundary conditions, the flow at high scales, where large momenta are relevant, barely changes. Hence the symmetry breaking still occurs around $k \approx k_{\chi SB}$. However, since the zero mode is absent, at low k values there are no fluctuations anymore. Consequently, there is no force to drive the restoration of the convexity of the potential. Hence, we end up with a potential that is not convex, and has a minimum at some nonzero σ. Clearly, this is unphysical. For this reason, we consider only periodic boundary conditions from this point on.

When periodic boundary conditions are employed, the zero mode is accounted for, and contributes to the flow all the way down to $k = 0$, hence it can potentially restore convexity and melt the condensate that evolved at intermediate RG scales. First let us consider the following analytical reasoning why spontaneous symmetry breaking cannot occur using periodic boundary conditions in the FRG framework.

In the chiral limit $H = 0$, where without spontaneous symmetry breaking the condensate has to vanish, the schematic form of the flow equation reads

$$\partial_k \Omega_k \propto \frac{1}{L^3} \frac{kT}{k^2 + m_k^2}, \tag{5.16}$$

where we consider sigma meson contribution and include the $\vec{n} = 0$ zero mode. Higher modes do not play an important role at small k, where the most important part of the FRG evolution takes place. Other degrees of freedom can be included as well, but they do not change the main conclusion. Furthermore, we consider only the “high-temperature” limit of the Bose-Einstein distribution function,

$$1 + 2n_B(\omega) \approx \frac{2T}{\omega}. \tag{5.17}$$

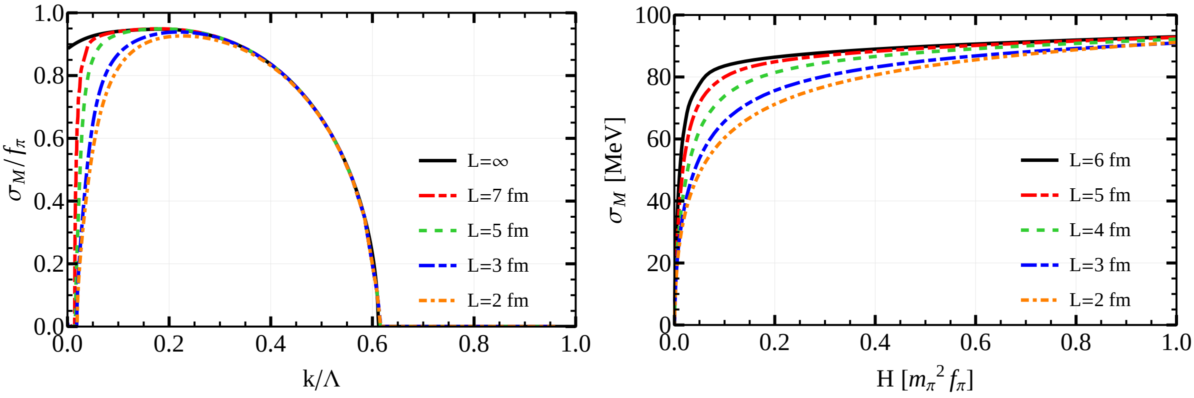

Figure 5.3.: Left: The dependence of the minimum of the potential on the FRG flow parameter k for different system sizes in the chiral limit $h=0$. The calculations are performed at $T=10$ MeV. For higher L, the nontrivial minimum of the potential is preserved by the FRG evolution to lower values of k, as expected. Right: Chiral condensate as a function of the external field for different system sizes.

This is a good approximation for the zero mode at $k \ll T$ and $m_k \ll T$. These restrictions are suitable for studying the spontaneous symmetry breaking.

Next we assume that $\lim_{k\to 0} \partial_k \Omega_k = 0$. This condition manifests the convergence of the FRG flow equation. It also implies that

$$\lim_{k\to 0} \frac{kT}{k^2+m_k^2} = 0\,, \tag{5.18}$$

which has a few important consequences. First of all, it restricts m_k^2 from being nonnegative to positive values only. Next, it also demands that at small k, m_k^2 cannot be proportional to a positive power of k larger than or equal to unity. That being said, the masses, and hence the curvature will either converge to a positive constant, in which case there is no spontaneous symmetry breaking, or go to zero with a power of k smaller than one. In the latter case however, since m_k^2 approaches zero slower than k^2, the bosonic modes will decouple. The dynamics is then purely fermionic, hence a Landau treatment is possible. The resulting potential is analytic, and which out the possibility of m_k^2 approaching zero with a power of k between 0 and 1. This also rules out the second possibility, so m_k^2 has to approach a positive constant, with no spontaneous symmetry breaking possible.

Note that the above argument does not restrict m_k^2 from being negative at some nonzero k. Indeed direct numerical simulations show that the transitional potential does develop a minimum at some nonzero σ. However, at small k it evolves to $\sigma=0$. This can be seen in the left panel of Fig. 5.3. Intuitively the transition between these two regimes starts at the values of k inversely proportional to the system size, L. This is confirmed numerically by the direct numerical calculations shown in Fig. 5.3.

As seen in Fig. 5.3, the initial evolution of the minimum is independent of the system size. The curves start to deviate from each other when the discreteness of the momentum start to play an important role for mesonic and quark fluctuations. The right panel of Fig. 5.3 shows that even though there is no spontaneous symmetry breaking, i.e. the condensate vanishes for $H=0$, there is a substantial condensate for finite values of the symmetry breaking field H, and curves with high volume converge to the infinite volume result. This can be understood as follows: the pion mass is proportional to $\sqrt{H}$, and the finite volume can be qualitatively understood as an infrared cutoff of $2\pi/L$. If the pion mass is considerably larger than this IR

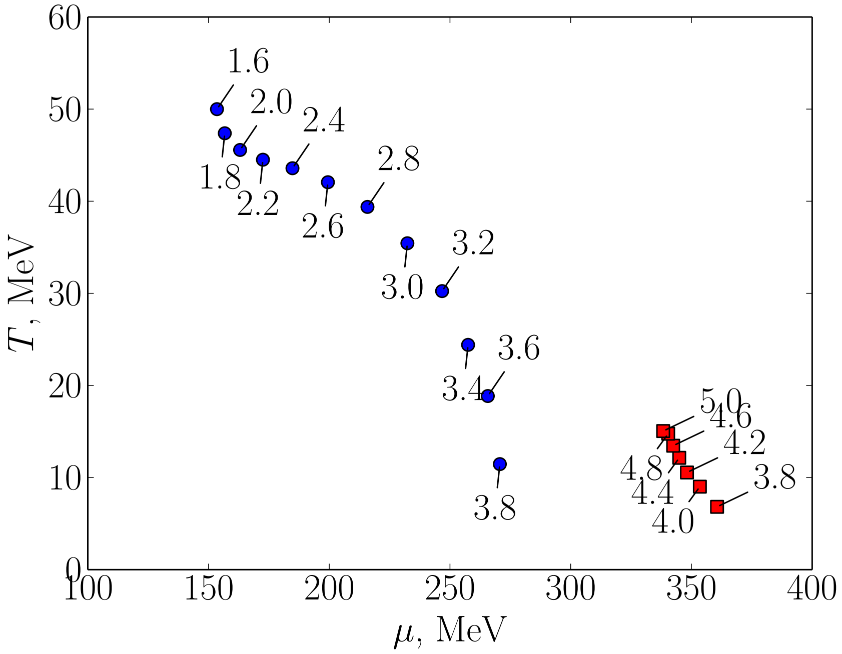

Figure 5.4.: The location of the ACPs as a function of the system size, L. Due to the numerical difficulties we were not able to resolve ACPs at temperatures below 5 MeV. The red points continuously approach the true critical point in the limit of infinite volume, which is already well approximated by $L = 5$ fm.

cutoff, no significant effects are expected to be seen. Hence, for larger symmetry breaking field, finite size effects kick in at a smaller system size.

5.3 Location of apparent critical point

We consider a system with a true critical point in an infinite volume. In a finite volume, instead there is an *apparent* critical point (ACP). There is some degree of arbitrariness in how one defines an apparent critical point. Here, we define the position of the apparent critical point as the location of the maximum in the corresponding chiral susceptibility, which is equivalent to a minimum in the sigma mass, m_σ. We should stress, however, that unlike the case of infinite volume, in a finite volume other definitions will give different positions for the apparent critical point.

With our definition, it is found that for some intermediate system size, the system has *two* apparent critical points, located at different values of T and μ. One of the apparent critical points, which we call ACP I, approaches the true critical point in the limit of infinite volume. As the volume decreases, the ACP I moves towards the zero temperature axis, in accordance with Ref. [161]. The second apparent critical point, which we call ACP II, appears near the zero temperature axis, and evolves to *higher* temperature as the volume decreases. The location of the two apparent critical points is depicted in Fig. 5.4. The emergence of a second apparent critical point influences the cumulants of the baryon number, and is studied in the next section.

To grasp the essence of the behavior of the critical point, let us consider a mean-field calculation by omitting the bosonic contribution. A recent study suggests that the apparent critical point within this approximation shows a qualitatively similar behavior [163]. In this calculation we fit the parameters to reproduce $m_q = 335$ MeV and $m_\sigma = 500$ MeV. For transparency,

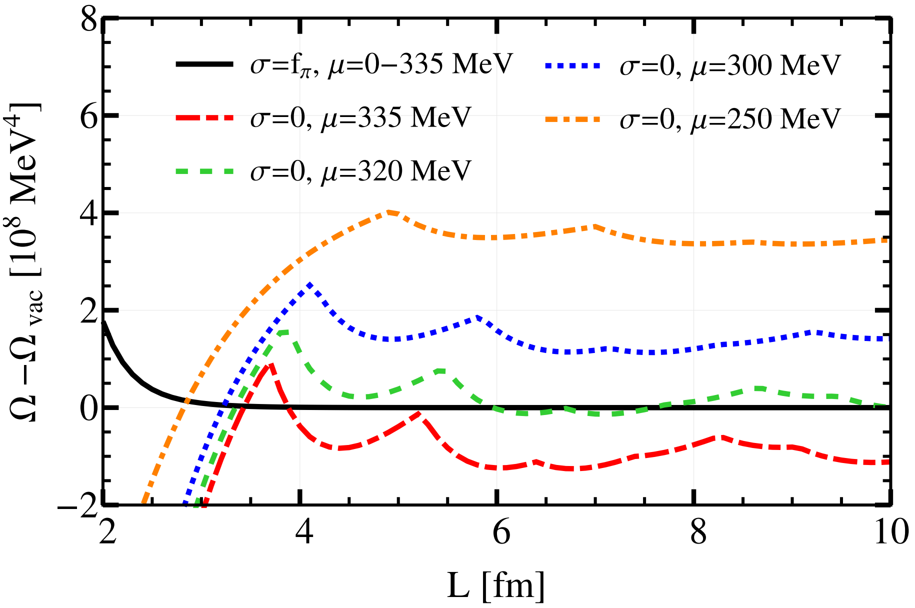

Figure 5.5.: The potential at $\sigma = f_\pi$ and $\sigma = 0$ as a function of the system size for different chemical potentials at vanishing temperature in the mean-field approximation.

we chose a slightly smaller sigma mass compared to the RG calculations. In this case the first-order phase transition occurs at slightly smaller chemical potential, and so the minimum of the potential at $\sigma = f_\pi$ is not influenced by finite density effects at the relevant chemical potentials.

In mean-field calculations one drops bosonic fluctuations, and there appears to be a second-order chiral phase transition even in finite volume. For simplicity, we consider the chiral limit at zero temperature. For each volume, at some intermediate chemical potential the system goes from the ground state at $\sigma = f_\pi$ to a chirally restored phase at $\sigma = 0$ through a first-order transition. We assume that where this transition happens on the $T = 0$ axis is related to the location of the critical end point in the plane of temperature and chemical potential.

At $T = 0$, the phase transition occurs when the condition

$$\Omega(\mu, L; \sigma = f_\pi) = \Omega(\mu, L; \sigma = 0) \tag{5.19}$$

is fulfilled. For chemical potentials $\mu < g_s f_\pi$, the left-hand side is independent of μ. After subtracting the value in infinite volume,

$$\Omega(\mu < g_s f_\pi, L; \sigma = f_\pi) - \Omega(0, \infty; f_\pi) = \nu_q \left(\frac{1}{L^3} \sum_{n_x, n_y, n_z} (E_1 - E_2) - \frac{1}{(2\pi)^3} \int d^3p \, (E_1 - E_2) \right), \tag{5.20}$$

with

$$E_1 = \sqrt{g_s^2 f_\pi^2 + q^2 + R_\Lambda(q)}, \quad E_2 = \sqrt{g_s^2 f_\pi^2 + q^2}, \quad q = \frac{2\pi}{L} \sqrt{n_x^2 + n_y^2 + n_z^2}. \tag{5.21}$$

This is depicted by the black, solid line in Fig. 5.5. The right-hand side of Eq. (5.19) depends on the chemical potential and is given by

$$\Omega(\mu, L; 0) = \frac{\nu_q}{L^3} \sum_{n_x, n_y, n_z} \left(\sqrt{q^2 + R_\Lambda(q)} - q - (\mu - q)\theta(\mu - q) \right), \tag{5.22}$$

where θ denotes again the Heaviside step function. Let us consider the finite density part of this function at constant chemical potential as the size of the system changes. It is expected that the finite density part [the μ-dependent term in Eq. (5.22)] will be affected by finite-volume effects stronger than the vacuum part, since we only probe modes up to the Fermi surface, and in small volumes they are few in number. The finite density part contributes with a negative sign, so as it gets larger, the value of the potential decreases driving a phase transition.

As the volume decreases, the contribution of each mode increases as $1/L^3$. On the other hand, as L decreases, the momentum of each mode goes up as $2\pi/L$, hence fewer modes fall below the Fermi momentum $q_f = \mu$ and less modes will contribute. In total, there is a balance between these two effects, so that at large L there is an oscillatory behavior, as shown in Fig. 5.5. If the volume is very small, say below $L = 3$ fm, only the zero mode contributes. This enhances the quark contribution to the potential at nonzero density at small volume, and triggers a first-order phase transition at lower values of the chemical potential. This is illustrated in Fig. 5.5, where the potential of the $\sigma = f_\pi$ solution is compared to the $\sigma = 0$ solution at different chemical potentials. When the two curves cross, there is a first-order phase transition in the given volume at the corresponding chemical potential. At relatively high volumes, i.e. above $L = 4$ fm, the phase transition occurs in the range $\mu = 320$-335 MeV. Its location as a function of system size is not monotonic due to oscillations. At low volumes, i.e. $L < 3.5$ fm, only the zero mode contributes to the finite density part, and the phase transition moves down to very low chemical potential: at $L = 3$ fm the chemical potential is $\mu = 250$ MeV. As the temperature is turned on, the transition line is expected to reach higher temperatures, since the phase transition at $T = 0$ is strengthened by the sudden change in the zero mode contribution to $\Omega(\sigma)$ at $\mu = g_s\sigma$.

This brief analysis suggests that the behavior of the ACP I is difficult to understand, as its location may show oscillatory behavior. In small volumes, the position of the apparent critical point is expected to move to very low chemical potentials, and its temperature is also expected to increase. This is in agreement with our findings about ACP II.

5.4 Cumulants

In this section we discuss the dependence of the cumulants of baryon number fluctuations on the size of the system. In particular, we consider the ratio of the fourth- to the second-order cumulant of quark number fluctuations. Up to an overall factor of 1/9, this corresponds to the same ratio for baryon number. The second- and fourth-order cumulants for quark number are

$$c_2 = \langle(\delta N_q)^2\rangle, \tag{5.23}$$

$$c_4 = \langle(\delta N_q)^4\rangle - 3\langle(\delta N_q)^2\rangle^2 \tag{5.24}$$

respectively, where $\delta N_q = N_q - \langle N_q\rangle$.

In the limit of infinite volume, as discussed in the previous chapter, a cumulant c_n is proportional to the volume times the susceptibility

$$c_n = VT^3\,\chi_n\,, \tag{5.25}$$

where

$$\chi_n = \frac{\partial^n}{\partial(\mu/T)^n}\left(\frac{p}{T^4}\right)\,. \tag{5.26}$$

Thus in infinite volume, it is natural to go from the experimentally observable cumulants to the susceptibilities by taking their ratio,

$$c_4/c_2 = \chi_4/\chi_2. \tag{5.27}$$

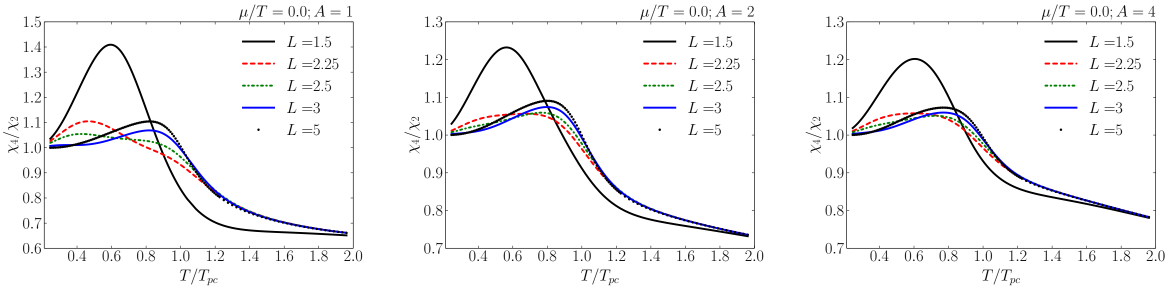

Figure 5.6.: The ratio of the fourth- to the second-order susceptibilities as a function of temperature for different system sizes and the anisotropy parameter A; the results are computed at zero chemical potential.

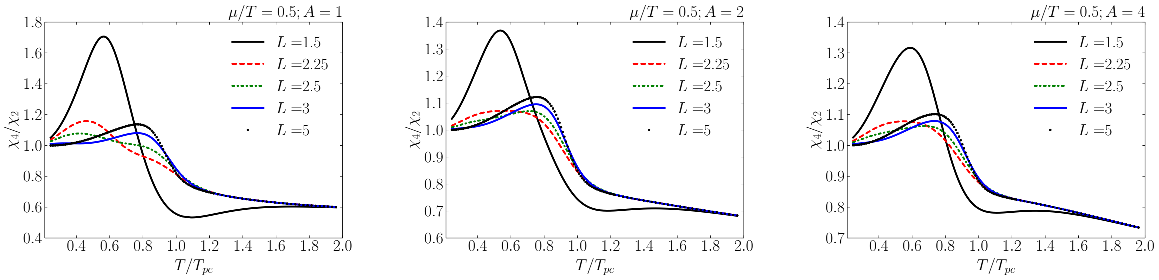

Figure 5.7.: The ratio of the fourth- to the second-order susceptibilities as a function of temperature for different system sizes and the anisotropy parameter A; the results are computed at $\mu/T = 0.5$.

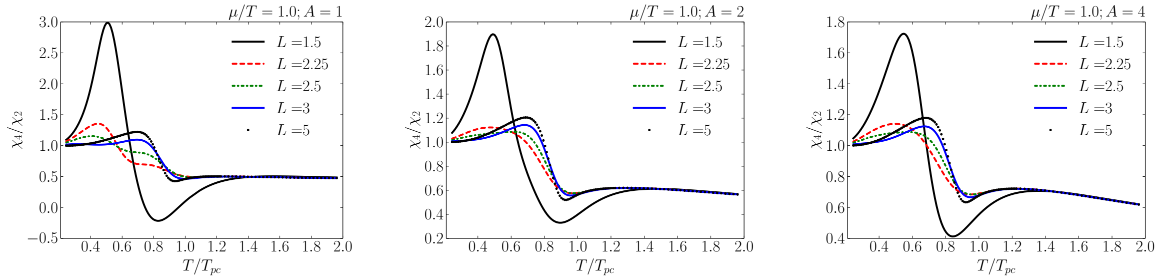

Figure 5.8.: The ratio of the fourth- to the second-order susceptibilities as a function of temperature for different system sizes and the anisotropy parameter A; the results are computed at $\mu/T = 1$.

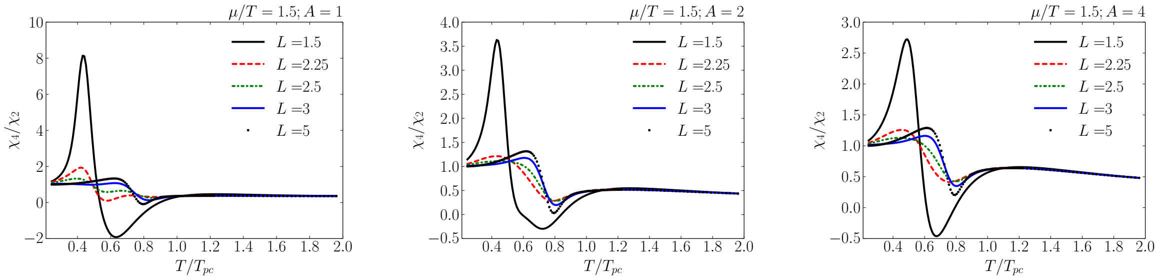

Figure 5.9.: The ratio of the fourth- to the second-order susceptibilities as a function of temperature for different system sizes and the anisotropy parameter A; the results are computed at $\mu/T = 1.5$.

In a finite volume, however, the factors of volume do *not* cancel. As we demonstrated in the previous section, the value of the chiral condensate depends upon the volume, and this influences the position of any apparent critical point.

In this calculation the flow equations were solved using the Chebyshev expansion of the potential. Additionally, a flow equation was solved for the density, which is closely related to χ_1. The higher order cumulants, i.e. χ_2 and χ_4 were extracted using numerical derivatives with respect to the chemical potential. In order to obtain the correct high-temperature behavior, quark contributions above the UV cutoff were taken into account perturbatively, as discussed in Sec. 2.5.

In Figs. 5.6, 5.7, 5.8 and 5.9, the dependence of the ratio χ_4/χ_2 on the temperature for different system sizes and different anisotropy parameters is shown. The calculations are done on lines of constant ratio of μ/T. We consider the values $\mu/T = 0, 0.5, 1, 1.5$. We can observe that the cumulant ratio does not vary much at high temperatures $T > 1.6T_{\mathrm{pc}}$ and is almost independent of the system size. However there is a significant variation in the vicinity of the phase transition and at lower temperatures. The figures also show that the location of the maximum of χ_4/χ_2 shifts to lower temperatures with the decreasing system size. The behavior of the maximal value of χ_4/χ_2 on the system size is nonmonotonic: with decreasing L, the maximum first decreases until L reaches about 3 fm and than increases. The dependence on the system size becomes more complicated at higher chemical potential, because the cumulants become sensitive to the ACP II.

These calculations suggest that there is a rather strong volume dependence of the ratio for system size less than 5 fm. This dependence becomes more significant with increasing value of chemical potential, because it probes regions of the phase diagram which are close to the apparent critical point ACP II.

The results indicate that an estimate of the effect of the volume fluctuations [136, 138] for system sizes less than 5 fm might be very challenging and should account not only for the explicit but also for the implicit volume dependence of the cumulants. It should be noted however that in this work we adopted periodic boundary conditions; obviously the system created in heavy-ion collision is not periodic, but rather a finite-volume system with inhomogeneity. The finite-volume effect discussed in this chapter thus can be quite different from those in the medium created in heavy-ion collisions.

Summary and outlook

In the present thesis we discussed aspects of chiral phase transitions in effective theories of QCD, mostly in thequark-meson (QM) and Polyakov-loop-extended quark-meson (PQM) models. The models were mainly treated using the functional renormalization group (FRG) approach, but often compared to mean-field studies. In Chapter 2, after the introduction to the model and to the FRG framework, a novel solution method to the FRG flow equations was outlined based on Chebyshev expansion. The method presented requires modest numerical efforts and is more accurate than the existing standard solution methods. Compared to the standard setup in the PQM model, we coupled the quarks to a vector field ω as well, which we treated on the mean-field level.

In Chapter 3 we discussed universal and nonuniversal aspects of the chiral phase transition and the corresponding magnetic equation of state in different effective models of QCD. The critical properties of the QM and PQM models were explored in the mean-field approximation, where only fermionic fluctuations are accounted for, and compared to those of a purely bosonic theory, the $O(N)$ linear sigma (LS) model in the $N \to \infty$ limit. In the QM and LS models the magnetic equation of state was computed analytically within the high temperature expansion. The effects of a gluonic background on the nonuniversal scaling parameters were assessed within the PQM model. The simple model studies were then compared to the FRG calculation of the QM model and to lattice QCD results.

We analyzed the scaling violation at nonzero quark masses in the context of recent lattice QCD results, which indicate that, at a physical pion mass, QCD lies in the scaling regime of the underlying second order phase transition. We showed that to understand the chiral critical properties of QCD it is not enough to have a model in the same universality class, but the model under question should approach criticality in a similar manner. We quantified this with dimensionless, nonuniversal parameters t_0, h_0 and z_0 that connect the physical quark mass and temperature scales with the dimensionless scaling variables of the universality class. We found that these nonuniversal quantities differ significantly from model to model and that this influences the size of the order parameter scaling window.

In the mean-field approximation of the QM and PQM models, the scaling violating contributions to the order parameter were found to remain small up to the physical pion mass. This is in qualitative agreement with the scaling behavior found in LQCD at the chiral crossover transition. On the other hand, in the $O(N)$ LS model, which we solved in the $N \to \infty$ limit, and in the FRG treatment of the QM model, we found that the fluctuations of the meson fields yield a much stronger scaling violation than that obtained in the mean-field models, which account only for fluctuations of fermions. In particular, we observed that the order parameter in the models with bosonic fluctuations follow the universal scaling law only for very small values of the pion mass. Consequently, at physical values of the pion mass, the chiral condensate in these models exhibits substantial deviations from the universal scaling law.

A very different scaling behavior of these models was linked to very different values of the nonuniversal scaling parameter z_0. In the mean-field calculations, z_0 was found to be roughly compatible with that obtained in LQCD, whereas in the LS model and in the FRG calculation of the QM model this parameter is almost an order of magnitude smaller. The value of z_0 is also reflected in the width of the crossover transition and the shift in the peak position of the chiral susceptibility with increasing pion mass. This analysis indicates that models where bosonic fluctuations are accounted for, tend to have a small z_0, a broad peak in the chiral susceptibility and a narrow critical region.

From general considerations in Landau theory we have obtained a connection between distinctive features of the scaling violation and specific properties of the coefficients of the effective potential. This provides a framework for discussing general characteristics of the scaling violation in terms of the model parameters and in particular to understand how the scaling function approaches the universal scaling curve. We found that, depending on the temperature dependence of the coefficients of the effective potential, the magnetic equation of state may exhibit a nontrivial structure with common crossing points for different values of the symmetry breaking field H. We have quantified these properties in the QM, PQM and LS models.

We also confirmed in the quark-meson model that as the tricritical point is approached along the $O(4)$ line, the size of the scaling window approaches zero. In the mean-field QM model we found that at intermediate chemical potentials the scaling window in one direction, namely in the h direction shows a peak. We related this behavior with the vanishing of the Landau coefficient c. Our FRG calculations indicated that similar peak survives in beyond mean-field calculations as well. There, we found a similar peak in both directions however.

The study of scaling in the FRG was based on the Taylor expansion of the potential. With this technique first order transitions cannot be studied and the method breaks down close to the TCP. To ensure that there are no artifacts caused by the breakdown of the method in the scaling window, a study based on the Chebyshev expansion of the potential is needed. This is postponed to a future work. A further possible improvement of the model is to include the running of the wave function renormalization factor. This improves the critical exponents and may provide a better description of the lattice QCD chiral transition.

In Chapter 4 we studied the influence of the chiral phase transition on fluctuation observables in a strongly interacting medium at finite temperature and net baryon number density. We focused on the properties of net-baryon-number fluctuations which are quantified by the n^{th}-order susceptibilities, χ_B^n. The cumulants χ_B^n are directly influenced by the chiral phase transition due to the coupling of the quarks to the scalar sigma field. Furthermore, since the χ_B^n are accessible experimentally, they are ideal observables for identifying the phase boundary and the critical structures in the QCD phase diagram.

The dynamics was modeled with the PQM model. To correctly account for the critical behavior at the chiral symmetry restoration transition in the $O(4)$ and $Z(2)$ universality classes, we employed the FRG in the presence of repulsive vector interactions.

The main point of our studies was to identify the relations between χ_B^n susceptibilities in different (T, μ_B) regions of the phase diagram. To reduce the influence of the noncritical characteristics of the model, like e.g. the mass spectrum or the kinematic cuts on particle momentum distributions, we computed ratios of susceptibilities. Here of particular interest are the ratios of the first and second order cumulants, χ_B^1/χ_B^2, the skewness, χ_B^3/χ_B^2, the kurtosis, χ_B^4/χ_B^2, and the sixth-order cumulant χ_B^6/χ_B^2. The higher-order ($n \geq 3$) cumulants are probes of chiral criticality and can be reconstructed experimentally in nucleus-nucleus collisions.

We have calculated, for the first time, the contour plots in the (T, μ_B) plane of the above ratios in the PQM model within FRG approach. We have quantified the systematic relations along the phase boundary and the phenomenological freeze-out line, extracted by fitting the skewness data. The influence of the repulsive interactions and the position of the critical endpoint on different χ_B^n ratios was also explored for the first time.

The model results were confronted with ratios of cumulants of net proton number measured by the STAR Collaboration in nucleus-nucleus collisions at energies ranging from $\sqrt{s} = 7.7$ GeV up to 200 GeV. Considering that the relations between different susceptibilities along the phase boundary are induced in part by the universal scaling functions common to QCD and PQM models, and the phenomenological observation that freeze-out in heavy-ion collisions appears near the QCD phase boundary, we have compared the experimental data and model results. The main objective was to verify if the systematics between net-baryon-number susceptibilities observed in the model calculations along the phase boundary are also reflected in the experimental data. To compare model predictions and data we have assumed that the $\sqrt{s}$-dependence of μ_q/T follows the phenomenological freeze-out conditions in nucleus-nucleus collisions. The validity of this assumption is supported by the observation that, for $\mu_q/T < 1$, the ratio of the first and second order cumulants is well approximated by $\chi_B^1/\chi_B^2 = \tanh(3\mu_q/T)$ in the model, in LQCD and in the data, using the adopted relation between beam energy and μ_q/T.

We have shown that the STAR data for the ratios composed of χ_B^n with $n = 1, 2, 3$ follow generic expectations, and thus that they are consistent with criticality at the chiral phase boundary. The quantitative agreement between the calculated cumulant ratios and STAR data is improved when the freeze-out line is determined by fitting χ_B^3/χ_B^1 to data. The data on the kurtosis ratio are also consistent with model systematics at energies $\sqrt{s} \geq 20$ GeV. However, the strong enhancement of $\kappa\sigma^2 > 1$, observed in nucleus-nucleus collisions at lower energies, is not reproduced by the model along the path in the (μ_q/T)- plane, where the ratios of lower order cumulants, χ_B^n with $n = 1, 2, 3$, are well described. We have shown, that this conclusion is not affected by the initial conditions nor by the parametrization of the Polyakov-loop potential.

Clearly, the comparison of model results and data is biased by the various assumptions and uncertainties, discussed in Sec. 4.4. However, in spite of all uncertainties, the ratios of net-proton-number susceptibilities obtained by STAR are, as shown in this study, largely consistent with the systematics expected near the chiral phase boundary.

Finally, in Chapter 5 we considered the QM model in a finite volume. We carried out our calculations using the FRG approach. We demonstrated that the use of the Litim regulator requires great care for finite-volume studies, and the use of an exponential regulator was proposed instead. We implemented finite volume with periodic boundary conditions, and we showed that in this case spontaneous symmetry breaking is absent, in agreement with the expectations.

We computed the chiral susceptibility in the phase diagram in a finite volume and we showed that for some volumes there are two distinct apparent critical points. One of them, which we called ACP I, is smoothly connected to the critical point of the infinite volume calculation when its location is considered as a function of volume. The location of this point moves to lower temperatures and higher chemical potentials with decreasing system size. The other apparent critical end point, ACP II, approaches the zero temperature axis and is not detectable for system size larger than 4 fm. For small system sizes however its location shifts towards higher temperatures and lower chemical potentials with decreasing system size.

Our main goal was to calculate the ratio of the fourth- to the second-order baryon number cumulant. We found that in small systems, $L < 5$ fm, there is a strong volume dependence, especially in the vicinity of the apparent critical points.

An obvious extension of the finite volume calculation is to implement the Polyakov loop and evaluate the finite-size effects on the baryon number cumulants with a realistic volume distribution. With the Polyakov loop included, direct comparison to the STAR data would be possible as discussed in Chapter 4. This is postponed to a future work.

Appendix A

Conventions

Here we briefly summarize the conventions used throughout this thesis. We work in natural units, in which energy, time, distance and temperature are all measured in *electronvolts* with appropriate prefactors. Due to this, throughout this work any combination and powers of the physical constants c, $\hbar$ and k_B will be omitted.

Square brackets and curly brackets with two arguments, if not stated otherwise, denote commutator and anticommutator, respectively,

$$[A,B] = AB - BA, \tag{A.1}$$

$$\{A,B\} = AB + BA. \tag{A.2}$$

In Minkowski space, we use the metric $\eta = \mathrm{diag}(+1,-1,-1,-1)$. We also apply a summation convention, namely for any internal index, such as flavor, spin, isospin or color, that appears two times in a term, automatic summation is meant, regardless of the position of the index (upper or lower). Internal indexes are denoted by Latin letters. Greek letters denote space-time indexes. Two lower indexes in a term implies contraction with Euclidean metric, while one upper and one lower index-pair implies Minkowski metric and summation,

$$a_\mu b_\mu = a_1 b_1 + a_2 b_2 + a_3 b_3 + a_4 b_4, \qquad a_\mu b^\mu = a_0 b_0 - a_1 b_1 - a_2 b_2 - a_3 b_3. \tag{A.3}$$

We use an explicit representation for the Gamma-matrices, and in Minkowski metric they are given by

$$\gamma^0 = \begin{pmatrix} 0 & I_{2\times2} \\ I_{2\times2} & 0 \end{pmatrix}, \quad \gamma^j = \begin{pmatrix} 0 & \tau^j \\ -\tau^j & 0 \end{pmatrix} \quad \text{for } j = 1,2,3. \tag{A.4}$$

Furthermore, one defines a fifth Gamma-matrix,

$$\gamma_5 = i\gamma^0\gamma^1\gamma^2\gamma^3 = \begin{pmatrix} -I_{2\times2} & 0 \\ 0 & I_{2\times2} \end{pmatrix}. \tag{A.5}$$

The Gamma matrices then fulfill the anticommutation relations

$$\{\gamma^\mu, \gamma^\nu\} = 2\eta^{\mu\nu} I_{4\times4}, \qquad \{\gamma^\mu, \gamma_5\} = 0. \tag{A.6}$$

The Euclidean Gamma matrices are defined using their Minkowski definition as

$$\gamma_1^E = -i\gamma^1, \qquad \gamma_2^E = -i\gamma^2, \qquad \gamma_3^E = -i\gamma^3, \qquad \gamma_4^E = \gamma^0 \equiv \gamma_0^E. \tag{A.7}$$

With γ_5 unchanged, they fulfill the anticommutation relations

$$\{\gamma_\mu^E, \gamma_\nu^E\} = 2\delta_{\mu\nu} I_{4\times4}, \qquad \{\gamma_\mu^E, \gamma_5\} = 0. \tag{A.8}$$

Appendix B

Special unitary matrix groups

In this appendix we briefly review some of the properties of special unitary matrix group of size N, which is usually denoted by $SU(N)$. Any matrix U in this group has the following properties:

- The dimension of U is $N \times N$.
- U is invertible, and the inverse of U equals the conjugate transpose of U. Formally, $U_{ij}U^*_{kj} = \delta_{ik}$.
- The determinant of U is unity.

The matrices fulfilling these properties form a continuous group with N^2-1 free parameters. In general each element of the group can be expressed by the parameters $\{\theta_1, \theta_2 \ldots, \theta_{N^2-1}\}$ using the *generators* of the group $\{T_1, T_2 \ldots, T_{N^2-1}\}$ and the exponential mapping,

$$U = \exp\left(i \sum_j T_j \theta_j \right). \tag{B.1}$$

Now we turn to the the most relevant instances of this class of groups, namely to $SU(2)$ and $SU(3)$. The group of special unitary matrices of size 2×2 are denoted by $SU(2)$. The three generators of this group are the Pauli matrices, and are given by

$$\tau^1 = \begin{pmatrix} 0 & 1 \\ 1 & 0 \end{pmatrix}, \quad \tau^2 = \begin{pmatrix} 0 & -i \\ i & 0 \end{pmatrix}, \quad \tau^3 = \begin{pmatrix} 1 & 0 \\ 0 & -1 \end{pmatrix}. \tag{B.2}$$

From their definition it is apparent that they are traceless, hermitian and their determinant equals -1. They obey the commutation and anticommutation relations

$$[\tau^i, \tau^j] = \tau^i\tau^j - \tau^j\tau^i = 2i\epsilon_{ijk}\tau^k, \tag{B.3}$$
$$\{\tau^i, \tau^j\} = \tau^i\tau^j + \tau^j\tau^i = 2\delta_{ij}I_{2\times 2}. \tag{B.4}$$

From this follows simply the identity

$$\tau^i\tau^j = \delta_{ij} + i\epsilon_{ijk}\tau^k \tag{B.5}$$

as well. Based on this identity, further useful properties are easy to prove:

$$(\vec{a}\vec{\tau})^2 = a_i a_j \left(\delta_{ij} + i\epsilon_{ijk}\tau_k\right) = a^2, \tag{B.6}$$

which in turn can be used to prove

$$\exp\left(ib\vec{n}\vec{\tau}\right) = \cos b + i\left(\vec{n}\vec{\tau}\right)\sin b, \tag{B.7}$$

where $\vec{n}$ is a unit vector.

The group of special unitary matrices of size 3 × 3 is denoted by $SU(3)$. The eight generators of this group are characterized by the Gell-Mann matrices,

$$\lambda^1 = \begin{pmatrix} 0 & 1 & 0 \\ 1 & 0 & 0 \\ 0 & 0 & 0 \end{pmatrix}, \quad \lambda^2 = \begin{pmatrix} 0 & -i & 0 \\ i & 0 & 0 \\ 0 & 0 & 0 \end{pmatrix}, \quad \lambda^3 = \begin{pmatrix} 1 & 0 & 0 \\ 0 & -1 & 0 \\ 0 & 0 & 0 \end{pmatrix},$$
$$\lambda^4 = \begin{pmatrix} 0 & 0 & 1 \\ 0 & 0 & 0 \\ 1 & 0 & 0 \end{pmatrix}, \quad \lambda^5 = \begin{pmatrix} 0 & 0 & -i \\ 0 & 0 & 0 \\ i & 0 & 0 \end{pmatrix},$$
$$\lambda^6 = \begin{pmatrix} 0 & 0 & 0 \\ 0 & 0 & 1 \\ 0 & 1 & 0 \end{pmatrix}, \quad \lambda^7 = \begin{pmatrix} 0 & 0 & 0 \\ 0 & 0 & -i \\ 0 & i & 0 \end{pmatrix}, \quad \lambda^8 = \frac{1}{\sqrt{3}} \begin{pmatrix} 1 & 0 & 0 \\ 0 & 1 & 0 \\ 0 & 0 & -2 \end{pmatrix}. \tag{B.8}$$

They fulfill the commutation relations of the $su(3)$ algebra

$$[t^a, t^b] = i f_{abc} t^c, \tag{B.9}$$

where $t^a = \lambda^a/2$ are the generators and f_{abc} are the totally antisymmetric structure constants. Their independent, nonvanishing elements are given by

$$f_{123} = 1, \quad f_{147} = f_{165} = f_{246} = f_{257} = f_{345} = f_{376} = \frac{1}{2}, \quad f_{458} = f_{678} = \frac{\sqrt{3}}{2}. \tag{B.10}$$

Appendix C

Basic properties of Chebyshev polynomials

The Chebyshev polynomials are defined on the interval $x \in [-1,1]$ as

$$T_n(x) = \cos\left(n \arccos(x)\right), \quad \text{or equivalently} \quad T_n(\cos\vartheta) = \cos(n\vartheta). \tag{C.1}$$

Using this simple trigonometric definition, many of their properties can be easily proven. The first few Chebyshev polynomials are

$T_0(x) = 1$	$T_2(x) = 2x^2 - 1$	$T_4(x) = 8x^4 - 8x^2 + 1$
$T_1(x) = x$	$T_3(x) = 4x^3 - 3x$	$T_5(x) = 16x^5 - 20x^3 + 5x$

One can immediately see that the polynomials of even indexes are even functions of x and the ones with odd indexes are odd functions. The Nth polynomial has exactly N number of zeroes, which can be simply deduced from the trigonometric form,

$$x_k = \cos\left(\frac{\pi(1/2+k)}{N}\right), \quad k = 0,\ldots,N-1. \tag{C.2}$$

The Chebyshev polynomials also fulfill the following relations:

- **Recurrence**: $T_{n+1}(x) = 2xT_n(x) - T_{n-1}(x)$. This identity can be simply proven using the trigonometric form as follows:

$$\cos(n+1)\theta + \cos(n-1)\theta = 2\cos\theta\cos n\theta \tag{C.3}$$

- **Recurrence for derivatives:** $\frac{T'_{n+1}(x)}{n+1} - \frac{T'_{n-1}(x)}{n-1} = 2T_n(x)$. Using the trigonometric form one can express the derivative of the Chebyshev polynomial the following way:

$$\partial_{\cos\theta} T_n(\cos\theta) = (\partial_\theta \cos\theta)^{-1} \partial_\theta T_n(\cos\theta) = n\frac{\sin n\theta}{\sin\theta}. \tag{C.4}$$

  On the left hand side now we can use the identity $\sin(n+1)\theta - \sin(n-1)\theta = 2\cos n\theta\sin\theta$ and replace $\cos\theta$ with x to yield the desired relation.

- **Orthogonality**:

$$\int_{-1}^{1} dx \frac{T_n(x)T_m(x)}{\sqrt{1-x^2}} = \int_0^\pi d\vartheta \cos n\vartheta \cos m\vartheta = \begin{cases} \pi & \text{if n = m = 0,} \\ \frac{\pi}{2}\delta_{nm} & \text{elsewise.} \end{cases} \tag{C.5}$$

- **Summation rule**:

$$\begin{aligned}\sum_{k=0}^{m-1} T_i(x_k)T_j(x_k) &= \sum_{k=0}^{m-1}\cos\left(\frac{i\pi(1/2+k)}{m}\right)\cos\left(\frac{j\pi(1/2+k)}{m}\right)\\ &= \frac{1}{2}\sum_{k=0}^{m-1}\left[\cos\left(\frac{(i+j)\pi(1/2+k)}{m}\right)+\cos\left(\frac{(i-j)\pi(1/2+k)}{m}\right)\right]\\ &= \begin{cases} m & \text{if i = j = 0,}\\ \frac{m}{2}\delta_{ij} & \text{elsewise.}\end{cases}\end{aligned} \tag{C.6}$$

Note that the same line of argument can be used if i and j have the same parity and we sum over the positive roots of T_{2m}:

$$\sum_{k=0}^{m-1} T_{2i}(x_k)T_{2j}(x_k) = \sum_{k=0}^{m-1}\cos\left(\frac{2i\pi(1/2+k)}{2m}\right)\cos\left(\frac{2j\pi(1/2+k)}{2m}\right) = \begin{cases} m & \text{if i = j = 0,}\\ \frac{m}{2}\delta_{ij} & \text{elsewise.}\end{cases} \tag{C.7}$$

Due to the orthogonality, any real function on $[-1,1]$ can be expressed in terms of Chebyshev polynomials and the coefficients are uniquely determined:

$$f(x) = \alpha_0 T_0(x) + \alpha_1 T_1(x) + \alpha_2 T_2(x) + \ldots, \tag{C.8}$$

$$\alpha_0 = \frac{1}{\pi}\int_{-1}^{1}\frac{dx}{\sqrt{1-x^2}}T_0(x)f(x), \tag{C.9}$$

$$\alpha_i = \frac{2}{\pi}\int_{-1}^{1}\frac{dx}{\sqrt{1-x^2}}T_i(x)f(x). \tag{C.10}$$

If given such an expansion, differentiation and integration can be performed analytically.

C.1 Differentiation and integration of Chebyshev expansion

To differentiate Chebyshev series we use the recurrence relation for the derivatives repeatedly. This gives us for even and odd polynomials, respectively,

$$\frac{T'_{2n}(x)}{2n} = 2(T_{2n-1} + T_{2n-3} + \ldots + T_1), \tag{C.11}$$

$$\frac{T'_{2n+1}(x)}{2n+1} = 2(T_{2n} + T_{2n-2} + \ldots + T_2) + T_0. \tag{C.12}$$

Consider we have a Chebyshev series containing only even polynomials,

$$f(x) = \sum_{n=0}^{N-1}\alpha_n T_{2n}(x). \tag{C.13}$$

The first and second derivatives can also be expressed as Chebyshev series as

$$f'(x) = \sum_{n=0}^{N-2}\beta_n T_{2n+1}(x), \qquad f''(x) = \sum_{n=0}^{N-2}\gamma_n T_{2n}(x), \tag{C.14}$$

where the coefficients are given by the linear combinations

$$\beta_n = 4\sum_{k=n+1}^{N-1} k\alpha_k, \qquad \gamma_n = (2-\delta_{n0})\sum_{k=n}^{N-2}(2k+1)\beta_k. \tag{C.15}$$

To integrate a Chebyshev series we start from the recurrence relation for the derivatives again. Integrating both sides yields

$$\int T_k(x)dx = \frac{1}{2}\left(\frac{T_{k+1}}{k+1} - \frac{T_{k-1}}{k-1}\right). \tag{C.16}$$

This formula does not apply for $k=0$ and $k=1$. In these cases we have to use

$$\int T_0(x)dx = \int dx = x = T_1(x), \qquad \int T_1(x)dx = \int x dx = \frac{x^2}{2} = \frac{T_2(x)}{4} + const. \tag{C.17}$$

If we consider a Chebyshev series containing both odd and even terms, $f(x) = \sum_{n=0}^{N-1} \alpha_n T_n(x)$, its integral is given by

$$\int f(x)dx = \sum_{n=0}^{N} \beta_n T_n(x), \quad \text{with} \quad \beta_1 = \frac{2\alpha_0 - \alpha_2}{2}, \quad \beta_i = \frac{\alpha_{i-1} - \alpha_{i+1}}{2i} \text{ for } i > 1. \tag{C.18}$$

Note that β_0 is the coefficient of the constant term and hence is undetermined.

C.2 Solution of partial differential equations

One can use the Chebyshev polynomial expansion to solve partial differential equations of the form

$$\partial_t f(x,t) = g(x), \tag{C.19}$$

where $g(x)$ may depend on the value of the function f and on any x derivatives of the function, and f is defined on $x \in [-1,1]$. We assume the boundary condition defines $f(x)$ for $t=0$ for all x and we wish to solve it up to $t=T$. Using the expansion formula (C.8), we expand the function $f(x)$ for $t=0$ up to order N and derive an equation for the t evolution of the expansion coefficients. We write hence

$$f(x,t) = \sum_{n=0}^{N-1} \alpha_n(t) T_n(x). \tag{C.20}$$

The flow of the coefficients can be determined at any x values:

$$\partial_t f(x,t) = \sum_{n=0}^{N-1} \partial_t \alpha_n(t) T_n(x). \tag{C.21}$$

In order to get N equations we need N extraction points. To minimize the sampling error we pick the roots of the N-th Chebyshev polynomial given by

$$x_k = \cos\left(\frac{(k+1/2)\pi}{N}\right), \qquad k = 0,1,2 \ldots N-1. \tag{C.22}$$

We now have N equations to determine the flow of the coefficients namely

$$\sum_{n=0}^{N-1} \partial_t \alpha_n(t) T_n(x_k) = g(x_k). \tag{C.23}$$

To have an explicit formula for the derivative of the coefficients we perform the following summation:

$$\sum_{n=0}^{N-1} \partial_t \alpha_n(t) \sum_{k=0}^{N-1} T_n(x_k) T_m(x_k) = \sum_{k=0}^{N-1} g(x_k) T_m(x_k). \tag{C.24}$$

Now we apply the summation rule (C.6) and we get

$$\partial_t \alpha_0(t) = \frac{1}{N} \sum_{k=0}^{N-1} g(x_k) T_0(x_k), \tag{C.25}$$

$$\partial_t \alpha_i(t) = \frac{2}{N} \sum_{k=0}^{N-1} g(x_k) T_i(x_k). \tag{C.26}$$

Appendix D

Model parameters, initial conditions, Polyakov-loop potentials

In this appendix, the model parameters are summarized that were used throughout this work in the QM and PQM models. Since the Polyakov loop does not couple to the vacuum fluctuations and the parameters are set by vacuum calculations, the parameters in the two models coincide. The exact values of the parameters depend on the solution scheme, and hence in Sec. D.1 these are provided for each scheme. Then, in Sec. D.2, parameters of the Polyakov-loop potential are given. In principle, any set of initial conditions can be used with any Polyakov-loop potential.

D.1 Chiral parameters

The constrains guiding our initial condition selection were sketched in Sec. 2.1, where we discussed the quark-meson model in the mean-field approximation. Using the FRG framework, the strength of the external field and the value of the Yukawa coupling, g_s, are still given by

$$\sigma_M(T=0,\mu=0)=f_\pi\approx 93\text{ MeV},\qquad H=m_\pi^2 f_\pi,\qquad g_s\sigma_M(T=0,\mu=0)=m_c, \tag{D.1}$$

where σ_M denotes the location of the minimum of the potential at $k=0$ and m_c stands for the constituent quark mass. In order to be able to tune the location of the minimum of the potential, σ_M, and the sigma meson mass, we need two parameters in the UV potential. Accordingly, the UV mesonic potential is parametrized as

$$U_{k=\Lambda}=\lambda\rho^2+m^2\rho=\frac{\lambda}{4}(\sigma^2+\vec{\pi}^2)^2+\frac{m^2}{2}(\sigma^2+\vec{\pi}^2). \tag{D.2}$$

The UV scale Λ, where the flow is started, the parameters of the potential, the constituent quark mass and the corresponding sigma mass are given by

$$\Lambda=700\text{ MeV},\quad m_\sigma\approx 410\text{ MeV},\quad \lambda=-1,\quad m^2=2.9\cdot10^5\text{ MeV}^2,\quad m_c=300\text{ MeV}, \tag{D.3}$$

$$\Lambda=950\text{ MeV},\quad m_\sigma\approx 500\text{ MeV},\quad \lambda=1.3,\quad m^2=5.668\cdot10^5\text{ MeV}^2,\quad m_c=300\text{ MeV}, \tag{D.4}$$

$$\Lambda=950\text{ MeV},\quad m_\sigma\approx 600\text{ MeV},\quad \lambda=4.22,\quad m^2=5.838\cdot10^5\text{ MeV}^2,\quad m_c=335\text{ MeV}, \tag{D.5}$$

$$\Lambda=950\text{ MeV},\quad m_\sigma\approx 650\text{ MeV},\quad \lambda=41.3,\quad m^2=7.85\cdot10^5\text{ MeV}^2,\quad m_c=335\text{ MeV}, \tag{D.6}$$

$$\Lambda=950\text{ MeV},\quad m_\sigma\approx 585\text{ MeV},\quad \lambda=27.8,\quad m^2=5.668\cdot10^5\text{ MeV}^2,\quad m_c=300\text{ MeV}, \tag{D.7}$$

where the parameters in Eq. (D.4), were introduced in Ref. [164]. The first four sets are for the Litim regulator. The parameter sets given in Eqs. (D.3) and (D.4) are to be used with the grid or pseudospectral methods, while the parameter set given in Eq. (D.5) is to be used with the Taylor method truncated after a_3, and the parameter set given in Eq. (D.6) is for the Taylor method truncated after a_4. The parameters in Eq. (D.7) are for the exponential regulator using the pseudospectral (or the grid) method. Using a parameter set with the wrong solution method or wrong regulator will result in wrong vacuum physics.

Using the Taylor method, the parameters of the UV potential have to be translated onto initial conditions for the Taylor coefficients. This can be done analytically. In the chiral limit the translation reads

$$a_1 = m^2, \quad a_2 = 2\lambda, \quad a_3 = 0, \quad a_4 = 0, \tag{D.8}$$

while for finite pion mass, after solving the cubic gap equation,

$$\rho = \frac{\sigma_\Lambda^2}{2}, \quad a_2 = 2\lambda, \quad a_3 = 0, \quad a_4 = 0. \tag{D.9}$$

with

$$\sigma_\Lambda = \frac{2m}{\sqrt{3\lambda}} \sinh\left(\frac{1}{3}\operatorname{arcsinh}\left(\frac{3H}{2m^3}\sqrt{3\lambda}\right)\right), \tag{D.10}$$

where $H = m_\pi^2 f_\pi$ is the external field, assuming that here we solve an equation for ρ rather than for a_1.

D.2 Polyakov-loop potential parameters

To verify possible model dependence of our results, we have considered different parameterizations of the Polyakov-loop potential.

We apply the polynomial Polyakov-loop potential [38], as

$$\frac{\mathcal{U}(T;\Phi,\bar{\Phi})}{T^4} = -\frac{b_2(T)}{2}\left(\Phi\bar{\Phi}\right) - \frac{b_3}{6}\left(\Phi^3 + \bar{\Phi}^3\right) + \frac{b_4}{4}\left(\Phi\bar{\Phi}\right)^2, \tag{D.11}$$

where $b_3 = 0.75$, $b_4 = 7.5$, and

$$b_2(T) = a_0 + a_1\left(\frac{T_0}{T}\right) + a_2\left(\frac{T_0}{T}\right)^2 + a_3\left(\frac{T_0}{T}\right)^3, \tag{D.12}$$

with $a_0 = 6.75$, $a_1 = -1.95$, $a_2 = 2.625$, $a_3 = -7.44$, and $T_0 = 270\,\mathrm{MeV}$.

The parameter T_0 corresponds to the value of the critical temperature at the first order deconfinement phase transition in a pure Yang-Mills theory. Effects of unquenching can be taken into account by changing T_0. In the case of two quark flavors, we use $T_0 = 208\,\mathrm{MeV}$ from Ref. [45].

The second potential applied in our calculations, accounts for the color group structure, and reproduces lattice results on the equation of state and fluctuations of the Polyakov loops, in a pure SU(3) gauge theory. The potential is parameterized [84], as

$$\begin{aligned}\frac{\mathcal{U}(T;\Phi,\bar{\Phi})}{T^4} &= -\frac{1}{2}a(T)\left(\Phi\bar{\Phi}\right) + b(T)\ln M_H(\Phi,\bar{\Phi}) \\ &\quad + \frac{1}{2}c(T)\left(\Phi^3 + \bar{\Phi}^3\right) + d(T)\left(\Phi\bar{\Phi}\right)^2,\end{aligned} \tag{D.13}$$

where

$$M_H(\Phi,\bar{\Phi}) = \left(1 - 6\Phi\bar{\Phi} + 4\left(\Phi^3 + \bar{\Phi}^3\right) - 3\left(\Phi\bar{\Phi}\right)^2\right). \tag{D.14}$$

a_1	a_2	a_3	a_4	a_5
-44.14	151.4	-90.0677	2.77173	3.56403
b_1	b_2	b_3	b_4	
-0.32665	-82.9823	3.0	5.85559	
c_1	c_2	c_3	c_4	c_5
-50.7961	114.038	-89.4596	3.08718	6.72812
d_1	d_2	d_3	d_4	d_5
27.0885	-56.0859	71.2225	2.9715	6.61433

Table D.1.: Parameters of the Polyakov-loop potential introduced in Eqs. (D.13) and (D.15).

SET	Initial conditions	Polyakov-loop potential
A	(D.3)	(D.13)
B	(D.3)	(D.11)
C	(D.4)	(D.13)
D	(D.4)	(D.11)

Table D.2.: Different combinations of the initial conditions and the Polyakov-loop potentials, used in the PQM model.

The temperature dependent coefficients are given by

$$a(T) = \frac{a_1 t^2 + a_2 t + a_3}{t^2 + a_4 t + a_5}, \quad b(T) = b_1 t^{-b_4}\left(1 - e^{b_2/t^{b_3}}\right),$$
$$c(T) = \frac{c_1 t^2 + c_2 t + c_3}{t^2 + c_4 t + c_5}, \quad d(T) = \frac{d_1 t^2 + d_2 t + d_3}{t^2 + d_4 t + d_5}, \tag{D.15}$$

where $t = T/T_0$. The numerical values of the constants in Eq. (D.15), are summarized in Table D.1. We set $T_0 = 270$ MeV for this potential. Lower values of T_0 would result in distinct position of the peaks of the Polyakov loop and chiral susceptibilities, which is in contrast to LQCD results.

A simplified parametrization of the potential is given in Ref. [40]. Here, the temperature dependent coefficients are

$$a(T) = a_0 + a_1\left(\frac{T_0}{T}\right) + a_2\left(\frac{T_0}{T}\right)^2, \quad b(T) = b_3\left(\frac{T_0}{T}\right)^3, \quad c(T) = 0, \quad d(T) = 0, \tag{D.16}$$

with the parameters

$$a_0 = 3.51, \quad a_1 = -2.47, \quad a_2 = 15.2, \quad b_3 = -1.75, \quad T_0 = 270\,\text{MeV}. \tag{D.17}$$

We used this simplified parametrization for the scaling study of the PQM model in the mean-field approximation. In all other cases the potential in Eq. (D.13) was used with the more complex parametrization (D.15).

From the two parametrization of the Polyakov-loop potentials, Eqs. (D.11) and (D.13), and the two chiral initial conditions defined in Eqs. (D.3) and (D.4), we define in Table D.2, the four different parameter sets that are used in our calculations to study the influence of the model assumptions on the final results. If the parameter set is not explicitly specified, then results refer to set A.

Bibliography

[1] M. Gell-Mann, “A Schematic Model of Baryons and Mesons,” Phys. Lett. **8**, 214 (1964).

[2] G. Zweig, “An SU(3) model for strong interaction symmetry and its breaking. Version 2,” in *Developments in the Quark Theory of Hadrons. Volume 1. 1964 - 1978*, edited by D. Lichtenberg and S. P. Rosen (1964) pp. 22–101.

[3] M. Breidenbach, J. I. Friedman, H. W. Kendall, E. D. Bloom, D. H. Coward, H. C. DeStaebler, J. Drees, L. W. Mo, and R. E. Taylor, “Observed Behavior of Highly Inelastic electron-Proton Scattering,” Phys. Rev. Lett. **23**, 935 (1969).

[4] E. D. Bloom *et al.*, “High-Energy Inelastic e p Scattering at 6-Degrees and 10-Degrees,” Phys. Rev. Lett. **23**, 930 (1969).

[5] J. I. Friedman and H. W. Kendall, “Deep inelastic electron scattering,” Ann. Rev. Nucl. Part. Sci. **22**, 203 (1972).

[6] J. D. Bjorken and E. A. Paschos, “Inelastic Electron Proton and gamma Proton Scattering, and the Structure of the Nucleon,” Phys. Rev. **185**, 1975 (1969).

[7] K. A. Olive *et al.* (Particle Data Group), “Review of Particle Physics,” Chin. Phys. C **38**, 090001 (2014).

[8] D. J. Gross and F. Wilczek, “Ultraviolet Behavior of Nonabelian Gauge Theories,” Phys. Rev. Lett. **30**, 1343 (1973).

[9] D. J. Gross and F. Wilczek, “Asymptotically Free Gauge Theories. 1,” Phys. Rev. D **8**, 3633 (1973).

[10] D. J. Gross and F. Wilczek, “Asymptotically Free Gauge Theories. 2,” Phys. Rev. D **9**, 980 (1974).

[11] H. D. Politzer, “Reliable Perturbative Results for Strong Interactions?” Phys. Rev. Lett. **30**, 1346 (1973).

[12] S. Bethke, “Experimental tests of asymptotic freedom,” Prog. Part. Nucl. Phys. **58**, 351 (2007).

[13] S. Schael *et al.* (ALEPH), “Branching ratios and spectral functions of tau decays: Final ALEPH measurements and physics implications,” Phys. Rept. **421**, 191 (2005).

[14] G. ’t Hooft, “On the Phase Transition Towards Permanent Quark Confinement,” Nucl. Phys. B **138**, 1 (1978).

[15] L. D. McLerran and B. Svetitsky, “A Monte Carlo Study of SU(2) Yang-Mills Theory at Finite Temperature,” Phys. Lett. B **98**, 195 (1981).

[16] L. D. McLerran and B. Svetitsky, “Quark Liberation at High Temperature: A Monte Carlo Study of SU(2) Gauge Theory,” Phys. Rev. D **24**, 450 (1981).

[17] A. M. Polyakov, "Thermal Properties of Gauge Fields and Quark Liberation," Phys. Lett. B **72**, 477 (1978).

[18] G. 't Hooft, "A Property of Electric and Magnetic Flux in Nonabelian Gauge Theories," Nucl. Phys. B **153**, 141 (1979).

[19] B. Svetitsky and L. G. Yaffe, "Critical Behavior at Finite Temperature Confinement Transitions," Nucl. Phys. B **210**, 423 (1982).

[20] L. G. Yaffe and B. Svetitsky, "First Order Phase Transition in the SU(3) Gauge Theory at Finite Temperature," Phys. Rev. D **26**, 963 (1982).

[21] B. Svetitsky, "Symmetry Aspects of Finite Temperature Confinement Transitions," Phys. Rept. **132**, 1 (1986).

[22] F. Karsch, "Lattice QCD at high temperature and density," Lect. Notes Phys. **583**, 209 (2002).

[23] A. Dumitru, R. D. Pisarski, and D. Zschiesche, "Dense quarks, and the fermion sign problem, in a SU(N) matrix model," Phys. Rev. D **72**, 065008 (2005).

[24] GSI Theory Department, FAIR Research Webpage .

[25] R. D. Pisarski and F. Wilczek, "Remarks on the Chiral Phase Transition in Chromodynamics," Phys. Rev. D **29**, 338 (1984).

[26] Y. Aoki, G. Endrodi, Z. Fodor, S. D. Katz, and K. K. Szabo, "The Order of the quantum chromodynamics transition predicted by the standard model of particle physics," Nature **443**, 675 (2006).

[27] S. Borsanyi, Z. Fodor, C. Hoelbling, S. D. Katz, S. Krieg, C. Ratti, and K. K. Szabo (Wuppertal-Budapest), "Is there still any T_c mystery in lattice QCD? Results with physical masses in the continuum limit III," JHEP **09**, 073 (2010).

[28] M. Asakawa and K. Yazaki, "Chiral Restoration at Finite Density and Temperature," Nucl. Phys. A **504**, 668 (1989).

[29] A. Barducci, R. Casalbuoni, S. De Curtis, R. Gatto, and G. Pettini, "Chiral Symmetry Breaking in QCD at Finite Temperature and Density," Phys. Lett. B **231**, 463 (1989).

[30] F. Wilczek, "Application of the renormalization group to a second order QCD phase transition," Int. J. Mod. Phys. A **07**, 3911 (1992).

[31] A. M. Halasz, A. D. Jackson, R. E. Shrock, M. A. Stephanov, and J. J. M. Verbaarschot, "On the phase diagram of QCD," Phys. Rev. D **58**, 096007 (1998).

[32] Z. Fodor and S. D. Katz, "A New method to study lattice QCD at finite temperature and chemical potential," Phys. Lett. B **534**, 87 (2002).

[33] C. R. Allton, S. Ejiri, S. J. Hands, O. Kaczmarek, F. Karsch, E. Laermann, C. Schmidt, and L. Scorzato, "The QCD thermal phase transition in the presence of a small chemical potential," Phys. Rev. D **66**, 074507 (2002).

[34] D. Sexty, "Simulating full QCD at nonzero density using the complex Langevin equation," Phys. Lett. B **729**, 108 (2014).

[35] Y. Nambu and G. Jona-Lasinio, “Dynamical Model of Elementary Particles Based on an Analogy with Superconductivity. I.” Phys. Rev. **122**, 345 (1961).

[36] Y. Nambu and G. Jona-Lasinio, “Dynamical Model of Elementary Particles Based on an Analogy with Superconductivity. II,” Phys. Rev. **124**, 246 (1961).

[37] K. Fukushima, “Chiral effective model with the Polyakov loop,” Phys. Lett. B **591**, 277 (2004).

[38] C. Ratti, M. A. Thaler, and W. Weise, “Phases of QCD: Lattice thermodynamics and a field theoretical model,” Phys. Rev. D **73**, 014019 (2006).

[39] C. Sasaki, B. Friman, and K. Redlich, “Susceptibilities and the Phase Structure of a Chiral Model with Polyakov Loops,” Phys. Rev. D **75**, 074013 (2007).

[40] S. Roessner, C. Ratti, and W. Weise, “Polyakov loop, diquarks and the two-flavour phase diagram,” Phys. Rev. D **75**, 034007 (2007).

[41] K. Fukushima, “Phase diagrams in the three-flavor Nambu-Jona-Lasinio model with the Polyakov loop,” Phys. Rev. D **77**, 114028 (2008).

[42] B.-J. Schaefer, J. M. Pawlowski, and J. Wambach, “The Phase Structure of the Polyakov-Quark-Meson Model,” Phys. Rev. D **76**, 074023 (2007).

[43] B.-J. Schaefer, M. Wagner, and J. Wambach, “Thermodynamics of (2+1)-flavor QCD: Confronting Models with Lattice Studies,” Phys. Rev. D **81**, 074013 (2010).

[44] A. J. Mizher, M. N. Chernodub, and E. S. Fraga, “Phase diagram of hot QCD in an external magnetic field: possible splitting of deconfinement and chiral transitions,” Phys. Rev. D **82**, 105016 (2010).

[45] T. K. Herbst, J. M. Pawlowski, and B.-J. Schaefer, “The phase structure of the Polyakov–quark-meson model beyond mean field,” Phys. Lett. B **696**, 58 (2011).

[46] V. Skokov, B. Stokic, B. Friman, and K. Redlich, “Meson fluctuations and thermodynamics of the Polyakov loop extended quark-meson model,” Phys. Rev. C **82**, 015206 (2010).

[47] V. Skokov, B. Friman, E. Nakano, K. Redlich, and B.-J. Schaefer, “Vacuum fluctuations and the thermodynamics of chiral models,” Phys. Rev. D **82**, 034029 (2010).

[48] V. Skokov, B. Friman, and K. Redlich, “Quark number fluctuations in the Polyakov loop-extended quark-meson model at finite baryon density,” Phys. Rev. C **83**, 054904 (2011).

[49] M. Mitter and B.-J. Schaefer, “Fluctuations and the axial anomaly with three quark flavors,” Phys. Rev. D **89**, 054027 (2014).

[50] T. K. Herbst, M. Mitter, J. M. Pawlowski, B.-J. Schaefer, and R. Stiele, “Thermodynamics of QCD at vanishing density,” Phys. Lett. B **731**, 248 (2014).

[51] M. Mitter, J. M. Pawlowski, and N. Strodthoff, “Chiral symmetry breaking in continuum QCD,” Phys. Rev. D **91**, 054035 (2015).

[52] J. Braun, L. Fister, J. M. Pawlowski, and F. Rennecke, “From Quarks and Gluons to Hadrons: Chiral Symmetry Breaking in Dynamical QCD,” Phys. Rev. D **94**, 034016 (2016).

[53] Fischer, Christian S. and Luecker, Jan and Welzbacher, Christian A., "Phase structure of three and four flavor QCD," Phys. Rev. D **90**, 034022 (2014).

[54] X. Luo (STAR), "Energy Dependence of Moments of Net-Proton and Net-Charge Multiplicity Distributions at STAR," PoS **CPOD2014**, 019 (2015).

[55] P. Braun-Munzinger, K. Redlich, and J. Stachel, "Particle production in heavy ion collisions," *invited review in Quark Gluon Plasma 3, eds. R.C. Hwa and X.N. Wang, (World Scientific Publishing, 2004)*, arXiv:nucl-th/0304013 [nucl-th] .

[56] M. M. Aggarwal *et al.* (STAR), "An Experimental Exploration of the QCD Phase Diagram: The Search for the Critical Point and the Onset of De-confinement," (2010), arXiv:1007.2613 [nucl-ex] .

[57] M. A. Stephanov, K. Rajagopal, and E. V. Shuryak, "Signatures of the tricritical point in QCD," Phys. Rev. Lett. **81**, 4816 (1998).

[58] M. A. Stephanov, K. Rajagopal, and E. V. Shuryak, "Event-by-event fluctuations in heavy ion collisions and the QCD critical point," Phys. Rev. D **60**, 114028 (1999).

[59] M. Asakawa, U. W. Heinz, and B. Muller, "Fluctuation probes of quark deconfinement," Phys. Rev. Lett. **85**, 2072 (2000).

[60] S. Jeon and V. Koch, "Charged particle ratio fluctuation as a signal for QGP," Phys. Rev. Lett. **85**, 2076 (2000).

[61] B. Friman, F. Karsch, K. Redlich, and V. Skokov, "Fluctuations as probe of the QCD phase transition and freeze-out in heavy ion collisions at LHC and RHIC," Eur. Phys. J. C **71**, 1694 (2011).

[62] S. Ejiri, C. R. Allton, M. Doring, S. J. Hands, O. Kaczmarek, F. Karsch, E. Laermann, and K. Redlich, "Fluctuations in the vicinity of the phase transition line for two flavor QCD," Nucl. Phys. Proc. Suppl. **140**, 505 (2005).

[63] C. R. Allton, M. Doring, S. Ejiri, S. J. Hands, O. Kaczmarek, F. Karsch, E. Laermann, and K. Redlich, "Thermodynamics of two flavor QCD to sixth order in quark chemical potential," Phys. Rev. D **71**, 054508 (2005).

[64] S. Ejiri, F. Karsch, and K. Redlich, "Hadronic fluctuations at the QCD phase transition," Physics Letters B **633**, 275 (2006).

[65] F. Karsch, S. Ejiri, and K. Redlich, "Hadronic fluctuations in the QGP," Nucl. Phys. A **774**, 619 (2006).

[66] F. Karsch and K. Redlich, "Probing freeze-out conditions in heavy ion collisions with moments of charge fluctuations," Phys. Lett. B **695**, 136 (2011).

[67] C. Sasaki, B. Friman, and K. Redlich, "Density fluctuations in the presence of spinodal instabilities," Phys. Rev. Lett. **99**, 232301 (2007).

[68] C. Sasaki, B. Friman, and K. Redlich, "Quark Number Fluctuations in a Chiral Model at Finite Baryon Chemical Potential," Phys. Rev. D **75**, 054026 (2007).

[69] H. Gies, "Introduction to the functional RG and applications to gauge theories," Lect. Notes Phys. **852**, 287 (2012).

[70] C. Wetterich, “Exact evolution equation for the effective potential,” Phys. Lett. B **301**, 90 (1993).

[71] T. R. Morris, “The Exact renormalization group and approximate solutions,” Int. J. Mod. Phys. A **09**, 2411 (1994).

[72] J. Berges, N. Tetradis, and C. Wetterich, “Nonperturbative renormalization flow in quantum field theory and statistical physics,” Phys. Rept. **363**, 223 (2002).

[73] J. Polonyi, “Lectures on the functional renormalization group method,” Central Eur. J. Phys. **1**, 1 (2003).

[74] P. Kopietz, L. Bartosch, and F. Schütz, “Introduction to the functional renormalization group,” Lect. Notes Phys. **798**, 1 (2010).

[75] M. Gell-Mann and M. Levy, “The axial vector current in beta decay,” Nuovo Cim. **16**, 705 (1960).

[76] V. Koch, “Aspects of chiral symmetry,” Int. J. Mod. Phys. E **06**, 203 (1997).

[77] B. C. Hall, *Lie Groups, Lie Algebras, and Representations* (Springer International Publishing, 2015).

[78] A. B. Migdal, “Pion Fields in Nuclear Matter,” Rev. Mod. Phys. **50**, 107 (1978).

[79] A. Andronic, P. Braun-Munzinger, and J. Stachel, “Hadron production in central nucleus-nucleus collisions at chemical freeze-out,” Nucl. Phys. A **772**, 167 (2006).

[80] A. Andronic, P. Braun-Munzinger, and J. Stachel, “Thermal hadron production in relativistic nuclear collisions: The Hadron mass spectrum, the horn, and the QCD phase transition,” Phys. Lett. B **673**, 142 (2009).

[81] J. Cleymans, H. Oeschler, K. Redlich, and S. Wheaton, “Comparison of chemical freeze-out criteria in heavy-ion collisions,” Phys. Rev. C **73**, 034905 (2006).

[82] K. Fukushima, “Effects of chiral restoration on the behavior of the Polyakov loop at strong coupling,” Phys. Lett. B **553**, 38 (2003).

[83] K. Fukushima, “Relation between the Polyakov loop and the chiral order parameter at strong coupling,” Phys. Rev. D **68**, 045004 (2003).

[84] P. M. Lo, B. Friman, O. Kaczmarek, K. Redlich, and C. Sasaki, “Polyakov loop fluctuations in SU(3) lattice gauge theory and an effective gluon potential,” Phys. Rev. D **88**, 074502 (2013).

[85] M. Kitazawa, T. Koide, T. Kunihiro, and Y. Nemoto, “Chiral and color superconducting phase transitions with vector interaction in a simple model,” Prog. Theor. Phys. **108**, 929 (2002).

[86] S. A. Antonenko and A. I. Sokolov, “Critical exponents for 3-D O(n) - symmetric model with n > 3,” Phys. Rev. E **51**, 1894 (1995).

[87] D. Nickel, “Inhomogeneous phases in the Nambu-Jona-Lasino and quark-meson model,” Phys. Rev. D **80**, 074025 (2009).

[88] S. Carignano, D. Nickel, and M. Buballa, “Influence of vector interaction and Polyakov loop dynamics on inhomogeneous chiral symmetry breaking phases,” Phys. Rev. D **82**, 054009 (2010).

[89] S. Carignano, M. Buballa, and B.-J. Schaefer, "Inhomogeneous phases in the quark-meson model with vacuum fluctuations," Phys. Rev. D **90**, 014033 (2014).

[90] M. Buballa and S. Carignano, "Inhomogeneous chiral condensates," Prog. Part. Nucl. Phys. **81**, 39 (2015).

[91] D. F. Litim, "Optimized renormalization group flows," Phys. Rev. D **64**, 105007 (2001).

[92] D. F. Litim, "Optimization of the exact renormalization group," Phys. Lett. B **486**, 92 (2000).

[93] J. Braun, H.-J. Pirner, and K. Schwenzer, "Linking the quark meson model with qcd at high temperature," Phys. Rev. D **70**, 085016 (2004).

[94] K. Kamikado, N. Strodthoff, L. von Smekal, and J. Wambach, "Fluctuations in the quark-meson model for QCD with isospin chemical potential," Phys. Lett. B **718**, 1044 (2013).

[95] R.-A. Tripolt, N. Strodthoff, L. von Smekal, and J. Wambach, "Spectral Functions for the Quark-Meson Model Phase Diagram from the Functional Renormalization Group," Phys. Rev. D **89**, 034010 (2014).

[96] F. Rennecke, "Vacuum structure of vector mesons in QCD," Phys. Rev. D **92**, 076012 (2015).

[97] J. Eser, M. Grahl, and D. H. Rischke, "Functional Renormalization Group Study of the Chiral Phase Transition Including Vector and Axial-vector Mesons," Phys. Rev. D **92**, 096008 (2015).

[98] B.-J. Schaefer and J. Wambach, "The Phase diagram of the quark meson model," Nucl. Phys. A **757**, 479 (2005).

[99] M. Galassi and B. Gough, *GNU Scientific Library: Reference Manual*, GNU manual (Network Theory, 2009).

[100] D. F. Litim, "Critical exponents from optimized renormalization group flows," Nucl. Phys. B **631**, 128 (2002).

[101] B. Stokic, B. Friman, and K. Redlich, "The Functional Renormalization Group and O(4) scaling," Eur. Phys. J. C **67**, 425 (2010).

[102] J. P. Boyd, *Chebyshev and Fourier Spectral Methods, Second Edition* (DOVER Publications, Inc., 2001).

[103] C. S. Fischer and H. Gies, "Renormalization flow of Yang-Mills propagators," JHEP **10**, 048 (2004).

[104] J. Borchardt and B. Knorr, "Global solutions of functional fixed point equations via pseudospectral methods," Phys. Rev. D **91**, 105011 (2015).

[105] J. Borchardt and B. Knorr, "Solving functional flow equations with pseudospectral methods," Phys. Rev. D **94**, 025027 (2016).

[106] S. Ejiri, F. Karsch, E. Laermann, C. Miao, S. Mukherjee, *et al.*, "On the magnetic equation of state in (2+1)-flavor QCD," Phys. Rev. D **80**, 094505 (2009).

[107] O. Kaczmarek, F. Karsch, E. Laermann, C. Miao, S. Mukherjee, *et al.*, "Phase boundary for the chiral transition in (2+1) -flavor QCD at small values of the chemical potential," Phys. Rev. D **83**, 014504 (2011).

[108] H. T. Ding, A. Bazavov, F. Karsch, Y. Maezawa, S. Mukherjee, and P. Petreczky, “Chiral phase transition of $N_f = 2+1$ QCD with the HISQ action,” PoS **LATTICE2013**, 157 (2014).

[109] H.-T. Ding and P. Hegde (Bielefeld-BNL-CCNU), “Chiral phase transition of $N_f = 2+1$ and 3 QCD at vanishing baryon chemical potential,” PoS **LATTICE2015**, 161 (2016).

[110] G. Amelino-Camelia and S.-Y. Pi, “Selfconsistent improvement of the finite temperature effective potential,” Phys. Rev. D **47**, 2356 (1993).

[111] G. Amelino-Camelia, “Thermal effective potential of the O(N) linear sigma model,” Phys. Lett. B **407**, 268 (1997).

[112] N. Petropoulos, “Linear sigma model and chiral symmetry at finite temperature,” J. Phys. G **25**, 2225 (1999).

[113] J. T. Lenaghan and D. H. Rischke, “The O(N) model at finite temperature: Renormalization of the gap equations in Hartree and large N approximation,” J. Phys. G **26**, 431 (2000).

[114] J. T. Lenaghan, D. H. Rischke, and J. Schaffner-Bielich, “Chiral symmetry restoration at nonzero temperature in the SU(3)(r) x SU(3)(l) linear sigma model,” Phys. Rev. D **62**, 085008 (2000).

[115] A. Jakovac, A. Patkos, Z. Szep, and P. Szepfalusy, “T - mu phase diagram of the chiral quark model from a large flavor number expansion,” Phys. Lett. B **582**, 179 (2004).

[116] J. O. Andersen, D. Boer, and H. J. Warringa, “Thermodynamics of O(N) sigma models: 1/N corrections,” Phys. Rev. D **70**, 116007 (2004).

[117] J. O. Andersen and T. Brauner, “Linear sigma model at finite density in the 1/N expansion to next-to-leading order,” Phys. Rev. D **78**, 014030 (2008).

[118] J. Zinn-Justin, *Quantum Field Theory and Critical Phenomena*, International series of monographs on physics (Clarendon Press, 2002).

[119] J. Engels and T. Mendes, “Goldstone mode effects and scaling function for the three-dimensional O(4) model,” Nucl. Phys. B **572**, 289 (2000).

[120] G. A. Almasi, W. Tarnowski, B. Friman, and K. Redlich, “Scaling violation and the magnetic equation of state in chiral models,” Phys. Rev. D **95**, 014007 (2017).

[121] L. Landau and E. Lifshitz, *Statistical Physics*, Bd. 5 (Elsevier Science, 2013).

[122] L. Dolan and R. Jackiw, “Symmetry Behavior at Finite Temperature,” Phys. Rev. D **9**, 3320 (1974).

[123] B. Klajn, “Exact high temperature expansion of the one-loop thermodynamic potential with complex chemical potential,” Phys. Rev. D **89**, 036001 (2014).

[124] T. S. Chang, A. Hankey, and H. E. Stanley, “Double-power scaling functions near tricritical points,” Phys. Rev. B **7**, 4263 (1973).

[125] T. S. Chang, A. Hankey, and H. E. Stanley, “Generalized scaling hypothesis in multi-component systems. i. classification of critical points by order and scaling at tricritical points,” Phys. Rev. B **8**, 346 (1973).

[126] G. Baym, “Selfconsistent approximation in many body systems,” Phys. Rev. **127**, 1391 (1962).

[127] J. M. Cornwall, R. Jackiw, and E. Tomboulis, “Effective Action for Composite Operators,” Phys. Rev. D **10**, 2428 (1974).

[128] H. van Hees and J. Knoll, “Renormalization in selfconsistent approximations schemes at finite temperature. 1. Theory,” Phys. Rev. D **65**, 025010 (2002).

[129] H. Van Hees and J. Knoll, “Renormalization of selfconsistent approximation schemes. 2. Applications to the sunset diagram,” Phys. Rev. D **65**, 105005 (2002).

[130] H. van Hees and J. Knoll, “Renormalization in selfconsistent approximation schemes at finite temperature. 3. Global symmetries,” Phys. Rev. D **66**, 025028 (2002).

[131] R. J. Baxter, *Exactly Solved Models in Statistical Mechanics* (Academic Press Inc., London, 1982).

[132] J. Engels and F. Karsch, “Finite size dependence of scaling functions of the three-dimensional O(4) model in an external field,” Phys. Rev. D **90**, 014501 (2014).

[133] O. Bohr, B. J. Schaefer, and J. Wambach, “Renormalization group flow equations and the phase transition in O(N) models,” Int. J. Mod. Phys. A **16**, 3823 (2001).

[134] J. Braun, B. Klein, and P. Piasecki, “On the scaling behavior of the chiral phase transition in QCD in finite and infinite volume,” Eur. Phys. J. C **71**, 1576 (2011).

[135] M. I. Gorenstein and M. Gaździcki, “Strongly intensive quantities,” Phys. Rev. C **84**, 014904 (2011).

[136] V. Skokov, B. Friman, and K. Redlich, “Volume fluctuations and higher-order cumulants of the net baryon number,” Phys. Rev. C **88**, 034911 (2013).

[137] V. Begun, “Participant number fluctuations for higher moments of a multiplicity distribution,” (2016), arXiv:1606.05358 [nucl-th] .

[138] P. Braun-Munzinger, A. Rustamov, and J. Stachel, “Bridging the gap between event-by-event fluctuation measurements and theory predictions in relativistic nuclear collisions,” Nuclear Physics A **960**, 114 (2017).

[139] S. Borsanyi, G. Endrodi, Z. Fodor, S. D. Katz, and K. K. Szabo, “Precision SU(3) lattice thermodynamics for a large temperature range,” JHEP **07**, 56 (2012).

[140] B.-J. Schaefer and J. Wambach, “Susceptibilities near the qcd (tri)critical point,” Phys. Rev. D **75**, 085015 (2007).

[141] Y. Hatta and T. Ikeda, “Universality, the QCD critical / tricritical point and the quark number susceptibility,” Phys. Rev. D **67**, 014028 (2003).

[142] A. Bazavov *et al.*, “The QCD Equation of State to $\mathcal{O}(\mu_B^6)$ from Lattice QCD,” Phys. Rev. D **95**, 054504 (2017).

[143] F. Karsch, “Lattice QCD results on cumulant ratios at freeze-out,” J. Phys. Conf. Ser. **779**, 012015 (2017).

[144] L. Adamczyk *et al.* (STAR Collaboration), “Energy dependence of moments of net-proton multiplicity distributions at rhic,” Phys. Rev. Lett. **112**, 032302 (2014).

[145] X. Luo, "Exploring the QCD Phase Structure with Beam Energy Scan in Heavy-ion Collisions," Nucl. Phys. A **956**, 75 (2016).

[146] A. Bzdak and V. Koch, "Acceptance corrections to net baryon and net charge cumulants," Phys. Rev. C **86**, 044904 (2012).

[147] A. Bzdak, V. Koch, and V. Skokov, "Baryon number conservation and the cumulants of the net proton distribution," Phys. Rev. C **87**, 014901 (2013).

[148] M. Kitazawa and M. Asakawa, "Revealing baryon number fluctuations from proton number fluctuations in relativistic heavy ion collisions," Phys. Rev. C **85**, 021901 (2012).

[149] M. Kitazawa and M. Asakawa, "Relation between baryon number fluctuations and experimentally observed proton number fluctuations in relativistic heavy ion collisions," Phys. Rev. C **86**, 024904 (2012).

[150] A. Bazavov *et al.*, "Freeze-out Conditions in Heavy Ion Collisions from QCD Thermodynamics," Phys. Rev. Lett. **109**, 192302 (2012).

[151] G. A. Almási, B. Friman, and K. Redlich, "Modeling chiral criticality and its consequences for heavy-ion collisions," Nucl. Phys. A **956**, 356 (2016).

[152] W.-j. Fu and J. M. Pawlowski, "Correlating the skewness and kurtosis of baryon number distributions," Phys. Rev. D **93**, 091501 (2016).

[153] R. Esha, "Measurement of the cumulant of net-proton multiplicity distribution in Au+Au collisions at $\sqrt{s_{NN}}$ =7.7-200 GeV from the STAR experiment," Quark Matter talk (2017).

[154] L. F. Palhares, E. S. Fraga, and T. Kodama, "Chiral transition in a finite system and possible use of finite size scaling in relativistic heavy ion collisions," J. Phys. G **38**, 085101 (2011).

[155] E. S. Fraga, L. F. Palhares, and P. Sorensen, "Finite-size scaling as a tool in the search for the QCD critical point in heavy ion data," Phys. Rev. C **84**, 011903 (2011).

[156] L. F. Palhares and E. S. Fraga, "Finite-size scaling as a tool for the search of the critical endpoint of QCD in heavy-ion data," Phys. Atom. Nucl. **75**, 906 (2012).

[157] M. Hippert, E. S. Fraga, and E. M. Santos, "Critical versus spurious fluctuations in the search for the QCD critical point," Phys. Rev. D **93**, 014029 (2016).

[158] G. Almasi, R. Pisarski, and V. Skokov, "Volume dependence of baryon number cumulants and their ratios," Phys. Rev. D **95**, 056015 (2017).

[159] J. Braun and B. Klein, "Scaling functions for the O(4)-model in d=3 dimensions," Phys. Rev. D **77**, 096008 (2008).

[160] J. Braun, B. Klein, and B.-J. Schaefer, "On the Phase Structure of QCD in a Finite Volume," Phys. Lett. B **713**, 216 (2012).

[161] R.-A. Tripolt, J. Braun, B. Klein, and B.-J. Schaefer, "Effect of fluctuations on the QCD critical point in a finite volume," Phys. Rev. D **90**, 054012 (2014).

[162] L. Fister and J. M. Pawlowski, "Functional renormalization group in a finite volume," Phys. Rev. D **92**, 076009 (2015).

[163] A. Juričić and B.-J. Schaefer, “Chiral Thermodynamics in a finite box,” (2016) arXiv:1611.03653 [hep-ph] .

[164] T. K. Herbst, J. M. Pawlowski, and B.-J. Schaefer, “Phase structure and thermodynamics of QCD,” Phys. Rev. D **88**, 014007 (2013).

Acknowledgements

I owe my deepest gratitude to my supervisor, Prof. Bengt Friman. He introduced me to this beautiful and complex field during my two-months stay at the GSI summer school. During the summer school and my PhD, his door was always open and he was always happy to have some discussions. He provided the guidance I needed yet he was always open to hear my ideas and he let me choose my path. Without him, this work would not have been possible. I also thank him for securing the financial background during my entire stay.

I am deeply grateful to Prof. Krzysztof Redlich as well, with whom I was lucky to be able to collaborate on several different topics. His insight into the field was invaluable during my work, and the discussions with him were always fruitful and interesting.

My special thanks to Vladimir Skokov and Robert Pisarski, who hosted me for a two-months stay at BNL. Thank you Vladimir for the motivating, intense and very fruitful collaboration and for sharing your passion towards science.

I am grateful to Prof. Tetyana Galatyuk not only for being in my PhD committee, but also for her suggestions and her guidance during these three and a half years. I want to thank Prof. Jochen Wambach as well for his valuable comments during my PhD committee meetings.

I would like to express my thanks to Maximilian Eller for the interesting work and stimulating discussions on black holes. I really enjoyed working on something out of the field for some time. I am also grateful to Thomas Jahn for the collaboration on the scaling properties of the QM model, for his perseverance in making the numerics work, and also for proofreading parts of my thesis and translating my abstract. I feel very lucky to be involved in their supervision.

I am indebted to HGS-HIRe for providing financial support and for organizing many interesting events. In particular, I am thankful for the organization of the HQM lecture weeks broadening my scientific horizon and for the organization of soft-skill courses, which, in my opinion, help the students to get along in the scientific world.

I owe a very important debt to GSI for providing me workspace and working conditions throughout my stay. I am also thankful to the former and current members of the Theory Department for the stimulating discussions and interesting seminars. I am particularly grateful to Enrico Speranza, Xiaoyu Guo and Sofija Antić, who were not only colleagues to me, but also friends.

Last but not least, I would like to thank my dear parents for their constant sacrifice to support me, for always motivating me and for always trusting me. Without their endless support, I would not be where I am today.

Curriculum vitae

Name: Gábor András Almási
Date of birth: 22/12/1989
Place of birth: Pécs, Hungary
Marital status: single

Education and degrees

2008 - 2011	Bachelor studies at the Eötvös Lóránd University, Budapest
2011 - 2013	Master studies at the Eötvös Lóránd University, Budapest
2013	Master of Science, Master thesis on: *Modification of vector-meson spectra in heavy-ion collisions*
2013 - 2017	Postgraduate studies at the Technische Universität Darmstadt